The Dissertation Committee for Reika Katsumata Certifies that this is the approved version of the following dissertation:

Effect of Interfaces on Thermophysical Properties and Block Copolymer Self-Assembly in Polymer Thin Films

Committee:

Christopher J. Ellison, Supervisor

Carlton G. Willson

Isaac C. Sanchez

Nanshu Lu

Effect of Interfaces on Thermophysical Properties and Block Copolymer Self-Assembly in Polymer Thin Films

by

Reika Katsumata, B.E.; M.E.

Dissertation

Presented to the Faculty of the Graduate School of

The University of Texas at Austin

in Partial Fulfillment

of the Requirements

for the Degree of

Doctor of Philosophy

The University of Texas at Austin

December 2016

Dedication

Dedicated to my family.

Acknowledgements

First, I would like to thank my advisor, Professor Christopher J. Ellison, who taught me that conducting research is not a 100-meter sprint, but more like running a marathon. I cannot think of going through all hardships and exciting findings that I face in grad school without his encouragements, mentoring, and dedication to helping me.

I would like to thank my parents, Akihiko and Hiromi Katsumata for all their support and love, and always being cheerful over the years. Your working style taught me to work on something that I have a passion for, and play hard to work hard.

I am grateful to wonderful current and former lab members in the Ellison and the Willson group: Chae Bin Kim, Sunshine Zhou, Yunping Fei, Gregory Blachut, Dr. Amanda Jones, Heonjoo Ha, Melanie Merrick, Alysha Helenic, Han Xiao, Michael Maher, Xiaohan Wang, Andrew Dick, Dr. Joon Hee Cho, Dr. Dustin Janes, Dr. Yichen Fang, Dr. Kadhir Shanmuganathan, Dr. Sateesh Peddini, Dr. Zhenpeng Li, Dr. Joshua Katzenstein, and Dr. William Durand. Even during the days when I struggled with research, you guys brought me to lab, and I am very lucky to have real friends in lab who helped me in both professional and casual ways. Also, I have been very fortunate to work with talented undergraduate and high school students: Austin Dulaney, Kendall Mueller, Neel Raman, and Helen Wong, who have been phenomenally helpful and gave me a lot of inspiration. I appreciate Professor C. Grant Willson, Professor Roger T. Bonnecaze, and Professor Nathaniel Lynd for their mentorship. I would like to thank to friendly and extremely helpful staff members as well.

I am also grateful to my mentors who guided me to the polymer world at Tokyo Institute of Technology. Professor Toshiaki Ougizawa, Professor Keiichi Kuboyama,

Effect of Interfaces on Thermophysical Properties and Block Copolymer Self-Assembly in Polymer Thin Films

Reika Katsumata, Ph.D.

The University of Texas at Austin, 2016

Supervisor: Christopher J. Ellison

When materials are tailored for use at the nanoscale, thermophysical properties can deviate from their bulk values, and these phenomena are broadly referred to as nanoconfinement effects.   In thin films, one of the critical factors of nanoconfinement effects is interfacial interactions; as the film thickness decreases, the interfacial area to volume ratio increases dramatically, often causing interfacial effects to dominate the properties of the entire film.   As polymers continue to be leveraged in nanotechnology, from nanocomposites to lithography, understanding the effects of interfaces is highly desired.

While numerous studies have revealed how thermophysical properties, (e.g., glass transition temperature (T_g), self-diffusion coefficient (D), and effective viscosity (η_{eff}) change with film thickness, correlations between these parameters are still unclear. Herein, the T_g, D, and η_{eff} are measured for a model system of unentangled poly(isobutyl methacrylate) (PiBMA, 16-300 nm thick) supported by SiO_x.   The non-bulk-like correlation between T_g, D, and η_{eff} is successfully explained using a three-layer model. To further investigate the effect of confining interfaces, the T_g and D of PiBMA are studied for four multilayer geometries, where the interfacial interactions are varied from strong to weak.   The T_g-D relationship of thin films deviates from bulk behavior, and the

magnitude of the deviations depends on the polymer-substrate interactions. A friction analysis reveals that this deviation originates from heterogeneous dynamics near the confining interfaces.

Engineering interfaces between polymers and substrates is also crucial for BCP lithography, especially on non-traditional substrates (e.g. flexible or 2D materials). In particular, precise control of the surface energy of the underlying substrate is required to produce lithographically useful structures, such as lamellar domains oriented perpendicular to the substrate. In this study, polydopamine is first exploited as a universal adhesive to enable BCP nanopatterning on a variety of flexible materials. In addition, we developed a potentially scalable graphene nanoribbon fabrication method using wetting-transparency assisted BCP lithography. Lastly, inspired by the wetting transparency phenomenon, possible techniques to control the microdomain orientations of BCPs *through* thin layers are explored using a model bi-layer substrate made from homopolymers of each block, along with a theoretical model based on van der Waals forces.

Table of Contents

List of Tables

List of Figures

xx

xxiv

NANOCONFINEMENT EFFECTS ON THERMOPHYSICAL PROPERTIES OF THIN FILMS

When materials are tailored for use at the nanoscale, material properties can deviate from their bulk values and these phenomena are broadly referred to as nanoconfinement effects. Examples of properties that can be impacted by nanoconfinement effects include the glass transition temperature (T_g),[1-7] viscosity (η),[8-11] modulus,[12-14] and self-diffusion coefficient (D),[15-17] among others. As polymers continue to be leveraged for use in nanotechnology applications, from nanocomposites to lithography, developing a more complete picture of how polymer mobility is influenced by nanoconfinement is highly desired.

The origin of the nanoconfinement effect is convoluted by two factors: finite size effects and interfacial effects.[18] The former is due to the intrinsic spatial restriction for nanoconfined materials while the latter is due to the higher surface area to volume ratio. Nanoconfinement can also be classified by the dimensions by which the molecules are restricted.[18] Based on this definition, thin films are one-, nanofibers are two-, and nanocomposites are three-dimensional examples of nanoconfinement, respectively. In this study, one-dimensional nanoconfinement in thin films is of primary interest because it is relatively easy to prepare well-controlled uniform samples with different interfaces.

In Chapter 1, background for studying and understanding mobility of nanoconfined polymers is introduced. To enable discussion of nanoconfinement effects, an overview of bulk relationships between thermophysical properties of interest (e.g., T_g, η, and D) is first presented. This overview additionally summarizes previous work on the measurements of T_g, η, and D as a function of film thickness. This chapter

concludes by discussing current challenges for studying the effect of nanoconfinement on different thermophysical properties and presents the main objectives of this dissertation.

Chapter 2 describes the development of a novel fluorescence technique to measure D in thin films. Specifically, this section includes control experiments to account for the effects of self-quenching and photobleaching, which have often been overlooked. This fluorescence-based methodology for evaluation of D could potentially be generalized to other polymer and non-polymer systems.

The T_g, D, and effective viscosity (η_{eff}) are measured for a thin film system of unentangled poly(isobutyl methacrylate) (PiBMA) supported by SiO_x in Chapter 3. Both the T_g and D were found to be independent of the film thickness, while η_{eff} decreased with decreasing film thickness. A three-layer model, considering interfacial effects, successfully described this unique thickness dependence.

The effects of interfaces on the relationship between T_g and D of unentangled PiBMA are investigated in Chapter 4. The T_g–D relationship of the PiBMA thin films deviated from the bulk behavior, and the magnitude of the deviations depended on polymer/substrate interactions. A friction analysis revealed that this deviation originated from the existence of heterogeneous dynamics near confining interfaces.

Chapter 1:   Introduction to mobility of nanoconfined polymers

By understanding polymer dynamics on a range of length scales, prediction of physical properties, from glass to melt states and *vice versa*, becomes possible.   These relationships between various thermophysical properties are especially important for polymer processing because polymers are often processed in the melt state, but are used in the glassy state.   Interestingly, when the target material dimensions are smaller than a few hundred nanometers, nanoconfinement effects often must be taken into consideration.   First, Chapter 1.1 defines thermophysical properties such as the T_g, η and D, which are the primary focus of this thesis because these properties are relatively well studied for both bulk polymers and thin films providing a basis for comparison. Then bulk relationships between those physical properties are described.   In Chapter 1.2, prior works that have investigated T_g, η and D in thin films are reviewed, and current challenges in studying these parameters are discussed.

1.1   CORRELATIONS BETWEEN THERMOPHYSICAL PROPERTIES IN BULK

Prior to discussing nanoconfinement effects, correlations between the thermophysical properties of bulk polymers are summarized in this section.   In terms of dynamic length scale, T_g reflects the cooperative segmental mobility of 10s-100s repeat units, whereas D and η are related to the large-scale transport motion of the entire chain. As shown in Figure 1.1, T_g-D, and T_g-η are related through the Williams-Landel-Ferry (WLF) equation[19] as described in Chapter 1.1.1, while the D-η relationship in bulk follows the Stokes-Einstein (SE) equation as described in Chapter 1.1.2.
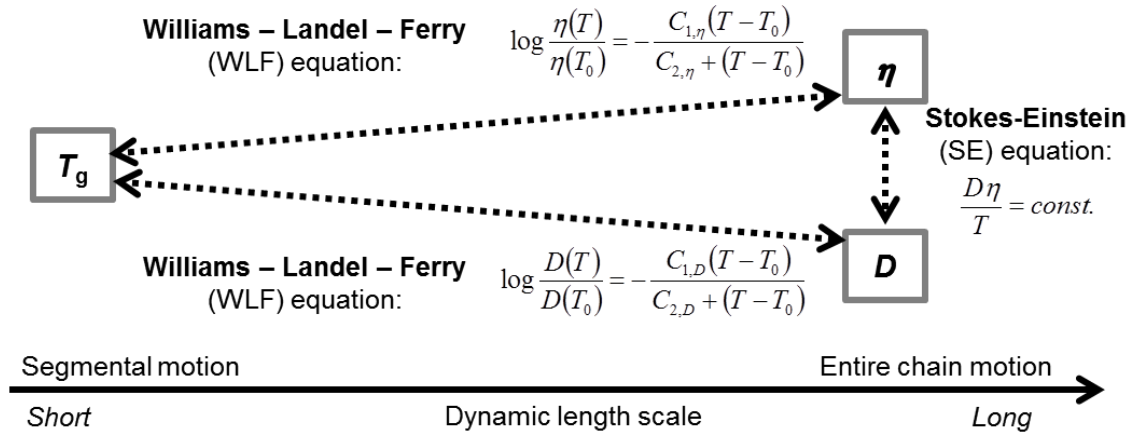
Figure 1.1: Schematic illustration of the bulk relationship between the T_g (glass transition temperature), η (viscosity), and the self-diffusion coefficient (D), where T is the absolute temperature, T_0 is the reference temperature, and C_1 and C_2 are the constants.

1.1.1 Williams-Landel-Ferry equation

The relationships of T_g-η and T_g-D are well accepted in bulk systems through the WLF equation.[19-22] The temperature dependence of η and D can be described using a shift factor a_T, corresponding to a ratio of the parameter of interest at the experimental temperature (T) to its value at a reference temperature (T_0).[23] In the case of η, for example, a_T can be expressed as Eq. 1.1.

$$a_T = \frac{\eta(T)}{\eta(T_0)} \tag{1.1}$$

and therefore, $\log a_T$ can be written as

$$\log a_T = -\frac{C_1(T - T_0)}{C_2 + (T - T_0)} \tag{1.2}$$

where, C_1 and C_2 are characteristic material constants (WLF equation). In practice, both D and η undergo large many order-in-magnitude increases as T_g is approached upon cooling.

4

1.1.2 Stokes-Einstein relationship

The SE equation describes the correlation between D and η via friction between molecules. From a force balance between the chemical potential gradient and drag force, D can be written with the friction constant (ζ) between molecules as shown in Eq. 1.3, where k_B is the Boltzmann constant.[24] Assuming the molecule behaves as a perfect sphere with a radius of R, D can be described as a function of η, which is the well-known the SE equation (Eq. 1.4), where the friction constant ζ is the factor that relates D and η.

$$D = k_B T / \zeta \tag{1.3}$$

$$D = \frac{k_B T}{6\pi\eta R} \tag{1.4}$$

The SE equation is not valid for all conditions, and the deviation from this relationship is known as the "breakdown in the Stokes-Einstein relationship." Figure 1.2 shows the relationship between $D\eta/T$ versus T/T_g for inorganic glass formers, tetracene and rubrene.[25] If the Eq. 1.4 is valid, $D\eta/T$ should be invariant with temperature. However, $D\eta/T$ starts to deviate as temperature approaches T_g, i.e. $T/T_g \rightarrow$ 1, for both glass formers.
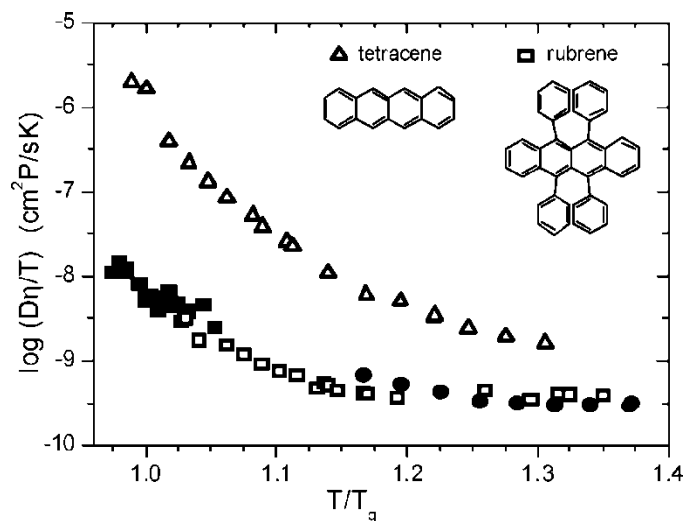
Figure 1.2: *Dη/T* versus *T/T*$_g$. Solid squares and solid circles are *D* multiplied by *η/T*, based on the *D* values from secondary ion mass spectrometry (SIMS) and nuclear magnetic resonance (NMR), respectively. The *η* values measured by a rotational rheometer was adapted from Plazek *et al.*[26] The *D* measurements are also shown for the two probe molecules in tris-naphthylbenzene (TNB). Open triangles and open squares represent tetracene and rubrene in TNB, respectively. The molecular structures of tetracene and rubrene are shown in the inset. Adapted with permission from Swallen *et al.*[25] Copyright 2009, American Chemical Society.

The breakdown of the SE relationship is often explained by a dynamic heterogeneity argument.[27, 28] Figure 1.3 schematically illustrates the regions of spatially heterogeneous dynamics at different temperatures. Near *T*$_g$, the characteristic sizes of slow (red) and fast (blue) domains with a size of ξ$_{het}$ are estimated to be ~ 3 nm, and the time scales of the "slow" and "fast" regions differ by a range of 1-5 orders of magnitude.[28] As temperature increases, ξ$_{het}$ decreases and the difference in characteristic relaxation times decreases as well. In other words, the dynamics of the polymer become more spatially homogeneous at higher temperatures. Such dynamic heterogeneity of glass formers has been observed by multiple experimental methods,

including nuclear magnetic resonance (NMR),[29] observing translation and rotation of fluorescent dyes,[30, 31] and dielectric relaxation.[32, 33]
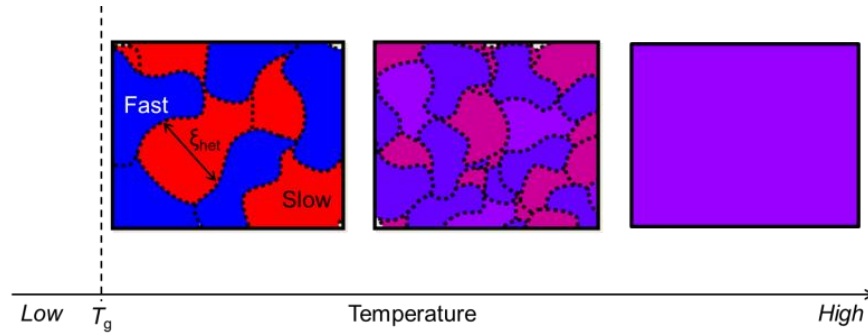
Figure 1.3:   Schematic illustration of regions of spatially heterogeneous segmental dynamics near T_g.   These areas are on the order of ξ_{het} in dimension (typically a few nanometers) and evolve in time.

1.2   GLASS TRANSITION TEMPERATURE, VISCOSITY, AND SELF-DIFFUSION COEFFICIENT IN THIN FILMS

1.2.1   Glass transition temperature

Since 1994, when Keddie *et al.* observed a 20°C T_g depression in polystyrene (PS) thin films using ellipsometry,[1] the effect of nanoconfinement on the T_g of polymer thin films have been extensively studied.[34, 35]   For the most well-studied system, PS supported on SiO_x substrates, numerous studies have reported a decrease in T_g as the PS film thickness decreases below 50 nm[1-4, 36] regardless of the measurement method, as shown in Figure 1.4.   This reduction in PS film T_g was attributed to a higher segmental mobility of the chains near the free surface, and the presence of a relatively weak interaction between the PS film and the SiO_x substrate.[35, 37, 38]   More generally, interactions between polymer films and the neighboring substrates are also known to alter the dynamics of polymers.[39-43]   For instance, the strong interaction between poly(2-vinyl pyridine) and a SiO_x substrate increases the film T_g by up to 40°C while the weaker

7

interaction between PS and SiO_x reduces the T_g by up to 40°C as the film thickness decreases.[5]
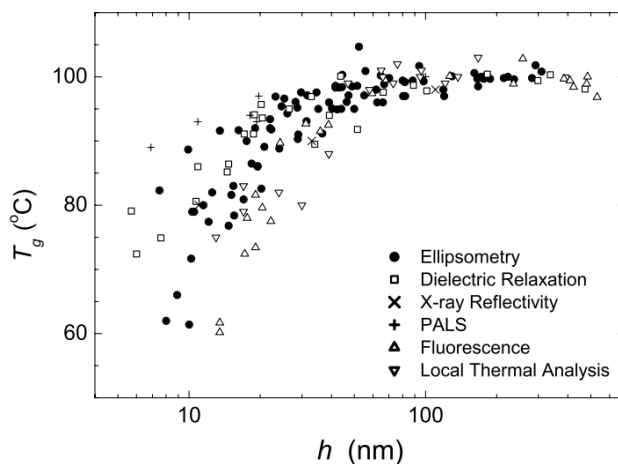
Figure 1.4: T_g as a function of film thickness (h) measured for PS films of different molecular weight (MW) supported on a variety of substrates using six different techniques: ellipsometry, dielectric relaxation, X-ray reflectivity, positron annihilation lifetime spectroscopy (PALS), fluorescence intensity, and local thermal analysis.   Adapted with permission from Roth *et al.*[44] Copyright 2004, Elsevier B.V.

1.2.2   Viscosity

To elucidate nanoconfined polymer dynamics on longer length scales than those related to T_g, the η of polymer thin films has been extensively studied as well.[8, 9, 45-51] The experimental approaches to measure the effective viscosity η_{eff} in polymer thin films include dewetting (hole-growth),[45, 46] embedding nanoparticles,[49, 50] capillary wave evolution,[9] and capillary leveling.[10, 48]   For the PS/SiO_x system, most studies[9, 46, 48] observed that η_{eff} decreased with decreasing film thickness, which is consistent with lower T_g in thin films.   For example, Figure 1.5 shows the low-shear η_{eff} of PS on a SiO_x/Si substrate reported by Masson and Green *et al.* using the hole growth method.

The decrease in η_{eff} was attributed to the lower η at the free surface,[46] which was observed by the embedding particle methods[49, 50].
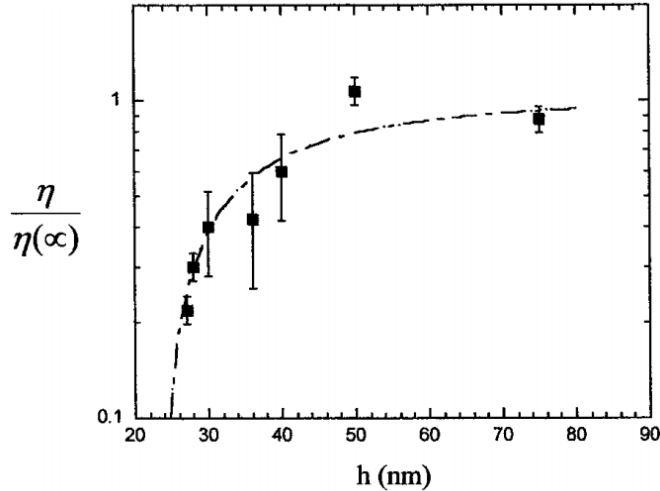
Figure 1.5: The low-shear effective viscosity of PS on SiO$_x$/Si determined by kinetic analysis of film dewetting, which decreases appreciably with decreasing film thickness. Adapted with permission from Masson *et al.*[46] Copyright 2002, American Physical Society.

For the case of a stronger interaction between the polymer film and substrate, the dependence of η on thickness is not as simple as the case of PS on SiO$_x$ substrates. For example, for poly(methyl methacrylate) (PMMA) thin films on SiO$_x$ substrates, the carbonyl group in PMMA can participate in hydrogen bonding with the SiO$_x$ substrate,[52] which is a stronger polymer-substrate interaction than that of PS on SiO$_x$. Due to the stronger polymer-substrate interaction, the T_g of PMMA on SiO$_x$ is reported to increase with a reduction of the PMMA film thickness.[8] Li and Tsui *et al.* measured the η_{eff} of PMMA thin films using the capillary wave method, and showed that the thickness dependence of the η_{eff} varies depending on the temperature (Figure 1.6).[8] At temperatures lower than ~105°C (= $T_{g,bulk}$ + 23°C), the thinner films exhibited lower η_{eff}

with decreasing film thickness, while viscosity increased with decreasing film thickness at temperatures higher than ~ 105°C. This complex behavior can not be described by the classical bulk understanding, such as that described by the WLF and the SE equations. Thus, this non-trivial temperature dependence of the η_{eff} indicates the importance of studying interfaces more systematically.
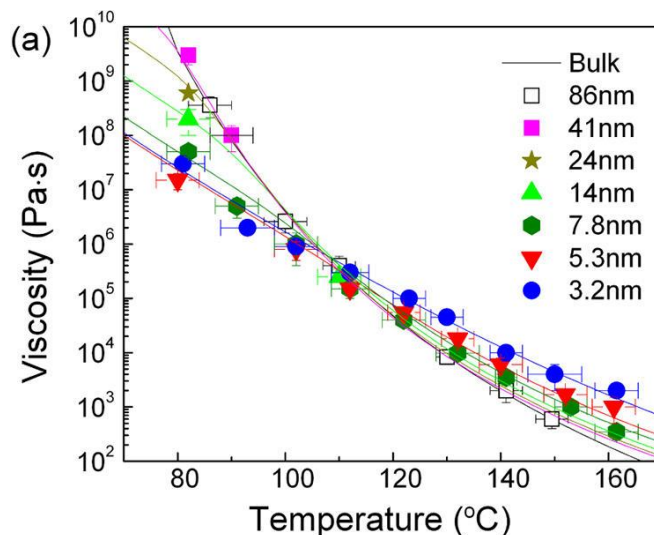
Figure 1.6: (a) Viscosity versus temperature for PMMA (MW = 2.7 kg/mol) films with different thicknesses as indicated in the legend. The solid lines are the best fit to a three-layer model taking the effect of interfaces into account. Adapted with permission from Li *et al.*[8] Copyright 2013, American Chemical Society.

1.2.3 Self-diffusion coefficient

Compared to T_g and the η, fewer studies have been reported for *D*, presumably because a limited number of techniques are available to study this in thin films. The *D* of thin films can be classified based on the direction of flow: out-of-plane (perpendicular to interfaces) and in-plane (parallel to interfaces). For the out-of-plane direction, the *D* of entangled PS on SiO_2 was reported to be reduced by a factor of 2 below a thickness of

≈ 100 nm (≈ 13 R_g) using secondary ion mass spectrometry (SIMS), where R_g is the radius of gyration of the polymer.[17]   For the in-plane direction, fluorescence recovery after patterned photobleaching (FRAPP) measurements showed that the in-plane D of entangled PS was also reduced to half of the bulk D below a thickness of ≈ 150 nm (≈ 50 R_g), as shown in Figure 1.7.[16]   These results suggest that the D in nanoconfined PS films is reduced in both the in-plane and out-of-plane directions, even though the T_g is lower. These observations contradict that expected from the bulk WLF and SE relationships. As has been reported in the previous studies of thin film T_g, the effect of interfacial interactions could play a critical role for thin film D as well.   However, systematic studies of the D of thin films with different interfaces have not yet been conducted.
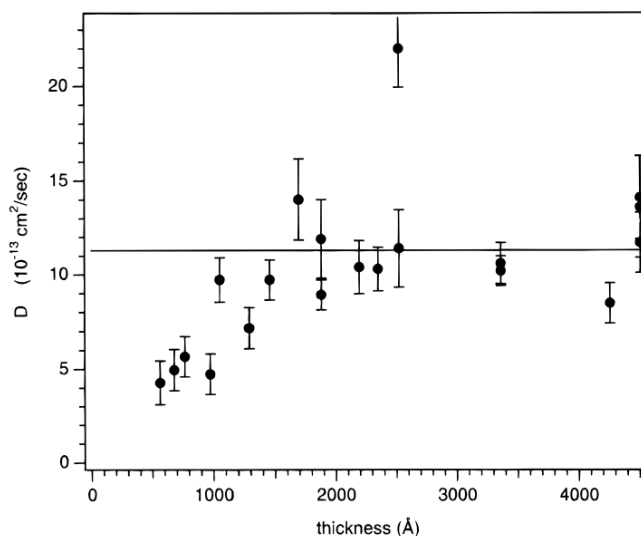
Figure 1.7: D as a function of PS film thickness.   The solid line represents the average of D measured in the thick film regime.   Adapted with permission from Frank et al.[16]   Copyright 1996, American Chemical Society.

11

1.2.3 Relationship between glass transition temperature, viscosity and self-diffusion coefficient

Reviewing the previous work on the PS thickness dependence of T_g, η and D, there are counterintuitive correlations between these parameters which clearly do not follow bulk relationships. For example, assuming the WLF and the SE equations are valid for PS thin films, lower T_g with a reduction of the film thickness should result in lower η and higher D, which conflicts with experimental observation of lower D in PS thin films compared to bulk.[16, 17] Potential interfacial effects between the thin film polymer and the confining interfaces are one explanation for such counter-intuitive correlations between T_g, η and D.

In this dissertation, it is hypothesized that the T_g, η, and D are influenced by nanoconfinement due to the heterogeneity of polymer dynamics (finite size effects) and interfacial interactions (interfacial effects) as shown in Figure 1.8. The heterogeneous dynamics can induce deviations from typical bulk relationships between T_g, η, and D. The finite size effect drastically increases the interfacial area to volume ratio of the system, and the interfaces could alter the spatially heterogeneous dynamics of the polymers depending on the nature of neighboring interfaces.
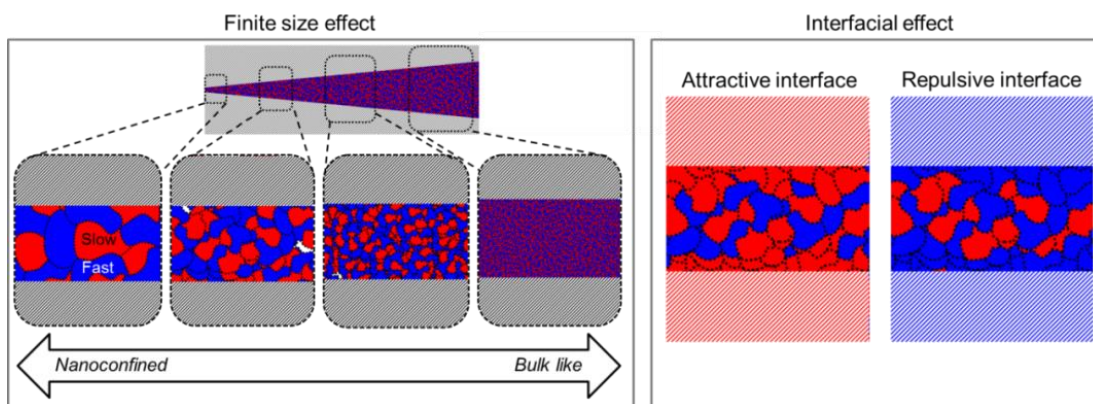
Figure 1.8:   Schematic diagram of the effect of nanoconfinement on segmental polymer dynamics.   The segmental relaxation time of the blue domains is faster than that of the red domains.

1.3   SUMMARY AND OBJECTIVES

Despite over two decades of extensive studies on nanoconfinement effects, the relationship between parameters which characterize polymer dynamics on different length scales is still elusive.[36, 53]   In this study, it is hypothesized that confining interfaces could cause deviations from the bulk correlations based on the WLF and SE equations.   Challenges in exploring this complex relationship under nanoconfinement result from a number of parameters affecting the polymer dynamics, such as entanglements and interfacial interactions.   Entanglement density is known to significantly affect long-range polymer mobility,[54] and it is also reported that the entanglement density could change with film thickness.[55, 56]   To circumvent issues of entanglements, a model polymer (unentangled PiBMA) is used in this study as a simplified system.   In addition, multilayer PiBMA thin film systems are designed to examine the influences of interfacial interactions systematically.   Correlations between T_g, η, and D of the PiBMA thin films with different confining interfaces is measured and discussed in later chapters.

13

1.4 REFERENCES

1. Keddie, J. L.; Jones, R. A. L.; Cory, R. A. *Europhys. Lett.* **1994,** 27, (1), 59-64.
2. Forrest, J. A.; Dalnoki-Veress, K.; Stevens, J. R.; Dutcher, J. R. *Phys. Rev. Lett.* **1996,** 77, (10), 2002-2005.
3. Dalnoki-Veress, K.; Forrest, J. A.; Murray, C.; Gigault, C.; Dutcher, J. R. *Phys. Rev. E Stat. Nonlin. Soft Matter Phys.* **2001,** 63, (3 Pt 1), 031801.
4. Alcoutlabi, M.; McKenna, G. B. *J. Phys.-Condens. Mat.* **2005,** 17, (15), R461-R524.
5. Roth, C. B.; McNerny, K. L.; Jager, W. F.; Torkelson, J. M. *Macromolecules* **2007,** 40, (7), 2568-2574.
6. Yoon, H.; McKenna, G. B. *Macromolecules* **2014,** 47, (24), 8808-8818.
7. Fukao, K.; Miyamoto, Y. *Phys. Rev. E Stat. Nonlin. Soft Matter Phys.* **2000,** 61, (2), 1743-54.
8. Li, R. N.; Chen, F.; Lam, C.-h.; Tsui, O. K. C. *Macromolecules* **2013,** 46, (19), 7889-7893.
9. Yang, Z.; Fujii, Y.; Lee, F. K.; Lam, C. H.; Tsui, O. K. *Science* **2010,** 328, (5986), 1676-9.
10. McGraw, J. D.; Jago, N. M.; Dalnoki-Veress, K. *Soft Matter* **2011,** 7, (17), 7832-7838.
11. Hutcheson, S. A.; McKenna, G. B. *Eur. Phys. J. E Soft Matter* **2007,** 22, (4), 281-6; discussion 287-91.
12. Stafford, C. M.; Vogt, B. D.; Harrison, C.; Julthongpiput, D.; Huang, R. *Macromolecules* **2006,** 39, (15), 5095-5099.
13. Torres, J. M.; Stafford, C. M.; Vogt, B. D. *ACS Nano* **2009,** 3, (9), 2677-85.
14. Evans, C. M.; Narayanan, S.; Jiang, Z.; Torkelson, J. M. *Phys. Rev. Lett.* **2012,** 109, (3), 038302-038302.
15. Sussman, D. M.; Tung, W.-S.; Winey, K. I.; Schweizer, K. S.; Riggleman, R. A. *Macromolecules* **2014,** 47, (18), 6462-6472.
16. Frank, B.; Gast, A. P.; Russell, T. P.; Brown, H. R.; Hawker, C. J. *Macromolecules* **1996,** 29, (20), 6531-6534.
17. Zheng, X.; Rafailovich, M. H.; Sokolov, J.; Strzhemechny, Y.; Schwarz, S. A.; Sauer, B. B.; Rubinstein, M. *Phys. Rev. Lett.* **1997,** 79, (2), 241-244.
18. Richert, R. *Annu. Rev. Phys. Chem.* **2011,** 62, 65-84.
19. Williams, M. L.; Landel, R. F.; Ferry, J. D. *J. Am. Chem. Soc.* **1955,** 77, (14), 3701-3707.
20. Vogel, H. *Phys. Z* **1921,** 22, 645-646.
21. Fulcher, G. S. *J. Am. Ceram. Soc.* **1925,** 8, (6), 339-355.
22. Tammann, G.; Hesse, W. *Z. Anorg. Allg. Chem* **1926,** 156, (1), 245-257.
23. Strobl, G., *The Physics of Polymers*. Springer-Verlag Berlin Heidelberg: 2007.
24. Deen, W. M., *Analysis of Transport Phenomena*. Oxford University Press: 2011.
25. Swallen, S. F.; Traynor, K.; McMahon, R. J.; Ediger, M. D.; Mates, T. E. *J. Phys. Chem. B* **2009,** 113, (14), 4600-8.
26. Plazek, D. J.; Magill, J. H. *J. Chem. Phys.* **1966,** 45, (8), 3038-3050.

27. Mallamace, F.; Branca, C.; Corsaro, C.; Leone, N.; Spooren, J.; Chen, S. H.; Stanley, H. E. *Proc. Natl. Acad. Sci. USA* **2010,** 107, (52), 22457-62.

28. Ediger, M. D. *Annu. Rev. Phys. Chem.* **2000,** 51, (1), 99-128.

29. Schmidt-Rohr, K.; Spiess, H. W. *Phys. Rev. Lett.* **1991,** 66, (23), 3020-3023.

30. Cicerone, M. T.; Blackburn, F. R.; Ediger, M. D. *Macromolecules* **1995,** 28, (24), 8224-8232.

31. Cicerone, M. T.; Blackburn, F. R.; Ediger, M. D. *J. Chem. Phys.* **1995,** 102, (1), 471-479.

32. Berthier, L.; Biroli, G.; Bouchaud, J.-P.; Cipelletti, L.; Masri, D. E.; L'Hôte, D.; Ladieu, F.; Pierno, M. *Science* **2005,** 310, (5755), 1797-1800.

33. Schiener, B.; Chamberlin, R. V.; Diezemann, G.; Böhmer, R. *J. Chem. Phys.* **1997,** 107, (19), 7746-7761.

34. Forrest, J. A.; Dalnoki-Veress, K. *Adv. Colloid Interface Sci.* **2001,** 94, (1–3), 167-195.

35. Ediger, M. D.; Forrest, J. A. *Macromolecules* **2014,** 47, (2), 471-478.

36. Roth, C. B.; Dutcher, J. R., Mobility on Different Length Scales in Thin Polymer Films. In *Soft Materials: Structure and Dynamics*, Dutcher, J. R.; Marangoni, A. G., Eds. Marcel Dekker: N.Y., 2005; pp 1-38.

37. Ellison, C. J.; Torkelson, J. M. *Nat. Mater.* **2003,** 2, (10), 695-700.

38. Sharp, J. S.; Forrest, J. A. *Phys. Rev. Lett.* **2003,** 91, (23), 235701.

39. Reid, D. K.; Alves Freire, M.; Yao, H.; Sue, H.-J.; Lutkenhaus, J. L. *ACS Macro Lett.* **2015,** 4, (2), 151-154.

40. Tsui, O. K. C.; Russell, T. P.; Hawker, C. J. *Macromolecules* **2001,** 34, (16), 5535-5539.

41. Gao, S.; Koh, Y. P.; Simon, S. L. *Macromolecules* **2013,** 46, (2), 562-570.

42. Lang, R. J.; Merling, W. L.; Simmons, D. S. *ACS Macro Lett.* **2014,** 3, 758-762.

43. Ye, C.; Weiner, C. G.; Tyagi, M.; Uhrig, D.; Orski, S. V.; Soles, C. L.; Vogt, B. D.; Simmons, D. S. *Macromolecules* **2015**.

44. Roth, C.; Dutcher, J. *J. Electroanal. Chem.* **2005,** 584, (1), 13-22.

45. Roth, C. B.; Dutcher, J. R. *J. Polym. Sci. Part B Polym. Phys.* **2006,** 44, (20), 3011-3021.

46. Masson, J.-L.; Green, P. F. *Phys. Rev. E Stat. Nonlin. Soft Matter Phys.* **2002,** 65, (3), 031806.

47. Chen, F.; Peng, D.; Lam, C.-H.; Tsui, O. K. C. *Macromolecules* **2015**.

48. Chai, Y.; Salez, T.; McGraw, J. D.; Benzaquen, M.; Dalnoki-Veress, K.; Raphaël, E.; Forrest, J. a. *Science* **2014,** 343, (6174), 994-9.

49. Fakhraai, Z.; Forrest, J. a. *Science* **2008,** 319, (5863), 600-4.

50. Koga, T.; Li, C.; Endoh, M. K.; Koo, J.; Rafailovich, M.; Narayanan, S.; Lee, D. R.; Lurio, L. B.; Sinha, S. K. *Phys. Rev. Lett.* **2010,** 104, (6), 066101.

51. Yang, Q.; Xu, Q.; Loos, K. *Macromolecules* **2015,** 48, (6), 1786-1794.

52. Keddie, J. L.; Jones, R. A. L.; Cory, R. A. *Farad. Discuss.* **1994,** 98, (0), 219-230.

53. Forrest, J. A. *Eur. Phys. J. E Soft Matter* **2002,** 8, (2), 261-266.

54.   Doi, M.; Edwards, S. F., *The Theory of Polymer Dynamics*. Clarendon Press: 1988.

55.   Si, L.; Massa, M. V.; Dalnoki-Veress, K.; Brown, H. R.; Jones, R. a. L. *Phys. Rev. Lett.* **2005,** 94, (12), 1-4.

56.   Ata, S.; Muramatsu, M.; Takeda, J.; Ohdaira, T.; Suzuki, R.; Ito, K.; Kobayashi, Y.; Ougizawa, T. *Polymer* **2009,** 50, (14), 3343-3346.

Chapter 2: Self-diffusion coefficient measurements by fluorescence recovery after patterned photobleaching

2.1 BACKGROUND

As discussed in Chapter 1, the self-diffusion coefficient (D) of nanoconfined polymer has been investigated far less compared to the glass transition temperature (T_g) and viscosity (η) due to a limited number of available methods. Therefore, a more versatile methodology to measure D in thin films is strongly desired in order to understand nanoconfined polymer dynamics on different length scales. This chapter reviews the development of fluorescence-based approaches for D measurement, and introduces a strategy to design experiments to measure D with smaller experimental error.

2.1.1 Basics of fluorescence recovery after photobleaching

Fluorescence recovery after photobleaching (FRAP) was developed in the 1970s by Axelrod *et al.* as a technique to measure the transport of fluorescently-labeled molecules in a living cell.[1, 2] As shown in Figure 2.1, in-plane D (i.e., migration of a molecule parallel to the substrate) of a labeled molecule can be measured by observing the fluorescence intensity from an area of interest. At $t = 0$, the area of the interest is bleached using a high-intensity light source, which decreases the fluorescence intensity from $F(i)$ to $F(0)$. Here, i stands for initial before bleaching and 0 for $t = 0$. As the unbleached molecules diffuse into the bleached region due to Brownian motion as a function of time, t, the intensity of the area of interest "recovers" to $F(t = \infty)$ ($\leq F(i)$). The fluorescence intensity normalized by the initial intensity profile, $f(t) = F(t)/F(i)$, can be described by Eq. 2.1 using the characteristic diffusion time τ_D (Eq. 2.2). Here w is defined as the half-width of the bleached region, and K is the bleach constant corresponding to the amount of the fluorescent dyes that are bleached.[3]

$$f(t) = \sum_{n=0}^{n=\infty} \frac{-K^n}{n!} \cdot \frac{1}{1 + n\left\{1 + \dfrac{2t}{\tau_D}\right\}} \tag{2.1}$$

$$\tau_D = \frac{w^2}{4D} \tag{2.2}$$
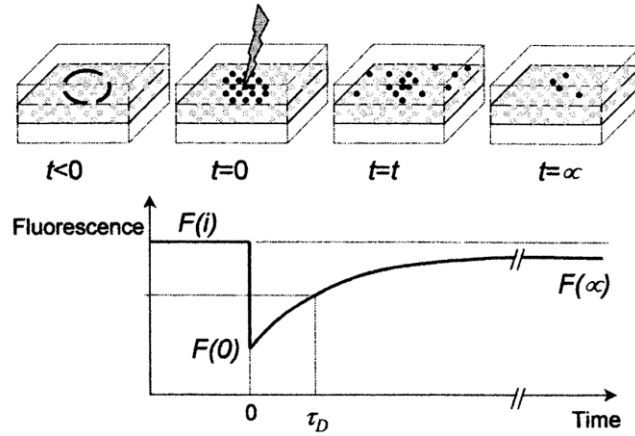
Figure 2.1: Schematic representation of FRAP.   Adapted with permission from Meyvis *et al.*[3]   Copyright 1999, Plenum Publishing Corporation.

Several years after FRAP was introduced, Smith and McConnell *et al.* developed the next generation of FRAP: fluorescence recovery after *patterned* photobleaching (FRAPP).[4]   While the physical mechanism of the measurement is similar to FRAP, FRAPP generates additional data sets, for a given time interval, which reduces experimental error.   Figure 2.2 shows representative data from a FRAPP measurement on a 120 nm-thick poly(isobutyl methacrylate) (PiBMA) polymer thin film.   In this example, a photomask with a 25 μm pitch size was placed on top of the fluorescently-labeled PiBMA film.   The sample was then photobleached using a broadband light source (Figure 2.2 (a)), and placed on the heating stage.   The fluorescence intensity profile was observed as a function of time while the sample was annealed and subsequently fitted to a sinusoidal function as shown in Eq. 2.3, where, $A(t)$ is the

18

amplitude of the sinusoidal intensity ($I(x,t),$), λ is the pitch size, and x_0 and C are fitting parameters.   As self-diffusion of the labeled PiBMA proceeded into the bleached regions, $A(t)$, the difference between the bleached and unbleached regions reduced, as shown in Figure 2.2 (b).   By fitting $A(t)$ to Eq. 2.4, D and τ_D can be obtained.   Here, the slope of $\ln[A(t)/A(0)]$ versus t in Figure 2.2 (c) corresponds to τ_D^{-1} and therefore it is proportional to D (Eq. 2.5).

$$I(x,t) = A(t)\cos\{2\pi(x + x_0)/\lambda\} + C \tag{2.3}$$

$$A(t) = A(0)\exp\left(-4\pi^2 Dt/\lambda^2\right) = A(0)\exp\left(-t/\tau_D\right) \tag{2.4}$$

$$\tau_D = \frac{\lambda^2}{4\pi^2 D} \tag{2.5}$$
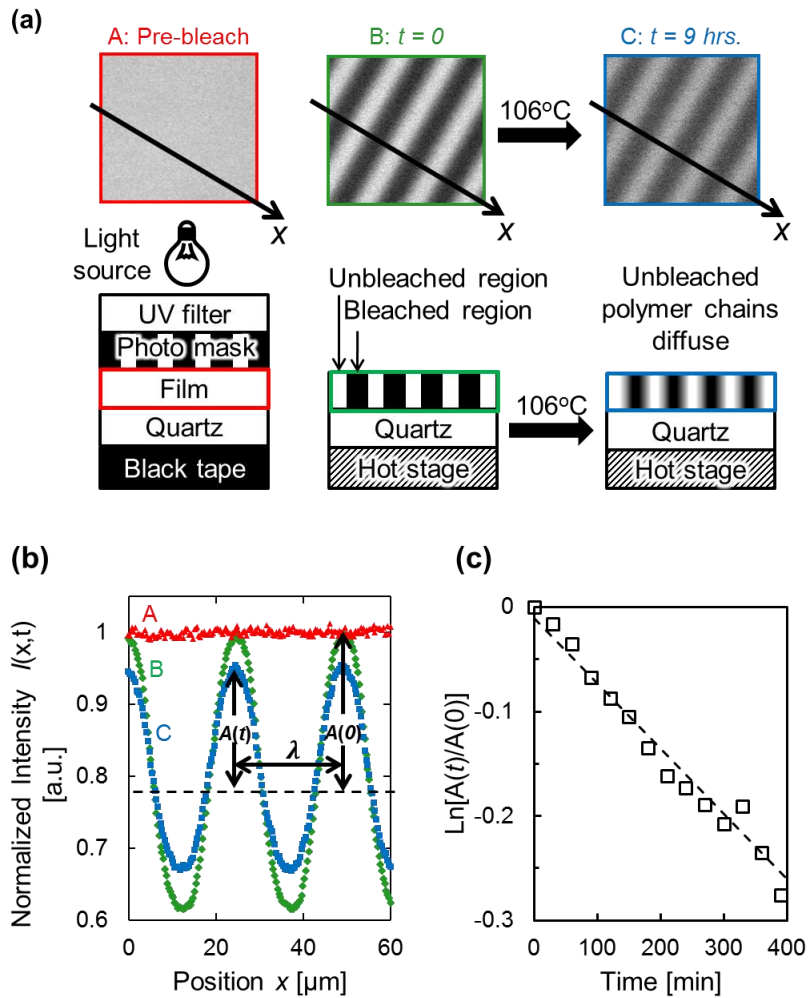
Figure 2.2: Schematic representation of FRAPP.   (a) Photobleaching and self-diffusion process of fluorescently labeled polymer.   The top images are sample fluorescence micrographs at each step where the bottom images are descriptions of the experimental setup.   (b) Fluorescence intensity profile along the *x*-axis in (a) at different times [I(x,t)].   (c) Ln[$A(t)/A(0)$] as a function of time as diffusion/fluorescence recovery proceeds.   The broken line represents the best fit from a linear regression, where the slope is proportional to the self-diffusion coefficient (*D*).

2.1.2   Previous work using FRAP and FRAPP for thin films

In this chapter, previous work relating to the measurement of *D* in polymer thin films using FRAP and FRAPP is introduced.   These *D* measurements can be classified

20

into two approaches based on how the fluorescent dye is incorporated into the polymer: 1) free/doped dye[5-11] and 2) dye covalently attached to the polymer.[12-16] The first approach using free dye is simpler because there is no synthesis requirement to attach it to the polymer. However, spatial segregation of the dye at the air/polymer or polymer/substrate interfaces may need to be considered.[11] Also, the free dye approach reveals the segmental motion of the polymer rather than the entire chain motion,[6, 9] the latter being the focus of this study.

The second method, FRAP/FRAPP with dye covalently attached to the polymer, enables measuring D of the labeled polymer in thin films. To our knowledge, FRAPP and FRAP in thin films have been conducted for polystyrene (PS),[12] polydimethylsiloxane (PDMS),[16] PiBMA,[13] and poly(methacrylic acid)/poly(2-(dimethylamino) ethyl methacrylate) (PMA/PDMA) and in multi-layer configurations.[14, 15, 17] As described in Chapter 1.2.3, pioneering work using FRAPP was conducted by Frank *et al.* for a PS thin film on a SiO$_x$ substrate in 1996, and the thinnest film they measured was 50 nm.[12] Wong and Granick *et al.* also developed a FRAP system with a surface force apparatus for *in-situ* thickness measurement for PDMS down to 1.8 nm thick. Lastly, Katzenstein *et al.* applied FRAPP to PiBMA on SiO$_2$ substrates, and successfully reported D values down to 30 nm thick films.[13]

2.1.3 Current challenges for FRAPP in thin films

As reviewed in Chapter 2.1.2, FRAPP measurements can be used to determine D for thin films where nanoconfinement becomes more significant as the thickness decreases. The main challenges for applying FRAPP to thin films are signal-to-noise ratio and maintaining the accuracy of the measurement. As a film becomes thinner, which is specifically relevant to any nanoconfinement study, the signal-to-noise ratio

decreases. At the same time, the most critical assumption of FRAPP that there is a linear relationship between fluorophore concentration and the fluorescent intensity must be valid. In ultrathin films, the consequences of deviations from this linear relationship become more significant than that of thick films. In order to conduct accurate FRAPP measurements in thin films, extra attention must be paid to ensure this linear relationship while maximizing the signal-to-noise ratio.

2.2   EXPERIMENTAL

2.2.1   Materials

In this study, PiBMA was used as a model polymer as described in previous work.[13]   Nearly monodisperse and labeled PiBMA was synthesized using a dye-labeled (nitrobenzofrazan, NBD) initiator for activators regenerated by electron transfer atom transfer radical polymerization as described in Katzenstein *et.al.*[13]   Unlabeled PiBMA analogs were synthesized with initiators lacking NBD substituents.   The absolute molecular weight was determined using gel permeation chromatography as follows: unlabeled PiBMA: M_n = 10.0 kg/mol, Đ = 1.06, NBD-labeled PiBMA (PiBMA-NBD): M_n = 12.2 kg/mol, Đ = 1.18.   To avoid fluorescence self-quenching[18] of NBD, unlabeled PiBMA and PiBMA-NBD were mixed such that the total concentration of NBD in the polymer film was lower than 0.18 wt%.   PiBMA films were spin-coated from n-butanol (1.0 - 8.0 wt% solids, 1800-3800 rpm) onto polished quartz substrates.   The films were annealed for 20 min under vacuum at 120°C ($T_{g,\text{PiBMA}}$ + 62°C) to remove residual stress and solvent.

2.2.2   FRAPP experimental setup

FRAPP measurements were conducted following the procedure discussed in Chapter 2.1.2 and a previous report.[13]   The photomasks and the UV filter (360 nm long

pass) for photobleaching were purchased from Edmund Optics. The polymer film sample was photobleached using a broadband (300 – 700 nm) light source (Optical Building Blocks Scope Lite 200) with a light intensity of 10 mW/cm^2 for 150 sec. The resulting film fluorescence intensity profile was observed using an Olympus BX 51 epifluorescence microscope attached to a Photon Technologies Quanta Master 40 fluorimeter. The excitation wavelength was 445 nm while the emission wavelength was > 520 nm.

The temperature for D measurements of PiBMA was 106°C ($T_{g,PiBMA}$+ 48°C). The specimens were placed on a hot stage at the measurement temperature for 4 min prior to each measurement to attain thermal equilibrium. During the FRAPP measurements, argon was purged slowly over the sample to avoid quenching by oxygen,[19] as described in the following chapters.

2.3   CONTROL EXPERIMENTS FOR FRAPP MEASUREMENTS

2.3.1   Pitch size of the photomask

As was shown in Eq. 2.5, the characteristic decay time of the intensity profile for a given D depends on the pitch size of the photomask, λ, and this relationship is commonly used to confirm successful FRAPP measurements.[20]   In our system, FRAPP experiments were performed with pitch sizes of 10.0, 12.5, 20.0 and 25.0 μm as shown in Figure 2.3. The solid line is a best-fit line using linear regression, and the slope is proportional to 1/D. Due to slower diffusion at lower temperatures, data sets at 80°C exhibit a steeper slope. This linear relationship is characteristic of the diffusion of irreversibly bleached fluorophores with a single decay time, τ_D.[20]   Also, these measurements are useful for determining a suitable λ for conducting FRAPP measurements over a reasonable time period.
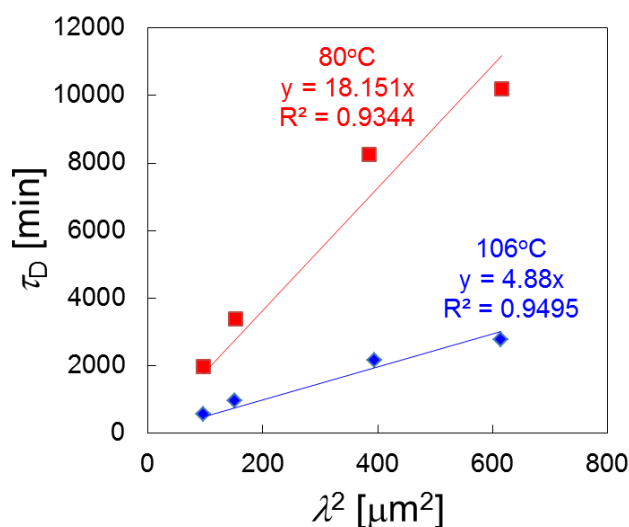
Figure 2.3: Characteristic decay time of the fluorescent pattern (τ_D) versus (pitch size)^2 (λ^2) at 80°C (red, square) and 106°C (blue, diamond) with 120 nm thick PiBMA films. The solid lines are best-fit lines from linear regression.

2.3.2 Sources of detrimental fluorescence intensity loss

2.3.2.1 Potential fluorescence intensity quenchers

As discussed in Chapter 2.1.3, the most important assumption for FRAPP measurements is that the fluorescence intensity is linear with the concentration of fluorophore; however, the so-called "quenching" effect limits the validity of this assumption. A variety of molecular interactions, including energy transfer and collision between molecules, can cause fluorescence quenching.[21] In the case of NBD and PiBMA in this study, the primary source of quenching is due to collisions between NBD and oxygen, residual metals or PiBMA. In the coming two sections, two intensity loss factors will be discussed in detail: 1) quenching of NBD itself, i.e. self-quenching, which is intrinsic to the system and avoidable by controlling NBD concentration, and 2) steady, long-term intensity loss during the measurement.

24

2.3.2.2 Intensity loss due to self-quenching

In order to avoid self-quenching, the concentration of NBD should be lower than a threshold value, but reducing NBD concentrations may also result in insufficient intensity. Thus, determining the threshold concentration is critical for FRAPP measurements to achieve the highest signal without self-quenching. The threshold NBD concentration was evaluated by measuring the fluorescence intensity of 120 ± 5 nm thick PiBMA films with different ratios of unlabeled PiBMA to labeled PiBMA, i.e. PiBMA-NBD. Figure 2.4 (a) shows a representative fluorescence micrograph of the PiBMA film at the measurement temperature, 106°C. By averaging the intensity of the squared area and then normalizing by the thickness, a normalized gray value is determined and plotted against the wt% NBD based on total PiBMA, as shown in Figure 2.4 (b). When the NBD concentration is lower than 0.18 wt%, a linear relationship between the NBD concentration and the normalized gray value is observed. Thus, this experiment indicates that the NBD content should be lower than 0.18 wt% to avoid self-quenching effects.
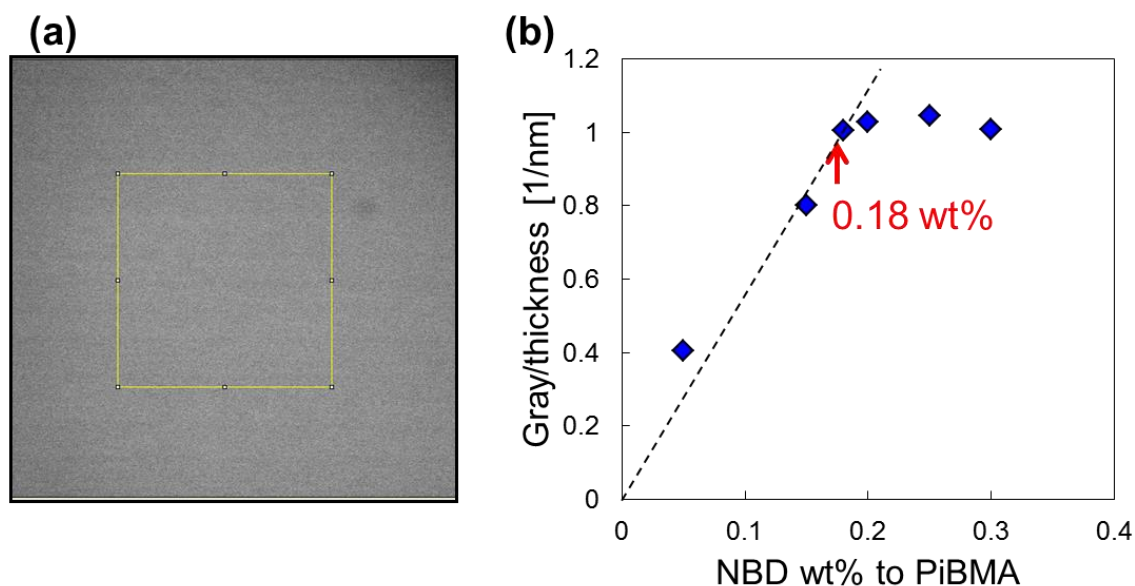
Figure 2.4: (a) Fluorescence micrograph of the film. (b) The gray value normalized by film thickness versus the wt% NBD in total PiBMA. The dashed line shows the linear relationship between NBD content and the normalized gray value. The maximum NBD amount, or threshold concentration, to be incorporated in PiBMA to avoid self-quenching is 0.18 wt%.

The effect of self-quenching on D measurements was simulated in a model system as shown in Figure 2.5. In this model system, the "no self-quenching" case assumes that the dye concentration (c) is linear with the fluorescence intensity (I), while the "self-quenching" case assumes a hyperbolic function, $I = \tanh(c)$. It is assumed that both cases exhibit the same D, and therefore τ_D. Figure 2.5 (a) shows the relationship between c and the intensity I. Based on this relationship, the sinusoidal photobleached profile at $t = 0$ was calculated as shown in Figure 2.5 (b) using Eq. 2.3. The initial intensity profile, $I(x, t = 0)$ of the self-quenched sample exhibits an asymmetric intensity profile, which was not seen in the "no self-quenching" sample. Based on $I(x, t = 0)$, Eq. 2.4 and 2.5 yield the time development of $I(x,t)$ for "no self-quenching" and "self-quenching" cases as illustrated in Figure 2.5 (c) and (d), respectively.

26
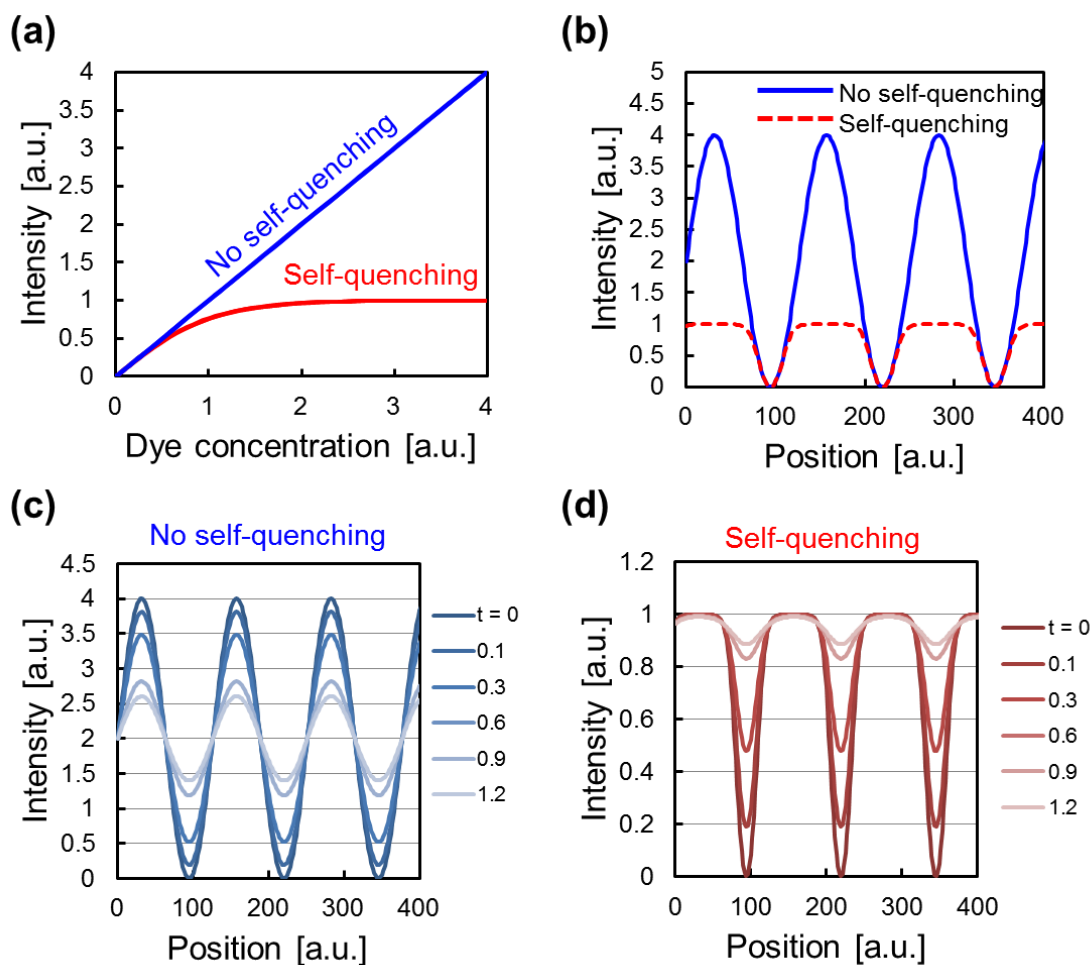
Figure 2.5: (a) Fluorescence intensity versus concentration of dye for self-quenching and no self-quenching cases. (b) Initial intensity profile. Changes in the intensity profile as a function of normalized time (t/τ_D) for the cases of (c) no self-quenching and (d) self-quenching.

The apparent D was calculated based on the amplitude of the intensity profile, $A(t)$ as a function of normalized time by τ_D. As shown in Figure 2.6 (a), even though these two systems exhibit the same D, the recovery of the $A(t)$ of the self-quenched sample is faster than the "no self-quenching" sample. In fact, when the recovery of $A(t)$ is replotted in a natural log form, the slope corresponding to apparent D of the self-

quenching sample is 1.6 times larger than the "no self-quenching sample" as shown in Figure 2.6 (b). Also, due to an asymmetric initial concentration profile in Figure 2.6 (b), the time variation of $\ln[A(t)/A(0)]$ is nonlinear for the self-quenching sample. This calculation demonstrates the importance to avoiding self-quenching for accurate D measurements using FRAPP.

(a)

(b)
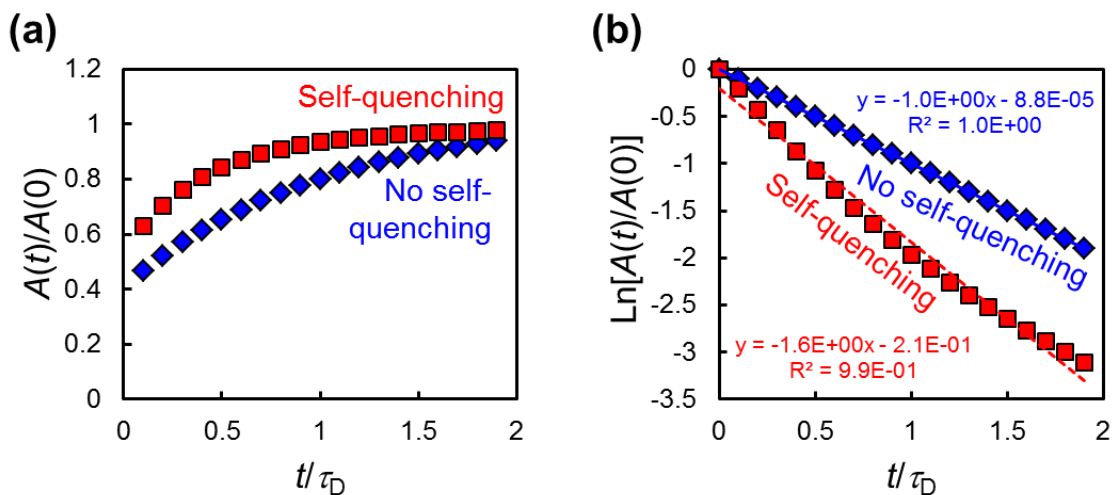
Figure 2.6: (a) Time development of the amplitude of the sinusoidal photobleaching pattern ($A(t)$) normalized by $A(0)$ of the "no self-quenching" (blue diamond) and "self-quenching" (red square) samples. (b) Natural log plot of (a). The solid blue line and broken red lines are best fits using linear regression for no self-quenching and self-quenching samples, respectively.

2.3.2.3 Steady, long-term intensity loss

In addition to self-quenching, steady, long-term intensity loss can also lead to inaccurate diffusion measurements. Dynamic quenching can contribute to this behavior and it can be caused by collisions with oxygen, residual metals from the synthesis catalyst, and PiBMA.[21] To study the effect of the long-term intensity loss, 120 nm-thick PiBMA films with a scratch were placed on the top of a hot plate. The scratched area

28

does not have PiBMA, and is therefore used as a dark reference. Figure 2.7 (a) shows the intensity decay as a function of imaging time, indicating that purging with argon significantly alleviates the reduction in intensity due to dynamic quenching by oxygen.

Also, bleaching by the excitation light from the fluorescent microscope can be an issue, depending on the excitation intensity. The imaging time should be minimized to avoid bleaching, while also holding the total imaging time constant (i.e., total imaging time = [imaging time/scan] $\times$ n, where n is a number of images), to allow direct comparison between samples. In our system, the typical imaging time was 10 sec, which yielded an acceptable signal-noise ratio, and the total number of images was 18, giving a total imaging time of 180 sec. Figure 2.7 (b) shows the intensity decay due to both dynamic quenching and unintentional bleaching from the microscope light source, which corresponds to a 5×10^{-4} loss in intensity over time with argon purging. We would like to note that unintentional bleaching becomes more severe with larger magnification lenses and higher temperatures. In our case, the use of a 100$\times$ magnification lens resulted in an unacceptable bleaching of intensity during imaging of PiBMA thin films, and as a result, 50$\times$ was the highest magnification used in this study.

(a)

(b)
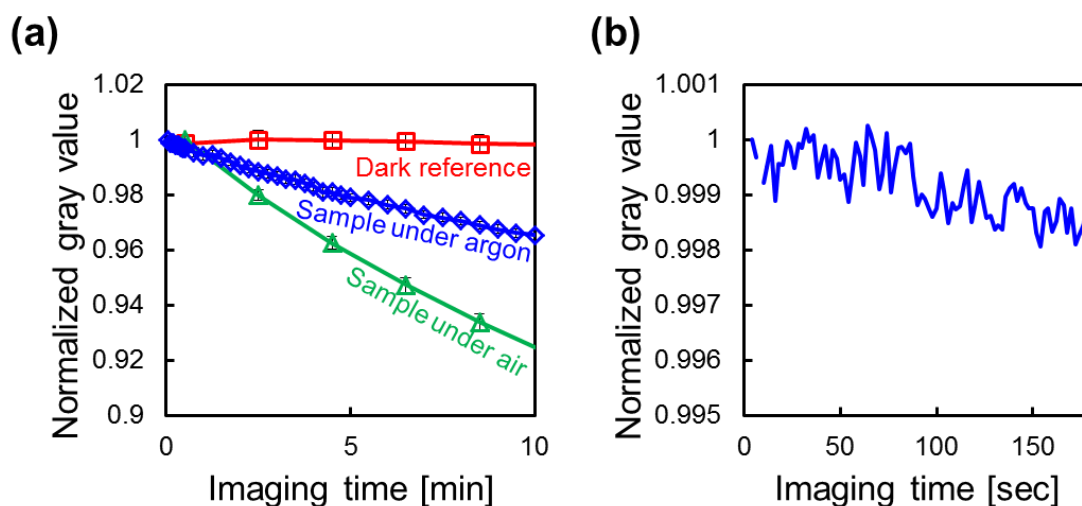
Figure 2.7: (a) Normalized gray value as a function of imaging time. The intensity of the scratched area (no PiBMA-NBD) of the sample under air was used as a dark reference. The error bars correspond to standard deviations of the gray value for 400 pixels area. (b) Intensity change as a function of time under light exposure at $106^{o}C$ (measurement temperature) with argon purging. 180 sec corresponds to the actual total imaging time during FRAPP measurements.

2.3.3 Signal-to-noise ratio

For polymer thin films, the signal-to-noise ratio is often the main reason for the larger error bars, because the signal-to-noise ratio becomes smaller as the film thickness decreases. The noise level in our system is shown in Figure 2.8 (a) and (b). At a measurement temperature of $106^{o}C$, the average intensity of a 120 nm-thick PiBMA film along the x- and y-axis was recorded. From the intensity profile, the noise level was determined as 0.5 gray value. This measurement is also important in order to ensure the spatial distribution of the intensity profile is not misinterpreted.
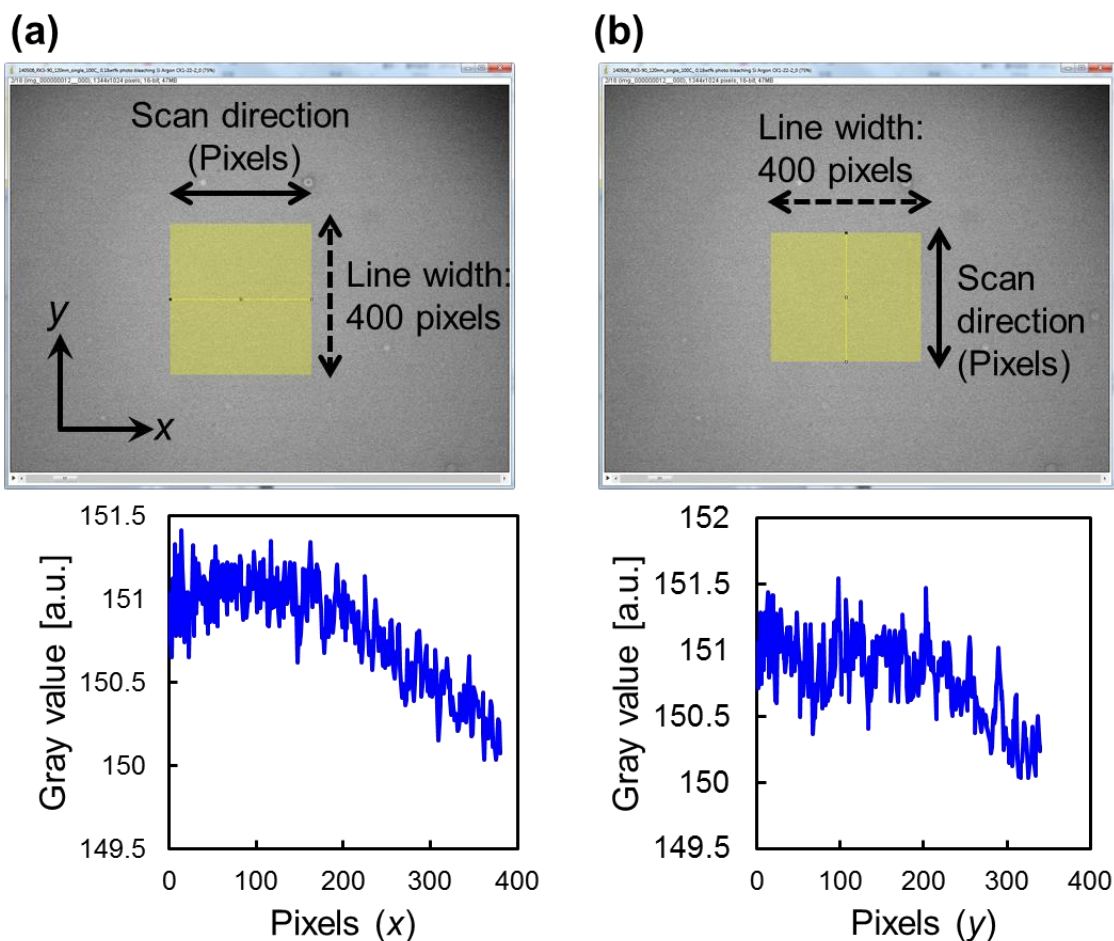
Figure 2.8: Intensity profile of a 120 nm thick PiBMA film along (a) x-axis and (b) y-axis at the measurement temperature, 106°C.

As the lowest signal-to-noise ratio, the intensity profile of an 18 nm-thick PiBMA film at 106°C is shown in Figure 2.9. The noise level of 0.5 gray value corresponds to a value of 1×10^{-3} when normalized by the highest value, while the corresponding signal, i.e. $A(t)$, is 6×10^{-3}, is roughly the smallest signal-to-noise ratio used to conduct FRAPP measurements in this study. Also, we would like to note that the intensity decay due to the long-term intensity loss described in Chapter 2.3.2.3 was 5×10^{-4}, which is negligible in this study relative to the signal. These systematic studies are required to design

FRAPP measurements for ultrathin films, and typically, the signal-to-noise ratio determines the lower limit of the film thickness.
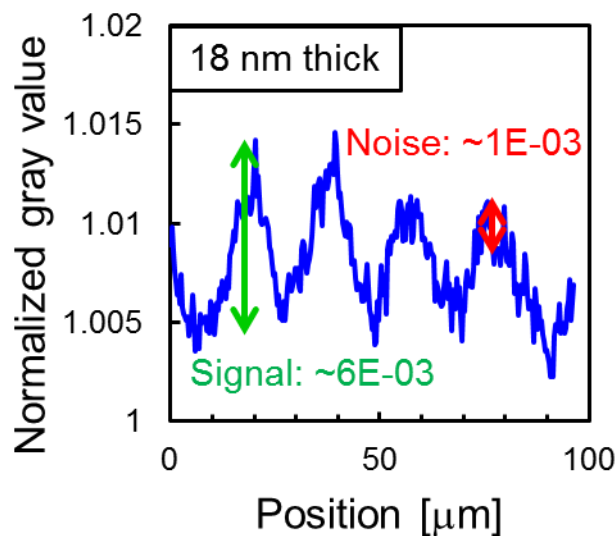
Figure 2.9:   Intensity profile of an 18 nm-thick PiBMA thin film.

2.3.4   Polymer/substrate interactions

As was discussed in Chapter 1.2, polymer-substrate interactions can influence polymer dynamics, including D.   The effect of interfaces could result in multiple D values or even a continuous distribution of D values depending on the location of the polymer in the film, such as at the air-polymer surface and polymer-substrate interface.[16] For instance, Jourdainne *et al.* reported non-linear decay of fluorescence intensity of poly(L-lysine)/hyaluronic acid multilayers (Figure 2.10 (a)), and extracted two D values using a Laplace transform (Figure 2.10 (b)).   This analysis could be very insightful for studying polymer thin films as well.
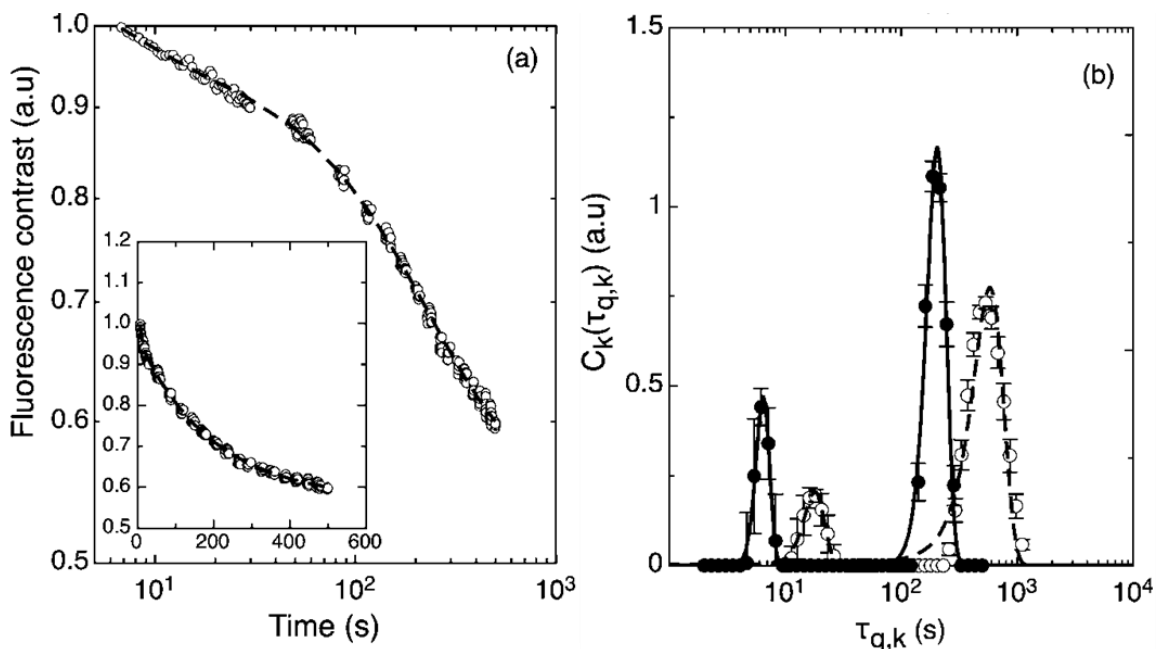
Figure 2.10: (a) Typical fluorescence recovery data of poly(L-lysine)/hyaluronic acid multilayers. The main figure is plotted on a log-log scale in order to enhance the short time region. The line represents the best fit obtained by using a double exponential decay law. The insert shows the same data on a linear-linear scale. (b) Analysis of data in terms of its inverse Laplace transform. A two-peak time distribution is observed, in agreement with a two-exponential decay. Adapted with permission from Jourdainne *et al*.[22] Copyright 2008, American Chemical Society.

Also, the selection of the polymer film's substrate is non-trivial. It is well-known that polymer can form an irreversibly adsorbed layer at the polymer-substrate interface.[23] Assuming these layers are completely immobilized, the FRAPP method will not detect a change in the intensity profile from these regions. Furthermore, the adsorbing process of the polymer chain has its own kinetics, which is difficult to differentiate from self-diffusion of the polymer. Therefore, it is better to avoid using systems that have strong polymer-substrate interactions, which lead to an irreversibly adsorbed layer.

2.4 CONCLUSIONS

The challenge for FRAPP measurements of thin polymer films is mainly the low signal-to-noise ratio. A strategy to improve the signal-to-noise ratio is summarized in Figure 2.11. Temperature, imaging time, and dye concentration are the available adjustable parameters and these parameters improve the signal-to-noise ratio with values that lie towards the right-hand side of Figure 2.11 (a), while each parameter has a trade-off shown under the potential issues listed in Figure 2.11 (b). By balancing these parameters, we may be able to achieve D measurements in thin films, even thinner than 10 nm. Also, implementing more advanced optics, such as a confocal microscope, may allow smaller pitch sizes in the bleaching pattern to be realized to measure extremely slow self-diffusion at lower temperatures.
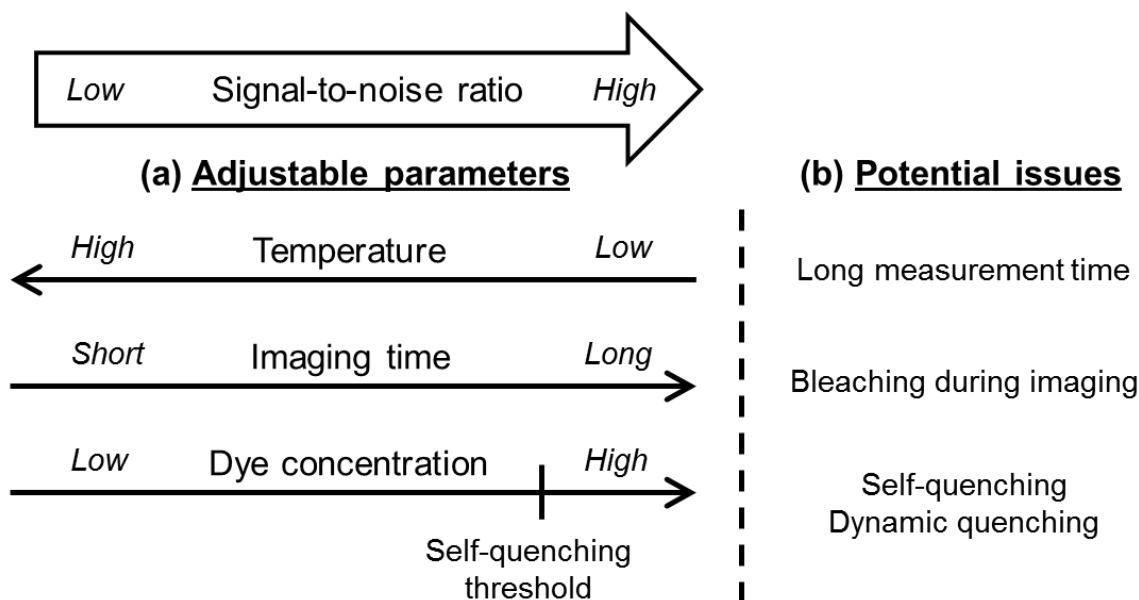
Figure 2.11: (a) Adjustable parameters and (b) associated potential issues to obtain a high signal-to-noise ratio in FRAPP.

2.5 REFERENCES

1. Axelrod, D.; Koppel, D. E.; Schlessinger, J.; Elson, E.; Webb, W. W. *Biophys. J.* **1976,** 16, (9), 1055-1069.
2. Schlessinger, J.; Koppel, D. E.; Axelrod, D.; Jacobson, K.; Webb, W. W.; Elson, E. L. *Proc. Natl. Acad. Sci. USA* **1976,** 73, (7), 2409-2413.
3. Meyvis, T. K. L.; De Smedt, S. C.; Van Oostveldt, P.; Demeester, J. *Pharmaceut. Res.* **1999,** 16, (8), 1153-1162.
4. Smith, B. A.; McConnell, H. M. *Proc. Natl. Acad. Sci. USA* **1978,** 75, (6), 2759-2763.
5. Smith, B. A. *Macromolecules* **1982,** 15, (2), 469-472.
6. Ediger, M. D. *Annu. Rev. Phys. Chem.* **1991,** 42, (1), 225-250.
7. Paeng, K.; Ediger, M. D. *Macromolecules* **2011,** 44, (17), 7034-7042.
8. Paeng, K.; Richert, R.; Ediger, M. D. *Soft Matter* **2012,** 8, (3), 819-819.
9. Paeng, K.; Swallen, S. F.; Ediger, M. D. *J. Am. Chem. Soc.* **2011,** 133, (22), 8444-7.
10. Deppe, D. D.; Dhinojwala, A.; Torkelson, J. M. *Macromolecules* **1996,** 29, (11), 3898-3908.
11. Tseng, K. C.; Turro, N. J.; Durning, C. J. *Phys. Rev. E Stat. Nonlin. Soft Matter Phys.* **2000,** 61, (2), 1800-1811.
12. Frank, B.; Gast, A. P.; Russell, T. P.; Brown, H. R.; Hawker, C. J. *Macromolecules* **1996,** 29, (20), 6531-6534.
13. Katzenstein, J. M.; Janes, D. W.; Hocker, H. E.; Chandler, J. K.; Ellison, C. J. *Macromolecules* **2012,** 45, (3), 1544-1552.
14. Li Xu; Veronika Kozlovskay; Eugenia Kharlampieva; John F. Ankner, a. S. A. S. *ACS Macro Lett.* **2012,** 2012, (1), 127-130.
15. Xu, L.; Selin, V.; Zhuk, A.; Ankner, J. F.; Sukhishvili, S. A. *ACS Macro Lett.* **2013,** 2, (865), 12-15.
16. Wong, J. S. S.; Hong, L. A.; Bae, S. C.; Granick, S. *J. Polym. Sci. Part B Polym. Phys.* **2010,** 48, (24), 2582-2588.
17. Selin, V.; Ankner, J. F.; Sukhishvili, S. A. *Macromolecules* **2015,** 48, (12), 3983-3990.
18. Robeson, J. L.; Tilton, R. D. *Biophys. J.* **1995,** 68, (5), 2145-55.
19. Lakowicz, J. R.; Weber, G. *Biochemistry* **1973,** 12, (21), 4161-4170.
20. Davoust, J.; Devaux, P. F.; Leger, L. *EMBO J.* **1982,** 1, (10), 1233-1238.
21. Lakowicz, J. R., *Principles of Fluorescence Spectroscopy* 3rd ed.; Springer US: 2006.
22. Jourdainne, L.; Lecuyer, S.; Arntz, Y.; Picart, C.; Schaaf, P.; Senger, B.; Voegel, J.-C.; Lavalle, P.; Charitat, T. *Langmuir* **2008,** 24, (15), 7842-7.
23. Aubouy, M.; Guiselin, O.; Raphaël, E. *Macromolecules* **1996,** 29, (22), 7261-7268.

Chapter 3: Glass transition temperature, self-diffusion coefficient, and effective viscosity of polymer thin films

3.1 INTRODUCTION

Nanoconfined polymer films with thickness in the range of ~1-100 nm often exhibit physical properties different from the bulk as was reviewed in Chapter 1. These include the glass transition temperature (T_g),[1-6] elastic modulus,[7-10] self-diffusion coefficient (D),[11-14] effective viscosity (η_{eff}), [15-19] and so on. While many of these observations can be rationalized by assuming that the free surface causes the local dynamics to speed up and the substrate surface causes the local dynamics to slow down, some observations remain unexplainable. A long-standing question concerns the inconsistent thickness (h_0) dependences demonstrated by the T_g[3, 20] and D[11, 12] of polystyrene (PS) films supported by silica (SiO_x) (PS/SiO_x). Specifically, both the $T_g(h_0)$ and $D(h_0)$ of these films exhibit reductions with decreasing h_0. Straightforward interpretation of the $T_g(h_0)$ would suggest that the dynamics of the films are dominated by the free surface, but that of $D(h_0)$ would imply that the substrate surface dominates. Given that the glass transition involves cooperative, local motions of the chain segments [4, 21-23] while D involves large-scale translational motions of the whole chains, it is thus perceivable that the T_g and D may exhibit different thickness dependences. But recent studies found that the η_{eff} of PS/SiO_x decreased with decreasing h_0 over polymer molecular weights (MW) from 2.4 to 2,300 kg/mol.[15, 17] Both D and η_{eff} describe transport phenomena of the polymer chain in the films and are known to depend on the same sort of local dynamic properties, namely the local segmental friction coefficients.[11,17] It is then unclear why D and η_{eff} displayed seemingly inconsistent h_0 dependences. In the present study, we simultaneously studied the effects of confinement on the T_g, D and η_{eff} of poly(isobutyl methacrylate) (PiBMA) films

supported by silica (PiBMA/SiO$_x$).   Previous experiments showed that the T_g of PiBMA/SiO$_x$ was independent of h_0,[13, 24] which is different from PS/SiO$_x$.   From the perspective of this study, the different behavior of these two systems is viewed as an advantage that will enable the development of better insight about the general phenomenon.   Ye *et al.* reconciled the incompatible depressions in T_g using inelastic neutron scattering (INS) characterizing segmental mobility of PS prepared on a SiO$_x$ substrate.[25]   The INS measurements revealed that the Debye-Waller factor ($\sim$exp[-$q^2<u^2>/3$] where q is the neutron wave vector) was $\sim$5 ns, which clearly more strongly weighs the slow components with smaller mean-square-displacements ($<u^2>$).[25]   They also noted that there can be contamination of the nanosecond $<u^2>$ by incipient relaxation processes.[25]   In this study, we seek reconciliation between dynamics with similar time-scales and quantitative descriptions thereof.

3.2   MATERIALS AND METHODS

3.2.1   Sample preparation

All chemicals were purchased from Fisher Scientific, Sigma-Aldrich or Alfa Aesar, and used as received unless otherwise noted.   To enable D measurements of the PiBMA/SiO$_x$ sample films by fluorescence recovery after patterned photobleaching (FRAPP), the fluorescent dye molecule nitrobenzofurazan (NBD) was covalently bonded to PiBMA as an end group forming PiBMA-NBD by following published procedures.[13] In short, NBD-labeled initiator was synthesized by attaching 4-chloro-7-nitrobenzofurazan (NBD-Cl) to ethyl α-bromoisobutyrate (EBIB).   Atom-transfer radical-polymerization (ATRP) was used to synthesize both PiBMA-NBD and PiBMA by using the NBD-labeled initiator (EBIB-NBD) and unlabeled initiator (EBIB), respectively.[13, 26]   Both products, PiBMA-NBD or PiBMA, were then eluted through an

alumina column at least three times to remove residual copper catalyst. PiBMA-NBD was precipitated in a 1:1 deionized water/acetonitrile solution ten times to remove unattached NBD. The unlabeled PiBMA was precipitated three times. Both the PiBMA-NBD and PiBMA were freeze dried from benzene after precipitation. The absolute MW was measured using a Viscotek GPCMax VE 2001 Gel Permeation Chromatography (GPC) equipped with a Viscotek Model 270 Dual viscometer/light scattering detector, and a Viscotek VE 3580 refractive index detector and two I-series mixed bed low-MW columns in which tetrahydrofuran (THF) was used as an eluent at a flow rate of 1 mL/min. Complete removal of the unattached NBD was confirmed by the use of a fluorescence detector (Jasco FP-2020; $\lambda_{excitation}$ = 465 nm, $\lambda_{emission}$ = 520 nm) attached to the GPC showing no small-molecule fluorescence peak from unattached NBD.

The number-average molecular weight (M_n) of the synthesized PiBMA-NBD was M_n = 12.2 kg/mol, with Đ = 1.18, and that of the unlabeled PiBMA was M_n = 10.0 kg/mol, with Đ = 1.06. The MWs of PiBMA used in this study were smaller than entanglement MW of PiBMA, ~28 kg/mol,[27] therefore these polymers are unentangled. The radius of gyration (R_g) of the neat PiBMA was ~1.5 nm.[28] In this study, the unlabeled PiBMA was used for T_g measurements because previous study [13] showed that the PiBMA-NBD and unlabeled PiBMA exhibited the same T_g within experimental uncertainty. For the FRAPP experiments, a mixture of unlabeled PiBMA and PiBMA-NBD with a NBD content lower than 0.18 wt% was used to avoid self-quenching as is described in Chapter 2. For consistency, PiBMA and PiBMA-NBD mixtures with the same NBD content were used for η_{eff} measurements as well.

Prior to spincoating, polymer solutions were filtered through 0.2 μm pore-size Teflon filters to remove dust particles. For the PiBMA films, PiBMA/n-butanol

solutions (1.0 - 8.0 wt%) were spincoated on quartz (for FRAPP measurements) or Si wafers containing a native oxide layer (for T_g and η_{eff} measurements) at spinning speeds of 1800 - 3800 rpm.   For the PS films, PS/toluene solutions (0.15 – 3.0 wt%) were spin-cast on oxide-coated Si at spinning speeds of 1900 - 4000 rpm. For FRAPP and T_g measurements, the substrates were cleaned by soaking in a mixture of potassium hydroxide, deionized water and ethanol solution in a 1:1:8 weight ratio, and then rinsed with deionized water and THF at least three times.   Afterward, the PiBMA films were annealed under vacuum at 120°C (= $T_{g,bulk}$ + 62°C) for 20 min to remove residual stress and solvent before FRAPP or T_g measurements.   For η_{eff} measurements, the substrates were first cleaned in a mixture of sulfuric acid and hydrogen peroxide in a 7:3 volume ratio at 130°C for 20 min.   Then the substrates were thoroughly rinsed in deionized water and dried with 99.99 % pure nitrogen gas.   Afterward the substrates were further cleaned in oxygen plasma for 20 min.   The two slightly different substrate treatment methods were found to produce the same measurement result for D within experimental errors and so should not affect our conclusion about the D-η_{eff} relationship.

3.2.2   Glass transition temperature measurements by ellipsometry

The T_g of silica-supported PiBMA films was measured using spectroscopic ellipsometry.   Figure 3.1 shows representative temperature dependence of PiBMA thickness data obtained from two PiBMA/SiO$_x$ films with a thickness of (a) 140 nm and (b) 17 nm at 25°C.   Because the local slope of the data shown in Figure 3.1 corresponds to the thermal expansion coefficients, the T_g can be determined using Eq. A.1 in Appendix A to be the point where the slope transitions between the glassy and rubbery state.   As shown in Figure 3.1 (a), the T_g of the 140 nm thick film was 58.6 ± 1°C, which was the same as its bulk value ($T_{g,bulk}$ = 58.0 ± 0.1^{o}C measured as the midpoint value

39

during second heat at a heating rate of 10°C/min) as determined by differential scanning calorimetry (DSC; Mettler Toledo DSC1).   Similarly, Figure 3.1 (b) shows that the T_g of the 17 nm thick film was 57.8 ± 1°C, which agreed with the value of $T_{g,bulk}$ within experimental uncertainty.   The ± 1°C error was typical for T_g measurements by ellipsometry,[29] which we have also confirmed by measuring the T_g of three separately prepared samples.
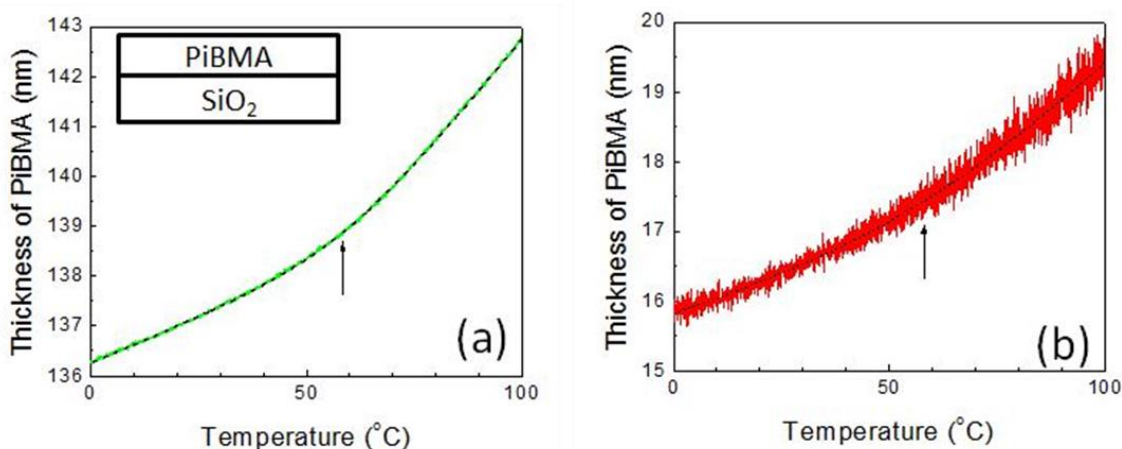
Figure 3.1:   Representative T_g measurements of PiBMA/SiO$_x$ as obtained by ellipsometry at a cooling rate of 2°C/min.   The thickness of PiBMA at 25°C was (a) 140 nm and (b) 17 nm.   The arrows correspond to the T_g of the films obtained by fitting the data to an empirical equation, Eq. A.1 in Appendix A.   The best-fit lines are shown by the smooth dashed lines. The T_g values were determined as 58.6°C and 57.8°C for (a) and (b), respectively.

3.2.3   Self-diffusion coefficient measurements by FRAPP

The in-plane self-diffusion coefficient, D, of silica-supported PiBMA films was measured using FRAPP, where temporal decays of a micron-scale photobleached fringe pattern previously applied to the films were monitored.   The methodology employed in this study is similar to that used before.[13]   The detailed procedure can be found in the

Chapter 2.2.2.   In essence, there are two steps: (1) Photo-bleach the sample and then (2) monitor the self-diffusion process.   In the first step, a photo mask containing equally sized chrome lines and spaces with 20 μm pitch (Edmund Optics) was placed on top of the films with a 360 nm long-pass filter to avoid undesirable photochemical reactions. The sample was photobleached using a broadband (wavelength range of 300 – 600 nm) light source (Optical Building Blocks ScopeLite 200).   Figure 3.2 (a) and (b) show the fluorescence micrograph of the sample film and the corresponding sinusoidal intensity profile, respectively, after photobleaching.   In Figure 3.2 (a), the photobleached regions appear darker than the unbleached regions while the film surface is topologically flat as confirmed by bright-field optical microscopy.   The intensity profile was fit to the sinusoidal function of Eq. 2.4 in Chapter 2,[13] from which the amplitude of the intensity profile ($A(t = 0)$) was determined.   The second step involves monitoring the temporal evolution of self-diffusion under thermal activation.   In the experiment, the specimen was placed on a hot stage (Linkham TMS91) where self-diffusion measurements were conducted at 106°C (= $T_{g,bulk} + 48^{\circ}$C) in an environment of slowly flowing argon gas to avoid quenching by oxygen.   Before the experiment, the specimen was kept at the measurement temperature in the presence of argon gas for 4 min to attain thermal equilibrium.   As the self-diffusion process proceeds, the intensity difference between the bleached and unbleached regions becomes smaller, which corresponds to a decrease of $A(t)$ with time.   Figure 3.2 (c) shows the time variation of the normalized intensity amplitude, $A(t)/A_0$, for 120 nm and 19 nm thick PiBMA films. The slope of $\ln(A(t)/A_0)$ versus time is proportional to D, where A_0 represents the A value at $t = 0$.   It is apparent from the 120 nm and 19 nm thick film data that the value of D is independent of the film thickness.   The experimental uncertainty of D was calculated based on the propagation of the error.[13]
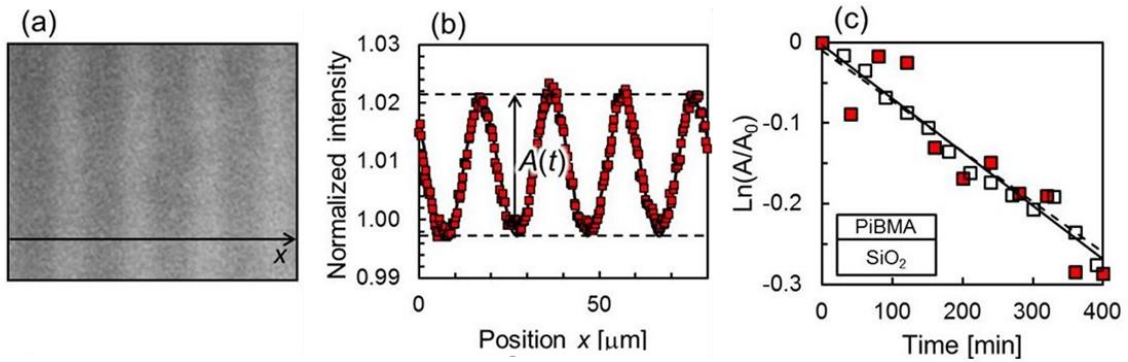
Figure 3.2:   (a) Fluorescence micrograph of a 120 nm thick PiBMA/SiO$_X$ film after photobleaching.   The total width of the image is 80 μm and the pitch size is 20 μm.   (b) Normalized intensity plotted as a function of position along the x-axis.   This profile can be fit with a sinusoidal function with an amplitude of $A(t)$.   (c) Representative fluorescence amplitude decays from 120 nm (open symbols) and 19 nm (filled symbols) PiBMA films obtained at the same pitch size and temperature of 106°C (= $T_{g, bulk}$ + 48°C).   The time variation of the intensity amplitude $A(t)$ was normalized by that at $t = 0$ denoted as A_0. The solid and dashed line denote the best fit to the 120 nm and 19 nm film data, respectively, using Eq. 2.4.

3.2.4   Effective viscosity measurements by atomic force microscopy

The mobility (M_{tot}) of a film or equivalently its effective viscosity (η_{eff}) was determined by monitoring the power spectral density (PSD) of the film at different times upon annealing it at the measurement temperature.   To determine the PSD, we measured the surface topography of the film using tapping-mode atomic force microscopy (AFM). The surface topography profile was then multiplied by a Welch function, Fourier-transformed and subsequently radial-averaged to produce the PSD.[30, 31]   Further details of the procedure can be found in the Appendix A.3.

As noted above, the PiBMA films are unentangled and so they are Newtonian-like.   In the case of the PS films, the MW was just above the characteristic MW for entanglement dynamics (namely, ≈ 31 kg/mol.[32]).   Since the measurement temperature was 40°C above $T_{g,bulk}$ and the resolvable time for η_{eff} measurements was only a few

42

seconds, the probed dynamics should also be Newtonian-like. For Newtonian liquid films, the time (t) varying PSD are describable by Eq. 3.1 and 3.2.[15, 30, 33, 34]

$$A_q^2(t) = A_q^2(0)\exp(2\Gamma t) + \left[\frac{k_B T}{d^2 G(h_0)/dh^2 + \gamma q^2}\right](1 - \exp(2\Gamma t)) \qquad (3.1)$$

$$\text{where, } \Gamma(\boldsymbol{q}) = -M_{\text{tot}}\left[(d^2 G(h_0)/dh^2)q^2 + \gamma q^4\right] \qquad (3.2)$$

Here, $A_q^2(t)$ denotes the PSD, $\boldsymbol{q}$ is the wavevector and $q \equiv |\boldsymbol{q}|$, k_B is the Boltzmann constant, T is the measurement temperature in degrees Kelvin, γ is the surface tension, h_0 is the average thickness of the film, $G(h_0)$ is the van der Waals potential, and M_{tot} is the mobility of the film.[15, 34] If the no-slip boundary condition applies at the substrate surface and the film possesses no dynamic heterogeneity or the viscosity η is spatially uniform, one can show that $M_{\text{tot}} = h_0^3/(3\eta)$. This relation allows the viscosity of a uniform film to be determined from M_{tot} by applying the relation $\eta = h_0^3/(3M_{\text{tot}})$.[34] But in general, the viscosity may vary within the film depth[15] and the no-slip condition may not apply.[17] We define η_{eff} by using the same expression in Eq. 3.3, where η_{eff} represents the average flow behavior of the film.

$$\eta_{\text{eff}} \equiv h_0^3/(3M_{\text{tot}}) \qquad (3.3)$$

Figure 3.3 shows two representative sequences of PSD, both taken from PiBMA films at 106°C. One has $h_0 = 10$ nm (Figure 3.3 (a)), and the other has $h_0 = 120$ nm (Figure 3 (b)). The circles (○) denote the experimental data and the solid lines denote the best fit to Eq. 3.1. In analyzing the data, we first fit the high-q portion of the PSD (namely the portion where different PSDs overlap) to $A_{q\rightarrow\infty}(t) = k_B T/(\gamma q^2)$, which enabled determination of the value of γ. Then, the whole sequence of PSD was fit by only varying the value of M_{tot}, while fixing γ to the value just determined and the values of T and h_0 to the experimental values. As for $G(h_0)$, $G(h_0)$ was defined as

43

$-A_{\text{Ham}}(h_0)/(12\pi h_0{}^2)$, following a previous work,[35] where $A_{\text{Ham}}(h_0)$ is the Hamaker function. For the PiBMA films, we adopted a constant value of -1×10^{-19} J for $A_{\text{Ham}}(h_0)$ based on Zhao *et al.*'s work[36] as discussed in Appendix A.3. From the fit lines shown in Figure 3.3, one can see that the model describes the data well. By using this method, η_{eff} of both the labeled (PiBMA-NBD/SiO$_x$) and unlabeled (PiBMA/SiO$_x$) films was measured. No discernible difference could be found between the measured η_{eff}.
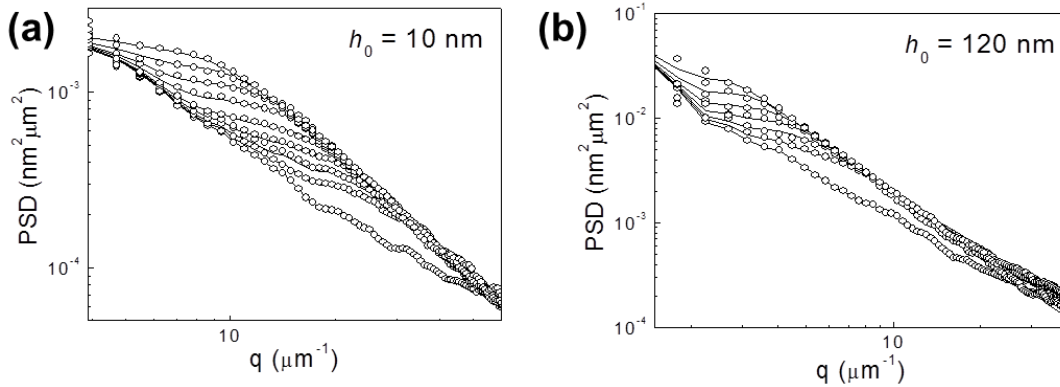
Figure 3.3: Illustration of the experimental data and model used to determine the effective viscosity (η_{eff}). The circles ($\circ$) represent the power spectral density (PSD) obtained from PiBMA/SiO$_x$ films with (a) $h_0 = 10$ nm and (b) 120 nm annealed at 106°C for various times. The annealing time of individual curves (from bottom) are (a) $t = 0, 5, 10, 20, 40, 90, 180, 360, 720$ s, and (b) $t = 0, 5, 10, 20, 40, 80$ s. The solid lines are model lines with (a) $\eta_{\text{eff}} = 4 \times 10^4$ Pa s and (b) 8.9×10^4 Pa·s.

3.3 RESULTS

3.3.1 Glass transition temperature and self-diffusion coefficient

In Figure 3.4, (a) T_g and (b) in-plane D measured at $T = 106°C$ as a function of film thickness ($h_0 = 15$ to ~300 nm) are shown. In Figure 3.4 (a), the dashed line denotes the value of $T_{g,\text{bulk}}$ determined by DSC. In Figure 3.4 (b), the dashed line

denotes the value of D_{bulk} obtained by averaging the measured values of D of 120 nm thick films with different photobleached pitch sizes at $106^{o}C$ (Figure 2.3 in Chapter 2). Figure 3.4 (a) clearly shows that the T_g is independent of h_0 and is consistent with $T_{g,bulk}$. This is in agreement with previous results of PiBMA/SiO$_x$ with $M_n = 8.7$[13] and 300 kg/mol[24] (c.f. the current M_n is 10.0 kg/mol). In a previous work,[24] a 14 nm thick fluorescently labeled PiBMA layer reported that the local T_g at the free surface was depressed by $6^{o}C$ while that at the substrate surface was enhanced by $5^{o}C$. The latter finding was attributed to the hydrogen-bonding interactions between PiBMA and the hydroxyl groups on the silica surface. Together, these results reveal that there is a distribution of T_g's in the films, and the effect of the substrate surface exactly balances that of the free surface.
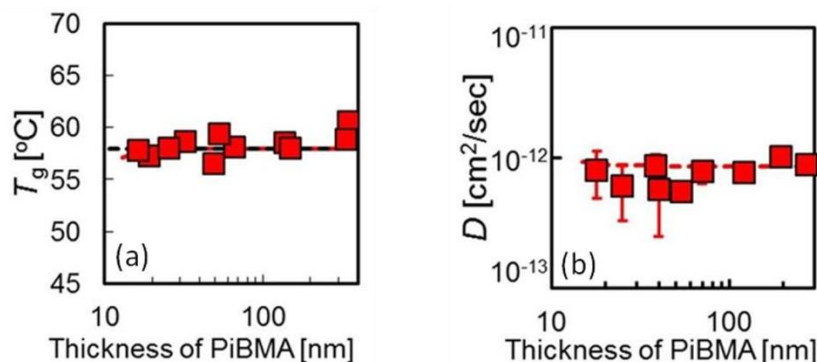
Figure 3.4: (a) Thickness dependence of T_g for PiBMA/SiO$_x$. The dashed line shows the T_g of bulk PiBMA ($58^{o}C$) as determined by differential scanning calorimetry (DSC). (b) Thickness dependence of D for PiBMA/SiO$_x$ as measured by FRAPP at $106^{o}C$ ($= T_{g,bulk} + 48^{o}C$). The dashed line corresponds to D_{bulk} taken to be the average D of the 120 nm thick films (Figure 2.3 in Chapter 2). The error bars indicate the 95% confidence intervals.

Now we turn to the D data in Figure 3.4 (b). D is also clearly independent of the film thickness and equal to the D_{bulk} value. These findings are consistent with those

45

observed by Katzenstein *et al.*[13] for fluorescently labeled PiBMA/SiO$_x$ with M_n = 8.7 kg/mol. Similar to the above arguments for T_g, the finding of constant $D(h_0)$ may imply cancellation between the effects of the substrate and free surface on the self-diffusion. We shall express these concepts mathematically in the next section.

3.3.2 Effective viscosity

Figure 3.5 (a) is the η_{eff} data plotted versus temperature T for PiBMA/SiO$_x$ with thicknesses h_0 varied between 10 and 120 nm and T from 74°C (= $T_{g,bulk}$ + 16°C) to 106°C (= $T_{g,bulk}$ + 48°C). The equivalent M_{tot} versus T data is shown in Figure 3.5 (b). We find that the η_{eff} measurement of the 120 nm films was consistent with the η of the bulk PiBMA determined by conventional rheometry in Figure A.1 in Appendix A. However, at the other film thicknesses, η_{eff} decreased with decreasing h_0 for the whole range of T studied. Comparing this trend with the h_0-invariance of D found above, one can conclude that D and η_{eff} of the films depend on the local dynamic properties differently.
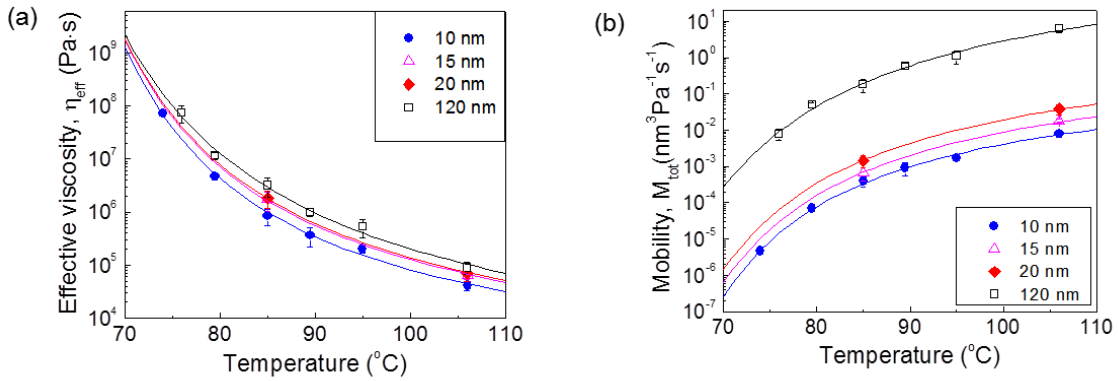
Figure 3.5: (a) Semi-log plot of η_{eff} versus temperature for PiBMA with different thicknesses (h_0) as indicated in the figure legend. (b) Semi-log plot of mobility [$M_{tot} \equiv h_0^3/(3\eta_{eff})$] versus temperature of the same data shown in (a). The solid lines are the best fit to the three-layer model assuming h_1 = 3.67 nm as described in Section 3.4.

46

3.4   DISCUSSIONS

3.4.1   Three-layer model

In accordance with current views and results,[2, 4, 13, 15] we interpret the confinement effects demonstrated by our data to arise from competition between the antagonistic effects of the free surface and substrate interface on the local dynamics of the polymer. With this, the thickness-invariant D and T_g measurements shown in Figure 3.4 suggest that the effects of the two surfaces cancel.   On the other hand, the $\eta_{eff}(h_0)$ data of Figure 3.5 suggests that the effect of the free surface dominates.   We first focus on the different h_0 dependences of $D(h_0)$ and $\eta_{eff}(h_0)$.   We attribute this finding to D and η_{eff} being different functions of the local segmental friction coefficient.   For a polymer melt with N segments per chain, the D scales with the segmental friction coefficient (ζ) as is shown in Eq. 3.4.[14, 37]

$$D = \frac{k_B T}{N \zeta} \tag{3.4}$$

As was in previous works,[2, 15] we incorporate dynamic heterogeneity in the films by using a layer model.   Specifically, we treat the films to be a stack of n dynamically different layers with thicknesses, h_i, and local viscosities η_i, or equivalently local segmental friction coefficient ζ_i, where $\zeta_i \propto \eta_i$ and $i = 1, 2, \ldots, n$.   In FRAPP measurements of D,[14] the pitch width of the photobleached patterns (which is ~µm) is much bigger than the film thickness ($\approx$ 10 to ~100 nm here).   Then the majority of the chains in the unbleached region should have diffused many times through all n layers of the films before reaching the bleached region and being detected.   Therefore, Eq. 3.4 yields Eq. 3.5 and 3.6.

$$D = \frac{k_B T}{N <\zeta_i>}, \tag{3.5}$$

47

where
$$\langle \zeta_i \rangle \propto \langle \eta_i \rangle = \frac{\sum_{i=1}^{n} \eta_i h_i}{\sum_{i=1}^{n} h_i} \tag{3.6}$$

As for η_{eff}, it is derived from the mobility M_{tot} from the definition, $\eta_{eff} = h_0^3/(3M_{tot})$ (Eq. 3.3). To find a relation between M_{tot} and the current model parameters, namely h_i and η_i, one solves the Navier-Stokes equation for the steady-state velocity profile in the film ($v(z)$), where z is the perpendicular distance from an interface of the film, upon application of a pressure gradient (∇P) parallel to the film. And then M_{tot} was estimated from the definition: $M_{tot} \equiv h_0 <v(z)>/(-\nabla P)$, where $<...>$ indicates averaging over z.[15] We find that the simplest model that can simultaneously account for the D (Figure 3.4 (b)) and η_{eff} (Figure 3.5 (a)) data is a three-layer model. By assuming the no-slip boundary condition at the substrate interface, which has been found applicable to polymer films with low MW ($< \sim 100$ kg/mol) like the films studied here,[17] we derive the following expression for M_{tot}:

$$M_{tot} = \frac{h_1^3}{3\eta_1} + \frac{h_2^3}{3\eta_2} + \frac{h_3^3}{3\eta_3} + \frac{h_1 h_2 (h_1 + h_2)}{\eta_2} + \frac{(h_1 + h_2)h_3(h_1 + h_2 + h_3)}{\eta_3} \tag{3.7}$$

where, $h_0 = h_1 + h_2 + h_3$, $i = 1, 2, 3$ labels the layers from top to bottom in order. We interpret the $i = 1$ top layer to be the surface mobile layer, the $i = 2$ layer to be the bulk-like middle layer, and the $i = 3$ layer the polymer/substrate interfacial layer. Accordingly, one expects $\eta_3 > \eta_2 = \eta_{bulk} > \eta_1$, which we find from our fit results as discussed below. Figure 3.6 shows a schematic illustration of the three-layer model described.
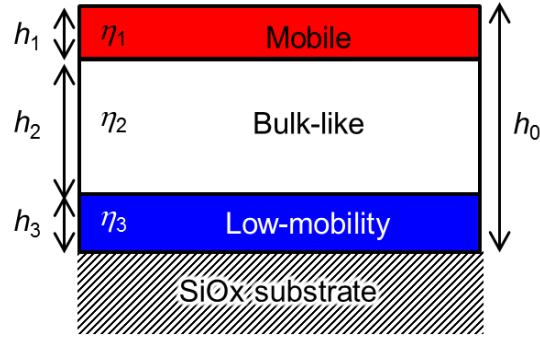
Figure 3.6: Schematic representation of the three-layer model discussed in the text. In this model, the film is assumed to be made up of (from top) a surface mobile layer ($i = 1$), a bulk-like middle layer ($i = 2$), and a low-mobility polymer layer ($i = 3$) immediate to the substrate surface. The layer thicknesses and viscosities are denoted by h_i and η_i, respectively.

In a previous study, Li *et al.* measured the η_{eff} of poly(methyl methacrylate supported by silica (PMMA/SiO$_x$), and found that a similar three-layer model was able to describe the experimental result. [16] In fitting the data, they had to incorporate a thickness dependence in the mobility of the surface mobile layer (M_t). Here, we find the same to be needed. Clearly, M_t depends directly on h_1 and $1/\eta_1$. Because the thickness of this layer h_1 has been shown to be independent of the film thickness h_0,[15, 38] we attribute the thickness dependence of M_t ($M_t(h_0)$) to $1/\eta_1$. Following the form of $M_t(h_0)$ proposed by Li *et al.*,[16] we write

$$\eta_1(h_0) = \eta_1(\infty)\{1 + \exp[-(h_0 - l_t)/\Delta l_t]\} \tag{3.8}$$

where, l_t denotes the film thickness at which $\eta_1 = 2 \cdot \eta_1(\infty)$, and Δl_t is the length scale over which the change takes place. Figure 3.7 displays a plot of $\eta_1(h_0)/\eta_1(\infty)$ found to describe the experimental results. In the following, we discuss how we apply the three-layer model to fit the D (Figure 3.4 (b)) and η_{eff} (Figure 3.5(a)) data simultaneously.

49
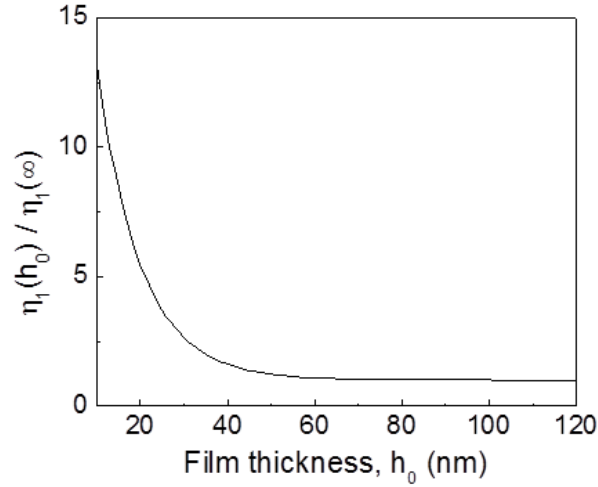
Figure 3.7: Plot of $\eta_1(h_0)/\eta_1(\infty)$ versus h_0 values used for the three-layer model (Figure 3.6) to fit the data in Figure 3.5 (a) and (b).

As observed above, $D \sim 1/\langle\eta\rangle$ yields $D(h_0)/D(\infty) = \langle\eta_i(\infty)\rangle/\langle\eta_i(h_0)\rangle$. Experimentally, $D(h_0)$ is thickness-independent as shown in Figure 3.4 (b), which means $\langle\eta_i(\infty)\rangle/\langle\eta_i(h_0)\rangle = 1$ or

$$\eta_{\text{bulk}} = \langle\eta(h_0)\rangle \equiv \frac{\eta_1 h_1 + \eta_2 h_2 + \eta_3 h_3}{h_1 + h_2 + h_3} \tag{3.9}$$

$$\Rightarrow \qquad \eta_3 = \eta_2 + \frac{h_1}{h_3}(\eta_2 - \eta_1) \tag{3.10}$$

where the assumption $\eta_2 = \eta_{\text{bulk}}$ was used. According to Eq. 3.10, if η_1 is small than η_{bulk}, η_3 should be larger than η_{bulk}. This warrants the above interpretation of the three-layer model.

3.4.2 Determination of parameters used in the three-layer model

In fitting the data, we simplify the procedure by making two additional assumptions. First, we assume the third layer thickness, h_3 to be equal to the thickness of the irreversibly adsorbed PiBMA layer found on the substrate. The adsorbed layer thickness was attained with a 120 nm thick PiBMA film on SiO_x, following a procedure

50

from a previous study.[39]   The film was annealed at 106°C for 18 h under argon atmosphere to mimic the environment during the FRAPP measurement.   After annealing, the film was subsequently washed with THF, a good solvent for PiBMA.   A more detailed procedure is available in Appendix A.5.   The adsorbed layer thickness was determined as $h_3 = 0.9 \pm 0.3$ nm.   The error is the standard deviation of five measurements at different locations on the sample.   Secondly, we assume that the temperature dependence of $M_t(T)$ ($\sim 1/\eta_1(T)$) is proportional to $1/\eta_{\text{eff}}(T)$ of the $h_0 = 10$ nm films, which was found to be described by

$$\eta_{\text{eff}}(h_0 = 10 \text{ nm}) = (723 \pm 456 \text{ Pa} \cdot \text{s}) \exp(\frac{211 \pm 34 \text{ K}}{T - (329 \pm 2) \text{ K}}) \tag{3.11}$$

This assumption came from the observation that the contribution of M_t to M_{tot} usually increases as h_0 decreases.[15, 16]   For h_1, we attempt two possible values.   In the first attempt, we assume $h_1 = R_{\text{EE}} = 3.67$ nm, where R_{EE} is the end-to-end distance of the polymer and $\approx 6^{1/2} \cdot R_g$.   This corresponds to the situation where enhanced surface flow occurs mainly in the top layer of polymer molecules.   In the second attempt, we set h_1 equal to the Kuhn length of the polymer, which is approximated to be ~1 nm.[40]   This choice of h_1 is due to a simulation result of Lam *et al.*[41] on ten-mer polymer films undergoing driven in-plane flow, which showed that enhanced surface flow existed mainly within a Kuhn length of the free surface.

The fit results based on the above model and assumptions are summarized in Table 3.1.   In comparing the fit values of the model parameters shown in different columns corresponding to different values set for h_1, one observes that in changing the value of h_1 from 3.67 to 1 nm, only the value of $h_1^3/3\eta_1$ (i.e., the first term on the right hand side of Eq. 3.7) needs to be adjusted while the other parameters maintain the same values.

	$h_1 = R_{EE} = 3.67$ nm	$h_1 = 1$ nm
$h_1^3/3\,\eta_1(\infty)$	$(4.3\pm0.2)\times\exp(-\dfrac{211\text{ K}}{T-329\text{ K}})$	$(4.0\pm0.2)\times\exp(-\dfrac{211\text{ K}}{T-329\text{ K}})$
l_t (nm)	35 ± 14	35 ± 14
Δl_t (nm)	10 ± 2	10 ± 2

Table 3.1: Result obtained from the three-layer model fits to the D and η_{eff} data for PiBMA/SiO$_x$ assuming two values of h_1, where R_{EE} is the end-to-end distance of PiBMA.[a]

To explore the reason, we examined the relative contributions of different terms in Eq. 3.7 to M_{tot} at 90°C, which is near the middle of the temperature range studied. Figure 3.8 (a) shows semi-log plots of the different relative contributions as a function of h_0, where M_i denotes $h_i^3/(3\eta_i)$ (i = 1,2,3) and "Cross terms" denotes the sum of the last two terms in Eq. 3.7. From these plots, one sees that M_1/M_{tot} exhibits the same h_0 dependence for both cases of $h_1 = 1$ and 3.67 nm. In fact, we find that the $M_1/M_{\text{tot}}(h_0)$ dependence of the $h_1 = 1$ nm curve can be described by multiplying that of the $h_1 = 3.67$ nm curve by 0.93. At this time, we do not know the reason for this simple relationship.

---

[a] The values of the other model parameters not given in the table were fixed according to the following: (1) $h_2 \equiv h_0 - (h_1 + h_3)$. (2) $\eta_2 \equiv \eta_{\text{bulk}} = \eta_{\text{eff}}$ of the 120 nm thick PiBMA/SiO$_x$ films = $(365 \pm 316$ Pas$)$ exp[(318 $\pm$ 47 K) / $(T - (323 \pm 3$ K$))$] (3) h_3 = thickness of the adsorbed layer of PiBMA/SiO$_x$ = (0.9 ± 0.3) nm. (4) $\eta_3 = [\eta_2(h_1 + h_3) - \eta_1 h_1]/h_3$ due to Eq. 3.9 and 3.10.
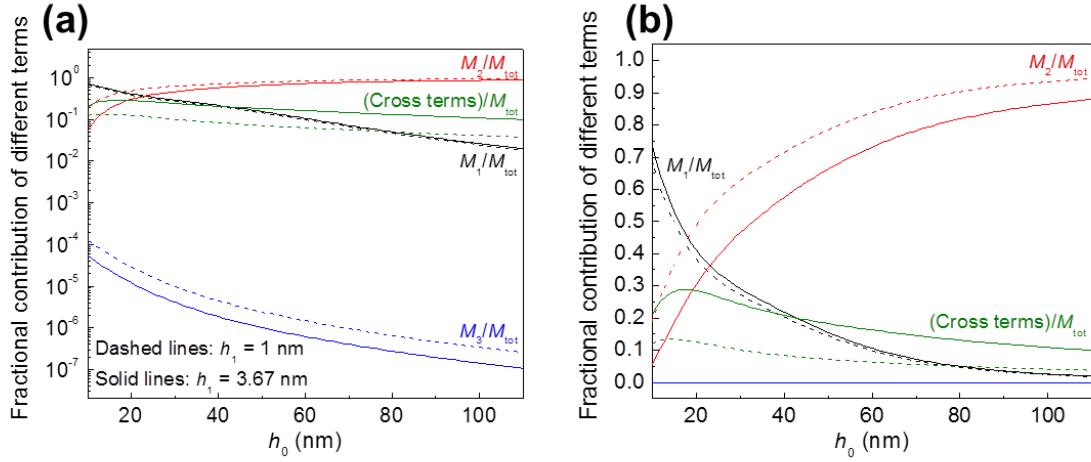
Figure 3.8: The relative contributions of M_1, M_2, M_3 and the cross terms to M_{tot} versus h_0 in semi-log (a) and linear (b) plots. These data were obtained under $T = 90^{\circ}C$ and $h_1 = 3.67$ nm (solid lines) and 1 nm (dashed lines), respectively.

Empirically, one sees from Figure 3.8 (b), which displays the same data from Figure 3.8 (a) but on a linear scale, that it is due to partial cancellation of the change in M_2/M_{tot} and that in (cross terms)/M_{tot} upon the change in h_1 that is incidentally balanced by a constant percentage change in M_1/M_{tot}. It is instructive to compare the fitting results of PiBMA/SiO$_x$ with those of PMMA/SiO$_x$.[16] According to Figure 3.8, the contribution of M_3 to M_{tot} is negligible. This means that in fitting the η_{eff} data for PiBMA/SiO$_x$, we could have set the bottom layer to be dynamically dead (i.e., $M_3 = 0 \Leftrightarrow \eta_3 = \infty$) as was done for PMMA/SiO$_x$.[16] But with the knowledge of $D(h_0)$, we are obliged to set the value of η_3 according to Eq. 3.10. Another important difference between the two results is that the temperature dependence of $M_1(h_0,T)$ was Arrhenius in PMMA/SiO$_x$, but it follows the Vogel-Fulcher-Tammann (VFT) dependence here (Figure 3.9). This result indicates that cooperativity is present in the transport dynamics of the surface mobile layer of the PiBMA films, but undetectable in the PMMA films. Alongside, one observes that the Kauzmann temperature (T_K) of our PiBMA polymer is

53

only $\sim$ 8K below the bulk T_g (based on the expression of $\eta_{bulk}(T)$ of PiBMA given in the footnote of Table 3.1) while the $T_{g,bulk} - T_K$ values for PMMA are much bigger, $\approx$ 72 and 64 K for M_w = 2.7 and 12.4 kg/mol, respectively.[16] Noting that the VFT cooperative dynamics approaches the Arrhenius (uncooperative) one in the limit of $T - T_K \rightarrow \infty$, then the notably smaller value of $T_{g,bulk} - T_K$ suggests that the extent of cooperativity in the transport dynamics of the PiBMA polymer is bigger than that of PMMA for the same $T - T_g$. A bigger extent of cooperativity is expected to bring about stronger coupling between different layers. This is in agreement with the bigger values of l_t and Δl_t found of the PiBMA/SiO$_x$ films compared to those of PMMA/SiO$_x$ where l_t and $\Delta l_t \approx$ 5 and 1 nm, respectively.[16] We should, however, clarify that the extent of cooperativity mentioned above may differ from the size of cooperativity at the T_g (ζ_c) commonly discussed of glassy dynamics.[20] In fact, different temperature dependences had been found between terminal flow and segmental relaxations in polymer melts near the T_g.[42] Previous experiments on a variety of polymer film systems found that the extent of variation of the thin film T_g from the bulk value did not correlate with the ζ_c value of the polymer.[20, 43] Thus we do not think that that ζ_c or extent of cooperativity mentioned above may explain our observations. As demonstrated in Section 3.4.1, our data can be accounted for by assuming that $1/D$ and η_{eff} are different functions of the local segmental friction (ξ_i).
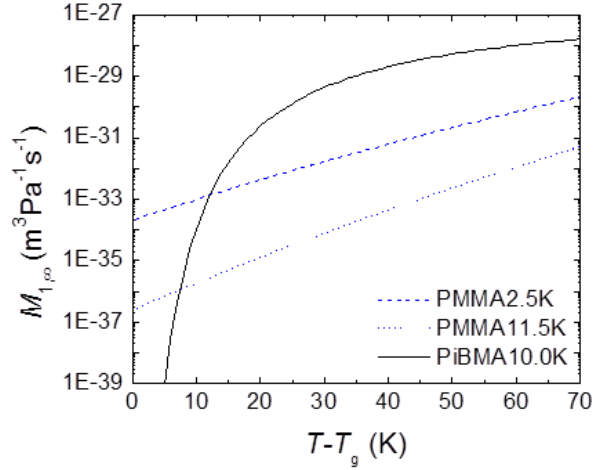
Figure 3.9:   Comparison of $M_{1,\infty}$ versus $T - T_g$ of the PiBMA/SiO$_x$ films ($M_n = 10.0$ kg/mol, solid line) and the PMMA/SiO$_x$ films ($M_n = 2.5$ and 11.5 kg/mol, dashed and dotted line, respectively) reported in Li et al[16] and reproduced with permission.   Copyright 2013, American Chemical Society.

3.4.3   Application of the three-layer model to PS/SiO$_x$ system

As discussed in Section 3.1, there is a long-standing question concerning the inconsistent $T_g(h_0)$,[3, 20] $D(h_0)$[11, 12] and $\eta_{eff}(h_0)$ [15, 17] dependences of the PS/SiO$_x$ films.   To address the incompatible T_g-D-η_{eff} relations of PS/SiO$_x$, we also measure the η_{eff} of PS/SiO$_x$.   PS used in this experiment was purchased from Scientific Polymer Products (Ontario, NY) and used as-received.   The M_n of the PS was 38 kg/mol (Đ = 1.11), the same as that used for the study of $D(h_0)$ in a work of Frank et al. for a comparison.[12]   In Figure 3.10 (a), we reproduce the data of Frank et al.[12] for the in-plane D of PS/SiO$_x$ with M_n = 38 kg/mol at T = 140°C.   Figure 3.10 (b) displays the $\eta_{eff}(h_0)$ data, upon normalization by η_{bulk} (taken to be η_{eff} = 70 ± 12 kPa·s at the limit of $h_0 \rightarrow \infty$ measured at the same temperature as Frank et al.[12]   We find that these data can be fit to the above three-layer model (solid lines in Figure 3.10 (a) and 3.10 (b)) with the model parameters and details of the fitting procedure are given in Table 3.2.   This provides further support

55

to the present proposal that D and η_{eff} are different functions of the local segmental friction coefficient and so can exhibit divergent h_0 dependences.
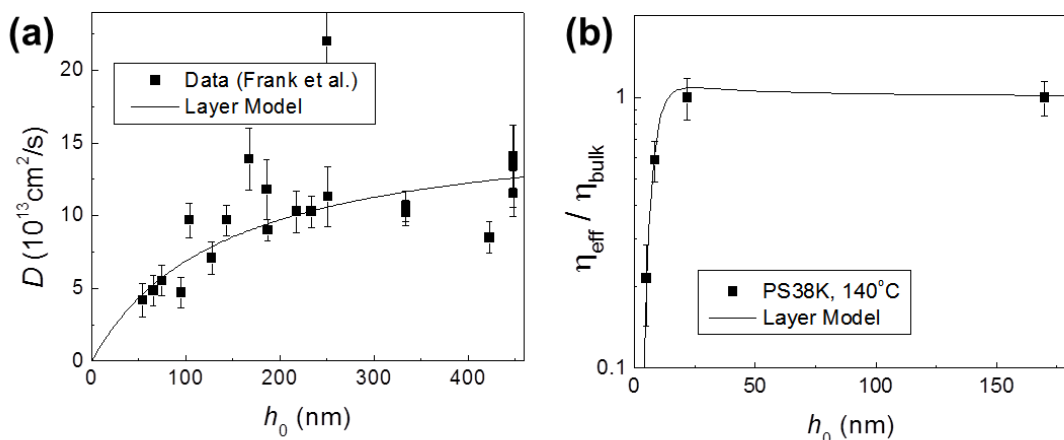
Figure 3.10: (a) The D versus h_0 data reported by Frank et al.[12] for PS/SiO$_x$ with $M_n = 38$ kg/mol at $T = 140^\circ$C. (b) Normalized effective viscosity η_{eff}/η_{bulk} versus h_0 for PS/SiO$_x$ obtained under the same condition as the D measurement. In both panels, the experimental data are shown by the symbols. The best fits to the three-layer model are displayed by the solid lines. Data of panel (a) was reproduced with permission from Frank et al.[12] Copyright 1996, American Chemical Society.

As for the $T_g(h_0)$ dependence, Lipson and Milner[44] pointed out that measurements like ours −that monitor changes in the thermal expansivity of the films at the glass transition− detect the unweighted average of the local T_g's if the films can be considered to be a stack of dynamically heterogeneous layers, each exhibiting the same liquid- and glassy- state thermal expansivities. We find that the $T_g(h_0)$ of our systems conforms this prediction. By using a fluorescently labeled layer that reports the local T_g,[4] Ellison and Torkelson found that the T_g of the top layer of PS/SiO$_x$ was significantly depressed (by ~ 30°C from $T_{g,bulk}$) while that of the bottom layer was relatively unaffected (although it is

important to note that the bottom layer examined the 12 nm nearest the substrate interface).[4]   Then an unweighted average T_g should decrease with decreasing h_0, as observed in experiment.   For PiBMA/SiO$_x$, Priestley $et\ al.$[24] found that the local T_g at the free surface was depressed by 6°C while that at the substrate surface was enhanced by 5°C.   By using these T_{gi} values and $h_1 = 3.67$ or 1 nm, the unweighted average T_g again accounts for experimental observations within typical measurement uncertainties.

$h_1 = 3$ nm	
η_1/η_2	0.049 ± 0.006
h_3 (nm)	1 ± 0.5
η_3/η_2	145 ± 20
D_∞ (10^{13} cm^{2}s^{-1})	16.6 ± 0.8

Table 3.2:   Result obtained from the three-layer model fits to the D and η_{eff} data for PS/SiO$_x$ assuming $h_1 = 3$ nm.[b]

3.5   CONCLUSIONS

In summary, we have examined the correlation between T_g, D and η_{eff} of nanoconfined polymer films supported by a solid substrate.   Two systems were considered, namely PiBMA/SiO$_x$ and PS/SiO$_x$.   For PiBMA/SiO$_x$, the T_g and D were invariant with the film thickness, but η_{eff} decreased with decreasing film thickness.   For PS/SiO$_x$, the T_g and η_{eff} decreased with decreasing film thickness while D exhibited an

[b] Note that D is not a constant here and determined by Eq. 3.5 and 3.6, which can be combined to give $D = D_\infty h_0/(h_1\eta_1/\eta_2 + h_2 + h_3\eta_3/\eta_2)$.   The use of this expression instead of Eq. 3.10 as was done before results in the need for an additional parameter, D_∞.   (2) It is assumed that $h_2 \equiv h_0 - (h_1 + h_3)$.   This is consistent with the previous observation that h_1 is no more than 3 nm for PS/SiO$_x$.[15]   Like above, we find that the value of η_1/η_2 co-varies with the value of h_1 according to $h_1^3/(3\eta_1) \approx$ constant.   Here, we assume that $h_1 = 3$ nm.

opposite trend.   To account for the observed divergent $D(h_0)$ and $\eta_{eff}(h_0)$ dependences, we proposed that they are different functions of the local viscosity η_i.   Specifically, $D \sim k_B T/\langle \eta_i \rangle$ and $\eta_{eff} = h_0^3/3M_{tot}(\eta_i)$.   By applying these assumptions to a three-layer model, we were able to describe the measurements well.   As for $T_g(h_0)$, we find that Lipson and Milner's proposal that it is the unweighted average T_g explains the observations. Considering the variety of confinement effects demonstrated by our systems, the proposed interpretations for $T_g(h_0)$, $D(h_0)$ and $\eta_{eff}(h_0)$ may provide a resolution to the decades-long controversy about how nano-confinement affects different dynamics of polymer films.

3.6   FUTURE WORK

3.6.1   Effects of polymer-substrate interface interactions

In this chapter, the relatively strong interaction between PiBMA and SiO_x due to hydrogen bonding led to non-trivial thickness dependent relationships between T_g, D and η_{eff}.   Based on this observation, it can be hypothesized that weaker polymer-substrate interactions may also alter the correlation between T_g, D and η_{eff} upon nanoconfinement. As will be discussed in Chapter 4, polycyclohexylethylene (PCHE) can be used as a substrate with a weaker interaction with PiBMA, because PCHE is hydrophobic and immiscible with PiBMA.   In addition, the T_g of PCHE is 85°C higher than the bulk value of the unentangled PiBMA utilized in this study so that a PCHE substrate would remain glassy during the D and η_{eff} measurements.

3.6.2   Glass transition temperature, viscosity, and self-diffusion coefficient measurements of polystyrene

Section 3.4.3 proposed a hypothesis to describe the counter-intuitive relationship between T_g, D and η of a PS thin film on a SiO_x substrate by using a three-layer model.

A seemingly easy experiment to test this hypothesis is simply measuring T_g, D and η_{eff} of PS. However, D measurements on PS thin films using the FRAPP technique are not straightforward because of a potential photochemical reaction during the photobleaching step. During photobleaching, UV light exposure induces dehydrogenation of PS as shown in Figure 3.11, which lowers the surface energy of the exposed area. Such surface energy gradient induces Marangoni flow upon annealing, which drives the formation of topological features. This topological feature formation due to dehydrogenation of PS was serendipitously discovered by Katzenstein *et al.* during FRAPP measurements,[45] but unfortunately this photochemical reaction also led to inaccurate FRAPP measurements. Therefore, careful design of the photobleaching process with optical filters is necessary to use the FRAPP technique on PS thin films.

Dehydrogenation of PS was reported to be primarily a result of wavelengths less than 200 nm,[46] but the formation of carbon-carbon double bonds was also observed after exposure using a broadband light source (300-600 nm).[47-49] Long-pass filters could be utilized to select an optimal wavelength range which allows enough contrast in the fluorescence intensity after photobleaching, but prevents the dehydrogenation reaction. The degree of dehydrogenation can be tracked by fluorescence measurements with an excitation wavelength of 310 nm and subsequently tracing a peak at a wavelength of ~ 350 nm originated from the formation of the double bond.[49] Once we address the chemical stability of PS under UV exposure, T_g and η_{eff} should be able to be evaluated in the same way as PiBMA in this chapter.
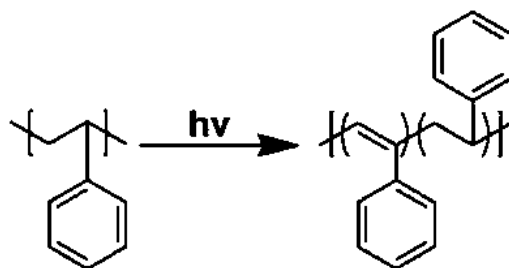
Figure 3.11: Dehydrogenation reaction of PS after exposure to UV light.   Adapted with permission from Katzenstein *et al.*[49]   Copyright   2012, American Chemical Society.

3.7   ACKNOWLEDGEMENTS

This project is a collaborative work with Professor Ophelia K.C. Tsui, Kun Geng, and Xuanji Yu at Boston University.   I would like to appreciate their contribution to this project, especially for the effective viscosity measurement and the development of the three-layer model.

3.8   REFERENCES

1.   Alcoutlabi, M.; McKenna, G. B. *J. Phys. Condens. Matter* **2005,** 17, R461-R524.
2.   Keddie, J. L.; Jones, R. A. L.; Cory, R. A. *Europhys. Lett.* **1994,** 27, 59-64.
3.   Tsui, O. K. C.; Zhang, H. F. *Macromolecules* **2001,** 34, 9139-9142.
4.   Ellison, C. J.; Torkelson, J. M. *Nature Mater.* **2003,** 2, 695-670.
5.   Pye, J. E.; Roth, C. B. *Phys. Rev. Lett.* **2011,** 107, 235701.
6.   Geng, K.; Tsui, O. K. C. *Macromolecs* **2016,** 49, 2671-2678.
7.   Stafford, C. M.; Vogt, B. D.; Harrison, C.; Julthongpiput, D.; Huang, R. *Macromolecules* **2006,** 39, 5095-5099.
8.   Torres, J. M.; Stafford, C. M.; Vogt, B. D. *ACS Nano* **2009,** 3, 2677-2685.
9.   Torres, J. M.; Stafford, C. M.; Vogt, B. D. *ACS Nano* **2010,** 4, 5357-5365.
10.   Stoykovich, M. P.; Yoshimoto, K.; Nealey, P. F. *Appl. Phys. A* **2008,** 90, 277-283.
11.   Zheng, X.; Rafailovich, M.; Sokolov, J.; Strzhemechy, Y.; Schwarz, S. A. *Phys. Rev. Lett.* **1997,** 79, 241-244.
12.   Frank, B.; Gast, A. P.; Russell, T. P.; Brown, H.; Hawker, C. *Macromolecules* **1996,** 29, 6531-6534
13.   Katzenstein, J. M.; Janes, D. W.; Hocker, H. E.; Chandler, J. K.; Ellison, C. J. *Macromolecules* **2012,** 45, 1544-1552.
14.   Lange, F.; Judeinstein, P.; Franz, C.; Hartmann-Azanza, B.; Ok, S.; Steinhart, M.; Saalwachter, K. *ACS Macro Lett.* **2015,** 4, 561-565.

15.   Yang, Z.; Fujii, Y.; Lee, F. K.; Lam, C.-H.; Tsui, O. K. C. *Science* **2010,** 328, 1676-1679.

16.   Li, R. N.; Chen, F.; Lam, C.-H.; Tsui, O. K. C. *Macromolecules* **2013,** 46, 7889-7893.

17.   Chen, F.; Peng, D.; Lam, C.-H.; Tsui, O. K. C. *Macromolecules* **2015,** 48, 5034-5039.

18.   Chen, F.; Peng, D.; Ogata, Y.; Tanaka, K.; Yang, Z.; Fujii, Y.; Yamada, N. L.; Lam, C.-H.; Tsui, O. K. C. *Macromolecules* **2015,** 48, 7719-7726.

19.   Chai, Y.; Salez, T.; McGraw, J. D.; Benzaquen, M.; Dalnoki-Veress, K.; Raphael, E.; Forrest, J. A. *Science* **2013,** 343, 994.

20.   Ellison, C. J.; Mundra, M. K.; Torkelson, J. M. *Macromolecules* **2005,** 38, 1767-1778.

21.   Adam, G.; Gibbs, J. H. *J. Chem. Phys.* **1965,** 43, 139-146.

22.   Hempel, E.; Hempel, G.; Hensel, A.; Schick, C.; Donth, E. *J. Phys. Chem. B* **2000,** 104, 2460-2466.

23.   Reinsberg, S. A.; Qiu, X. H.; Wilhelm, M.; Spiess, H. W.; Ediger, M. D. *J. Chem. Phys.* **2001,** 114, 7299-7302.

24.   Priestley, R. D.; Mundra, M. K.; Barnett, N. J.; Broadbelt, L. J.; Torkelson, J. M. *Aust. J. Chem.* **2007,** 60, 765-771.

25.   Ye, C.; Wiener, C. G.; Tyagi, M.; Uhrig, D.; Orski, S. V.; Soles, C. L.; Vogt, B. D.; Simmons, D. S. *Macromolecules* **2015,** 48, 801-808.

26.   Pintauer, T.; Matyjaszewski, K. *Chem. Soc. Rev.* **2008,** 37, 1087-1097.

27.   Bicerano, J., *Prediction of Polymer Properties*. Marcel Dekker, Inc.: New York, 2002.

28.   Brandrup, J.; Immergut, E. H.; Grulke, E. A., *Polymer Handbook*. 4th ed.; Wiley-Interscience: New York, 1999.

29.   Kim, S.; Hewlett, S. A.; Roth, C. B.; Torkelson, J. M. *Eur. Phys. J. E* **2009,** 30, 83-92.

30.   Wang, Y. J.; Tsui, O. K. C. *Langmuir* **2006,** 22, 1959-1963.

31.   Yang, Z.; Lam, C.-H.; DiMasi, E.; Bouet, N.; Jordan-Sweet, J.; Tsui, O. K. C. *Appl. Phys. Lett.* **2009,** 94, 251906.

32.   Fetters, L. J.; Lohse, D. J.; Milner, S. T. *Macromolecules* **1999,** 32, 6847-6851.

33.   Tsui, O. K. C.; Wang, Y. J.; Lee, F. K.; Lam, C.-H.; Yang, Z. *Macromolecules* **2008,** 41, 1465-1468.

34.   Lam, C.-H.; Tsui, O. K. C.; Peng, D. *Langmuir* **2012,** 28, 10217-10222.

35.   Israelachvili, J., *Intermolecular and Surface Forces*. Academic Press: London, UK, 1992.

36.   Zhao, H.; Wang, Y. J.; Tsui, O. K. C. *Langmuir* **2005,** 21, 5817-5824.

37.   Pearson, D. S.; Ver Strate, G.; Von Meerwall, E.; Schilling, F. C. *Macromolecules* **1987,** 20, 1133-1141.

38.   Paeng, K.; Swallen, S. F.; Ediger, M. D. *J. Am. Chem. Soc.* **2011,** 133, 8444-8447.

39.   Fujii, Y.; Yang, Z.; Leach, J.; Atarashi, H.; Tanaka, K.; Tsui, O. K. C. *Macromolecules* **2009,** 42, 7418-7422.

40.   Hiemenz, P. C.; Lodge, T. P., *Polymer Chemistry*. 2nd ed.; CRC Press: Boca Raton, FL, 2007.

41.   Lam, C.-H.; Tsui, O. K. C. *Phys. Rev. E* **2013,** 88, 042604.

42.   Roland, C. M.; Ngai, K. L.; Santangelo, P. G.; Qiu, X. H.; Ediger, M. D.; Plazek, D. J. *Macromolecules* **2001,** 34, 6159-6160.

43.   Campbell, C. G.; Vogt, B. D. *Polymer* **2007,** 48, 7169-7175.

44.   Lipson, J. E. G.; Milner, S. T. *Macromolecules* **2010,** 43, 9874-9880.

45.   Katzenstein, J. M.; Janes, D. W.; Hocker, H. E.; Chandler, J. K.; Ellison, C. J. *Macromolecules* **2012,** 45, (3), 1544-1552.

46.   Simons, J. K.; Chen, J. M.; Taylor, J. W.; Rosenberg, R. A. *Macromolecules* **1993,** 26, (13), 3262-3266.

47.   Arshad, T. A.; Kim, C. B.; Prisco, N. A.; Katzenstein, J. M.; Janes, D. W.; Bonnecaze, R. T.; Ellison, C. J. *Soft Matter* **2014**.

48.   Kim, C. B.; Janes, D. W.; Zhou, S. X.; Dulaney, A. R.; Ellison, C. J. *Chem. Mater.* **2015,** 27, (13), 4538-4545.

49.   Katzenstein, J. M.; Janes, D. W.; Cushen, J. D.; Hira, N. B.; McGuffin, D. L.; Prisco, N. a.; Ellison, C. J. *ACS Macro Lett.* **2012,** 1, (10), 1150-1154.

Chapter 4: Understanding the influence of interfacial interactions on glass transition temperature and self-diffusion coefficient

4.1 INTRODUCTION

Nanoconfined polymer films often exhibit different physical properties compared to bulk polymer, including the glass transition temperature (T_g),[1-7] viscosity (η),[8-11] modulus,[12-14] self-diffusion coefficient (D),[15-17] and others as was discussed in Chapter 1 and 2. As the film thickness decreases, the interfacial area to volume ratio increases dramatically, causing interfacial effects to dominate the entire film properties. While numerous studies have revealed how physical properties, e.g., T_g[1-7] and D[15-17] change with film thickness, these two properties are infrequently studied for identical nanoconfined systems and therefore, correlations between nanoconfined T_g and D are still unclear.[18] In terms of dynamic length scale, T_g reflects cooperative segmental mobility of 10s-100s of repeat units, whereas D reflects the large scale transport motion of the entire chain.

For bulk polymers, the Williams-Landel-Ferry (WLF) equation well correlates T_g and D.[19, 20] Under nanoconfinement, however, such a relationship between T_g and D has yet to emerge.[18] For polystyrene (PS) supported on SiO_2 substrates, numerous researchers have reported a decrease in T_g as the PS film thickness decreases below 50 nm.[1-4, 18] This decrease in T_g has been attributed to a higher segmental mobility of the chains near the free surface, and the presence of a relatively weak interaction between the PS film and the SiO_2 substrate.[21-23] If these nanoconfined PS films also follow the WLF equation, an increase in D would be expected with decreasing film thickness. Counterintuitively, D of both in-plane (parallel to the interfaces)[16] and out-of-plane (perpendicular to the interfaces)[17] have been reported to be reduced with decreasing PS film thickness. In contrast, faster dewetting[24] and leveling of both unentangled and

entangled PS on SiO$_2$ substrates have also been reported,[25] corresponding to higher D than that of bulk as the WLF equation predicts.   In order to clarify these seemingly contradictory results, a comprehensive study of the thermophysical parameters that reflect nanoconfined polymer dynamics on different length scales is strongly desired.

It is a challenge to study such complex T_g–D relationships in nanoconfined systems because there are many potential factors that could affect the behavior, such as chain entanglements and interfacial interactions.   Entanglement density is known to significantly affect polymer mobility,[26] and it is also reported that the entanglement density could change with film thickness.[27, 28]   Interactions between polymer films and neighboring substrates are also known to alter the dynamics of polymers.[29-33]   For instance, a strong interaction between poly(2-vinyl pyridine) and SiO$_2$ substrate increases the film T_g by tens of degrees C while a weaker interaction between PS and SiO$_2$ reduces the T_g by the same magnitude as the film thickness decreases.[5]

To address these issues, we designed a system to investigate the T_g–D relationship of an unentangled polymer confined by various interfaces.   To exclude the effect of entanglements, a nearly monodispersed poly (isobutyl methacrylate) (PiBMA) below its entanglement molecular weight (= ~28 kg/mol)[34] was synthesized and used.   The interfacial effects were systematically investigated using four multi-layered geometries with corresponding sample names as shown in Figure 4.1.   The top row in Figure 4.1 displays the sample arrangements with a stronger interaction between PiBMA and the SiO$_2$ substrate, due to hydrogen bonds between the ester groups on PiBMA and the hydroxyl groups on the SiO$_2$ substrate.[35]   The bottom row in Figure 4.1 shows the sample arrangements of PiBMA on polycyclohexylethylene (PCHE) substrates, exhibiting a weaker interaction due to the relative hydrophobicity of the PCHE.   To investigate influence of free surfaces, PCHE was also used as a capping layer due to its

excellent transparency to ultraviolet and visible light. Moreover, PCHE is immiscible with PiBMA[36] and remains in the glass state during measurements due to its higher T_g than PiBMA ($T_{g,PCHE} = T_{g,PiBMA\ bulk} + 85^oC$) as shown in Figure B.1 in Appendix B. For all PiBMA thin films, the T_g and D were characterized by ellipsometry and fluorescence recovery after patterned photobleaching (FRAPP), respectively.
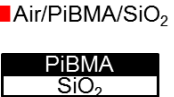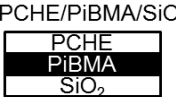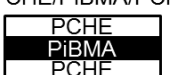
Top / Bottom	Air (Uncapped surface)	PCHE (Capped surface)
SiO$_2$ (Stronger interaction)	■ Air/PiBMA/SiO$_2$ PiBMA SiO$_2$	▲ PCHE/PiBMA/SiO$_2$ PCHE PiBMA SiO$_2$
PCHE (Weaker interaction)	● Air/PiBMA/PCHE PiBMA PCHE	◆ PCHE/PiBMA/PCHE PCHE PiBMA PCHE

Figure 4.1: Schematic diagram of film geometries in this study.

4.2 EXPERIMENTAL

4.2.1 Materials and sample preparation

A nearly monodisperse and unentangled PiBMA was synthesized by activators regenerated by electron transfer atom transfer radical polymerization.[37] Absolute number-averaged molecular weight (M_n) was determined as follows; unlabeled: absolute M_n = 10.0 kg/mol, Đ = 1.06, fluorescent dye-labeled: absolute M_n = 12.2 kg/mol, Đ = 1.18 by gel permeation chromatography. Unperturbed radius of gyration (R_g) of dye-labeled PiBMA was estimated as ~ 1.5 nm.[38] PiBMA films were spin-coated from n-butanol (1.0 - 8.0 wt%, 1800-3800 rpm) onto polished quartz substrates (for FRAPP measurements) or Si wafers (for T_g measurement) with 1.5-2.0 nm thick native oxide. PCHE layers (105 ± 5 nm) were also spincoated onto Si wafers from 2 wt% toluene at 1800 rpm. Prior to the spincoating, the substrates were cleaned in a solution of 10:10:80

65

wt% potassium hydroxide: deionized water: ethanol solution and rinsed with deionized water and tetrahydrofuran at least three times. The films were annealed for 20 min under vacuum at 120°C ($T_{\text{g,PiBMA}}$ + 62°C) for PiBMA and 150°C ($T_{\text{g,PCHE}}$ + 7°C) for PCHE to remove residual stress and solvent. The PCHE capping layers were prepared by floating the spincoated PCHE film on cold (< 5°C) water. The final multi-layered samples were dried at 35°C overnight and then annealed at 150°C for 10 min under vacuum.

4.2.2 Glass transition temperature (T_{g}) measurement by ellipsometry

To evaluate the film T_{g}, PiBMA film thicknesses were measured as a function of temperature with a cooling rate of 2°C/min by a spectroscopic ellipsometer (J.A. Woollam M-2000D).[39] Figure 4.2 (a) and (b) show representative data of the T_{g} measurements of Air/PiBMA/PCHE with PiBMA thickness of (a) 122 nm and (b) 14.3 nm, respectively. The different slopes in Figure 4.2 (a) and (b) at low and high temperature correspond to thermal expansion coefficients in the glass and melt states, respectively. Since T_{g} is the temperature at which polymer transforms from an equilibrium melt to a glass, T_{g} can be defined as the point where the slope changes.[3] As shown in Figure 4.2 (a), the T_{g} of the 122 nm thick film was 58.6°C, which is identical to the bulk value (58°C) measured by differential scanning calorimetry (DSC) with a heating rate of 10°C/min. On the other hand, the T_{g} of the 14.3 nm thick film was 46.1°C, which is approximately 12°C lower than the bulk value. The lower T_{g} in the thinner Air/PiBMA/PCHE film was attributed to contributions of both the free surface and the weaker interaction between PiBMA and the PCHE substrate, as discussed in detail later.

66

4.2.3 Self-diffusion coefficient (*D*) measurement by fluorescence recovery after patterned photobleaching

The *D* of labeled PiBMA under nanoconfinement was measured by FRAPP at 106$^\text{o}$C ($T_{\text{g,bulk}}$ + 48$^\text{o}$C).   For FRAPP measurements, a nitrobenzofurazan (NBD) dye was covalently attached to PiBMA as an end group.   Our previous study determined that end-chain-labeled and middle-chain-labeled PiBMA-NBD exhibited the same *D* within 95% confidence of error.[37]   To avoid self-quenching[40] of NBD, unlabeled PiBMA and labeled PiBMA (PiBMA-NBD) were mixed to limit the NBD content in the polymer film to lower than 0.18 wt%.   The *D* of PiBMA can be measured after photobleaching a pattern (20 μm in pitch) then observing how the intensity profile changes as molecular diffusion occurs.[37]   A detailed procedure is available in Section 2.1.2.   Figure 4.2 (c) shows a fluorescence micrograph and the corresponding intensity profile along the *x*-axis, where the excitation wavelength was 445 nm and the emission intensity was collected for wavelengths > 520 nm.   The intensity profile *I*(*x*,*t*) was fit to a sinusoidal function,[37] where *A*(*t*) is an amplitude of the sinusoidal intensity, *λ* is the pitch size of the photomask.   The specimens were placed on a hot stage at the measurement temperature (106$^\text{o}$C = $T_{\text{g,bulk}}$ + 48$^\text{o}$C) for 4 min prior to each measurement to attain equilibrium. During the FRAPP measurements, argon gas was purged over the sample slowly to avoid quenching by oxygen.[41]   As self-diffusion of the labeled PiBMA proceeded, the intensity amplitude, *A*(*t*), i.e., the difference in intensity between bleached and unbleached regions, also decreased.   By fitting *A*(*t*) to Eq. 4.1, *D* and the characteristic decay time (*τ*) can be obtained.

$$A(t) = A(0)\exp\left(-4\pi^2 Dt/\lambda^2\right) = A(0)\exp\left(-t/\tau\right) \tag{4.1}$$

Figure 4.2 (d) shows the time variation of *A*(*t*) for two Air/PiBMA/PCHE films, where the open symbols and closed symbols represent 120 nm and 19 nm thick films,

respectively. The slope of $A(t)$ versus time is proportional to D. The steeper slope of $A(t)$ of the thinner film indicates that the D of Air/PiBMA/PCHE is significantly increased by decreasing the thickness of PiBMA.
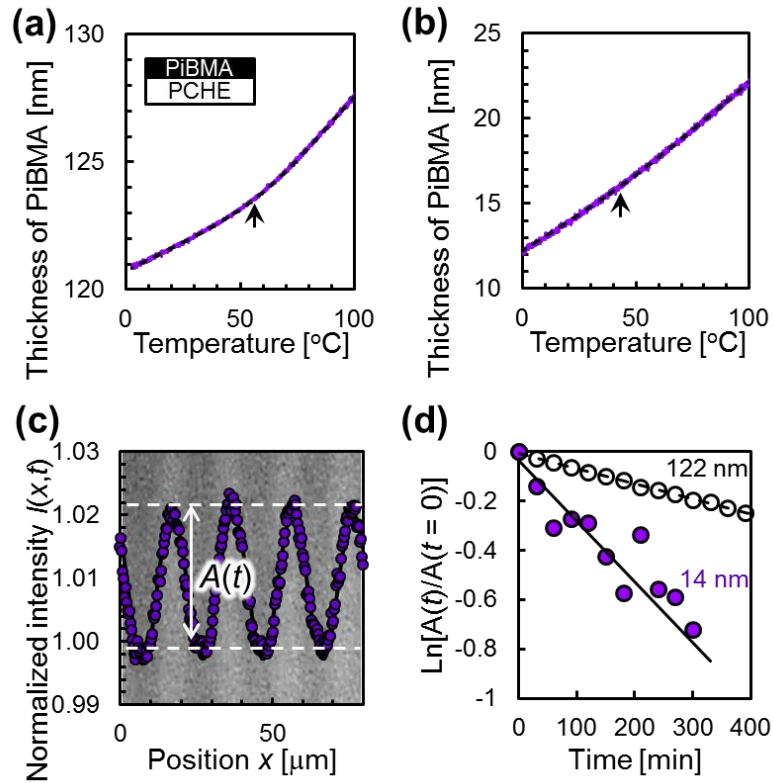
Figure 4.2: Representative data used to measure T_g and D for Air/PiBMA/PCHE samples. (a,b) Representative T_g measurement data of PiBMA film thickness as a function of temperature prepared on PCHE substrates and measured by a spectroscopic ellipsometer with a cooling rate of 2°C/min. The PiBMA thickness at 25°C was (a) 122 nm and (b) 14 nm. Arrows correspond to $T_g =$ (a) 58.6°C and (b) 46.1°C. (c) Top down view fluorescence micrograph of a 120 nm thick PiBMA film on PCHE substrate. The overlaid graph shows normalized intensity as a function of position along the x-axis. (d) Representative data of a FRAPP measurement at 106°C ($T_{g, bulk} + 48^\circ$C). Variation with time of the amplitude of the intensity normalized by the value at $t = 0$. Open and closed symbols represent a 120 nm thick film and 19 nm thick film, respectively. The solid and dashed lines are the best fit of data using Eq. 4.1.

4.3 RESULTS AND DISCUSSION

4.3.1 T_g and D as a function of film thickness

The trends of T_g and D with PiBMA film thickness were different depending on the multi-layered arrangement. The first row of Figure 4.3 shows T_g of PiBMA as a function of thickness measured by ellipsometry, and the second row in Figure 4.3 shows the thickness dependence of D of PiBMA at $106^{\circ}C$ ($= T_{g,bulk} + 48^{\circ}C$) measured by FRAPP. The dashed lines in the first row of each plot are bulk values of T_g measured by DSC with a heating rate of $10^{\circ}C/min$. The solid lines are obtained by fitting these experimental data to an empirical equation, $T_g(h) = T_{g,bulk}\{1\pm(\alpha/h)^{\delta}\}$,[1] where α, and δ are fitting parameters and h is the thickness of PiBMA. The obtained fitting parameters are listed in Table B.2 in Appendix B.

Regardless of the neighboring interfaces, the T_g and D of thick films ($> \sim100$ nm) are in good agreement with $T_{g,bulk}$ and D_{bulk}. Here, D_{bulk} (8.65×10^{-13} cm^2/sec) was evaluated based on Eq. 4.1 by measuring τ of a 120 nm thick PiBMA film with different pitch sizes, λ, ranging from 10 to 25 μm. The raw data of τ as a function of λ^2 is available in Figure 2.3 in Chapter 2. From Figure 4.3, it can be seen that the thickness dependences of both T_g and D strongly depend on the nature of interfaces.

The different trends for T_g with film thickness in the fist row of Figure 4.3 can be interpreted by considering effects of the confining interfaces. The constant T_g with film thickness for Air/PiBMA/SiO$_2$ can be attributed to counterbalancing of two contributing interfaces: the free surface locally decreasing the T_g and the strong interaction between PiBMA and SiO$_2$ locally increasing the T_g.[35] In contrast, the T_g of Air/PiBMA/PCHE decreased as the thickness decreased due to the weaker interaction between PiBMA and PCHE compared to that with SiO$_2$. Comparing PCHE/PiBMA/SiO$_2$ (capped) with Air/PiBMA/SiO$_2$ (uncapped), a higher T_g was observed in PCHE/PiBMA/SiO$_2$ (capped)

69

thin films due to the absence of the free surface, which locally lowers the mobility of PiBMA. In a symmetric confinement system, the T_g of PCHE/PiBMA/PCHE was in between the T_g of Air/PiBMA/PCHE and T_g of PCHE/PiBMA/SiO$_2$, as expected.
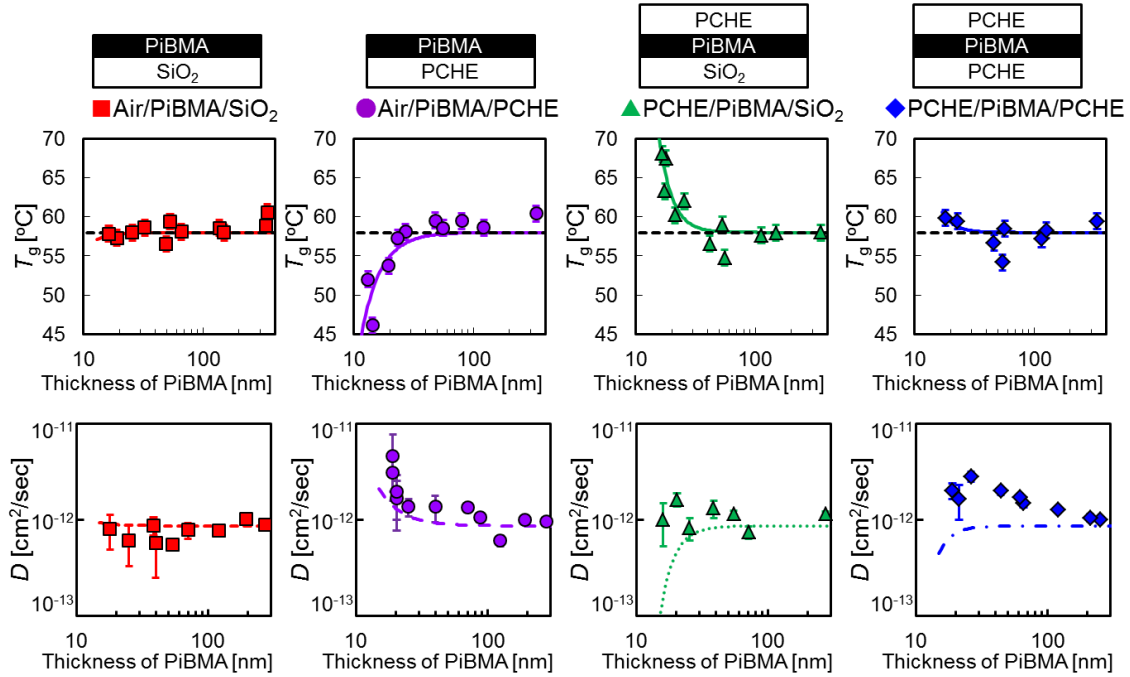
Figure 4.3:   First row: Thickness dependence of T_g for PiBMA in Air/PiBMA/SiO$_2$ (red squares), Air/PiBMA/PCHE (purple circles), Air/PiBMA/SiO$_2$ (green triangles) and PCHE/PiBMA/PCHE (blue diamonds) measured by ellipsometry.   The dashed line shows T_g of bulk PiBMA ($= 58^o$C) measured by DSC.   The solid lines are fitting curves based on an empirical equation.   The error bars represent a typical experimental uncertainty of the T_g measurement ($\pm 1^o$C).   Second row: Thickness dependence of D for PiBMA measured by FRAPP at 106°C ($T_{g,bulk}$ + 48°C).   The broken lines correspond to D values predicted from T_g values in the first row using Eq. 4.2.   Error bars represent 95% confidence intervals.

4.3.2   *D* prediction from *T_g* assuming the bulk relationship

The broken lines in Figure 4.3 in the second row are D estimated from the measured T_g-thickness relationship, $T_g(h)$, shown in the first row of Figure 4.3.   This

estimation assumed spatially homogeneous polymer dynamics and a bulk relationship between T_g, viscosity (η), and D based on the WLF and Stokes-Einstein equations. To estimate D from η, the Stokes-Einstein relationship ($D\eta$ = constant at a constant T), was employed and rewritten as Eq. 4.2, where $T_g(h)$ corresponds to solid lines in the first row of Figure 4.3. The D as a function of T_g (h) was calculated with Eq. 4.3, from the zero-shear η of bulk PiBMA as a function of temperature measured by a rheometer (TA Instruments, AR-2000EX) using a 20 mm cone-plate with a gap of 143 µm under steady shear. The zero-shear η from $T = 85^{\circ}C$ to $140^{\circ}C$ (raw data is available at Appendix B.3) was fit to the WLF equation as shown in Eq. 4.4, where $\eta_0 = 1.61 \times 10^5$ Pa·sec, $c_1 = 28.8$, and $c_2 = 160^{\circ}C$ are the fitting parameters and $T_0 = 143^{\circ}C = T_{g,bulk} + 85^{\circ}C$. Substituting these WLF parameters (c_1, c_2, and T_0), D as a function of $T_g(h)$ can be calculated as shown in Eq. 4.2 and 4.3.

$$\left. D\big(T_g(h)\big) \middle/ D_{T_{g,bulk}} = \eta_{T_{g,bulk}} \middle/ \eta\big(T_g(h)\big) \right.$$

(4.2)

$$D\big(T_g(h)\big) = D_{T_{g,bulk}} \cdot \eta_{T_{g,bulk}} \cdot \left\{ \eta_0 \exp\left[-\frac{c_1\big(T - T_g + T_0\big)}{c_2 + \big(T - T_g + T_0\big)} \right] \right\}^{-1}$$

(4.3)

$$\eta\big(T_g\big) = \eta_0 \exp\left[-\frac{c_1\big(T - T_g + T_0\big)}{c_2 + \big(T - T_g + T_0\big)} \right]$$

(4.4)

Experimentally obtained D values deviated from the prediction derived from the bulk Stokes-Einstein and WLF relationships depending on the type of interfaces that were present. For instance, a ~20 nm thick PiBMA film of PCHE/PiBMA/SiO$_2$ exhibited a T_g of ~ $68^{\circ}C$ ($T_{g,bulk} + 10^{\circ}C$) which corresponds to a lower predicted D than D_{bulk}, but the experimentally measured D(PCHE/PiBMA/SiO$_2$) did not follow this bulk prediction. It is important to note that the bulk prediction assumes spatially homogeneous dynamics, therefore these deviations suggest the existence of spatially heterogeneous dynamics.

Since the differences between the bulk prediction and measured D depend on the interfaces between PiBMA and air/substrates in Figure 4.3, the deviations from the prediction could be due to interfacial effects on self-diffusion of PiBMA.

4.3.3 Friction model

To take interfacial effects on nanoconfined D into account, a friction analysis was conducted. Friction coefficients can be used to characterize the effect of neighboring confining interfaces on dynamics of polymer melts.[26, 42, 43] By modifying Lange *et al.*'s equation[43] for symmetric confinement to asymmetric confinement as in this study, the effect of the substrates on D of PiBMA can be expressed as Eq. 4.5:

$$D(h)\Big/D_{bulk} = \left\{ \frac{h_i}{h} \left(\frac{\zeta_{top} + \zeta_{bottom}}{\zeta_0} - 2 \right) + 1 \right\}^{-1}$$

(4.5)

where, h_i is the effective interfacial thickness for all the interfaces to simplify the fitting, and ζ_0 and ζ_X correspond to the friction coefficients between PiBMA itself and of PiBMA/X interfaces as shown in Figure 4.4 (a), respectively. The four fitting parameters (h_i, $\zeta_{PiBMA/air}$, $\zeta_{PiBMA/PCHE}$, ζ_{PiBMA/SiO_2}) are listed in Table 4.1. Here, as the ζ_X/ζ_0 or ζ_Y/ζ_0 decreases, higher PiBMA melt mobility at or near the interface X or Y is expected.

In Figure 4.4 (b), it is noteworthy that the solid line for PCHE/PiBMA/SiO$_2$ using Eq. 4.5 described the experimental data well without further adjustable parameters. As previously reported,[43, 44] the friction coefficient at a free surface ($\zeta_{PiBMA/air}$) was close to zero, indicating enhanced mobility of PiBMA compared to the bulk. Also, a higher $\zeta_{PiBMA/SiO2}$ than $\zeta_{PiBMA/PCHE}$ can be attributed to the stronger interaction between PiBMA and SiO$_2$ than that with PCHE. The Figure 4.4 (b) demonstrates that the friction analysis describes the D-thickness relationship better than

the WLF and the Stokes-Einstein predictions, meaning that the deviation from the bulk relationship is due to the heterogeneous dynamics of the PiBMA melt influenced by different interfacial frictions.
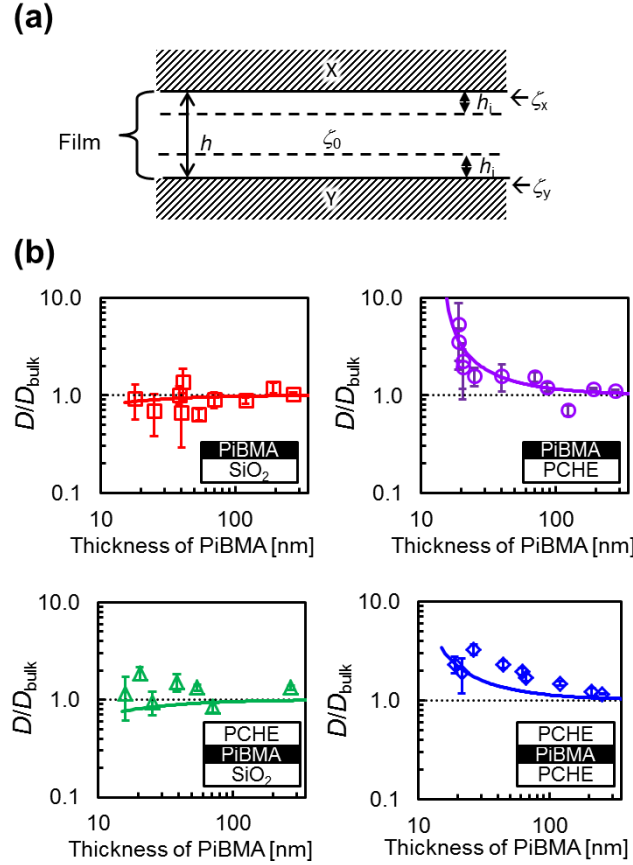
Figure 4.4: (a) Schematic of the model used in the friction analysis. (b) D normalized by the bulk value (D_{bulk}) as a function of PiBMA thickness. The solid lines represent fitting using the friction analysis.

h_i [nm]	$\xi_{PiBMA/air}/\xi_0$	$\xi_{PiBMA/PCHE}/\xi_0$	$\xi_{PiBMA/SiO_2}/\xi_0$
8.6	9.0×10^{-2}	0.31	2.2

Table 4.1: Fitting parameters obtained by the friction analysis.

Larger deviations of the thin film T_g-D relationship from the bulk prediction for capped samples could be explained by differences between the measurement temperature and the thin film T_gs. Although the D was measured at the same temperature for all experiments, $106\,^o\text{C}$ ($T_{g,bulk}+48\,^o\text{C}$) in this study, the T_g of the thin films were different depending on the multi-layered arrangement and thickness. For example, in the case of the 20 nm thick PiBMA on SiO_2, the T_g of the film with the capped [uncapped] surface was $T_{g,bulk}+10\,^o\text{C}$ [$T_{g,bulk}-10\,^o\text{C}$], meaning that the temperature gap between the measurement temperature ($106\,^o\text{C}$) and the film T_g was $38\,^o\text{C}$ for the capped samples, while it was $58\,^o\text{C}$ for the uncapped samples. As a result, the measurement temperature for the capped samples ($T_{g,\ film}+38\,^o\text{C}$) is a relatively lower measurement temperature than the uncapped samples ($T_{g,\ film}+58\,^o\text{C}$). As a comparison, Urakawa and Ediger *et al.* reported that $T_g+\sim40\,^o\text{C}$ was the temperature where heterogeneous dynamics, i.e. the breakdown of the Stokes-Einstein relationship, was observed.[20] Therefore, these different measurement temperatures of D relative to film T_g resulted in the more pronounced effect of heterogeneous dynamics for the capped samples.

4.4   CONCLUSIONS

In summary, we examined the relationship between T_g measured by ellipsometry and D measured by FRAPP for unentangled PiBMA under nanoconfinement. The experimentally obtained T_g-D relationship deviated from the bulk prediction using the WLF and the Stokes-Einstein equations. In order to elucidate the mechanism, we employed a model based on friction coefficients between the film and confining interfaces. This friction analysis revealed that the existence of heterogeneous dynamics near confining interfaces could play a crucial role for correlating segmental mobility characterized by T_g and entire chain motion characterized by D. Since the friction

coefficient is a strong function of temperature, further investigation on the temperature

dependence of *D* would give more insight towards understanding the nanoconfined self-

diffusion.

4.5 REFERENCES

1. Keddie, J. L.; Jones, R. A. L.; Cory, R. A. *Europhys. Lett.* **1994,** 27, (1), 59-64.
2. Forrest, J. A.; Dalnoki-Veress, K.; Stevens, J. R.; Dutcher, J. R. *Phys. Rev. Lett.* **1996,** 77, (10), 2002-2005.
3. Dalnoki-Veress, K.; Forrest, J. A.; Murray, C.; Gigault, C.; Dutcher, J. R. *Phys. Rev. E Stat. Nonlin. Soft Matter Phys.* **2001,** 63, (3 Pt 1), 031801.
4. Alcoutlabi, M.; McKenna, G. B. *J. Phys. Condens. Matter* **2005,** 17, (15), R461-R524.
5. Roth, C. B.; McNerny, K. L.; Jager, W. F.; Torkelson, J. M. *Macromolecules* **2007,** 40, (7), 2568-2574.
6. Yoon, H.; McKenna, G. B. *Macromolecules* **2014,** 47, (24), 8808-8818.
7. Fukao, K.; Miyamoto, Y. *Phys. Rev. E Stat. Nonlin. Soft Matter Phys.* **2000,** 61, (2), 1743-54.
8. Li, R. N.; Chen, F.; Lam, C.-h.; Tsui, O. K. C. *Macromolecules* **2013,** 46, (19), 7889-7893.
9. Yang, Z.; Fujii, Y.; Lee, F. K.; Lam, C. H.; Tsui, O. K. *Science* **2010,** 328, (5986), 1676-9.
10. McGraw, J. D.; Jago, N. M.; Dalnoki-Veress, K. *Soft Matter* **2011,** 7, (17), 7832-7838.
11. Hutcheson, S. A.; McKenna, G. B. *Eur. Phys. J. E Soft Matter* **2007,** 22, (4), 281-6; discussion 287-91.
12. Stafford, C. M.; Vogt, B. D.; Harrison, C.; Julthongpiput, D.; Huang, R. *Macromolecules* **2006,** 39, (15), 5095-5099.
13. Torres, J. M.; Stafford, C. M.; Vogt, B. D. *ACS Nano* **2009,** 3, (9), 2677-85.
14. Evans, C. M.; Narayanan, S.; Jiang, Z.; Torkelson, J. M. *Phys. Rev. Lett.* **2012,** 109, (3), 038302-038302.
15. Sussman, D. M.; Tung, W.-S.; Winey, K. I.; Schweizer, K. S.; Riggleman, R. A. *Macromolecules* **2014,** 47, (18), 6462-6472.
16. Frank, B.; Gast, A. P.; Russell, T. P.; Brown, H. R.; Hawker, C. J. *Macromolecules* **1996,** 29, (20), 6531-6534.
17. Zheng, X.; Rafailovich, M. H.; Sokolov, J.; Strzhemechny, Y.; Schwarz, S. A.; Sauer, B. B.; Rubinstein, M. *Phys. Rev. Lett.* **1997,** 79, (2), 241-244.
18. Roth, C. B.; Dutcher, J. R., Mobility on Different Length Scales in Thin Polymer Films. In *Soft Materials: Structure and Dynamics*, Dutcher, J. R.; Marangoni, A. G., Eds. Marcel Dekker: 2005; pp 1-38.
19. Williams, M. L.; Landel, R. F.; Ferry, J. D. *J. Am. Chem. Soc.* **1955,** 77, (14), 3701-3707.

20.   Urakawa, O.; Swallen, S. F.; Ediger, M. D.; von Meerwall, E. D. *Macromolecules* **2004,** 37, (4), 1558-1564.

21.   Ellison, C. J.; Torkelson, J. M. *Nat. Mater.* **2003,** 2, (10), 695-700.

22.   Sharp, J. S.; Forrest, J. A. *Phys. Rev. Lett.* **2003,** 91, (23), 235701.

23.   Ediger, M. D.; Forrest, J. A. *Macromolecules* **2014,** 47, (2), 471-478.

24.   Reiter, G. *Europhys Lett* **1993,** 23, (8), 579.

25.   Karapanagiotis, I.; Gerberich, W. W. *Surf. Sci.* **2006,** 600, (5), 1178-1184.

26.   Doi, M.; Edwards, S. F., *The Theory of Polymer Dynamics*. Clarendon Press: 1988.

27.   Si, L.; Massa, M. V.; Dalnoki-Veress, K.; Brown, H. R.; Jones, R. a. L. *Phys. Rev. Lett.* **2005,** 94, (12), 1-4.

28.   Ata, S.; Muramatsu, M.; Takeda, J.; Ohdaira, T.; Suzuki, R.; Ito, K.; Kobayashi, Y.; Ougizawa, T. *Polymer* **2009,** 50, (14), 3343-3346.

29.   Reid, D. K.; Alves Freire, M.; Yao, H.; Sue, H.-J.; Lutkenhaus, J. L. *ACS Macro Lett.* **2015,** 4, (2), 151-154.

30.   Tsui, O. K. C.; Russell, T. P.; Hawker, C. J. *Macromolecules* **2001,** 34, (16), 5535-5539.

31.   Gao, S.; Koh, Y. P.; Simon, S. L. *Macromolecules* **2013,** 46, (2), 562-570.

32.   Lang, R. J.; Merling, W. L.; Simmons, D. S. *ACS Macro Lett.* **2014,** 3, 758-762.

33.   Ye, C.; Weiner, C. G.; Tyagi, M.; Uhrig, D.; Orski, S. V.; Soles, C. L.; Vogt, B. D.; Simmons, D. S. *Macromolecules* **2015**.

34.   Bicerano, J., *Prediction of Polymer Properties*. CRC Press: New York, 2002.

35.   Priestley, R. D.; Mundra, M. K.; Barnett, N. J.; Broadbelt, L. J.; Torkelson, J. M. *Aust. J. Chem.* **2007,** 60, (10), 765-771.

36.   See Supplemental Material. Differential scanning calorimetry confirmed that a PiBMA/PCHE mixture exhibits two different Tgs after annealing at 200°C for 20 mins.

37.   Katzenstein, J. M.; Janes, D. W.; Hocker, H. E.; Chandler, J. K.; Ellison, C. J. *Macromolecules* **2012,** 45, (3), 1544-1552.

38.   Brandup, J.; Immergut, E. H.; Grulke, E. A., *Polymer handbook Fourth edition*. 4th editio ed.; A Wiley-Interscience Publication: 1999.

39.   Unlabeled PiBMA was used for Tg measurement because the previous study showed PiBMA-NBD and PiBMA exhibit the same Tg within a range of the experimental error [28]. Argon was purged during the measurement to avoid water condensation.

40.   Robeson, J. L.; Tilton, R. D. *Biophys. J.* **1995,** 68, (5), 2145-55.

41.   Lakowicz, J. R.; Weber, G. *Biochemistry* **1973,** 12, (21), 4161-4170.

42.   Sokolov, A. P.; Schweizer, K. S. *Phys. Rev. Lett.* **2009,** 102, (24), 248301.

43.   Lange, F.; Judeinstein, P.; Franz, C.; Hartmann-Azanza, B.; Ok, S.; Steinhart, M.; Saalwächter, K. *ACS Macro Lett.* **2015**, 561-565.

44.   Koga, T.; Li, C.; Endoh, M. K.; Koo, J.; Rafailovich, M.; Narayanan, S.; Lee, D. R.; Lurio, L. B.; Sinha, S. K. *Phys. Rev. Lett.* **2010,** 104, (6), 066101.

TAILORING INTERFACES FOR BLOCK COPOLYMER NANOPATTERNING

Nanofabrication and nanopatterning are defined as "fields of study in which methods are developed to manufacture nanomaterials, or pattern materials on a nanometer scale (i.e., below 100 nm in at least one dimension)."[1]   Such fine control of small features could allow fabrication of next-generation magnetic data storage media,[2] and metasurfaces exhibiting extraordinary optoelectrical properties by tailoring the structure size and its interactions with electric fields,[3] among others.

Lithographic strategies, including conventional photolithography and imprint lithography, have been widely used to mass produce nanopatterns.   The spatial resolutions of these approaches are limited by the wavelength of the light that is used for patterning (photolithography) or the size/density of the relief structure that can be formed on an imprint template.   While extensive research has been conducted to explore shorter wavelengths of light, including 157 nm and extreme UV (EUV, 13.5 nm) among others, the throughput or materials challenges prevent these technologies from commercial implementation.[4]   However, block copolymer (BCP) lithography, which is a primary focus of this dissertation, could offer an alternative approach for nanopatterning which can supplement existing patterning infrastructure.

BCPs consist of two chemically distinct polymers, blocks A and B, which are linked by a single covalent bond.   Typically, the two blocks have a non-favorable segmental interaction causing the blocks to micro/nanophase separate into A and B rich domains.   The size of each domain is determined by the molecular weight and the segment-segment interaction parameter (χ), and feature sizes down to several nanometers are theoretically possible.[5]   Depending on the volume fraction of block A, the BCP may exhibit different morphologies as shown in Figure 5.1.   In this dissertation, the lamellar

structure is of particular interest because of its geometric relevance to device structures after BCP thin films serve as etch masks for pattern transfer into substrates of interest.
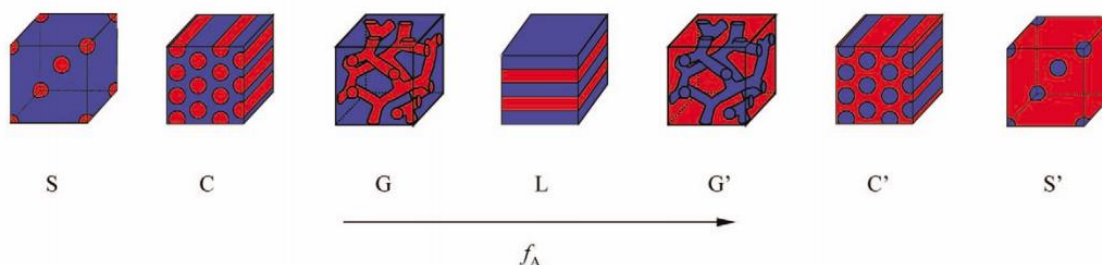
Figure 5.1: Mean-field prediction of the thermodynamic equilibrium phase structures for conformationally symmetric diblock melts.   Phases are labeled as L (lamellar), C (hexagonal cylinders), G (bicontinuous cubic), S (body-centered cubic spheres). f_A is the volume fraction of block A.   Adapted with permission from Li *et al.*[6]   Copyright 2006, Elsevier Ltd.

The ultimate goal of this dissertation is to pattern a variety of target materials, such as soft and 2D materials, using BCPs and then understand the physical mechanisms needed to generalize BCP lithography and nanopatterning more broadly.   An introduction to BCP lithography is included in Chapter 5 along with an overview of various applications.   In particular, the effect of the surface energy of the underlying substrate of the BCP is highlighted for production of the most lithographically useful structures, lamellae oriented perpendicular to the substrate.   Lastly, this overview also summarizes current challenges for application of these techniques to a wide range of materials, including flexible substrates and graphene.

In Chapter 6, polydopamine (PDA) is exploited as a universal, catechol-containing adhesive to enable BCP nanopatterning on a variety of soft material surfaces in a way that can potentially be applied to flexible electronic devices.   Successful BCP nanopatterning was performed on Teflon, poly(ethylene terephthalate) (PET), and

Kapton. Furthermore, it is demonstrated that a perfectly nanopatterned PDA-PET substrate can be bent without distorting or damaging the nanopattern in conditions that far exceed typical bending curvatures in roll-to-roll manufacturing.

In Chapter 7, we developed a new and potentially scalable graphene nanoribbon (GNR) fabrication method using wetting-transparency assisted BCP lithography. Extensive contact angle and surface energy measurements indicated that the surface neutrality of the underlying substrate is mostly retained even with a single layer of graphene coating on top of the underlying substrate. This is due to the wetting transparency of graphene, i.e. a sufficiently thin layer of graphene does not alter the surface energy or wetting properties of the underlying substrate. Using the wetting transparency-assisted BCP lithography, we successfully fabricated large-area (cm^2 scale) GNR arrays with 14, 22, and 51 nm nanoribbon widths.

Inspired by the wetting transparency of graphene, Chapter 8 explores possible techniques to control the microdomain orientations of BCPs *through* thin (< 10 nm thick) layers. To gain fundamental knowledge regarding control of the surface energy of the underlayer of a BCP, a model bi-layer substrate made from homopolymers of each block was developed. A theoretical model based on van der Waals (vdW) forces qualitatively explained how surface energy varies with the thickness of the bilayer substrate.

Chapter 5: Introduction to block copolymer lithography

5.1 APPLICATIONS OF BCP NANOPATTERNING ON A VARIETY OF SUBSTRATES

Well-defined nanopatterns with sizes down to several nanometers exhibit enormous potential for numerous applications, such as next-generation magnetic data storage[7-9] and metasurfaces with extreme optoelectronic performance.[3] These complicated structures can be achieved by directed self-assembly (DSA) of BCPs.[10-12] Among various approaches, graphoepitaxy (i.e., guiding self-assembly with topographical features) and chemoepitaxy (i.e., guiding self-assembly with patterned surface chemistry) DSA schemes are some of the most well-studied techniques.

Segalman and Kramer *et al.* first demonstrated graphoepitaxy DSA of a sphere-forming polystyrene-*block*-poly(2-vinylpridine) using a tailored step height (30 nm high, ~L_0 of the BCP), where L_0 is the natural domain periodicity of the BCP.[13] Alternatively, Stoykovich and Nealey demonstrated that nonregular device-oriented structures can be fabricated using a chemoepitaxy approach with chemically modified pre-patterns (Figure 5.2).[9] Recently, combined approaches of graphoepitaxy and chemoepitaxy self-assembly have demonstrated significant improvements in cross-sectional structure as well as spatial resolution.[14, 15] Therefore, once a perpendicularly oriented lamellae structure is obtained, these DSA strategies enable fabrication of sophisticated structures for various applications.
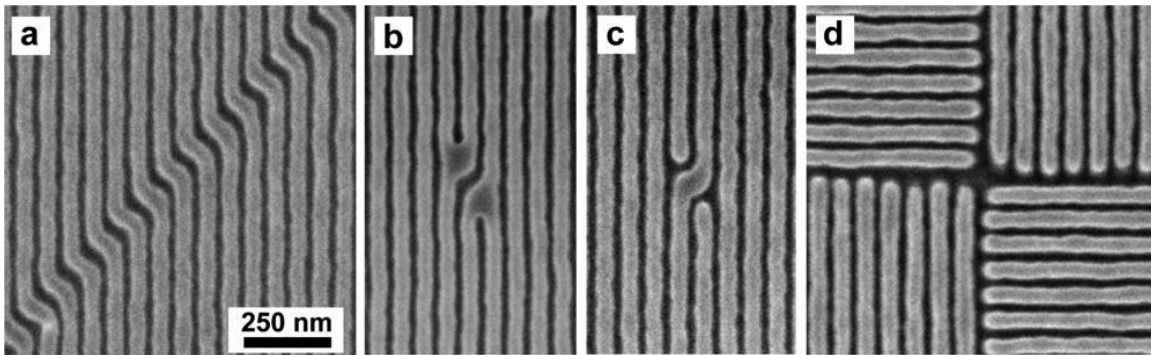
Figure 5.2: Top-down scanning electron microscope (SEM) images of the ternary blend of PS, PMMA and PS-*b*-PMMA directed to assemble into (a) nested arrays of jogs, (b) isolated PMMA jogs, (c) isolated PS jogs, and (d) arrays of T-junctions. In all the SEM images, the PS domains are displayed in light gray, while the PMMA domains are dark gray or black. Adapted with permission from Stoykovich *et al.*[9] Copyright 2007, American Chemical Society.

5.2 ORIENTATION CONTROL OF LAMELLAE-FORMING BCP

To produce a lithographically useful morphology, lamellae perpendicularly oriented relative to the substrate must be produced. The interfacial energy above and below the BCP layer needs to be controlled for forming such structures.[16, 17] Polystyrene-*block*-poly(methyl methacrylate) (PS-*b*-PMMA) has been the most studied[18] and tested BCP so far,[2] likely because it does not require interfacial energy control at the BCP-air interface. Fortuitously, PS and PMMA have nearly identical surface energies at elevated temperatures used for thermal annealing, meaning neither block prefers to occupy the air interface over the other.[19] Therefore, we will focus on lamellae-forming PS-*b*-PMMA for simplicity and ease of comparison, even though this system is limited to about 20 nm full pitch (~10 nm wide lines) due to its relatively low χ value.[18]

For PS-*b*-PMMA, tailoring the wetting behavior of the BCP at the substrate interface is the key to inducing perpendicular lamellae structure. Figure 5.3 is a schematic diagram showing the BCP microdomain orientation on three substrates, which

81

pose different preferences to each block, PS and PMMA. As can be seen in the figure, the non-preferential (i.e. "neutral" where neither block preferentially contacts the substrate) wetting by either block of the BCP promotes the perpendicular orientation of the lamellae structure.[20] A surface neutralization treatment (SNT), or thin and cross-linked polymer layer that equally prefers to establish contact with each block, has been widely used.[17, 20]
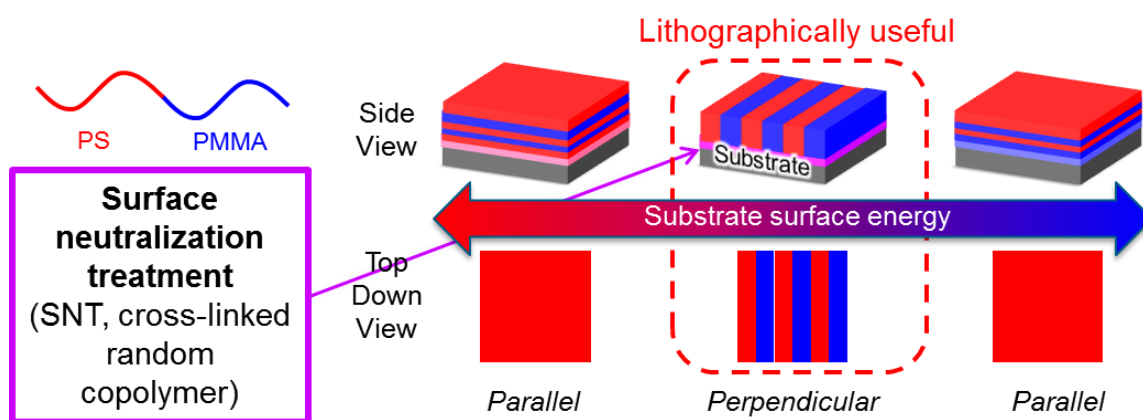
Figure 5.3:   Schematic diagram of orientations of BCP microdomains. Lithographically useful, perpendicularly oriented lamellae structure can be achieved only when the underlayer of the BCP is neutral to each block.

5.2.1   Review of current approaches for SNT

The most widely used SNT for lamellae-forming PS-*b*-PMMA are comprised of random copolymers of PS and PMMA (PS-*r*-PMMA) with functional groups to cross-link or covalently graft them onto the substrates.[17]   In 1997, Mansky and Hawker *et al.* reported the first SNT using a hydroxyl-terminated PS-*r*-PMMA where the hydroxyl end-group is hypothesized to react with the silanols on the substrate surface.[20]   Since then, benzocyclobutene,[21] glycidyl methacrylate,[22] and azido[23] functionalized monomers in the

copolymers have all been utilized as successful functional groups as summarized in Figure 5.4.
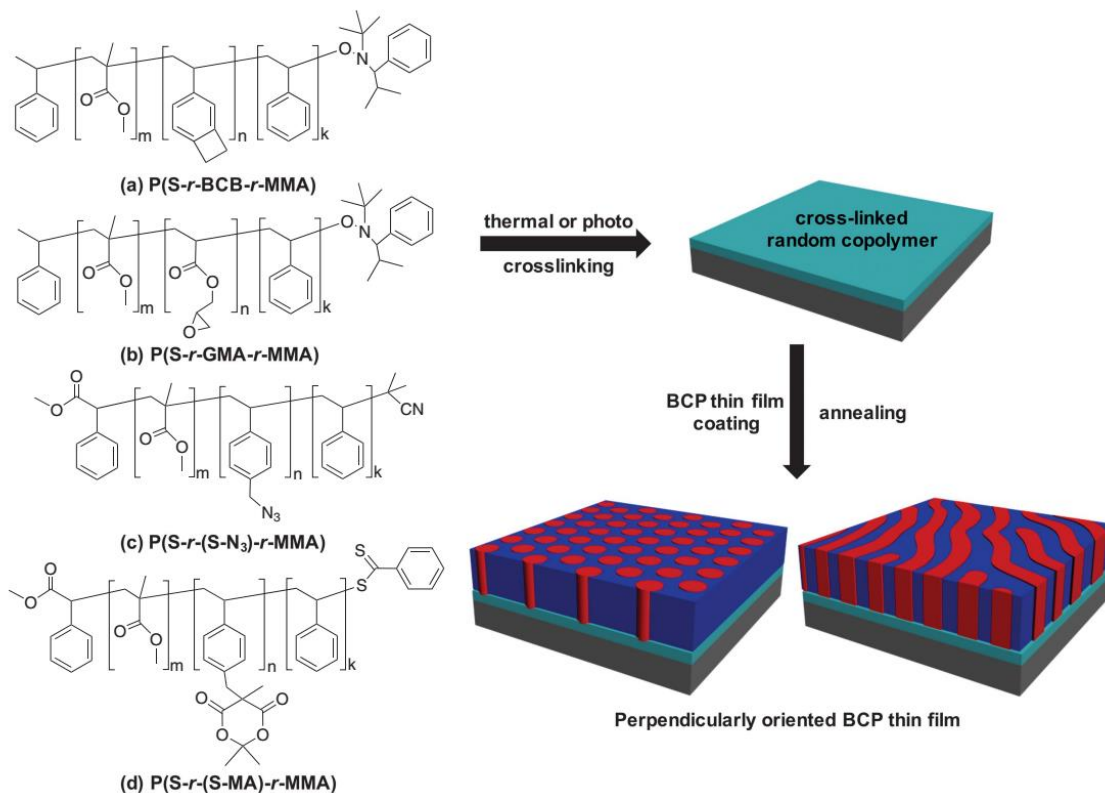
Figure 5.4:   Schematic illustration of substrate neutralization with various cross-linkable random copolymers for the perpendicular orientation of domains for a PS-*b*-PMMA thin film. BCP, block copolymer; GMA, glycidyl methacrylate; *r*, random.   Adapted with permission from Kim *et al.*[17]   Copyright 2016, Nature Publishing Group.

5.2.2   Challenges of using SNT for flexible substrates and 2D materials

As reviewed in Chapter 5.2.1, cross-linked SNT layers are most commonly used to achieve perpendicular orientation of BCP microdomains.   However, these cross-linked layers also introduce challenges when the SNTs are applied for nanopatterning non-conventional substrates, e.g. flexible substrates, and 2D materials, e.g. graphene.

Flexible substrates are challenging for BCP nanopatterning for several reasons. First, many typical flexible substrates pose low surface energy and conventional slit- or spin- coating processes do not form continuous, uniform films on such substrates due to their wetting characteristics.   Also, the low surface energy of many flexible substrates can result in poor adhesion between the substrate and the SNT layer.   Reinforcing the adhesion could be also challenging because these flexible substrates, including Teflon, are often chemically inert.

When BCP lithography is utilized to nanopattern 2D materials such as graphene, removal of the cross-linked SNT layer could make processing unnecessarily complicated. For example, in pioneering work showing graphene nanoribbon (GNR) fabrication using BCP lithography, Son and Ross *et al.* successfully demonstrated fabrication of sub-10 nm wide GNRs.[24]   However, the cross-linked SNT layer remained on top of the GNR array, and several etching steps (Figure 5.5 (e)-(g)) were required to remove these layers which can potentially damage the graphene or other components.   To fully exploit the potential of BCP lithography, a simpler process for the pattern transfer is desired.
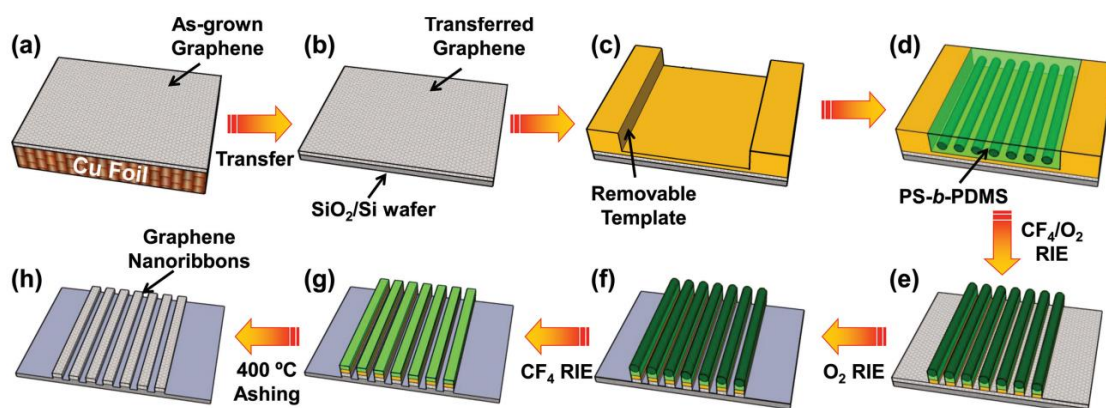
Figure 5.5: Schematic of the formation of GNR arrays using polystyrene-*block*-polydimethylsiloxane (PS-*b*-PDMS) as an etch mask.   The processing steps include (a) growing a graphene monolayer on Cu foil at 1000°C by chemical vapor deposition; (b) transferring graphene to a SiO_2/Si wafer; (c) spin-coating and patterning a polymeric antireflective coating (ARC) template to direct the self-assembly of the BCP; (d) spin-coating and solvent annealing of PS-*b*-PDMS cylindrical BCP; (e) simultaneously etching the polymeric template and the PS microdomains of the BCP patterns by CF_4 followed by O_2 reactive ion etching (RIE); (f) removing exposed graphene by additional O_2 RIE; (g) removing the oxidized PDMS above the GNRs by CF_4 RIE; and (h) annealing at 400 °C for 10 min to remove residual polymer on the GNR arrays.   Adapted with permission from Son *et al.*[24]   Copyright 2013, WILEY-VCH Verlag GmbH & Co. KGaA.

5.3 SUMMARY AND OBJECTIVES

In order to use BCP lithography for flexible electronics and 2D materials, new approaches to control microdomain orientation of BCPs and transfer their patterns into underlying materials are strongly desired.   In the study shown in the following chapter, a lamellae-forming BCP, PS-*b*-PMMA, is utilized as a model system.   First, BCP nanopatterning on various flexible substrates is explored by modifying the SNT layer with a bio-inspired universal adhesive layer.   Also, the SNT strategy is extended to GNR fabrication and the effects of atomically-thin graphene layers on BCP orientation are discussed.   Finally, we design a bilayer system to fundamentally investigate the effect of the thin layer on achieving perpendicular orientation using very thin SNT layers.

5.4 REFERENCES

1. Nanofabrication and nanopatterning. http://www.nature.com/subjects/nanofabrication-and-nanopatterning

2. Bates, C. M.; Maher, M. J.; Janes, D. W.; Ellison, C. J.; Willson, C. G. *Macromolecules* **2014,** 47, (1), 2-12.

3. Meinzer, N.; Barnes, W. L.; Hooper, I. R. *Nat. Photon.* **2014,** 8, (12), 889-898.

4. van Schoot, J.; van Ingen Schenau, K.; Valentin, C.; Migura, S. In *EUV lithography scanner for sub-8nm resolution*, 2015; pp 94221F-94221F-12.

5. Bates, F. S.; Fredrickson, G. H. *Phys. Today* **1999,** 52, (2), 32-38.

6. Li, M.; Ober, C. K. *Mater. Today* **2006,** 9, (9), 30-39.

7. Ruiz, R.; Kang, H.; Detcheverry, F. A.; Dobisz, E.; Kercher, D. S.; Albrecht, T. R.; de Pablo, J. J.; Nealey, P. F. *Science* **2008,** 321, (5891), 936-939.

8. Stoykovich, M. P.; Müller, M.; Kim, S. O.; Solak, H. H.; Edwards, E. W.; de Pablo, J. J.; Nealey, P. F. *Science* **2005,** 308, (5727), 1442-1446.

9. Stoykovich, M. P.; Kang, H.; Daoulas, K. C.; Liu, G.; Liu, C.-C.; de Pablo, J. J.; Müller, M.; Nealey, P. F. *ACS Nano* **2007,** 1, (3), 168-175.

10. Koo, K.; Ahn, H.; Kim, S.-W.; Ryu, D. Y.; Russell, T. P. *Soft Matter* **2013,** 9, (38), 9059-9071.

11. Hu, H.; Gopinadhan, M.; Osuji, C. O. *Soft Matter* **2014,** 10, (22), 3867-3889.

12. Jeong, S.-J.; Kim, J. Y.; Kim, B. H.; Moon, H.-S.; Kim, S. O. *Mater. Today* **2013,** 16, (12), 468-476.

13. Segalman, R. A.; Yokoyama, H.; Kramer, E. J. *Adv. Mater.* **2001,** 13, (15), 1152-1155.

14. Cushen, J.; Wan, L.; Blachut, G.; Maher, M. J.; Albrecht, T. R.; Ellison, C. J.; Willson, C. G.; Ruiz, R. *ACS Appl. Mater. Interfaces* **2015,** 7, (24), 13476-13483.

15. Ji, S.; Wan, L.; Liu, C.-C.; Nealey, P. F. *Prog. Polym. Sci.* **2016,** 54–55, 76-127.

16. Hawker, C. J.; Russell, T. P. *MRS Bull.* **2005,** 30, (12), 952-966.

17. Kim, S.; Wang, H. S.; Choe, Y.; Choi, S.-H.; Bang, J. *Polym. J.* **2016,** 48, (4), 333-340.

18. Wan, L.; Ruiz, R.; Gao, H.; Patel, K. C.; Albrecht, T. R.; Yin, J.; Kim, J.; Cao, Y.; Lin, G. *ACS Nano* **2015,** 9, (7), 7506-14.

19. Wu, S. *J. Phys. Chem. A* **1970,** 74, (3), 632-638.

20. Mansky, P.; Liu, Y.; Huang, E.; Russell, T. P.; Hawker, C. *Science* **1997,** 275, (5305), 1458-1460.

21. Ryu, D. Y.; Shin, K.; Drockenmuller, E.; Hawker, C. J.; Russell, T. P. *Science* **2005,** 308, (5719), 236-239.

22. Han, E.; Stuen, K. O.; Leolukman, M.; Liu, C.-C.; Nealey, P. F.; Gopalan, P. *Macromolecules* **2009,** 42, (13), 4896-4901.

23. Bang, J.; Bae, J.; Löwenhielm, P.; Spiessberger, C.; Given-Beck, S. A.; Russell, T. P.; Hawker, C. J. *Adv. Mater.* **2007,** 19, (24), 4552-4557.

24. Son, J. G.; Son, M.; Moon, K.-J.; Lee, B. H.; Myoung, J.-M.; Strano, M. S.; Ham, M.-H.; Ross, C. A. *Adv. Mater.* **2013,** 25, (34), 4723-4728.

Chapter 6: Ultrasmooth polydopamine modified surfaces for block copolymer nanopatterning on flexible substrates[*]

6.1 INTRODUCTION

As was introduced in Chapter 5, block copolymers (BCPs) have gained considerable attention over the past several decades due to their ability to self-assemble into prescribed, well-ordered morphologies on the 5-100 nm size scale.[1]   In particular, thin films of BCPs in which the orientation and alignment of microdomains are precisely directed could serve as etch-selective nanopatterns for lithography applications. Researchers are currently developing a suite of materials[2-6] and processes[7-13] that the microprocessor and data storage industries could utilize to generate sub-10 nm features in their future products.   While directed self-assembly (DSA) and other next-generation techniques represent the leading edge of miniaturization efforts for the highest-performance electronics built upon semiconductor substrates, it stands to reason that the benefits of incorporating self-assembling materials in nanopatterning will extend to related technologies, such as flexible electronics.[14-19]   Flexible electronics can be printed on soft plastic substrates in continuous, roll-to-roll processes,[17, 20] and the final devices may possess improved portability,[17, 21, 22] wearability,[14, 17, 19, 21, 22] and durability.[21] Therefore, materials that generalize DSA processes for other types of substrates could broaden their impact.

Interfacial modifications that control the wetting of block copolymer microdomains in thin films represent a unifying feature in nearly all DSA methodologies. Specifically, interfaces that are non-preferentially wetted (i.e. "neutral") by either block of the BCP promote perpendicular orientation of microdomains,[23] and lithographically patterned pinning lines preferentially wetted by one of the blocks chemoepitaxially direct the long-range alignment of microdomains into device-oriented structures.[24-26]   In contrast to native oxide surfaces present on semiconductor substrates, flexible films may be chemically inert or possess such low surface energy that conventional slit- or spin-coating depositions can not form continuous, uniform films.   In order to apply DSA methodologies to roll-to-roll processes on a wide range of flexible substrates, BCP thin films need to be strongly adhered to the substrate and mechanically robust.   The fast processing speeds and roller manipulations will exert bending forces and lateral strains that can potentially delaminate or stretch the BCP pattern, but very rarely has the quality of the BCP pattern been characterized under realistic deformations.

Mussel-inspired surface engineering strategies have attracted much attention in recent years[27-30] due to their universal adhesive nature.[28, 31-34]   The exceptional wet-adhesion property of mussels is known to be due to a unique amino acid composition of proteins near the plaque-substrate interface, which are rich in 3,4-dihydroxy-L-phenylalanine (DOPA) and lysine amino acids.   Dopamine is a commercially available synthetic organic chemical that mimics the natural mussel proteins by containing its two key moieties, DOPA (catechol) and lysine (amine).[31]   Due to its chemical nature, immersing a substrate in a mildly basic solution of dopamine quickly forms a conformal and uniform functional polydopamine (PDA) layer on virtually all surfaces regardless of its topography or chemical composition,[31, 35, 36] producing a chemically functional ad-layer with many surface reaction sites available for secondary reactions.[31, 37, 38]   PDA is

a mechanically robust and thermochemically stable material; as such, it can withstand a variety of post-processing steps.[28, 39]   Since the precursor to PDA is already present in living organisms, it may have additional advantages over potentially toxic or environmentally unfriendly substrate-specific modifiers, such as chlorosilanes, isocyanates, or residual azide salts.[40]   In fact, the mussel-inspired surface engineering for BCP lithography has been utilized by Kim, Lee, and coworkers[35, 38] to demonstrate the successful perpendicular orientation of BCP lamellae on various substrates, including low-surface energy substrates, poly(tetrafluoroethylene) (PTFE),[35] and graphene[38]. However, due to its strongly adhesive nature, PDA self-aggregates[41] during the substrate coating procedure, yielding substrates with too much roughness for most applications of BCP nanopatterning.   To the best of the authors' knowledge, strategies to avoid or remove PDA particle deposition and the impact of these steps on the quality of resulting BCP nanopatterns have not been reported.

Our focus in this work is to investigate coating protocols to form an exceptionally thin and smooth PDA layer, which are critical attributes for integration in the lithography process.   To demonstrate the diversity of polymer surfaces which can be patterned by BCPs using this strategy, PTFE, polyimide, and poly(ethylene terephthalate) (PET) substrates were employed.   First, a smooth and continuous PDA layer was deposited onto the substrates, with the deposition time and cleaning process carefully optimized to preclude deposition of large PDA granules.   This step is especially important because a smooth surface is a critical attribute for lithography process integration.   The thickness and roughness of the PDA layer were monitored *ex situ* by spectroscopic ellipsometry, optical microscopy, atomic force microscopy (AFM), and scanning electron microscopy (SEM).   A PDA deposition time of 1 h followed by bath sonication in aqueous base yielded a 3 nm thick PDA layer with root-mean-squared roughness of 0.4 nm.   Next, a

surface neutralization treatment (SNT) layer was grafted to the PDA-coated substrate. Finally, poly(styrene-block-methyl methacrylate) (PS-*b*-PMMA) was spin-coated on top of the SNT and oriented perpendicularly by thermal annealing. Furthermore, by generalizing the approach to flexible substrates, we demonstrate that BCP patterns obtained on these substrates are stable under the bending they would be subjected to in a typical roll-to-roll process.[17, 20, 42]

6.2　EXPERIMENTAL

6.2.1　Materials

Dopamine-HCl and osmium tetroxide were purchased from Sigma-Aldrich. Tris (tris(hydroxymethyl)aminomethane) base was obtained from Fisher Scientific. PET film (Melinex® ST506) was kindly provided by Dupont Teijin Films and used as received. Adhesive-backed Kapton® polyimide film (3M 5413) and PTFE film (3M 5180) were purchased from 3M. Polyimide P84® was kindly provided by Evonik Industries. (Tridecafluoro-1,1,2,2,-tetrahydrooctyl) methyldichlorosilane was purchased from Gelest, Inc. Si wafers were purchased from NOVA Electronic Materials, LLC. Ultrapure water (18.2 MΩ-cm) was obtained from a Thermo Scientific Barnstead E-pure water purification system. Symmetric PS-*b*-PMMA was purchased from Polymer Source, Inc. with each block possessing a molecular weight of 37 kDa. The microdomain periodicity of this lamellae-forming BCP is ~ 42 nm.[43] GL51 and GL57 refer to two random copolymers of P(S-*r*-MMA-*r*-G), which were synthesized by conventional free-radical copolymerization in 70°C toluene solution using benzoyl peroxide as an initiator.[44] Styrene, methyl methacrylate, and toluene were stirred over calcium hydride and alumina (0.1 g/mL) and filtered prior to use; glycidyl methacrylate was used as received. 51 mol% styrene was used in the feed of GL51 and 57 mol%

styrene was used in the feed of GL57, with 1 mol% glycidyl methacrylate present in the feed of both. GL51 and GL57 were precipitated into methanol and freeze dried from benzene.

The M_n of GL51 and GL57 were 26.7 kDa (Đ = 1.6) and 23.6 kDa (Đ = 1.6), respectively. The molecular weight and polydispersity data were determined using a Viscotek GPC Max VE 2001 size exclusion chromatography (SEC) equipped with a Viscotek Model 270 dual detector of viscometer/light scattering detector, a Viscotek VE 3580 refractive index detector, and two I-Series mixed bed low MW columns. The molar ratio between styrene, methyl methacrylate, and glycidyl methacrylate in the resultant random copolymers of GL51 and GL57 were 71:28:1 and 77:22:1, respectively, as measured by ^{1}H NMR. ^{1}H NMR spectra were recorded in deuterated chloroform solution with a Varian Unity Plus 400 MHz spectrometer. We note that the styrene composition of GL51 and GL57 is consistent with that of the random copolymers synthesized by Register and coworkers to produce a perpendicular microdomain orientation of lamellae-forming PS-*b*-PMMA.[45]

6.2.2 Substrate preparation

A perfluorinated silane layer was assembled onto the Si wafer surface. 0.1 mL of (tridecafluoro-1,1,2,2, - tetrahydrooctyl) methyldichlorosilane was added to 100 mL of toluene. A piranha cleaned Si wafer was immersed in this solution, which was subsequently heated to 75°C and kept at this temperature overnight. After the grafting reaction, the treated Si wafer was thoroughly washed several times with toluene and isopropanol, and then dried under vacuum. Polyimide films were spin-coated (3000 rpm, 180 s) on Si wafers from *n*-methyl-2-pyrrolidone (NMP) solutions (10 wt%) at 70°C with the aid of an infrared lamp, and then annealed at 160°C for 4 h under vacuum (<50

mTorr) to completely remove residual solvent. The thickness of the polyimide thin films was 540 nm, as determined by a spectroscopic ellipsometer (VB-400 VASE Ellipsometer, J. A. Woollam Co., Inc.) using wavelengths from 382 to 984 nm with a 65° angle of incidence. Si wafers were immersed in piranha solution (80% sulfuric acid: 20% hydrogen peroxide) at 100°C for 30 min. The other polymer substrates were rinsed with isopropanol and dried by filtered air before use.

6.2.3   PDA coating

The substrates were taped on Si wafers by double sided copper tape. Dopamine-HCl (2 mg/mL, 200 mL) was completely dissolved in aqueous 10 mM (tris(hydroxymethyl)aminomethane)-hydrochloride (Tris-HCl) (pH 8.5) for one minute at 850 rpm, and substrates were then quickly immersed in this solution for the designated time. During dopamine polymerization, the substrates were oriented vertically in solution while stirring at 400 rpm. After PDA deposition, the coated substrates were rinsed with DI water, then quickly immersed in a basic water (10mM Tris-HCl, pH 8.5), followed by sonication for 100 min (Branson 2510 Ultrasonic Cleaner). Finally, the samples were dried with a filtered airgun, thoroughly rinsed with DI water, and then dried under vacuum for one day.

Between the PDA coating and sonication procedures, the coated samples were kept immersed in Tris-HCl (pH 8.5) buffer solution. Otherwise, polydopamine granules adhered too strongly to be separated from the substrate by sonication. During the sonication process, the samples were steeply tilted or vertically oriented in the basic solution during sonication so that PDA grains did not redeposit. The thicknesses of the PDA layers were measured using a spectroscopic ellipsometer.

6.2.4   BCP nanopatterning process

A 0.4 wt% solution in cyclopentanone (CPN) of two random copolymers of P(S-*r*-MMA-*r*-G), GL51 and GL57, mixed at a 1:1 weight ratio was prepared.   This solution was spin-coated onto PDA-coated substrates at 1500 rpm for 40 s, and the resulting films were annealed under vacuum at 160°C for 48 hours to graft the SNT layer to the underlying PDA coating.   The annealed films were then thoroughly washed with tetrahydrofuran several times to completely remove unbound GL51 and GL57.   The resulting SNT layer was 7-8 nm thick, which is identical to that obtained upon the native silicon oxide surfaces of Si wafers.   Subsequently, 1.2 wt% of PS-*b*-PMMA/toluene solution was spincoated on the sample and a 44 nm thick PS-*b*-PMMA layer was achieved.   The PDA coated substrates did not swell or crack as a result of the spincoating process.   The annealing conditions were chosen with the thermal stability of each substrate in mind.   For example, PS-*b*-PMMA films on a Si wafer, polyimide-coated wafer, or Kapton tape were annealed on a 250°C hotplate for 5 min in air while PS-*b*-PMMA films on Teflon tape and PET film were annealed under vacuum at 185°C for 3 h and 160°C for 3 h, respectively.   Before imaging, all samples were etched in an O$_2$ plasma cleaner (PCD-32G, Harrick) at 10.5 W for 45 s to enhance scanning electron microscopy (SEM) imaging contrast by selectively removing the PMMA domain.

6.2.5   Scanning electron microscope

Self-assembled BCP thin films on thick polymer substrates such as PET film and Teflon tape were treated with osmium tetroxide vapor for 23-28 h to limit charging. Top-down SEM micrographs were acquired on a Zeiss Supra 40 VP SEM using the in-lens detector, an accelerating voltage of 1 keV, and a working distance of 3-6 mm. Micrographs were judged to be representative when the same consistent nanopattern

quality was observed on at least five micrographs viewed at different spots over a minimum 2 cm^2 sample size.

6.2.6   Atomic force microscopy

Phase images of samples were recorded using an Asylum Research MFP-3D AFM in tapping mode.   AFM images were taken using 300 series tapping mode AFM tips (tip radius < 10nm, Ted Pella) with a resonant frequency of 300 kHz and a force constant of 42 N/m.

6.2.7   Contact angle goniometry

Static water contact angles (θ_w) were measured using a Ramé-Hart, Inc.   NRL C.A. goniometer (model #100-00). A 6 μL drop of deionized water was placed on the sample for the measurement, and the image was taken within 15 s of placing the drop on the sample.   The samples were cleaned with filtered air to remove dust particles.

6.3   RESULTS AND DISCUSSION

6.3.1   PDA film growth and surface topography

We studied the growth of PDA during deposition and its resultant surface topography so that we might produce a conformal and smooth functional nano-layer on a variety of soft material surfaces.   Substrates were coated with polydopamine by immersion in a basic water (pH 8.5) solution during spontaneous dopamine polymerization[31] (Figure 6.1 (a)).   PDA films were formed by a three-dimensional island growth mechanism that is concurrent with bulk solution-phase production of secondary grains with sizes ranging up to several hundred nm.[41, 46]   The respective thickness and size of these features grow over time.   A SEM micrograph of roughly 200 nm diameter granules formed after 3 days of polymerization is shown in Figure 6.1 (b).

94
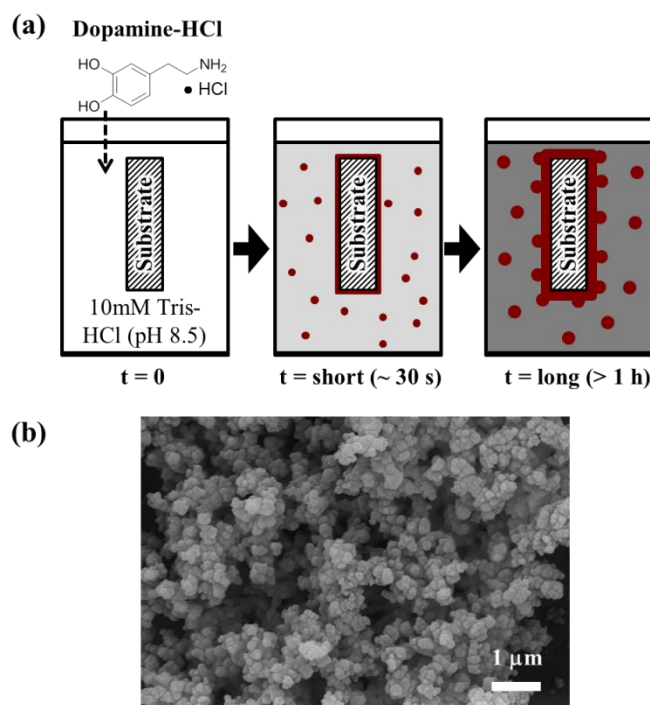
Figure 6.1: (a) Schematic of dopamine oxidative polymerization process. (b) SEM of particles formed in solution after 3 days of dopamine polymerization.

The surface roughness of PDA coatings was characterized *ex situ* after various deposition times by optical microscopy and AFM. Micrographs taken after 5 h and 24 h coating times are shown in Figure 6.2. The films obtained immediately after PDA deposition (Figure 6.2 (a) and (d)) are littered with PDA microgranules and are unacceptably rough. Recently, Klosterman *et al.* showed that PDA deposited on surfaces revealed distinct spherical particles on a planar PDA sublayer which consisted of mound-like structured small islands with nearly uniform size and shape by high-resolution AFM.[41] In an attempt to clean the surfaces, the substrates were bath sonicated for 100 min in basic solution. After sonication, the sample with 5 h PDA deposition time was much smoother, with few particles on its surface (Figure 6.2 (b) and (c)). The root-mean-square (RMS) roughness (3 μm × 3 μm) was 3.2 nm. The sample

subjected to 24 h of PDA deposition was still very rough even after sonication (Figure 6,2 (e) and 6.2 (f), RMS roughness = 9.5 nm). The adhesion is likely due to some combination of hydrogen bonding, charge transfer, and π-π interactions among catechols on the interface between the PDA particles and the sublayer. These characteristics help explain the insolubility of PDA and its notable stability as a coating.[34, 41, 46-50] The adsorbed, surface-bound granules are a source of particulate defects when a secondary material is layered on top of them. A continuous, thin and smooth functional PDA layer is much more desirable and a critical consideration for merging PDA surface engineering with BCP nanopatterning.
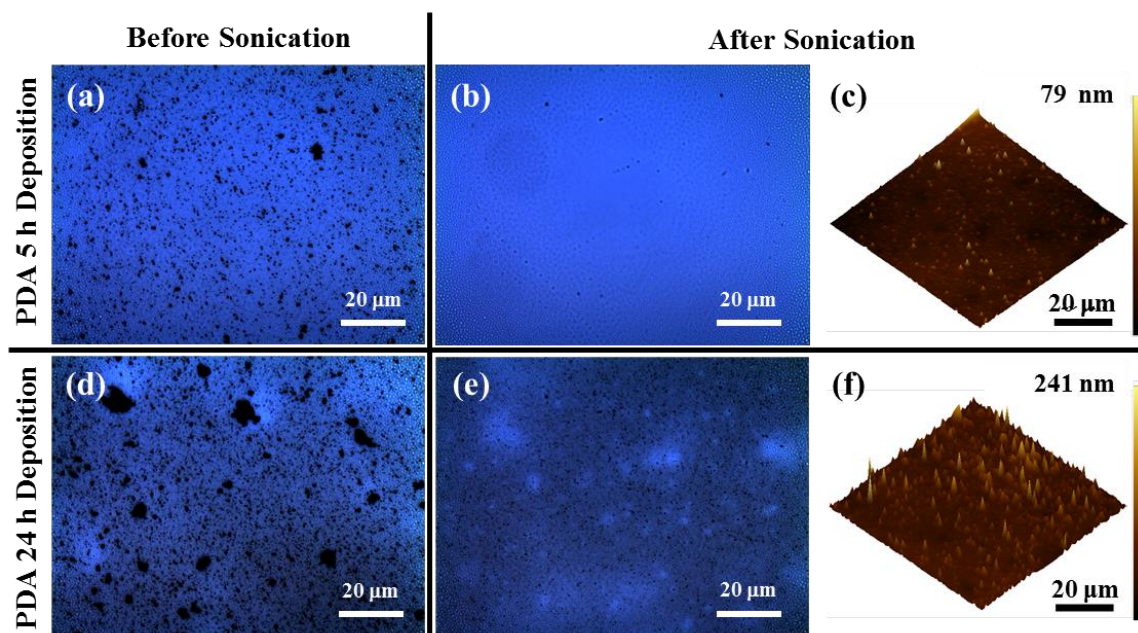
Figure 6.2: (a, b) Optical micrographs of PDA coatings after 5 h (d, e) after 24 h on a Si wafer (a, d) before and (b, e) after sonication. (c, f) AFM images (third column, 50 μm × 50 μm) of Si wafers that were PDA-coated for 5 h (c) and 24 h (f) after sonication.

To explore the feasibility of even shorter PDA coating times, thicknesses and water contact angles (θ_w) of PDA layers grown on Si wafers were measured after various coating times as shown in Figure 6.3.   Our PDA thicknesses measured by spectroscopic ellipsometry quantitatively agree with AFM values reported by Ball *et al.*[46]   The PDA layer thickness gradually increased, reaching 18 nm after 5 h.   Sonication in basic water (pH 8.5) reduced the apparent thickness of the PDA layer, presumably due to the removal of weakly-bound granules.   Encouragingly, a 2-3 nm thick film is obtained with only 30 min of PDA deposition, and its thickness is not appreciably reduced by sonication.   This suggests that PDA deposition times < 1 h may produce films with very few adsorbed granules.   The static water contact angles grow rapidly at short PDA deposition times and reach a plateau of 52°-62° after only 1 h.   This is consistent with the substrates being conformally coated by PDA at only relatively short deposition times.   The thickness and contact angle data for longer deposition times (> 8 h) are provided in Appendix C (Figure C.1).
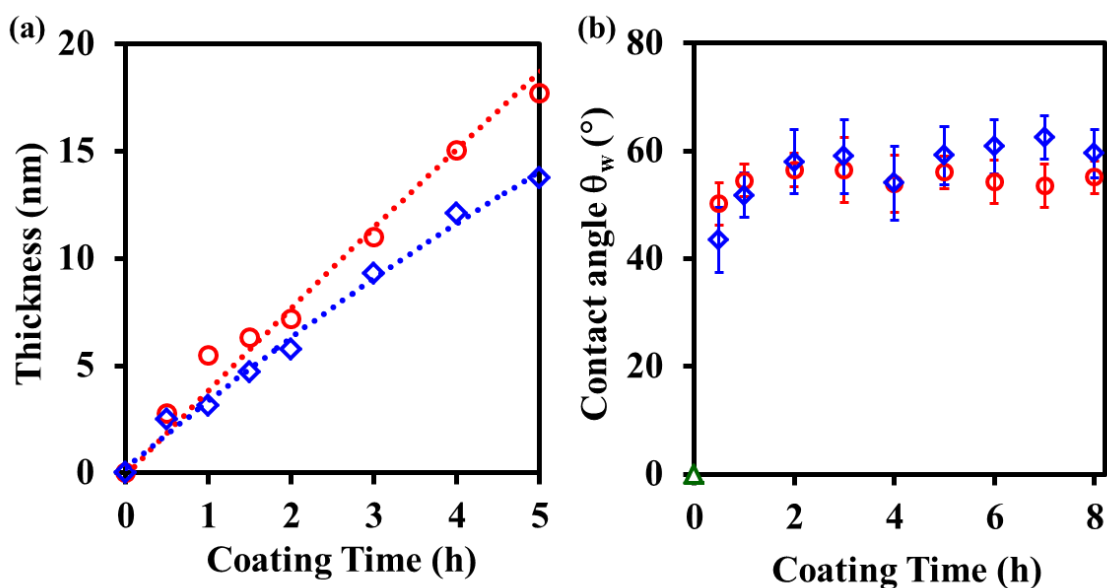
Figure 6.3: (a) Thicknesses and (b) water static contact angles of PDA coatings before (red open circles) and after (blue open diamonds) sonication on a bare Si wafer (green open triangle) after various coating times.   Error bars in (b) represent the standard deviation of 10 separate measurements.

SEM was used to observe the surface topography of PDA coatings on Si wafers before (Figure C.2 in Appendix C) and after (Figure C.3 in Appendix C) sonication.   For a PDA surface coating applied for less than 1 h, nanoparticles were successfully removed from the surface by sonication in basic water without damaging the PDA conformal surface layer; the resulting 2-4 nm-thick PDA layer appeared suitable for defect-free BCP nanopatterning.   Zangmeister *et. al.* found that ~3 nm was the thinnest continuous PDA layer possible.[51]   On the other hand, for PDA coatings applied for longer than 1 h, numerous nanoparticles remained on the surface even after sonication (Figure C.2 in Appendix C).

6.3.2 PDA-assisted surface engineering process

Figure 6.4 (a) shows our process flow for PDA-assisted BCP lithography. Substrates were immersed for 1 h in a dopamine solution (2 mg/mL) in 10 mM Tris-HCl (pH 8.5), followed by sonication in basic water (pH 8.5). The mussel-inspired universal adhesive nature of the PDA enabled modification of the surface energy on a variety of substrates. As shown in Figure 6.4 (c) and Table 6.1, the PDA treatment allowed convergence of water contact angles on a wide variety of substrates (native surfaces with contact angles of 0°-113°) within a range of 52°-68°, demonstrating a PDA-like chemical environment. Subsequently, P(S-*r*-MMA-*r*-G) (surface neutralization treatment, SNT) was grafted onto the PDA sublayer via coupling of the glycidyl groups of the random copolymer with the catechol and amine on the PDA-coated surface as Liebscher *et al.* proposed.[49] After thermal annealing and thorough rinsing with tetrahydrofuran, a 7-8 nm thick SNT layer was obtained. Annealing/rinsing experiments performed atop PDA coated Si wafers indicated that crosslinking of our SNT materials is not significant (Figure C.6). Then after spin-coating and annealing a PS-*b*-PMMA layer, the lamellar microdomains were vertically oriented because the SNT is non-preferentially wetted by either BCP domain.[23] Subsequent incorporation of a SNT onto the PDA sublayer and following self-assembly of PS-*b*-PMMA finally resulted in consistent contact angles falling within the range of 81°-88°, the expected contact angle of a PS-*b*-PMMA surface.[9] All contact angles eventually converged to the specific values expected of pure PDA and PS-*b*-PMMA for each step, regardless of the type of underlying substrate material, thus demonstrating an efficient and substrate-independent surface modification technique.

99
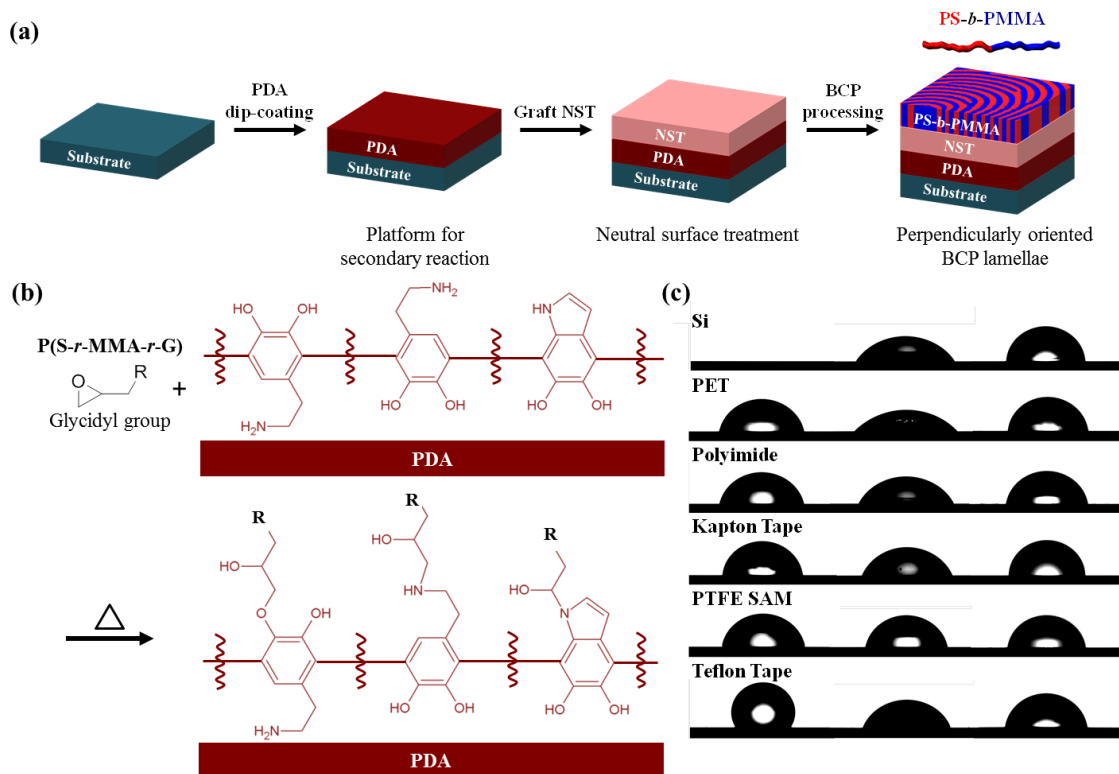
Figure 6.4: (a) A schematic of PDA-assisted PS-*b*-PMMA BCP lithography for soft material surfaces.   (b) Grafting mechanism of a surface neutralization treatment (SNT) on top of a PDA layer, where R represents P(S-*r*-MMA-*r*-G).   (c) Pictures of water droplets on bare (left), polydopamine-treated (middle), and perpendicularly oriented PS-*b*-PMMA (right) surfaces.

Substrate	Bare (°)	1 h PDA Coating (°)	Vertically Oriented PS-*b*-PMMA (°)
Si	< 5	52 ± 4	86 ± 1
Polyimide	76 ± 2	64 ± 3	81 ± 1
Kapton tape	88 ± 1	68 ± 3	88 ± 2
PTFE SAM	85 ± 4	60 ± 2	82 ± 2
Teflon tape	113 ± 3	68 ± 2	83 ± 2
PET	66 ± 3	56 ± 2	85 ± 2

Table 6.1: Static contact angles on various substrates after surface modification. Range indicates standard deviation from 10 separate measurements.

6.3.3 BCP lithography on soft materials

The effect of the PDA layer roughness on the BCP nanopattern fidelity is shown in Figure 6.5.   A smooth coating was obtained with a 1 h PDA deposition time and 100 min sonication in mild aqueous base as shown in Figure 6.5 (a),(b) and (c).   Its root-mean-square roughness (3 μm × 3 μm) was 0.4 nm, which is nearly equivalent to that of the underlying Si wafer (~ 0.3 nm).   Consequently, the BCP nanopattern obtained on this surface is free of granule defects.   On the other hand, the PDA coating surface after a 5 h deposition time and sonication reveals many particles with heights ranging up to 77 nm (Figure 6.5 (d) and (f)).   These are larger than the total thickness of the polymer ad-layers consisting of an SNT layer (8 nm) and of BCP film (44 nm).   The large particles spanned the depth of the BCP thin film and protruded from the nanopatterned surface (Figure 6.5 (e)).
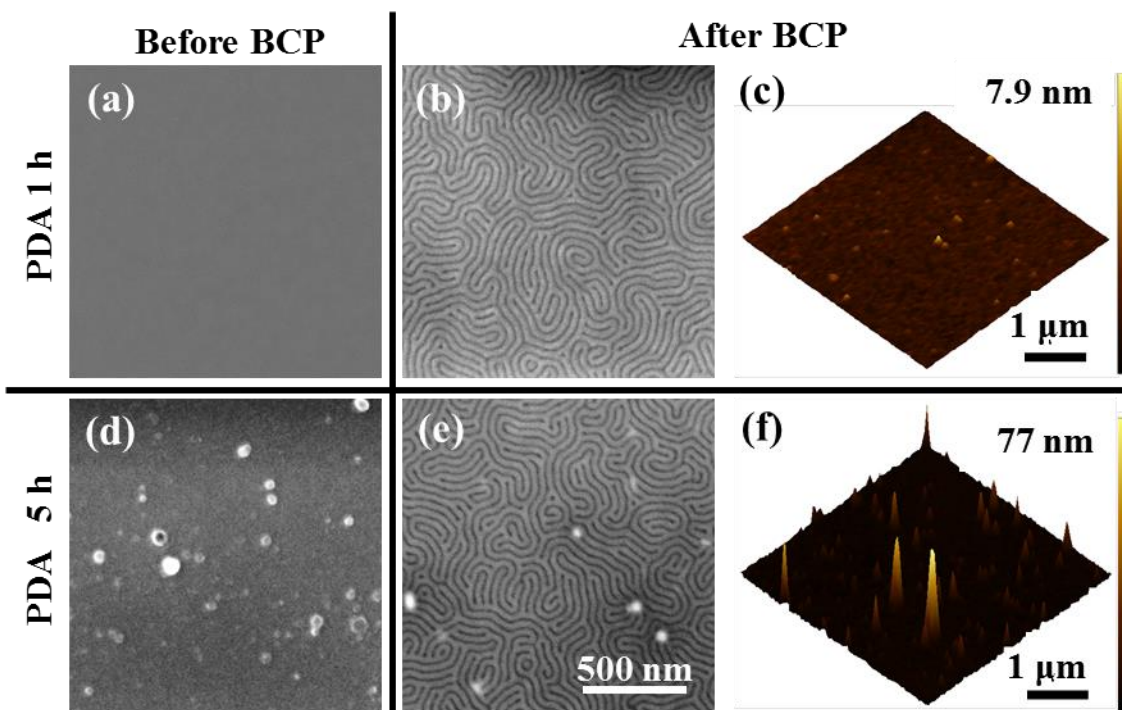
Figure 6.5: Representative SEM and AFM micrographs of (a, b, c) 1 h and (d, e, f) 5 h
PDA deposition times (a, d) after sonication, and (b, c, e, f) after subsequent
BCP nanopatterning.   Full SEM micrographs are provided in Figure C.3 in
Appendix C.

As shown in Figure 6.6, BCP lithography was successfully achieved on not only
smooth organic and inorganic surfaces but also on flexible commercial polymer films.
For example, this BCP lithography approach readily generated uniform and periodic
fingerprint BCP nanodomains on diverse substrates from an extremely hydrophilic SiO_2
surface ($\theta_w = \sim5°$) to an exceptionally hydrophobic Teflon surface ($\theta_w = 113°$, Table 6.1).
Furthermore, perpendicular lamellae orientation of PS-*b*-PMMA was successfully
fabricated on not only a smooth PTFE brush SAM (Figure 6.6 (a)) but also on
commercial Teflon tape with a highly wrinkled surface texture (Figure 6.6 (b)).   This is

in spite of the well-known chemical inertness of perfluorinated materials.[35]   In fact, BCP nanopatterning was unsuccessful on Teflon tape without PDA treatment because the SNT solution could not be coated on Teflon tape due to its low surface energy (Figure C.5 in Appendix C).

This demonstrates that our surface engineering approach depends neither on surface energy/chemistry nor on the physical topography of the substrates as a previous study demonstrated.[35]   Moreover, BCP nanopatterns were also successfully introduced onto polyimide (Figure 6.6 (c)), its commercial relative Kapton (Figure 6.6 (d)), Teflon tape (Figure 6.6 (b)) and PET (Figure 6.6 (e)).   The implication of these successes is the approach's wide applicability to a variety of commercially important polymer substrates, especially flexible materials suitable for high-throughput roll-to-roll processing.   The reader may note that the nanopatterns formed atop commercial, rough films (Figure 6.6 (b), (d), and (e)) show more defects than those atop coated, planarized wafers (Figure 6.6 (a), (c), and (f)).   We attribute those defects to topological defects on the uncoated commercial films, such as the Teflon film surface shown in Figure C.5 (a) in Appendix C.   Planarization of the commercial substrates would be necessary to remove topological defects.
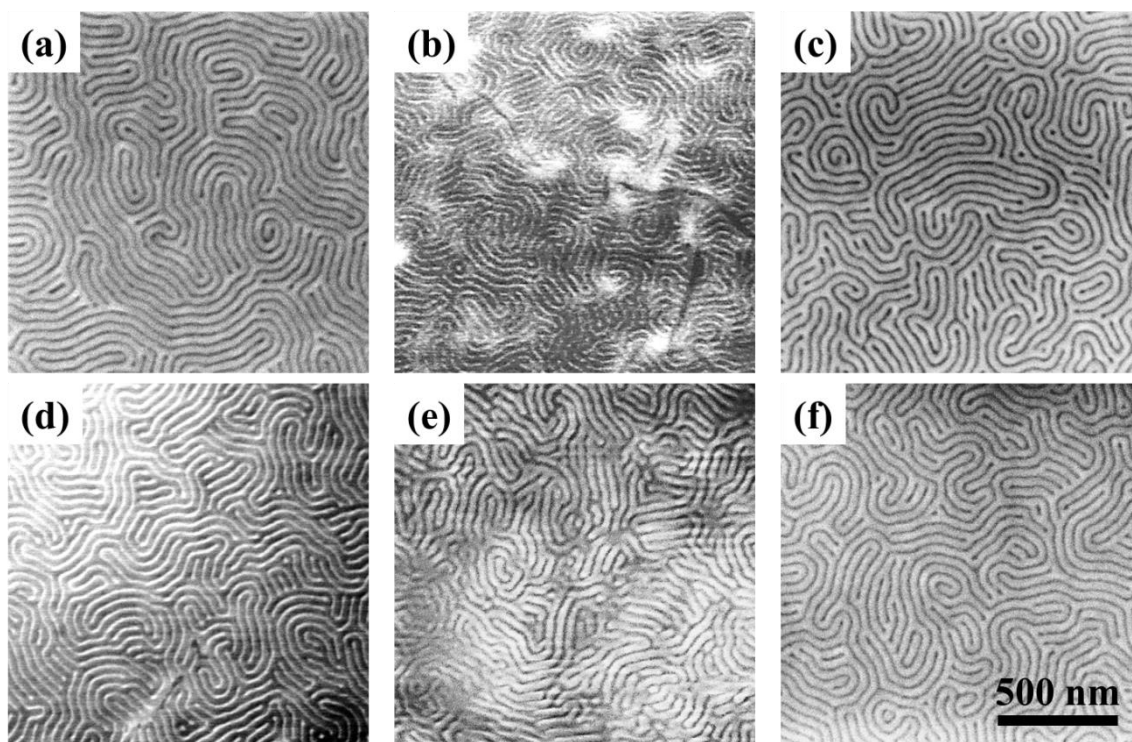
Figure 6.6:   Representative SEM images of perpendicularly oriented PS-*b*-PMMA
domains on (a) PTFE brush SAM, (b) Teflon tape, (c) polyimide thin film,
(d) Kapton tape, (e) PET film, and (f) Si wafer.   Full micrographs (1.9 μm
× 2.8 μm) are provided in Figure C.4 in Appendix C.

To emphasize the flexibility of the substrates employed here, SEM imaging was
performed on one of the most common roll-to-roll substrates, PET film while it was
bowed across a microscopy stub as shown in Figure 6.7 (a).   A representative
micrograph from its surface observed by SEM is shown in Figure 6.7 (b).   Based on the
initial length of the sample and the chord length once affixed to the stub, we estimate the
bending radius as ~0.5 cm, which is smaller than a safe bending radius of plastic
substrates in a roll-to-roll process (4 cm).[42]   Because the PDA, SNT, and BCP coating
stack is very thin and strongly adhered to the underlying flexible substrate, the
nanopattern remains affixed and its microdomains are still isotropically aligned.   In
addition, this mussel-inspired interfacial engineering approach for BCP lithography could

be relatively non-destructive to the electronic properties of the underlying material,[35] unlike alternative adhesion strategies that rely on plasma.[52-54]   Therefore we anticipate that nanopatterns formed by this process flow would be suitably robust for roll-to-roll manufacturing processes.
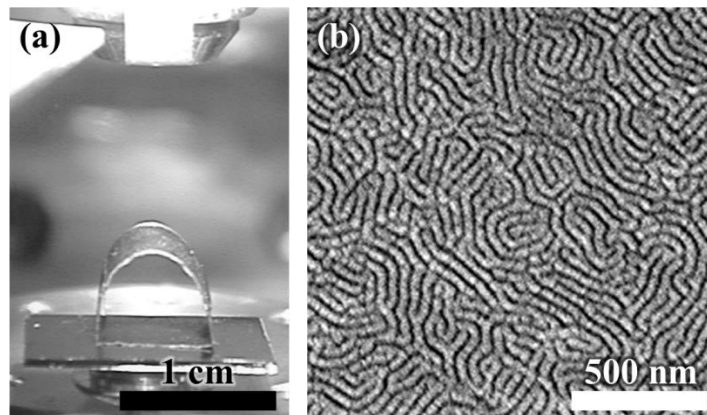
Figure 6.7:   (a) A nanopatterned PET substrate in SEM imaging chamber, demonstrating mechanical robustness to bending.   (b) Representative SEM micrograph of the surface of the BCP coated PET substrate during bending.

6.4   CONCLUSIONS

A mussel-inspired universal strategy for surface treatment resulted in vertically oriented BCP domains on a variety of demanding but technologically important surfaces, including flexible organic substrates.   Sonication of the initially grown PDA deposition (< 1 h) in mild alkaline water (pH 8.5) resulted in thin, smooth (RMS roughness ~ 0.4 nm) and conformal functional PDA ad-layers with dense functionality available for secondary reactions.   PDA grew quickly on a wide spectrum of polymeric substrates with varying hydrophilicity ($\theta_w = 0°\text{-}113°$) to converge in 1 h to a surface hydrophilicity consistent with pure PDA ($\theta_w = 52°\text{-}68°$).   This demonstrates a fast, efficient, and universal surface engineering method.   This biomimetic, universally adhesive surface

modification approach represents a potentially useful processing tool to complement current BCP lithography procedures by allowing simple functionalization of any surface that is compatible with conventional thermal annealing.

6.5 FUTURE WORK

6.5.1 Universally adhesive SNT

In the present study, a multi-layer approach was employed for BCP self-assembly; PDA thin layers atop the flexible substrates served as a universal adhesive layer as well as provided reactive sites for subsequent grafting of the SNT layer. This fabrication method requires two polymer deposition steps of the PDA and SNT layers respectively, which could be simplified by synthetic approaches. As shown in Figure 6.8 (a), instead of having two layers consisting of SNT and PDA separately, a single layer (SNT-PDA) could serve as a new SNT layer that can adhere on a variety of substrates with less coating steps. Here, the SNT-PDA needs to possess both styrene and methyl methacrylate to achieve a neutral surface for PS-*b*-PMMA, in addition to a DOPA related moiety for promoting adhesion to the substrates.

Incorporating a DOPA moiety into polymers has already been developed, including for PS[55] and PMMA,[39, 55] among others. One potential structure for SNT-PDA is shown in Figure 6.8 (b) where N-methacryloyl-3,4-dihydroxyl-$_L$-phenylalanine (MDOPA) was chosen as the DOPA moiety based on the successful conventional radical polymerization by Chung and Grubbs *et al.*[27] This report also demonstrated that incorporating only 15 mol% of the MDOPA component led to a doubling of the shear strength of adhesives on the substrate. In the random copolymer, SNT-PDA, optimizing x and y while minimizing z to maintain solubility in organic solvent could result in a one-component universal adhesive SNT which does not require the initial PDA coating step.

In order to reinforce the mechanical and BCP coating solution stability of the SNT-PDA, adding a cross-linkable moiety, such as glycidyl or azido groups described in Chapter 5.2.1, may be required.
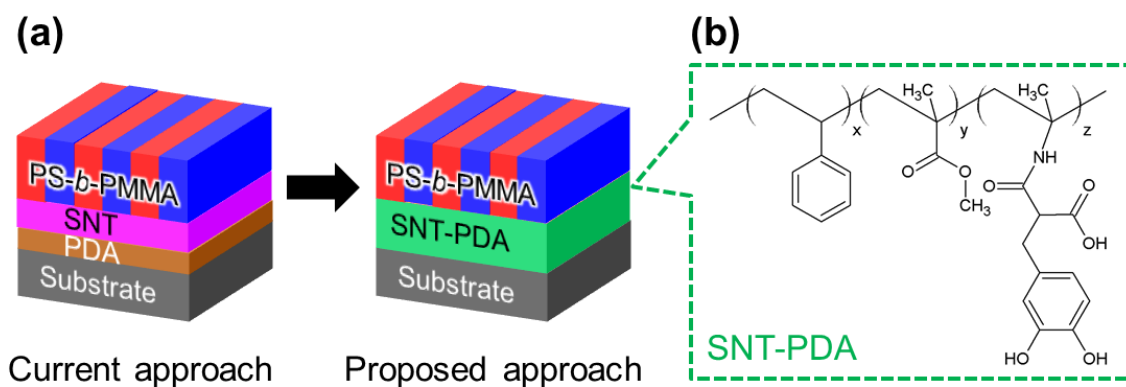
Figure 6.8: (a) Schematic of proposed approach for a one-component SNT-PDA layer.
(b) One potential structure of SNT-PDA.

6.5.2 PDA lithography

A patterned PDA layer could have potential for a variety of applications, such as cell adhesion, metal deposition, and surface grafting.[56] Such patterning has been attempted using the polydimethylsiloxane (PDMS) stamping method.[56, 57] However, this approach cannot be applied to all substrates, such as Teflon or PET, due to their low surface energy. In order to pattern PDA on a variety of substrates, precise spatial control using a non-contact technique is strongly desired.

To this end, a traditional photolithographic approach using photobase generator (PBG) may address this issue. Figure 6.9 illustrates a schematic of a PDA patterning process using PBG. Here, PBG generates base upon UV radiation and annealing, and one of the candidates for PBG is Nifedipine, which has been widely employed in polymeric systems.[58] First, dopamine-HCl and PBG is co-cast on the potential substrate

with a binder, such as PEG, to tune the viscosity during spincoating. Subsequently, patterned UV light (365 nm for Nifedipine)[58] and heating will induce patterned base (Figure 6.9 (a) and (b)). Since dopamine polymerization is sensitive to pH, the basic conditions in light exposed regions should initiate the development of PDA (Figure 6.9 (c)). A series of blanket exposures would be needed to first determine the optimal processing parameters (e.g., light dose, PBG loading, etc.). And finally, the residual layers could be washed away by acid resulting in a patterned PDA layer as shown in Figure 6.9 (d).
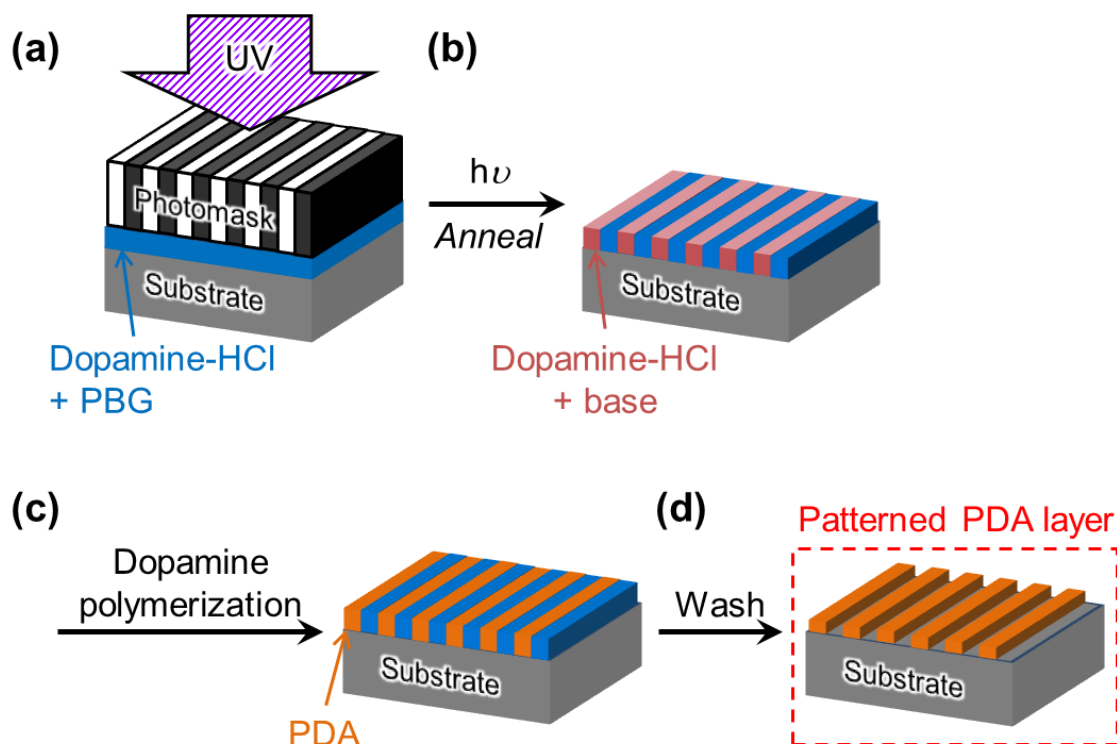
Figure 6.9: Schematic diagram of fabrication of patterned PDA. (a) Dopamine-HCl and photobase generator (PBG) are first spin coated on the substrate. (b) Subsequent patterned light exposure and thermal annealing produce patterned base. (c) Due to pH change in the exposed area, a PDA pattern is generated. (d) Washing the residual layer with acid results in the patterned PDA layer.

6.6 REFERENCES

1. Bates, F. S.; Fredrickson, G. H. *Phys. Today* **1999,** 52, (2), 32-38.
2. Hirai, T.; Leolukman, M.; Liu, C. C.; Han, E.; Kim, Y. J.; Ishida, Y.; Hayakawa, T.; Kakimoto, M.-a.; Nealey, P. F.; Gopalan, P. *Adv. Mater.* **2009,** 21, (43), 4334-4338.
3. Bates, C. M.; Seshimo, T.; Maher, M. J.; Durand, W. J.; Cushen, J. D.; Dean, L. M.; Blachut, G.; Ellison, C. J.; Willson, C. G. *Science* **2012,** 338, (6108), 775-779.
4. Cushen, J. D.; Otsuka, I.; Bates, C. M.; Halila, S.; Fort, S.; Rochas, C.; Easley, J. a.; Rausch, E. L.; Thio, A.; Borsali, R.; Willson, C. G.; Ellison, C. J. *ACS Nano* **2012,** 6, (4), 3424-33.
5. Maher, M. J.; Bates, C. M.; Blachut, G.; Carlson, M. C.; Self, J. L.; Janes, D. W.; Durand, W. J.; Lane, A. P.; Ellison, C. J.; Willson, C. G. *ACS Macro Lett.* **2014,** 3, (8), 824-828.
6. Luo, Y.; Montarnal, D.; Kim, S.; Shi, W.; Barteau, K. P.; Pester, C. W.; Hustad, P. D.; Christianson, M. D.; Fredrickson, G. H.; Kramer, E. J.; Hawker, C. J. *Macromolecules* **2015,** 48, (11), 3422-3430.
7. Cheng, J. Y.; Rettner, C. T.; Sanders, D. P.; Kim, H.-C.; Hinsberg, W. D. *Adv. Mater.* **2008,** 20, (16), 3155-3158.
8. Liu, C.-C.; Han, E.; Onses, M. S.; Thode, C. J.; Ji, S.; Gopalan, P.; Nealey, P. F. *Macromolecules* **2011,** 44, (7), 1876-1885.
9. Janes, D. W.; Thode, C. J.; Willson, C. G.; Nealey, P. F.; Ellison, C. J. *Macromolecules* **2013,** 46, (11), 4510-4519.
10. Kim, J.; Wan, J.; Miyazaki, S.; Yin, J.; Cao, Y.; Her, Y. J.; Wu, H.; Shan, J.; Kurosawa, K.; Lin, G. *J. Photopolym. Sci. Technol.* **2013,** 26, (5), 573-579.
11. Wan, L.; Ruiz, R.; Gao, H.; Patel, K. C.; Albrecht, T. R.; Yin, J.; Kim, J.; Cao, Y.; Lin, G. *ACS Nano* **2015,** 9, (7), 7506-14.
12. Cushen, J.; Wan, L.; Blachut, G.; Maher, M. J.; Albrecht, T. R.; Ellison, C. J.; Willson, C. G.; Ruiz, R. *ACS Appl. Mater. Interfaces* **2015,** 7, (24), 13476-13483.
13. Stein, G. E.; Mahadevapuram, N.; Mitra, I. *J. Polym. Sci., Part B: Polym. Phys.* **2015,** 53, (2), 96-102.
14. Rogers, J. A.; Someya, T.; Huang, Y. *Science* **2010,** 327, (5973), 1603-1607.
15. Wei, Q.; You, E.; Hendricks, N. R.; Briseno, A. L.; Watkins, J. J. *ACS Appl. Mater. Interfaces* **2012,** 4, (5), 2322-2324.
16. Beaulieu, M. R.; Baral, J. K.; Hendricks, N. R.; Tang, Y.; Briseño, A. L.; Watkins, J. J. *ACS Appl. Mater. Interfaces* **2013,** 5, (24), 13096-13103.
17. Akinwande, D.; Petrone, N.; Hone, J. *Nat. Commun.* **2014,** 5, 5678.
18. Zhu, W.; Yogeesh, M. N.; Yang, S.; Aldave, S. H.; Kim, J.-S.; Sonde, S.; Tao, L.; Lu, N.; Akinwande, D. *Nano Lett.* **2015,** 15, (3), 1883-1890.
19. Yang, S.; Chen, Y.-C.; Nicolini, L.; Pasupathy, P.; Sacks, J.; Becky, S.; Yang, R.; Daniel, S.; Chang, Y.-F.; Wang, P.; Schnyer, D.; Neikirk, D.; Lu, N. *Adv. Mater.* **2015,** 27, (41), 6423-6430.
20. Singh, G.; Batra, S.; Zhang, R.; Yuan, H.; Yager, K. G.; Cakmak, M.; Berry, B.; Karim, A. *ACS Nano* **2013,** 7, (6), 5291-5299.

21.   Cui, N.; Liu, J.; Gu, L.; Bai, S.; Chen, X.; Qin, Y. *ACS Appl. Mater. Interfaces* **2015,** 7, (33), 18225-18230.

22.   Ha, M.; Park, J.; Lee, Y.; Ko, H. *ACS Nano* **2015,** 9, (4), 3421-3427.

23.   Mansky, P.; Liu, Y.; Huang, E.; Russell, T. P.; Hawker, C. *Science* **1997,** 275, (5305), 1458-1460.

24.   Kim, S. O.; Solak, H. H.; Stoykovich, M. P.; Ferrier, N. J.; de Pablo, J. J.; Nealey, P. F. *Nature* **2003,** 424, (6947), 411-414.

25.   Stoykovich, M. P.; Müller, M.; Kim, S. O.; Solak, H. H.; Edwards, E. W.; de Pablo, J. J.; Nealey, P. F. *Science* **2005,** 308, (5727), 1442-1446.

26.   Inoue, T.; Janes, D. W.; Ren, J.; Suh, H. S.; Chen, X.; Ellison, C. J.; Nealey, P. F. *Adv. Mater. Interfaces* **2015,** 2, (10), 1500133.

27.   Chung, H.; Grubbs, R. H. *Macromolecules* **2012,** 45, (24), 9666-9673.

28.   Dreyer, D. R.; Miller, D. J.; Freeman, B. D.; Paul, D. R.; Bielawski, C. W. *Chem. Sci.* **2013,** 4, (10), 3796-3802.

29.   Yang, H.-C.; Luo, J.; Lv, Y.; Shen, P.; Xu, Z.-K. *J. Membr. Sci.* **2015,** 483, 42-59.

30.   Maier, G. P.; Rapp, M. V.; Waite, J. H.; Israelachvili, J. N.; Butler, A. *Science* **2015,** 349, (6248), 628-632.

31.   Lee, H.; Dellatore, S. M.; Miller, W. M.; Messersmith, P. B. *Science* **2007,** 318, (5849), 426-430.

32.   d'Ischia, M.; Napolitano, A.; Pezzella, A.; Meredith, P.; Sarna, T. *Angew. Chem., Int. Ed.* **2009,** 48, (22), 3914-3921.

33.   Ye, Q.; Zhou, F.; Liu, W. *Chem. Soc. Rev.* **2011,** 40, (7), 4244-4258.

34.   Lee, H.; Scherer, N. F.; Messersmith, P. B. *Proc. Natl. Acad. Sci. USA* **2006,** 103, (35), 12999-13003.

35.   Kim, B. H.; Lee, D. H.; Kim, J. Y.; Shin, D. O.; Jeong, H. Y.; Hong, S.; Yun, J. M.; Koo, C. M.; Lee, H.; Kim, S. O. *Adv. Mater.* **2011,** 23, (47), 5618-5622.

36.   Clodt, J. I.; Filiz, V.; Rangou, S.; Buhr, K.; Abetz, C.; Höche, D.; Hahn, J.; Jung, A.; Abetz, V. *Adv. Funct. Mater.* **2013,** 23, (6), 731-738.

37.   Dreyer, D. R.; Miller, D. J.; Freeman, B. D.; Paul, D. R.; Bielawski, C. W. *Chem Sci* **2013,** 4, (10), 3796-3802.

38.   Park, S.; Yun, J. M.; Maiti, U. N.; Moon, H.-S.; Jin, H. M.; Kim, S. O. *Nanotechnology* **2014,** 25, (1), 014008.

39.   Cho, J. H.; Shanmuganathan, K.; Ellison, C. J. *ACS Appl. Mater. Interfaces* **2013,** 5, (9), 3794-802.

40.   Postma, A.; Yan, Y.; Wang, Y.; Zelikin, A. N.; Tjipto, E.; Caruso, F. *Chem. Mater.* **2009,** 21, (14), 3042-3044.

41.   Klosterman, L.; Riley, J. K.; Bettinger, C. J. *Langmuir* **2015,** 31, (11), 3451-3458.

42.   Wong, W. S.; Salleo, A., *Flexible electronics: materials and applications.* Springer: New York, 2009; Vol. 11.

43.   Liu, G.; Stoykovich, M. P.; Ji, S.; Stuen, K. O.; Craig, G. S. W.; Nealey, P. F. *Macromolecules* **2009,** 42, (8), 3063-3072.

44.   Han, E.; Stuen, K. O.; La, Y. H.; Nealey, P. F.; Gopalan, P. *Macromolecules* **2008,** 41, (23), 9090-9097.

45.   Pujari, S.; Keaton, M. A.; Chaikin, P. M.; Register, R. A. *Soft Matter* **2012,** 8, (19), 5358-5363.

46.   Ball, V.; Frari, D. D.; Toniazzo, V.; Ruch, D. *J. Colloid Interface Sci.* **2012,** 386, (1), 366-372.

47.   Dreyer, D. R.; Miller, D. J.; Freeman, B. D.; Paul, D. R.; Bielawski, C. W. *Langmuir* **2012,** 28, (15), 6428-6435.

48.   Hong, S.; Na, Y. S.; Choi, S.; Song, I. T.; Kim, W. Y.; Lee, H. *Adv. Funct. Mater.* **2012,** 22, (22), 4711-4717.

49.   Liebscher, J.; Mrówczyński, R.; Scheidt, H. A.; Filip, C.; Hădade, N. D.; Turcu, R.; Bende, A.; Beck, S. *Langmuir* **2013,** 29, (33), 10539-10548.

50.   Guardingo, M.; Esplandiu, M. J.; Ruiz-Molina, D. *Chem. Commun.* **2014,** 50, (83), 12548-12551.

51.   Zangmeister, R. A.; Morris, T. A.; Tarlov, M. J. *Langmuir* **2013,** 29, (27), 8619-8628.

52.   Shin, Y. J.; Wang, Y.; Huang, H.; Kalon, G.; Wee, A. T. S.; Shen, Z.; Bhatia, C. S.; Yang, H. *Langmuir* **2010,** 26, (6), 3798-3802.

53.   Kim, B. H.; Kim, J. Y.; Jeong, S.-J.; Hwang, J. O.; Lee, D. H.; Shin, D. O.; Choi, S.-Y.; Kim, S. O. *ACS Nano* **2010,** 4, (9), 5464-5470.

54.   Zhou, Y.-f.; Yuan, Y.-b.; Cao, L.-f.; Zhang, J.; Pang, H.-q.; Lian, J.-r.; Zhou, X. *J. Lumin.* **2007,** 122–123, 602-604.

55.   Guvendiren, M.; Brass, D. A.; Messersmith, P. B.; Shull, K. R. *J. Adhesion* **2009,** 85, (9), 631-645.

56.   Chien, H.-W.; Kuo, W.-H.; Wang, M.-J.; Tsai, S.-W.; Tsai, W.-B. *Langmuir* **2012,** 28, (13), 5775-5782.

57.   Ku, S. H.; Lee, J. S.; Park, C. B. *Langmuir* **2010,** 26, (19), 15104-15108.

58.   Kim, C. B.; Janes, D. W.; Zhou, S. X.; Dulaney, A. R.; Ellison, C. J. *Chem. Mater.* **2015,** 27, (13), 4538-4545.

Chapter 7: Large area fabrication of graphene nanoribbons by wetting transparency-assisted block copolymer lithography

7.1 INTRODUCTION

Graphene has captured tremendous attention as a two-dimensional (2D) material for its high electron mobility, thermal conductivity, optical transparency, and mechanical strength.[1-4] In particular, graphene has longer plasmon lifetimes than that of noble metals such as gold and silver,[5] which indicates huge potential for using graphene as a plasmonic material in the mid-infrared (MIR) and visible light regimes.[6] When graphene is spatially confined into a graphene nanoribbon (GNR) or graphene nanomesh, the wide tunability of the graphene plasmon is revealed, and such graphene nanopatterned arrays can be used in various applications ranging from protein biosensing[7] to MIR-terahertz (THz) spectroscopy.[6, 8-10] For example, Rodrigo *et al.* recently reported a high-sensitivity tunable plasmonic biosensor fabricated with GNR arrays (from 20 nm to 60 nm in width).[7] Also, Silveiro *et al.* showed an exceptional tunability of GNR's plasmonic properties by controlling width, doping, and edge formation of GNRs.[11] However, most current plasmonic GNR arrays are fabricated using electron beam lithography (EBL), which is a low throughput method that does not easily scale to large areas ($\sim cm^2$) in a cost-effective way.[12]

There have been numerous attempts to fabricate GNRs, and existing methods have both advantages and limitations.[12] Bottom-up approaches, such as self-assembly of small molecules[13] and sonochemistry,[14] can produce GNRs with widths down to 5 nm,[14] sometimes with controlled edge conformations.[13] The limitations associated with bottom-up approaches are difficulties in handling and positioning GNRs for device fabrication and scale-up.[12] On the other hand, top-down approaches, including lithographic,[15, 16] nanowire-assisted,[17] and unzipping of carbon nanotubes,[18] can more

easily locate GNRs for device applications[12] but typically have difficulties with resolution, width control, and scale-up.[12]   In the case of using GNR arrays in a MIR-THz spectroscopy or heat harvesting device, arrays over large areas are crucial for achieving suitable signal to noise ratio.   In fact, Zhang *et al.* recently reported successful fabrication of cm^2 scale graphene nanodot arrays.[19]   Another challenge to be addressed is the production of GNR arrays by a simpler and potentially scalable methodology to further enable plasmonic GNR devices.

Block copolymer (BCP) lithography[20] is a very promising way to fabricate nanopatterned graphene,[21-24] including GNRs.[25-31] BCPs are polymers that consist of two chemically different polymer segments, or blocks, joined with a single covalent bond. Since intermixing of the two blocks is usually thermodynamically unfavorable, the blocks phase segregate into domains as small as 5 nm[32] that can be used as etch masks to transfer the BCP domain patterns into the underlying graphene. The tunability in BCP domain size is afforded during synthesis by adjusting block lengths which in turn allows control over the widths of GNRs[22, 27] and diameters of graphene nanomeshes[22, 23] following etch transfer of the BCP pattern into the graphene.   For instance, Son *et al.*[27] and Liang *et al.*[22] have successfully fabricated sub-10 nm GNRs using BCP lithography. Of particular importance is that BCP lithography is generally known to be capable of large-scale fabrication over ~cm^2 areas.[33]

Since thin BCP films are used as etch masks for GNR fabrication, perpendicular orientation of the BCP domains is crucial.   Perpendicular orientation can be achieved only when the surface energy of the underlying substrate is neutral; in other words, the substrate must not prefer to contact one block of the BCP over the other.[34]   Otherwise, one of the blocks will preferentially contact or wet the substrate, inducing a domain orientation that is parallel to the substrate surface which is useless as an etch mask.   To

control the surface energy of underlying substrates, a thin cross-linked polymer layer termed a surface neutralization treatment (SNT) is often used as was introduced in Section 5.2.1.[34-36]   In past GNR fabrication studies, the SNT layer has often been placed between the BCP and the graphene layer and it remains on top of the GNR after etching processes.[22, 26-28] Therefore, previous BCP-assisted GNR fabrication methods required additional steps to remove the cross-linked SNT layer, such as baking the specimen at $1000^{o}C$ under a mixture of argon and hydrogen, to reveal the underlying GNR.[27]

In this study, we propose that graphene's unique surface energy characteristic, so-called "wetting transparency (WT),"[37, 38] can be exploited for GNR production. Examples of the WT of graphene include a report that the wettability of water on graphene is dominated by the underlying substrate because graphene is atomically thin.[37] We note that there are some exceptions for substrates with strong short-range interactions, such as hydrogen-bonding.[37, 38]   Taking advantage of the WT of graphene in the present study, we demonstrate a robust procedure to fabricate GNRs by placing the cross-linked SNT layer *underneath* graphene where the WT enables the SNT layer to control the orientation of BCP *through* the graphene.   This way, the BCP layer can be placed directly on graphene, which simplifies the GNR fabrication process.   Very recently, poly(styrene-*block*-methyl methacrylate) (PS-*b*-PMMA) has been perpendicularly oriented on graphene by exploiting the WT of graphene, but its lithographic potential as an etch mask and a detailed study of surface energy have not been demonstrated.[39]

Another advantage is that the WT-assisted GNR fabrication method could also be compatible with chemo-epitaxial directed self-assembly (DSA), which can be used to guide the alignment of BCP lamellae patterns along pre-patterned lines into device relevant arrangements.[40]   Chemo-epitaxial DSA has been successfully demonstrated on

a large scale (7.6 μm × 5.7 μm) with very few defects.[41]   Applying the WT-assisted GNR fabrication approach to DSA will open up opportunities to fabricate GNRs into prescribed arrangements, which can potentially improve both optical and electrical properties of GNRs, such as their plasmonic resonance[42] and band gap.[43]

7.2   EXPERIMENTAL

7.2.1   Materials

All chemicals were purchased from Sigma-Aldrich or Fisher Scientific and used as received unless otherwise noted. Monolayer graphene was grown on a 35 μm thick copper foil (Oak-Mitsui, Miller-Cu) by low-pressure chemical vapor deposition (LPCVD) according to a previously reported procedure.[44]   The copper foil (1.5 cm × 7 cm) was used as received and loaded in a fused silica tube (22 mm ID) housed in a furnace, and the tube was evacuated to a pressure lower than 1×10^{-4} mTorr.   Once the pressure reached equilibrium, hydrogen gas was introduced at 2 sccm.   The pressure in the tube was at ~25 mTorr, and the tube was heated to 1030°C.   After keeping the temperature at 1030°C for 15 min, methane gas was added at 4 sccm for 10 min for graphene growth, and the pressure inside the tube was ~ 60 mTorr.   After stopping the methane purge, the silica tube was cooled down to room temperature, maintaining hydrogen flow.

In order to prepare GNRs with different widths, PS-*b*-PMMA polymers with three different molecular weights were used: 1. 18 kg/mol-*b*-18 kg/mol (18k-18k), 2. 33 kg/mol-*b*-33 kg/mol (33k-33k), and 3. 105 kg/mol-*b*-106 kg/mol (105k-106k).   PS-*b*-PMMA (33k-33k, and 105k-106k) samples were purchased from Polymer Source, Inc. and used as received.   PS-*b*-PMMA (18k-18k) was synthesized by anionic polymerization as described in the following paragraph.   The bulk period of the BCP

(L_0) was 27 nm (18k-18k), 40 nm (33k-33k), 104 nm (105k-106k) as estimated by Fast Fourier Transform analysis of scanning electron microscope (SEM) micrographs by ImageJ. The SNT layer for PS-*b*-PMMA was an azide-containing poly(4-*tert*-butylstyrene-*random*-methyl methacrylate-*random*-4-vinylbenzyl azide) (poly(tBuS-*r*-MMA-*r*-VBzAz)), which was synthesized following a previously reported procedure.[35, 45] The molar ratio of tBuS: MMA: VBzAz was 27: 68: 5 for 18k-18k, and 40: 56: 4 for 33k-33k and 105-106k, which were confirmed by combustion analysis.

7.2.2 Anionic polymerization of 18k-18k PS-*b*-PMMA

The 18k-18k PS-*b*-PMMA was synthesized using anionic polymerization. HPCL-grade tetrahydrofuran (THF) was purchased from J.T. Baker and purified with an Innovative Technology Pure Solv MD-2 solvent purification system equipped with two activated alumina columns. Styrene was purified by distilling twice over di-n-butylmagnesium (1.0 M in heptane, dried on Schlenk line before use). Methyl methacrylate (MMA) was purified by first stirring with calcium hydride (1 g/100 g MMA) then distilled. Trioctylaluminum was added to the distilled MMA until a faint yellow color held, then the MMA was distilled again. The purified monomers were brought into a drybox. The reactor vessel was flame dried five times, and then the appropriate amount of THF was added to the reactor vessel and cooled to -78°C. The appropriate amount of sec-butyllithium was added to initiate the reaction. Styrene was added dropwise to the reactor vessel using an airtight glass syringe, and the solution color was orange. After 1 h, an appropriate amount of diphenylethylene was added to the reactor (five times the molar amount of chain ends), and the solution color was blood red. An aliquot was taken, and MMA was added dropwise to the reactor. The solution turned clear after the addition of MMA. After the reaction was allowed to proceed for 2 h at -

116

78°C, degassed methanol was used to terminate the reaction. The polymer was precipitated in methanol and dried in vacuo.

7.2.3   Sample preparation

All spin coating solutions were filtered with 200 nm pore size Teflon filters (CHROMAFIL Xtra PTTE 20/25) to remove particles, and the thickness of each layer was measured after spin coating by a spectroscopic ellipsometer (J.A. Woollam M-2000D) with a fitting wavelength range of 400-1000 nm.   The SNT layer was prepared by spin coating a 0.5 wt% solution of P(tBuS-r-MMA-r-VBzAz) from toluene onto a high resistance and undoped double-sided Si wafer (University WAFER 2772) with a 1.5 nm native silicon oxide layer used as received, and the sample was annealed at 250°C for 5 min in air.   The un-crosslinked polymer was removed by placing the sample on the spincoater for 45 sec at 3500 rpm, where it was washed 5 times with excess toluene.   To remove residual solvent, the sample was annealed at 100°C for 5 min under atmospheric conditions, and the resulting SNT layer thickness was 15 nm.

The LPCVD-grown graphene layer (1.5 cm × 1.5 cm) was transferred onto SNT using a poly(methyl methacrylate) (PMMA) supported graphene transfer process.[46]   The PMMA (996 kg/mol as reported by the manufacturer) was purchased from Sigma-Aldrich and used as received.   A 60 mg/mL solution of PMMA in anisole was spin coated at 4000 rpm for 1 min onto the graphene/copper sample whose edges were taped on a glass slide.   The sample was annealed at 130°C for 15 min on a hot plate to remove residual solvent and to relax residual stress in the PMMA film.   The copper foil and the graphene grown on the underside of the copper foil were removed by a two-step etch process.   First, the side without PMMA on top was treated with a nitric acid/water solution (1:2 by volume) for ~ 1 min until bubbles were observed.   Second, the sample

was floated on a 0.1 mol/L ammonium persulfate (APS, $(NH_4)_2S_2O_8$))/deionized water solution overnight.   The samples were floated on 300 mL of deionized water for at least 2 h to remove residual APS, after which the graphene was finally transferred onto the SNT substrate.   The transferred graphene on SNT was dried at room temperature for 1 h then at $130^{\circ}C$ for 15 min under atmospheric pressure.   The sample was soaked in ~100 mL of acetone and stirred at 120 rpm overnight to remove the PMMA.   Then, the graphene, which has now been transferred onto the SNT, was treated by a basic plasma cleaner (HARRICK PDC-32G) for 20 sec with an oxygen partial pressure of 350 ± 5 mTorr and 6.8 W applied to a radio frequency coil to enhance the wettability of the graphene to the BCP solution.

A 1.25 wt% solution of PS-*b*-PMMA in cyclopentanone was prepared and spincoated at 1800 rpm onto the graphene/SNT substrate, resulting in a 45 nm thick film. The samples were then annealed at $200^{\circ}C$ for 2 min for 18k-18k, and $250^{\circ}C$ for 5 min for 33k-33k and 105k-106k to orient the domains perpendicularly.   To selectively remove the PMMA and transfer the pattern into the graphene to form GNR, the sample stack was exposed to a CO_2-based reactive ion etching (RIE) process using a commercial 300 mm capacitively coupled plasma reactor (Lam Research Flex™ E Series dielectric etch system).   For all RIE tests, coupons (~400 mm^2) containing the sample stack were thermally pasted (Type 120 silicone, Wakefield Solutions) onto the center of 300 mm ArF resist carrier wafers prior to plasma etching.   The remaining PS layer on top of the GNR was washed away by soaking the sample in 100 mL of THF for at least 12 h and subsequently washed with isopropanol and blown dry by filtered air. The sample was dried at room temperature under vacuum for at least 2 h to remove residual solvent.

118

7.2.4 Scanning electron microscope

The SEM images in Figure 7. 2 (a)-(f) were collected using a Hitachi S-9380II CD-SEM operating at an accelerating voltage of 800 V and a working distance of 2.7 - 2.8 mm.   For Figure 2 (g)-(i), a Hitachi S-4500 SEM was used with an acceleration voltage of 5.0 kV and a working distance of 5 mm.

7.2.5 Atomic force microscopy

Atomic force microscopy (AFM) was used to image the GNR after etching.   The data was collected on an Asylum Research MFP-3D Origin AFM.   The silicon tips used had a radius of 9 ± 2 nm with a resonance frequency of 300 kHz and were purchased from Asylum Research.   Each scan had 1024 points/line and 1024 lines, and the scan rate was 3 μm/s.

7.2.6 Contact angle measurement

Dynamic contact angles were measured by the Ramé-hart NRL C.A. goniometer (model no. 100-00) using the needle-in-the-sessile-drop method.   All measurements were performed at room temperature with the needle embedded inside the liquid droplet. After the substrate was cleaned with isopropanol and dried with filtered air, a liquid droplet with volume around 7 μL was manually deposited for 2 sec on the surface by a Gilmont micrometer dispenser syringe.   The contact angle was measured with a time interval of 0.24 sec based on the image captured by a CCD camera of the goniometer using the DROPimage (version 1.5.06) software.   The droplet was allowed to grow to the maximum droplet size for 10-15 sec.   After the droplet settled, the liquid was withdrawn with the needle for another 2 sec. Again, the droplet was allowed to recede to the lowest contact angle for 10-15 sec.   This expansion and retraction cycle of the liquid was repeatedly performed for around 2 min to create the contact angle hysteresis. The

procedure was performed at least five times for each combination of liquid type and substrate sample.

7.2.7 Raman microscopy

Transferred graphene on Si wafers was characterized by Raman microscopy (Witec Micro-Raman Spectrometer Alpha 300). The excitation wavelength was 488 nm, and the laser power was 20 mW. The spectrum was obtained with an objective lens with a magnification of 100× and a numerical aperture of 0.95. Integration time was 4 sec.

7.3 RESULTS AND DISCUSSION

7.3.1 Graphene nanoribbon (GNR) fabrication

A schematic diagram of the WT-assisted GNR fabrication process is shown in Figure 7.1. Monolayer graphene grown on a copper foil by LPCVD was transferred onto a SNT coated (15 nm thick) Si wafer using a modified PMMA-assisted transfer method (Figure 7.1 (a) and (b)).[46, 47] Before spin coating the PS-*b*-PMMA BCP solution, the graphene surface was treated by O_2 plasma at a lower power (6.8 W) and shorter time (15 sec) than typical O_2 plasma treatments (called a "mild O_2 plasma treatment"[48]) to enhance the wettability of the BCP solution during spin coating (Figure 7.1 (c)) on the graphene. In order to prepare GNRs with different widths, PS-*b*-PMMA polymers with three different molecular weights ,18k-18k, 33k-33k, and 105k-106k were used. The resulting BCP layers was 45 nm thick, for all molecular weights, on the graphene/SNT substrate. The samples were then annealed to provide mobility to the polymer such that the domain structure can form and organize into perpendicular lamellae (Figure 7.1 (d)). In order to use the BCP layer as an etch mask for the graphene, PMMA was selectively removed using a CO_2 based etch process (Figure 7.1

(e)).   The remaining PS pattern then acted as an etch mask, and the pattern was etch transferred into the underlying graphene layer, resulting in a GNR decorated surface (Figure 7.1 (f)).
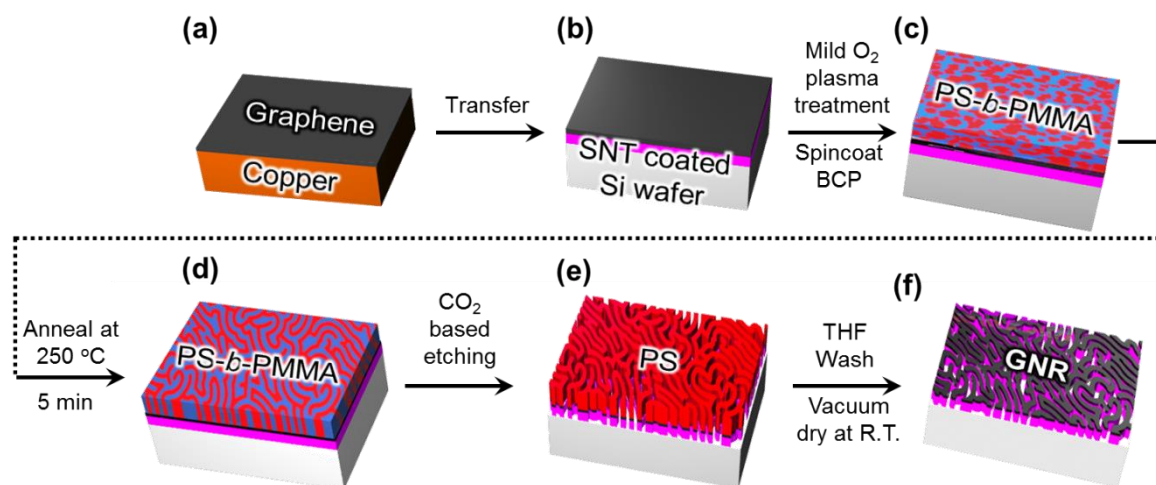
Figure 7.1:   Schematic diagram of WT-assisted BCP lithography for GNR fabrication. (a) Monolayer graphene was grown on a copper foil.   (b) The graphene was transferred onto a SNT-coated Si wafer using a PMMA-assisted transfer method.   (c) PS-*b*-PMMA was spin-coated on the mild plasma treated graphene substrate, and (d) annealed to achieve perpendicular domain orientation.   (e) The PMMA domain of the BCP was selectively removed by a CO_2 based etching process and the pattern was transferred into the underlying graphene.   (f) The remaining PS was removed by soaking in THF, and then the sample was dried at room temperature under vacuum.

The order in which the BCP, graphene, and SNT layers are stacked is the key to simplifying the GNR fabrication process.   Since the GNR is formed on top of the cross-linked or immobilized SNT layer, the process described in this paper does not require additional steps to remove the cross-linked SNT layer after etching.   Instead of baking the GNR at a high temperature, the residual un-crosslinked PS mask layer at the top of the graphene can be simply removed by washing with THF (Figure 7.1 (e) and (f)), which

eliminates the risk of damaging the graphene or other integrated device structures during the removal of the crosslinked SNT layer.

Another novel aspect of the WT-assisted GNR fabrication method is the use of lamellae-forming PS-*b*-PMMA. In most previous studies, cylinder-forming BCPs were used as the etch mask.[25, 27, 29] Using parallel cylinders to make GNRs required a more complicated etch process because the cylinders are not uniform in width throughout the depth of the thin film.[20] In contrast, the lamellar width is uniform throughout the depth of the film regardless of the etching depth, which can offer more precise control of etching processes. Also, PS and PMMA have almost identical surface energies at the thermal annealing temperatures used here, which simplifies the BCP orientation process because no solvent annealing or top coats are needed to control orientation at the air interface.[49]

7.3.2 Top-down and cross-sectional structure

Successful GNR fabrication was confirmed by SEM and AFM. Figure 7.2 (a)-(f) are the SEM images before the removal of PS fingerprint pattern corresponding to Figure 7.1 (f). The tilted-top view (Figure 7.2 (a)-(c)) shows the etching process successfully removed the PMMA block, and the cross-sectional view (Figure 7.2 (d)-(f)) shows that the polymer layers (BCP and SNT) are cleared by the etching process. Considering that the graphene is placed between the BCP and SNT, this observation indicates that the graphene is etched through transforming it into GNRs. After removing the PS layer at the top, the structure of GNRs was identical to the PS fingerprinting pattern, demonstrating pattern transfer from the BCP mask to fabricate the GNRs. The GNR widths were estimated to be 13 nm (± 5 nm), 22 nm (± 4 nm) and 51 nm (± 15 nm) by analyzing AFM phase images as shown in Appendix D. AFM phase

images in Figure D.1 in Appendix D indicates successful fabrication of a GNR arrays without a significant number of defects (i.e., no regions showing GNR lift-off or damage) in an area of 3 μm × 3 μm.
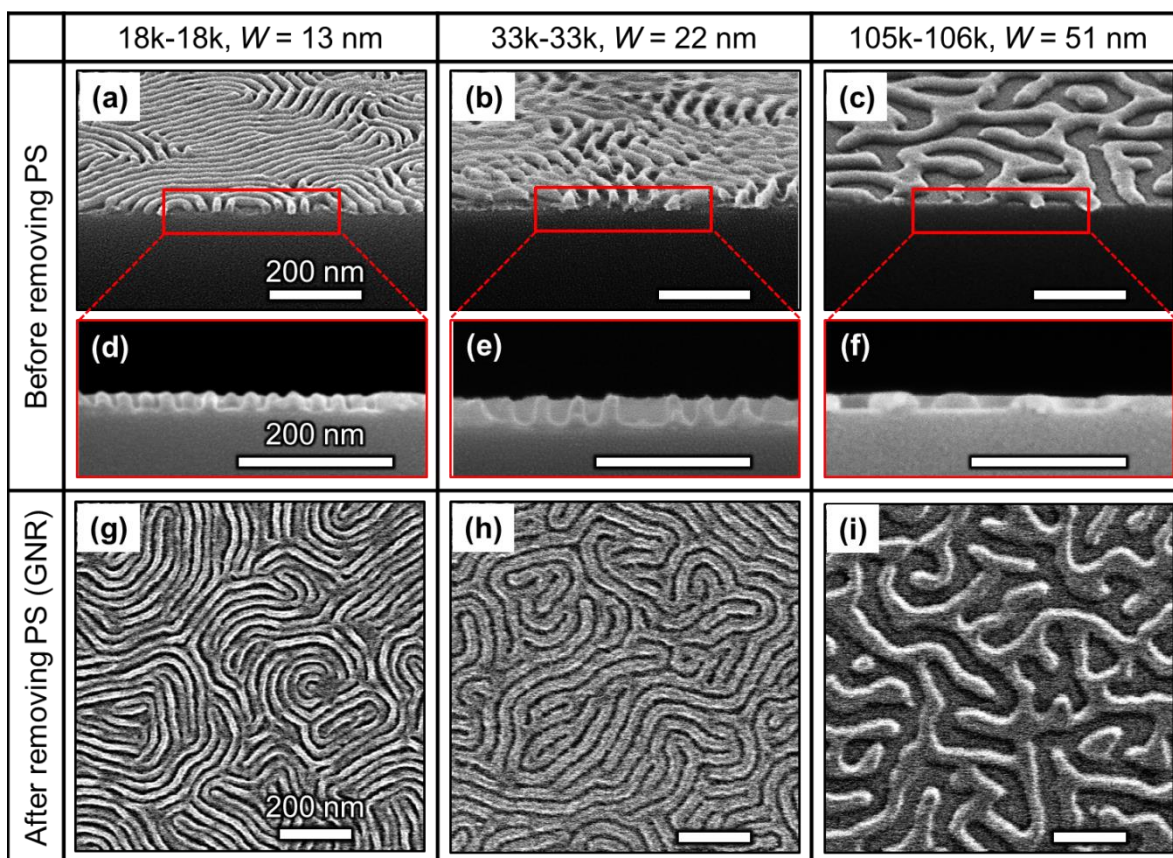
Figure 7.2: Representative scanning electron microscope (SEM) images of (a-f) etched PS "fingerprint" patterns, corresponding to Figure 7.1 (e) and (g-i) GNR arrays after removing the PS etch mask, corresponding to Figure 7.1 (f). All scale bars represent 200 nm. The widths of GNR are (g) 13 ± 5 nm, (h) 22 ± 4 nm, and (i) 51 ± 15 nm.

In the WT-assisted GNR fabrication process, both the mild plasma treatment and the underlying SNT contribute to the neutral surface energy of the substrate, leading to perpendicular orientation of the BCP domains. Earlier work by Kim *et al.* demonstrated

that the surface energy of reduced graphene oxide films can be tailored by optimizing the reducing conditions of graphene oxide to successfully achieve perpendicular orientation of BCP domains without a SNT.[30]   In our case, when the PS-*b*-PMMA solution was spin coated on the mild plasma treated graphene supported by a Si wafer without a SNT layer, only a parallel domain orientation was observed (Figure D.2 in Appendix D).   This can be explained by the fact that graphene is more hydrophobic than graphene oxide, and the ability to change surface energy dramatically under mild plasma is limited; more aggressive treatment conditions are not desirable because they could adversely disturb the other desirable properties of graphene.

7.3.3   Surface energy evaluation of graphene and SNT substrates

In order to obtain fundamental insights into the WT-assisted GNR fabrication method, we investigated the surface energy of the substrates, which is one of the most critical factors in controlling the orientation of the BCPs.[34, 50]   The Owens-Wendt model[51] is known as a simple and reliable method to evaluate surface energies of graphene[52] and other substrates.[50]   This model is based on an assumption that the surface energy γ_S is a sum of the dispersive ($\gamma_S^{Dispersive}$) and polar (γ_S^{Polar}) components.[51]   The dispersive and the polar contributions can be estimated by measuring the contact angles of diiodomethane (DIM) (θ_{DIM}) and water (θ_{water}) droplets, respectively, deposited on the substrate surface using Eq. 7.1,[51]

$$\left(1 + \cos\theta_{water}\right)\gamma_{L,water} = 2\left(\sqrt{\gamma_S^{Dispersive}\gamma_{L,water}^{Dispersive}} + \sqrt{\gamma_S^{Polar}\gamma_{L,water}^{Polar}} \right)$$

$$\left(1 + \cos\theta_{DIM}\right)\gamma_{L,DIM} = 2\left(\sqrt{\gamma_S^{Dispersive}\gamma_{L,DIM}^{Dispersive}} + \sqrt{\gamma_S^{Polar}\gamma_{L,DIM}^{Polar}} \right) \tag{7.1}$$

where $\gamma_{L,X}^{Dispersive}$ and $\gamma_{L,X}^{Polar}$ represent the dispersive and polar components of liquid X (DIM or water), respectively, and these values were taken from literature.[51]   Dynamic contact angle measurements were measured to improve reproducibility,[53] and Figure 7.3

(a) shows a set of representative data for a SNT layer. By using an 8th order Fourier series to fit the dynamic contact angle hysteresis, θ_A and θ_R were determined, and Young's contact angle (θ_Y), equivalent to the static contact angle, was calculated using Tadmor *et al.*'s theory[54] as shown in Figure D.3 in Appendix D.
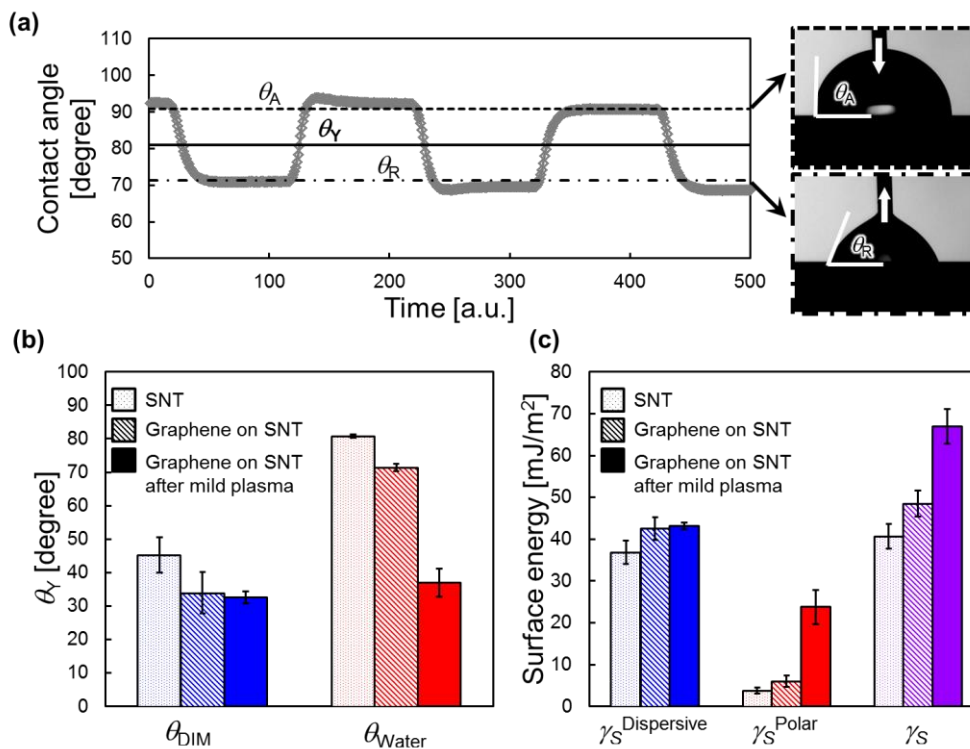
Figure 7.3: Determination of the contact angle of water and diiodomethane (DIM) for surface energy characterization. (a) A set of representative dynamic water contact angle measurements for the SNT layer. Inserted images are snapshots of the advancing and receding water droplets. (b) Young's contact angles (θ_Y) of DIM (blue) and water (red) estimated by dynamic contact angle measurements for SNT (open), and graphene on top of the SNT before (cross hatched) and after mild plasma treatment (filled). Error bars are the standard deviations from five measurements. (c) Surface energy of substrates estimated by contact angle measurements with DIM for the dispersive component (blue) and water for the polar component (red). The total surface energy is the sum of the dispersive and polar contributions (purple) for each sample. Error bars are propagated error from the contact angle measurements as shown in the Appendix D.3.

The θ_{DIM} and θ_{water} are shown in Figure 7.3 (b) for SNT without graphene, graphene on SNT, and mild plasma treated graphene on SNT. From these contact angles, the surface energies of the substrates were calculated using Eq. 7.1 and are plotted in Figure 7.3 (c). Comparing with and without graphene on the SNT layer, θ_{DIM} did not change significantly within error, while θ_{water} increased by 9 degrees. As a result, $\gamma_S^{Dispersive}$ was identical with and without graphene, while γ_S^{Polar} increased by ~2 mJ/m^2. Similarly, only γ_S^{Polar} increased by ~18 mJ/m^2 for mild plasma treated graphene, and the increase of the total surface energy was dominated by the effect of the polar component.

At first glance, the change in surface energy for mild plasma treated graphene on SNT compared to graphene on SNT in Figure 7.3 (b) and (c) seems to suggest that there is a breakdown of the WT of graphene. However, it is not clear that WT should be observed for mild plasma treated graphene given that a small amount of oxygen containing species are expected to be generated on the surface during this treatment. From the perspective of forming the desired structures, perpendicularly orientated BCP domains were observed both on SNT substrates and on mild plasma treated graphene on SNT substrates, which implies that those two substrates both have a suitable surface energy for this application. If the surface energies were too far from neutral for the BCP, one of the systems would have resulted in parallel BCP domains. Furthermore, it was observed that the BCP solution could not be spin coated evenly on graphene without the mild plasma treatment, and the perpendicular orientation of BCP domains was never observed on mild plasma treated graphene without an underlying SNT. Considering all this experimental evidence together suggests that, while graphene may be nearly wetting transparent, mild plasma treated graphene may only be partially wetting transparent in some circumstances.

Aside from the chemical nature of the surface, roughness could be another contributing factor for wettability.[55, 56] The effect of the surface roughness on the contact angles can be described by the Wenzel model:[55]

$$\cos\theta' = r\cos\theta \tag{7.2}$$

where r is a roughness ratio between rough and flat surfaces (always > 1), and θ' and θ are the contact angles on rough and flat surfaces, respectively. The graphene on the SNT substrate is intrinsically rougher than the bare SNT surface because the grain boundaries in the copper foil used in LPCVD are templated in the resulting graphene (Figure 7.1 (a)).[44] Therefore, Equation 7.3 suggests that the contact angle of graphene should decrease, and surface energy of the graphene should increase due to the rougher graphene surface. The rougher graphene surface is one possible explanation for the decrease of θ_{water} after graphene transfer onto SNT (Figure 7.3 (b)). A competing factor is that airborne contaminants are reported to increase the water contact angle of graphene (corresponding to decreased surface energies) after exposing graphene to air.[52, 57] In our system, the mild plasma treatment should remove the airborne contaminants at the surface in addition to slightly oxidizing the graphene as is shown in Figure D.4 in Appendix D.[48] Both the removal of the airborne contaminants and slight oxidation of graphene explain the reduction of water contact angles after mild plasma treatment in Figure 7.3 (b).

7.3.4 GNR structure and integrity

The quality of the GNR in a area of 3 μm × 3 μm was investigated with Raman microscopy, and Figure 7.4 (a) shows a representative spectrum of a 22 nm-wide etched PS-*b*-PMMA (no graphene present) and 13, 22, and 51 nm-width GNRs, all on a SNT layer. The spectrum of GNR was identical to that of untreated graphene, including the *D* band at ~1350 cm^{-1}, the *G* band at ~1580 cm^{-1}, and the 2*D* band at ~ 2680 cm^{-1}.[58] The larger *D* band relative to the *G* band in GNR spectra could be due to slight oxidization during the etching process. Comparing the spectrum of the etched PS-*b*-PMMA with that of GNRs, the etched PS-*b*-PMMA does not exhibit either *D*, *G* or 2*D* bands, indicating the signal originated from the GNRs. Large-area uniformity of the 22 nm-width GNR was investigated by Raman mapping with a 100× magnification lens, and the integrated intensity for *D* (1250-1450 cm^{-1}) and *G* (1500-1720 cm^{-1}) band mappings are shown in Figure 7.4 (b) and (c), respectively. In the observed area (3 μm × 3 μm), no significant defects in the GNR were found. We would like to note that the finger print pattern is not detectable given that each pixel size is 150 nm × 150 nm in this experiment, but 3 μm × 3 μm AFM phase images also indicate that the patterns (Figure D.1 in Appendix D) are essentially uniform over large areas without displaying any major damage. These observations show that this WT-assisted GNR fabrication method allows for the efficient preparation of GNRs over large areas.
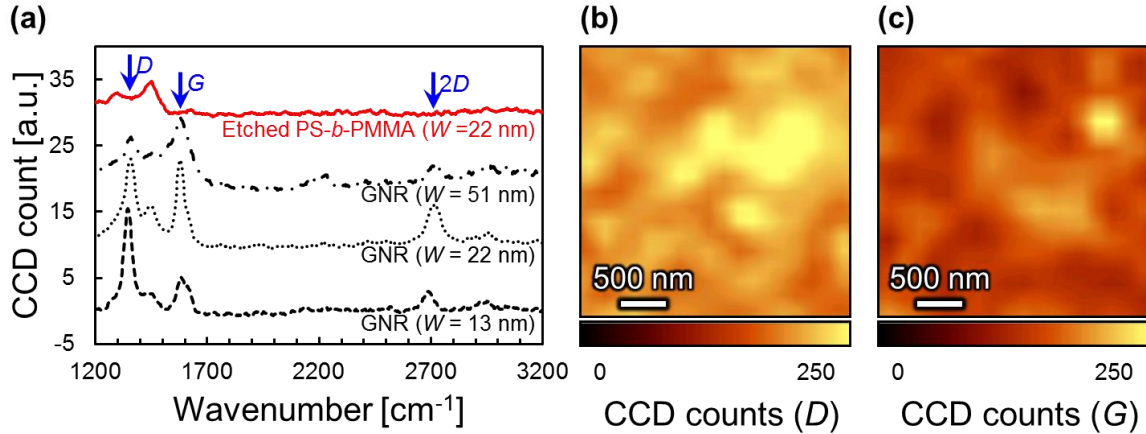
Figure 7.4: (a) A representative Raman spectrum of etched 22 nm-width PS-*b*-PMMA in absence of graphene (red solid line) and 13, 22, and 51 nm-width GNRs (black broken lines), all on a SNT layer. (b,c) 3 μm × 3 μm integrated intensity Raman maps of 22 nm-width GNR of (b) D (1250-1450 cm^{-1}) and (c) G (1500-1720 cm^{-1}) bands. Each pixel size is 150 nm × 150 nm.

7.4 CONCLUSIONS

In conclusion, the large-area fabrication of 13, 22 and 51 nm-wide GNR arrays were demonstrated using the WT-assisted GNR fabrication method, which could enable tunability of plasmonic resonance in the MIR regime. There are four steps to optimize in order to use BCPs as an etch mask for graphene in this way: (1) identify a neutral substrate (SNT) for the BCP to obtain perpendicular orientation of the BCP domains, (2) transfer graphene on top of the SNT substrate, (3) treat graphene on the SNT substrate with a mild plasma treatment to facilitate uniform coating of the BCP solution and (4) thermally anneal to facilitate perpendicular orientation. Comprehensive contact angle/surface energy measurements revealed that the underlying SNT layer is necessary to orient the BCP perpendicularly; in other words, the wetting transparency of the graphene is a crucial consideration to orienting the BCP domains. This result, in addition to the fact that this method is compatible with chemo-epitaxial DSA, allows for

129

sophisticated patterning and device integration of GNRs along with control of their potential control over their plasmonic properties.

7.5 ACKNOWLEDGEMENTS

7.6 REFERENCES

1. Xia, F.; Wang, H.; Xiao, D.; Dubey, M.; Ramasubramaniam, A. *Nat. Photonics* **2014,** 8, (12), 899-907.
2. Akinwande, D.; Petrone, N.; Hone, J. *Nat. Commun.* **2014,** 5, 5678.
3. Lee, C.; Wei, X.; Kysar, J. W.; Hone, J. *Science* **2008,** 321, (5887), 385-388.
4. Matsumoto, H.; Imaizumi, S.; Konosu, Y.; Ashizawa, M.; Minagawa, M.; Tanioka, A.; Lu, W.; Tour, J. M. *ACS Applied Materials & Interfaces* **2013,** 5, (13), 6225-6231.
5. Jablan, M.; Buljan, H.; Soljačić, M. *Phys. Rev. B: Condens. Matter Mater. Phys.* **2009,** 80, (24), 245435.
6. Thongrattanasiri, S.; Manjavacas, A.; García de Abajo, F. J. *ACS Nano* **2012,** 6, (2), 1766-1775.
7. Rodrigo, D.; Limaj, O.; Janner, D.; Etezadi, D.; García de Abajo, F. J.; Pruneri, V.; Altug, H. *Science* **2015,** 349, (6244), 165-168.
8. García de Abajo, F. J. *ACS Photonics* **2014,** 1, (3), 135-152.
9. Low, T.; Avouris, P. *ACS Nano* **2014,** 8, (2), 1086-1101.
10. Yan, H.; Li, X.; Chandra, B.; Tulevski, G.; Wu, Y.; Freitag, M.; Zhu, W.; Avouris, P.; Xia, F. *Nat. Nanotechnol.* **2012,** 7, (5), 330-334.
11. Silveiro, I.; Ortega, J. M. P.; de Abajo, F. G. *Light: Sci. Appl.* **2015,** 4, e241.
12. Tour, J. M. *Chem. Mater.* **2014,** 26, (1), 163-171.
13. Vo, T. H.; Perera, U. G. E.; Shekhirev, M.; Mehdi Pour, M.; Kunkel, D. A.; Lu, H.; Gruverman, A.; Sutter, E.; Cotlet, M.; Nykypanchuk, D.; Zahl, P.; Enders, A.; Sinitskii, A.; Sutter, P. *Nano Lett.* **2015,** 15, (9), 5770-5777.
14. Li, X.; Wang, X.; Zhang, L.; Lee, S.; Dai, H. *Science* **2008,** 319, (5867), 1229-1232.
15. Tapasztó, L.; Dobrik, G.; Lambin, P.; Biro, L. P. *Nat. Nanotechnol.* **2008,** 3, (7), 397-401.
16. Chen, Z.; Lin, Y.-M.; Rooks, M. J.; Avouris, P. *Physica E: Low Dimens. Syst. Nanostruct.* **2007,** 40, (2), 228-232.

17.	Kang, S. H.; Hwang, W. S.; Lin, Z.; Kwon, S. H.; Hong, S. W. *Nano Lett.* **2015,** 15, (12), 7913-7920.

18.	Kosynkin, D. V.; Higginbotham, A. L.; Sinitskii, A.; Lomeda, J. R.; Dimiev, A.; Price, B. K.; Tour, J. M. *Nature* **2009,** 458, (7240), 872-876.

19.	Zhang, K.; Zhang, L.; Yap, F. L.; Song, P.; Qiu, C.-W.; Loh, K. P. *Small* **2016,** 12, (10), 16.

20.	Bates, C. M.; Maher, M. J.; Janes, D. W.; Ellison, C. J.; Willson, C. G. *Macromolecules* **2014,** 47, (1), 2-12.

21.	Mi, H.; Mikael, S.; Liu, C.-C.; Seo, J.-H.; Gui, G.; Ma, A. L.; Nealey, P. F.; Ma, Z. *Appl. Phys. Lett.* **2015,** 107, (14), 143107.

22.	Liang, X.; Jung, Y.-S.; Wu, S.; Ismach, A.; Olynick, D. L.; Cabrini, S.; Bokor, J. *Nano Lett.* **2010,** 10, (7), 2454-2460.

23.	Bai, J.; Zhong, X.; Jiang, S.; Huang, Y.; Duan, X. *Nat. Nanotechnol.* **2010,** 5, (3), 190-194.

24.	Kim, M.; Safron, N. S.; Han, E.; Arnold, M. S.; Gopalan, P. *Nano Lett.* **2010,** 10, (4), 1125-1131.

25.	Jiao, L.; Xie, L.; Dai, H. *Nano Res.* **2012,** 5, (4), 292-296.

26.	Liu, G.; Wu, Y.; Lin, Y.-M.; Farmer, D. B.; Ott, J. A.; Bruley, J.; Grill, A.; Avouris, P.; Pfeiffer, D.; Balandin, A. A.; Dimitrakopoulos, C. *ACS Nano* **2012,** 6, (8), 6786-6792.

27.	Son, J. G.; Son, M.; Moon, K.-J.; Lee, B. H.; Myoung, J.-M.; Strano, M. S.; Ham, M.-H.; Ross, C. A. *Adv. Mater.* **2013,** 25, (34), 4723-4728.

28.	Choi, J. W.; Kim, M.; Safron, N. S.; Han, E.; Arnold, M. S.; Gopalan, P., A facile route for fabricating graphene nanoribbon array transistors using graphoepitaxy of a symmetric block copolymer. In *Proc. of SPIE*, 2015; Vol. 9428, pp 94280T-94280T-10.

29.	Liang, X.; Wi, S. *ACS Nano* **2012,** 6, (11), 9700-9710.

30.	Kim, B. H.; Kim, J. Y.; Jeong, S.-J.; Hwang, J. O.; Lee, D. H.; Shin, D. O.; Choi, S.-Y.; Kim, S. O. *ACS Nano* **2010,** 4, (9), 5464-5470.

31.	Park, S.; Yun, J. M.; Maiti, U. N.; Moon, H.-S.; Jin, H. M.; Kim, S. O. *Nanotechnology* **2014,** 25, (1), 014008.

32.	Bates, F. S.; Fredrickson, G. H. *Phys. Today* **1999,** 52, (2), 32-38.

33.	Jeong, S.-J.; Moon, H.-S.; Kim, B. H.; Kim, J. Y.; Yu, J.; Lee, S.; Lee, M. G.; Choi, H.; Kim, S. O. *ACS Nano* **2010,** 4, (9), 5181-5186.

34.	Mansky, P.; Liu, Y.; Huang, E.; Russell, T. P.; Hawker, C. *Science* **1997,** 275, (5305), 1458-1460.

35.	Bates, C. M.; Strahan, J. R.; Santos, L. J.; Mueller, B. K.; Bamgbade, B. O.; Lee, J. A.; Katzenstein, J. M.; Ellison, C. J.; Willson, C. G. *Langmuir* **2011,** 27, (5), 2000-2006.

36.	Han, E.; Stuen, K. O.; Leolukman, M.; Liu, C.-C.; Nealey, P. F.; Gopalan, P. *Macromolecules* **2009,** 42, (13), 4896-4901.

37.	Rafiee, J.; Mi, X.; Gullapalli, H.; Thomas, A. V.; Yavari, F.; Shi, Y.; Ajayan, P. M.; Koratkar, N. A. *Nat. Mater.* **2012,** 11, (3), 217-222.

38.   Shih, C.-J.; Wang, Q. H.; Lin, S.; Park, K.-C.; Jin, Z.; Strano, M. S.; Blankschtein, D. *Phys. Rev. Lett.* **2012,** 109, (17), 176101.

39.   Wu, M.-L.; Wang, D. *RSC Adv.* **2016,** 6, (9), 7527-7531.

40.   Stein, G. E.; Mahadevapuram, N.; Mitra, I. *J. Polym. Sci., Part B: Polym. Phys.* **2015,** 53, (2), 96-102.

41.   Liu, C.-C.; Ramírez-Hernández, A.; Han, E.; Craig, G. S. W.; Tada, Y.; Yoshida, H.; Kang, H.; Ji, S.; Gopalan, P.; de Pablo, J. J.; Nealey, P. F. *Macromolecules* **2013,** 46, (4), 1415-1424.

42.   Farmer, D. B.; Rodrigo, D.; Low, T.; Avouris, P. *Nano Lett.* **2015,** 15, (4), 2582-2587.

43.   Chen, Y.-C.; Cao, T.; Chen, C.; Pedramrazi, Z.; Haberer, D.; de Oteyza, D. G.; Fischer, F. R.; Louie, S. G.; Crommie, M. F. *Nat. Nanotechnol.* **2015,** 10, (2), 156-160.

44.   Li, X.; Cai, W.; An, J.; Kim, S.; Nah, J.; Yang, D.; Piner, R.; Velamakanni, A.; Jung, I.; Tutuc, E.; Banerjee, S. K.; Colombo, L.; Ruoff, R. S. *Science* **2009,** 324, (5932), 1312-1314.

45.   Maher, M. J.; Bates, C. M.; Blachut, G.; Sirard, S.; Self, J. L.; Carlson, M. C.; Dean, L. M.; Cushen, J. D.; Durand, W. J.; Hayes, C. O.; Ellison, C. J.; Willson, C. G. *Chem. Mater.* **2014,** 26, (3), 1471-1479.

46.   Li, X.; Zhu, Y.; Cai, W.; Borysiak, M.; Han, B.; Chen, D.; Piner, R. D.; Colombo, L.; Ruoff, R. S. *Nano Letters* **2009,** 9, (12), 4359-4363.

47.   Suk, J. W.; Kitt, A.; Magnuson, C. W.; Hao, Y.; Ahmed, S.; An, J.; Swan, A. K.; Goldberg, B. B.; Ruoff, R. S. *ACS Nano* **2011,** 5, (9), 6916-6924.

48.   Shin, Y. J.; Wang, Y.; Huang, H.; Kalon, G.; Wee, A. T. S.; Shen, Z.; Bhatia, C. S.; Yang, H. *Langmuir* **2010,** 26, (6), 3798-3802.

49.   Wan, L.; Ruiz, R.; Gao, H.; Patel, K. C.; Albrecht, T. R.; Yin, J.; Kim, J.; Cao, Y.; Lin, G. *ACS Nano* **2015,** 9, (7), 7506-14.

50.   Shelton, C. K.; Epps, T. H. *Macromolecules* **2015,** 48, (13), 4572-4580.

51.   Owens, D. K.; Wendt, R. C. *J. Appl. Polym. Sci.* **1969,** 13, (8), 1741-1747.

52.   Kozbial, A.; Li, Z.; Conaway, C.; McGinley, R.; Dhingra, S.; Vahdat, V.; Zhou, F.; D'Urso, B.; Liu, H.; Li, L. *Langmuir* **2014,** 30, (28), 8598-8606.

53.   Korhonen, J. T.; Huhtamäki, T.; Ikkala, O.; Ras, R. H. A. *Langmuir* **2013,** 29, (12), 3858-3863.

54.   Tadmor, R. *Langmuir* **2004,** 20, (18), 7659-7664.

55.   Wenzel, R. N. *Ind. Eng. Chem. Res.* **1936,** 28, (8), 988-994.

56.   Rafiee, J.; Rafiee, M. A.; Yu, Z.-Z.; Koratkar, N. *Adv. Mater.* **2010,** 22, (19), 2151-2154.

57.   Li, Z.; Wang, Y.; Kozbial, A.; Shenoy, G.; Zhou, F.; McGinley, R.; Ireland, P.; Morganstein, B.; Kunkel, A.; Surwade, S. P.; Li, L.; Liu, H. *Nat. Mater.* **2013,** 12, (10), 925-931.

58.   Ferrari, A. C.; Meyer, J. C.; Scardaci, V.; Casiraghi, C.; Lazzeri, M.; Mauri, F.; Piscanec, S.; Jiang, D.; Novoselov, K. S.; Roth, S.; Geim, A. K. *Phys. Rev. Lett.* **2006,** 97, (18), 187401.

Chapter 8: Controlling the surface energy of polymer bilayers for perpendicular orientation of block copolymer thin films

8.1 INTRODUCTION

In Chapter 7, wetting-transparency assisted block copolymer (BCP) lithography was demonstrated for graphene nanoribbon (GNR) fabrication. This methodology is based on control of surface energy *through* the graphene layer, which is atomically thin, and therefore, the so-called "wetting transparency of graphene"[1] was effective. However, the surface energy of graphene is also affected by surface roughness and the quality of the graphene layer (e.g. defects, the degree of oxidization, density and nature of wrinkles, etc.). These convoluted factors makes the BCP/graphene system undesirable for fundamental studies that require precise attention to controllable and easily characterized variables. As described in Chapter 5, non-preferential or neutral wetting of BCP microdomains is desired for promoting perpendicular domain orientations for lithographic purposes. Therefore, fundamentally understanding the effect of wetting transparency on BCP orientation more broadly has enormous potential to generalize this patterning technique to other 2D materials.[2]

To this end, we hypothesized that surface neutrality (or non-preferential wetting) could be achieved by controlling the thickness of an originally non-neutral bilayer substrate. A model system was designed to investigate BCP wetting behavior further using a bilayer substrate as shown in Figure 8.1 (a). In this study, a lamellae forming poly(styrene-block-methyl methacrylate) (PS-*b*-PMMA) was used as a model BCP. Homopolymer analogues (PS and PMMA) of the BCP are utilized as each layer of the bilayer substrate. As shown in Figure 8.1 (b), it is hypothesized that when the PS layer thickness (h_{PS}) is thin (PMMA preferential surface) or too thick (PS preferential surface), PS-*b*-PMMA microdomains would orient parallel to the substrate because of the

preferential wetting of one block with its corresponding homopolymer underlayer. In between those two thicknesses, there should be a PS thickness that induces non-preferential wetting of PS-*b*-PMMA atop the bilayer and the hypothesis is that this wetting transition should be a reflection of the distances over which interactions can exert influence (more on this later).

In the bilayer system illustrated in Figure 8.1, the PS layer thickness should be very thin in order to achieve wetting transparency of the PS layer. However, often times, fabricating such thin, continuous polymer layers is non-trivial even with a simple spincoating approach due to spontaneous dewetting of the thin layer. To address this issue, cross-linkable PS and PMMA homopolymers are used in this study. With these polymers, relatively thick (20 nm) polymer films can be spincoated, and the thickness can be tailored by controlling the gel fraction of each layer. After the cross-linking process, a good solvent could be used to remove the sol fraction and achieve a prescribed thickness. With this approach, sufficiently thin and continuous layers of polymers were fabricated without dewetting.

In order to gain physical insight into the wetting transparency, we estimated the free energy and van der Waals (vdW) potential of a BCP thin film on the bilayer substrate. Both calculations were correlated with the experimentally observed BCP morphology/domain orientation on the bilayer substrates. This work not only provides evidence of the physical mechanism of wetting transparency of polymer films, but also could also potentially yield a new route to perpendicularly oriented BCP microdomains. These bilayers composed of two homopolymers can be prepared without synthesis of a specifically tailored surface neutralization treatment (SNT) layer, which can be a time consuming and expensive step as described in Chapter 5.[3]

134
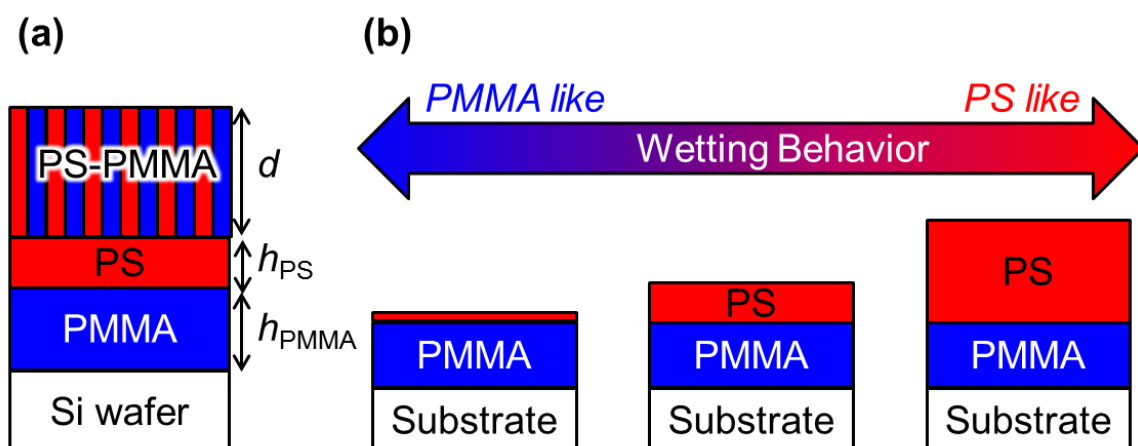
Figure 8.1: (a) The model bilayer system used in this study.   (b) The general concept of this study where the block copolymer (BCP) wetting behavior on bilayer substrates is expected to vary with different thicknesses of PS (h_{PS}).

8.2   EXPERIMENTAL

8.2.1   Materials

Chemicals used in this study were purchased from Fisher Scientific or Sigma-Aldrich and used as received unless otherwise noted.   PS (M_n = 43 kg/mol, Đ = 1.07) was synthesized by activators regenerated by electron transfer atom transfer radical polymerization (ARGET-ATRP) following an established procedure.[4]   As the first layer of the bilayer substrate, PMMA containing 5 mol% of 4-vinylbenzyl azide (PMMA-azide) was synthesized by conventional free radical polymerization as described in previous work.[5]   The azide mol% was determined using [1]H-nuclear magnetic resonance spectroscopy (Varian Unity Plus 400MHz).   Omnipol BP (Bis-benzophenone: BB) was used as a photo-crosslinker and was provided by IGM Resins.   A lamellae forming PS-*b*-PMMA (M_n for PS: 33 kg/mol, for PMMA: 33 kg/mol, Đ = 1.16) was purchased from Polymer Source Inc. and used as received.

135

8.2.2 Film preparation

A schematic that describes the bilayer system under investigation is shown in Figure 8.1 (a).   First, PMMA-azide thin films with a uniform thickness ($h_{PMMA} \sim$ 20 nm) were spin-coated (Specialty Coating Systems Spincoat G3-8) from toluene onto clean silicon wafers, and then thermally crosslinked.   Upon heating at 250°C for 5 min, highly reactive nitrene intermediates are generated from the azide groups in PMMA-azide, which form covalent adducts and cross-link PMMA.[6]   Then, the crosslinked PMMA was rinsed with toluene to remove soluble materials, followed by heating at 120 °C for 5 mins.   Subsequently, PS and BB (5 wt% relative to PS weight) were co-casted atop the crosslinked PMMA, and then also crosslinked, but by broadband light exposure (Optical Building Blocks Scopelite 200).   BB possesses two benzophenone end groups on each side of the linear molecule, which form covalent adducts and crosslink adjacent polymer chains upon 254 nm UV exposure.[7, 8]   The typical intensity for exposure at a distance of 20 mm was measured to be 700 mW/cm^2 using a radiometer (Fieldmax TO, Coherent, Inc.).   The thickness of the PS layer (2-8 nm) was controlled by both the initial film thickness and the exposure dose.   The un-crosslinked PS and other soluble components were removed with toluene.   More detailed studies on the relationship between photo-conversion of BB and the film gel fraction using an analogous photo-crosslinker can be found elsewhere.[7]   Lastly, the PS-*b*-PMMA films were spincoated on top of prepared bilayer substrates.   In this system, the thickness of the BCP (*d*) was varied from 20 - 80 nm, corresponding to $0.5L_0$ - $2.0L_0$.   The samples were annealed at 180°C for 1 hour under vacuum to induce BCP self-assembly.

8.2.3 Characterization

The thickness of films prepared on silicon substrates was characterized by ellipsometry using a J.A. Woollam M-2000D spectroscopic ellipsometer.   Atomic force

microscopy in tapping mode (AFM, Asylum Research MFP-3D Origin) was used to characterize the orientations of BCP microdomains.   The silicon tips used had a radius of 9 ± 2 nm with a resonance frequency of 300 kHz and were purchased from Asylum Research.   Each scan had 1024 points/line and 1024 lines, and the scan rate was 3 μm/s. A scanning electron microscope (SEM, Hitachi 4500) was used for top-down imaging of the BCP films.   Prior to imaging, the samples were O_2 etched (Harrick PDC-VP) for 45 sec to etch PMMA blocks selectively for contrast.   The periodicity of the lamellae structure (L_0) is 40 nm determined by Fourier transform of the SEM images.
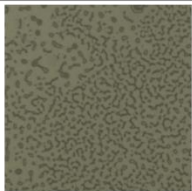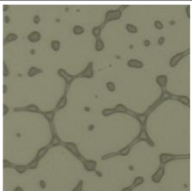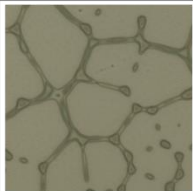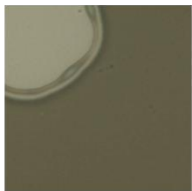
8.3   PRELIMINARY RESULTS

8.3.1   Microdomain orientation of block copolymer

The bilayer substrates with a given PS thickness ($h_{PS} = 0$ and 3 nm) and a constant PMMA thickness ($h_{PMMA} \sim 20$ nm) were prepared on a silicon wafer as described in the experimental section.   A PS-*b*-PMMA film, with different thicknesses, *d*, was spin-coated on top of the bilayer substrates.   Representative optical micrographs for $h_{PS} = 0$ and 3 nm are shown in Figure 8.2.   For a sample with $h_{PS} = 0$ nm, i.e. a PMMA substrate, different topological features of PS-*b*-PMMA were observed.   The topology shown for both $d = 52$ and 72 nm on a substrate with $h_{PS} = 0$ nm is the well-known "hole" structure, which is documented in the literature for PS-*b*-PMMA on top of PMMA substrates.[9, 10]   In contrast, the PS-*b*-PMMA on top of $h_{PS} = 3$ nm bilayer substrates were uniform for all *d*.   These contrasting behaviors, which apparently depended on h_{PS}, indicate that the PS layer, even only 3 nm thick, can drastically change the wetting behavior of the PS-*b*-PMMA.   In the other PS thicknesses ($h_{PS} = 3$, 6, and 8 nm), neither hole/island structures nor dewetting was observed.

137

(a)

d [nm]	$21 \sim 0.50 L_0$	$31 \sim 0.75 L_0$	$40 \sim 1.0 L_0$	$52 \sim 1.25 L_0$
$h_{PS} = 0$ nm	Dewetting	Dewetting	Dewetting	Hole

d [nm]	$61 \sim 1.5 L_0$	$72 \sim 1.75 L_0$	$79 \sim 2.0 L_0$	
$h_{PS} = 0$ nm		Hole		

(b)
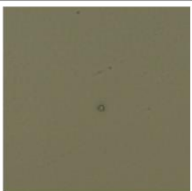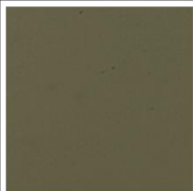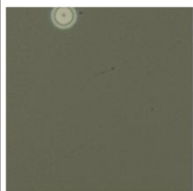
d [nm]	$22 \sim 0.50 L_0$	$30 \sim 0.75 L_0$	$40 \sim 1.0 L_0$	$48 \sim 1.25 L_0$
$h_{PS} = 3$ nm				

d [nm]	$62 \sim 1.5 L_0$	$69 \sim 1.75 L_0$	$79 \sim 2.0 L_0$	
$h_{PS} = 3$ nm				

Figure 8.2:   Representative optical microscope images of d nm-thick PS-b-PMMA films on two bilayer substrates: (a) $h_{PS} = 0$ nm, $h_{PMMA} = 20$ nm and (b) $h_{PS} = 3$ nm, $h_{PMMA} = 20$ nm.   The width of each image is 50 μm.

In order to study the orientation of the BCP microdomains, AFM phase image analysis was conducted as shown in Figure 8.3. For this analysis, samples with various PS thicknesses (h_{PS} = 0, 3, 6, and 8 nm) on top of h_{PMMA} = 20 nm were used. These AFM phase images highlight that the orientations of the BCP are drastically affected by changing h_{PS}. For the substrate with h_{PS} = 0 nm, i.e. a PMMA substrate, the perpendicular orientation of PS-*b*-PMMA was observed at d = 60 nm (1.5L_0), which is consistent with previous studies.[10] In contrast, as h_{PS} increases, the range of d which show the perpendicular orientation of the PS-*b*-PMMA becomes wider. In particular, for the system with h_{PS} = 6 nm, a perpendicular orientation was observed over the widest range of d (20, 30, 50,60, and 70 nm). Above and below h_{PS} = 6 nm, the "window" of d for perpendicular orientation becomes smaller. Thus, the perpendicular orientation of PS-*b*-PMMA on bilayer substrates was achieved, but the formation of the perpendicular orientation also depended on d and h_{PS}.

h_{PS}\d	0.5 L_0 20 nm	0.75 L_0 30 nm	1.0 L_0 40 nm	1.25 L_0 50 nm	1.5 L_0 60 nm	1.75 L_0 70 nm	2.0 L_0 80 nm
0 nm	Dewetting	Dewetting	Dewetting				
3 nm							
6 nm							
7-8 nm							
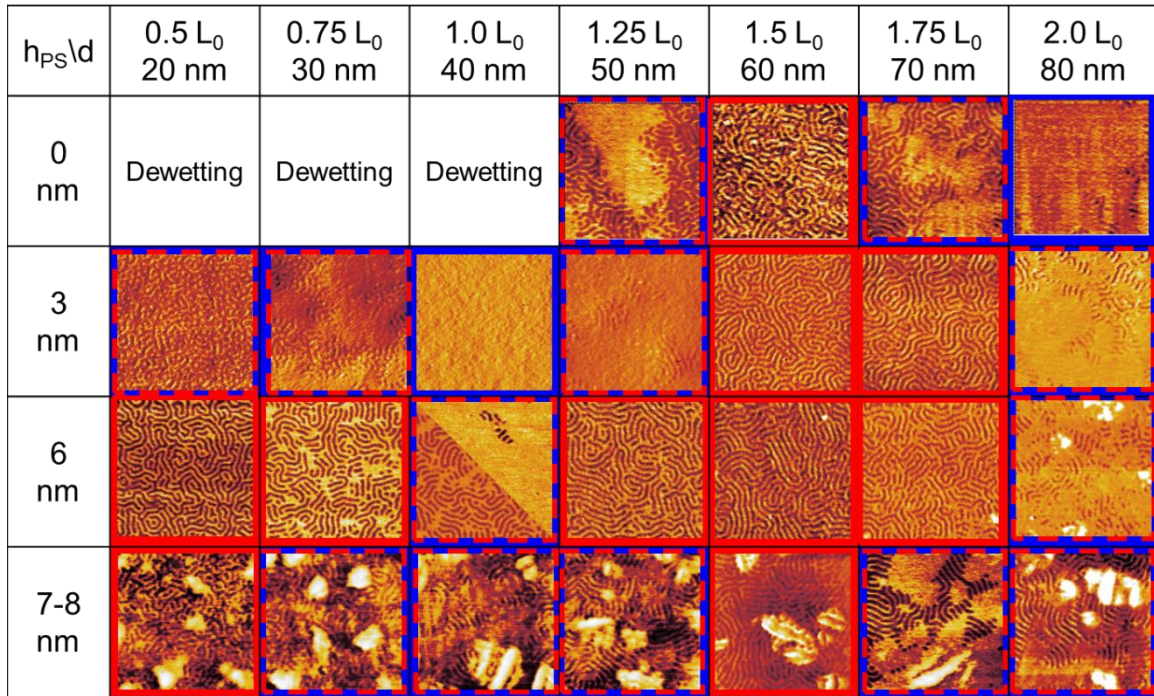
Figure 8.3: Atomic force microscope (AFM) phase images of microdomain orientation of *d* nm-thick PS-*b*-PMMA on bilayer substrates with h_{PS} = 0, 3, 6, 7-8 nm and h_{PMMA} = 20 nm. The width of each image is 1 μm, and the red and blue squares indicate perpendicular and parallel orientations of BCP, respectively.

8.3.2 Surface energy calculations for the bilayer substrates

To understand the mechanism behind the domain orientation dependence on BCP layer thickness, the next phase of this study was to compare the experimental results to free energy predictions. A free energy analysis was adapted from literature[11] that takes entropic penalties of BCP upon confinement into account. Using this method, the BCP domain orientation between air and either PS or PMMA rich substrates can be predicted as a function of *d* by estimating the differences in the thin-film free energies of the possible orientations (perpendicular or parallel to the substrate). Free energies of PS-*b*-PMMA thin films confined between dissimilar interfaces (air and substrate) were calculated as reported by Walton *et al.* [11] For this study, a symmetric AB diblock

copolymer is modeled using PS and PMMA constituents and these relationships are expressed as follows (Eq. 8.1 to 8.2):

$$\frac{F_h}{F_{bulk}} = \frac{1}{3}\left\{ \lambda^2 + \frac{2}{\lambda^2} + \frac{1}{m\lambda}\left[\Gamma_1 + \Gamma_2 + \delta_1\left(\frac{1 - 1(-1)^{2m}}{2} \right) \right] \right\} \tag{8.1}$$

$$\frac{F_v}{F_{bulk}} = \frac{1}{3}\left\{ 3 + \frac{1}{m\lambda}\left[\left(\Gamma_1 + \frac{\delta_1}{2} \right) + \left(\Gamma_2 + \frac{\delta_2}{2} \right) \right] \right\} \tag{8.2}$$

where the free energies, F, are normalized by the bulk values, F_{bulk}, and subscripts h and v correspond the horizontal and vertical orientation, respectively. The material parameters are defined as $\Gamma_1 = \gamma_{PS/Air}/\gamma_{PS/PMMA}$, $\Gamma_2 = \gamma_{PS/sub}/\gamma_{PS/PMMA}$, $\delta_1 = (\gamma_{Air/PMMA} - \gamma_{Air/PS})/\gamma_{PS/PMMA}$ and $\delta_2 = (\gamma_{PMMA/sub} - \gamma_{PS/sub})/\gamma_{PS/PMMA} \approx 2\phi_{PS} - 1$ where 'sub' indicates substrate. The surface energies and interfacial energies at 180°C were adapted from literature as $\gamma_{PS/Air} = 30.1$ dyne/cm, $\gamma_{PMMA/Air} = 29.6$ dyne/cm, and $\gamma_{PS/PMMA} = 1.30$ dyne/cm.[12] These interfacial energy parameters are calculated for the PS-rich substrate ($\phi_{PS} = 0.9$) and the PMMA rich substrate ($\phi_{PS} = 0.1$). Here, $\phi_{PS} = 0.9$ was chosen to mimic the condition of a PS-rich substrate, because varying ϕ_{PS} from 0.80 to 0.99 did not alter the d values that give perpendicular orientation of BCP domains. The values used as input for this estimation are summarized in Table 8.1 at the temperatures considered. Note that $m = n+1/2$ for a PS rich substrate and $m = n$ for a PMMA rich substrate in Eq. 8.1.[11]

	Γ_1	Γ_2	δ_1	δ_2
PS rich ($\phi_{PS} = 0.9$)	23.1	0	-0.351	22.7
PMMA rich ($\phi_{PS} = 0.1$)	23.1	1	-0.351	-23.1

Table 8.1: Interfacial energy parameters used in this study.

141

The normalized BCP thin film free energies (F/F_{bulk}) are plotted as a function of reduced thickness (d/L_0) and shown in Figure 8.4. Note that this plot assumes the BCP is directly coated on homopolymer-rich substrates instead of a bilayer substrate. The perpendicular orientation of the BCP is only energetically favorable when $F_{parallel} > F_{perpendicular}$. On a PS rich substrate (Figure 8.4 (a)), the BCP prefers to orient perpendicularly only when $d = nL_0$, while the BCP with $d = (n+0.5)L_0$ prefers a perpendicular orientation on PMMA rich substrates (Figure 8.4 (b)), where n represents an integer. This result agrees with observations in Figure 8.3, which shows the perpendicular orientation at $d = 1.5L_0$ for PMMA ($h_{PS} = 0$ nm) substrate. However, this calculation cannot explain the microdomain orientations for other PS thicknesses. Since a perpendicular orientation of PS-b-PMMA atop the bilayer substrate was experimentally observed for a broad range of d, it can be concluded that the BCP wetting behavior on the bilayer substrate deviated from the wetting behavior of either homopolymer substrate. Consequently, the bilayer substrate with 3-8 nm of PS thickness effectively yielded wetting transparency from the PMMA underlayer. Also, this result suggests that the wetting behavior of PS-b-PMMA for $h_{PS} = 7-8$ nm is still not identical to that of a PS substrate.
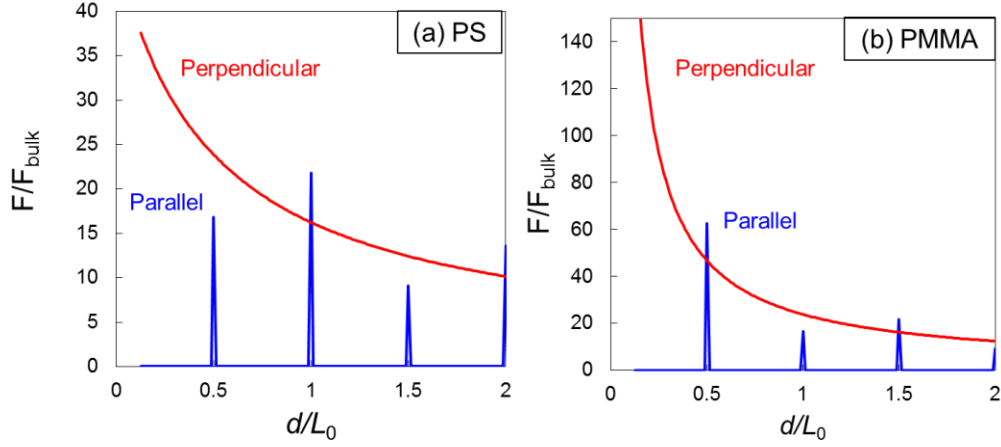
Figure 8.4: Estimated free energies of a BCP layer on (a) PS-rich and (b) PMMA-rich substrates as a function of d/L_0.

Predicting interfacial energy in a multi-layer system is often very challenging. However, we simplified the system by assuming that the vdW force is the dominating factor for prediction of the interfacial energy. The vdW potential for the bilayer substrate was estimated using Eq. 8.3 in order to gain further insight into the interfacial energies between PS-*b*-PMMA and the bilayer substrate. For this estimation, the contribution of short-range interactions was neglected since these effects only become relevant at length scales of *d* much smaller than those of interest here.[13]

$$\Phi(h_{PS})_{vdW} = -\frac{A_{PS-PMMA/PS}}{12\pi d^2} + \frac{A_{PS-PMMA/PS} - A_{PS-PMMA/PMMA}}{12\pi(d + h_{PS})^2}$$

(8.3)

$A_{PS-PMMA/PS}$ and $A_{PS-PMMA/PMMA}$ are the Hamaker constants of PS-*b*-PMMA on PS and PMMA substrates, respectively. These constants were estimated using Eq. 8.4 along with literature values for dielectric constants (ε) and refractive indices (*n*) of the materials in Table 8.2, assuming that the vdW forces are spatially uniform.[14] Here, material 3 is air, and 1 and 2 are neighboring materials such as PS-*b*-PMMA and PS or PMMA. The parameters *k*, *h*, and *T* are the Boltzmann constant, Plank constant, and

143

temperature (= 180°C), respectively. In visible and UV light, ν_e is 3×10^{-15} sec^{-1}.[14] Based on the calculations, $A_{\text{PS-PMMA/PS}}$ and $A_{\text{PS-PMMA/PMMA}}$ were estimated as 8.2×10^{-20} J and 7.0×10^{-20} J, respectively.

$$A_{12} \approx \frac{3}{4} kT \left(\frac{\varepsilon_1 - \varepsilon_3}{\varepsilon_1 + \varepsilon_3} \right) \left(\frac{\varepsilon_2 - \varepsilon_3}{\varepsilon_2 + \varepsilon_3} \right)$$

$$+ \frac{3h\nu_e}{8\sqrt{2}} \frac{\left(n_1^2 - n_3^3\right)\left(n_2^2 - n_3^2\right)}{\left(n_1^2 + n_3^2\right)^{1/2}\left(n_2^2 + n_3^2\right)^{1/2}\left\{\left(n_1^2 + n_3^2\right)^{1/2} + \left(n_2^2 + n_3^2\right)^{1/2}\right\}} \tag{8.4}$$

	Air	PS	PMMA	PS-b-PMMA
n	1	1.582	1.482	1.51
ε [1/sec]	1	2.5	3.6	3.6

Table 8.2: Refractive indices (n) and dielectric constants (ε) and used in this study.

By substituting the calculated Hamaker constants into Eq. 8.3, the vdW potential of the BCP (Φ) on top of the bilayer system was predicted. Figure 8.5 shows Φ as a function of h_{PS} for PS-b-PMMA thickness of $d = 20 - 80$ nm. The symbols correspond to the orientation of the BCP based on the AFM phase images presented in Figure 8.3. The change of $\Phi(d, h_{\text{PS}})$ with h_{PS} is more dramatic as d decreases, meaning that the interfacial energy is less sensitive to h_{PS} for larger d. This trend can also be observed in Figure 8.5: the symbols based on the AFM observations are mostly consistent for all h_{PS} as d increases to its largest values.

144
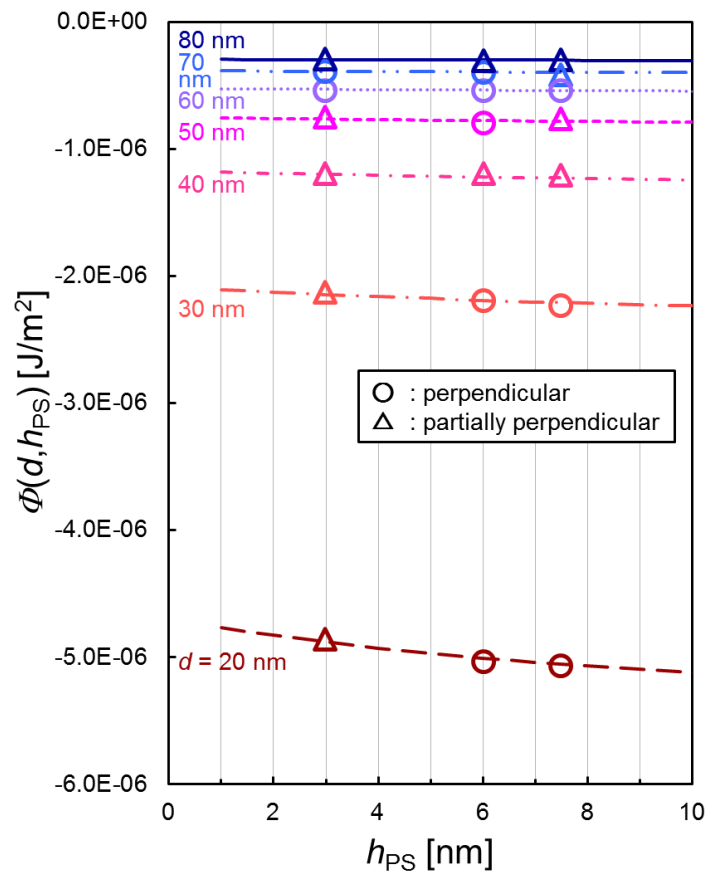
Figure 8.5: The vdW potential (Φ) as a function of PS thickness (h_{PS}) and PS-b-PMMA thickness (d). The symbols represent the microdomain orientation of PS-b-PMMA observed using phase images of AFM.

This calculation can be practically useful to estimate pairs of d and h_{PS}, which induce perpendicularly oriented BCP on a bilayer substrate. It should also be noted that, since the entropy contribution was ignored, the expression may have some limitations. For example, the perpendicular orientation of the BCP can be entropically prohibited even if the expression predicted "neutral." However, this simple estimation can serve as a useful initial step toward understanding how the long range vdW potentials and free energies affect the wetting behavior of BCPs *through* ultrathin polymer layers.

8.4   CONCLUSIONS

In this study, we have successfully prepared a PS/PMMA bilayer substrates and systematically varied the BCP thickness, d, at various h_{PS} and fixed h_{PMMA} to investigate how the PS thickness affects the BCP orientation on a bilayer substrate.   A lithographically useful perpendicular orientation of the BCP microdomains on a bilayer substrate was observed for specific pairs of h_{PS} and d.   This unique BCP wetting behavior was clearly different from those on PS and PMMA rich substrates, as confirmed by comparing experimental observations with calculated thin film free energies. Finally, the vdW potential calculations agreed well with experimental observations of the BCP orientation, indicating that this simple estimation could be a useful guide to design bilayer substrates.   From these observations, we demonstrated that the thin PS layer exhibits wetting transparency, and it significantly altered the orientation of BCP microdomains.

8.5   FUTURE WORK

8.5.1   Characterization of bilayer substrates

Even though we carefully designed a PS/PMMA bilayer substrate, confirmation of the bilayer structure would reinforce our arguments.   For example, additional AFM examination of the surface of the bilayer would be helpful to prove uniformity of the bilayer substrates.   We would also expect to see a typical wetting behavior of PS-*b*-PMMA on a PMMA substrate with a thick (~20 nm) cross-linked PS substrate based on an assumption that the PS substrate is chemically and physically uniform.

8.5.2   Cross-sectional structure of BCP microdomains

The perpendicular orientation of the lamellar structure of PS-*b*-PMMA was observed by AFM phase images and top-view SEM.   However, occasionally

perpendicular orientations are observed on the surface, while microdomains are oriented parallel nearer to the substrate depending on interfacial interactions.[15]   Additional cross-sectional SEM observations would confirm whether the structure of the BCP in this study is perpendicular throughout the entire cross section.

8.5.3   Experimental approach for estimation of the vdW potential

In Section 8.3.2, we showed that the vdW potential at the interface between a BCP and a bilayer substrate was affected by thin PS layers.   To confirm the changes in the vdW potential with varying thicknesses of PS layers, force curve experiments using AFM could be effective.   The experiment setup will be similar to existing studies on PMMA grafted substrates in the literature,[16] but an AFM tip grafted by PS-*random*-PMMA with a ratio of PS:PMMA =1:1 would be more representative of our system.

8.6   ACKNOWLEDGEMENTS

8.7   REFERENCES

1.   Rafiee, J.; Mi, X.; Gullapalli, H.; Thomas, A. V.; Yavari, F.; Shi, Y.; Ajayan, P. M.; Koratkar, N. A. *Nat. Mater.* **2012,** 11, (3), 217-222.
2.   Akinwande, D.; Petrone, N.; Hone, J. *Nat. Commun.* **2014,** 5, 5678.
3.   Kim, S.; Wang, H. S.; Choe, Y.; Choi, S.-H.; Bang, J. *Polym. J.* **2016,** 48, (4), 333-340.

4.   Katzenstein, J. M.; Janes, D. W.; Cushen, J. D.; Hira, N. B.; McGuffin, D. L.; Prisco, N. a.; Ellison, C. J. *ACS Macro Lett.* **2012,** 1, (10), 1150-1154.

5.   Bates, C. M.; Strahan, J. R.; Santos, L. J.; Mueller, B. K.; Bamgbade, B. O.; Lee, J. A.; Katzenstein, J. M.; Ellison, C. J.; Willson, C. G. *Langmuir* **2011,** 27, (5), 2000-2006.

6.   Janes, D. W.; Maher, M. J.; Carroll, G. T.; Saylor, D. M.; Ellison, C. J. *Macromolecules* **2015,** 48, (22), 8361-8368.

7.   Carroll, G. T.; Sojka, M. E.; Lei, X.; Turro, N. J.; Koberstein, J. T. *Langmuir* **2006,** 22, (18), 7748-7754.

8.   Katzenstein, J. M.; Kim, C. B.; Prisco, N. A.; Katsumata, R.; Li, Z.; Janes, D. W.; Blachut, G.; Ellison, C. J. *Macromolecules* **2014,** 47, (19), 6804-6812.

9.   Bassereau, P.; Brodbreck, D.; Russell, T. P.; Brown, H. R.; Shull, K. R. *Phys. Rev. Lett.* **1993,** 71, (11), 1716-1719.

10.   Russell, T. P.; Coulon, G.; Deline, V. R.; Miller, D. C. *Macromolecules* **1989,** 22, (12), 4600-4606.

11.   Walton, D. G.; Kellogg, G. J.; Mayes, A. M.; Lambooy, P.; Russell, T. P. *Macromolecules* **1994,** 27, (21), 6225-6228.

12.   Wu, S. *J. Phys. Chem. A* **1970,** 74, (3), 632-638.

13.   Seemann, R.; Herminghaus, S.; Neto, C.; Schlagowski, S.; Podzimek, D.; Konrad, R.; Mantz, H.; Jacobs, K. *J. Phys. Condens. Matter* **2005,** 17, (9), S267-S290.

14.   Israelachvili, J. N., Chapter 14 - Electrostatic Forces between Surfaces in Liquids. In *Intermolecular and Surface Forces (Third Edition)*, Israelachvili, J. N., Ed. Academic Press: San Diego, 2011; pp 291-340.

15.   Liu, G.; Detcheverry, F.; Ramírez-Hernández, A.; Yoshida, H.; Tada, Y.; de Pablo, J. J.; Nealey, P. F. *Macromolecules* **2012,** 45, (9), 3986-3992.

16.   Yamamoto, S.; Ejaz, M.; Tsujii, Y.; Matsumoto, M.; Fukuda, T. *Macromolecules* **2000,** 33, (15), 5602-5607.

Appendices

APPENDIX A: GLASS TRANSITION TEMPERATURE, SELF-DIFFUSION COEFFICIENT, AND EFFECTIVE VISCOSITY OF POLYMER THIN FILMS

A.1   Glass transition temperature measurements using ellipsometry

A spectroscopic ellipsometer (J.A. Woollam M-2000D) was used for the measurement.   The Cauchy model was employed to fit the film thickness and the A, B, C parameters as defined in the manual of the ellipsometer in the wavelength range of 400-900 nm.   The thickness of the specimen film was measured on cooling from 120 to -10°C at a cooling rate of 2°C/min.   The measurement took place in a custom-made chamber purged with argon gas to avoid water condensation.   The T_g was the point where the slope of thickness versus temperature plot changes qualitatively.   We determined the T_g by fitting the data of such a plot to the following hyperbolic tangent type function:[1]

$$h(T) = w\left(\frac{M-G}{2}\right)\ln\left[\cosh\left(\frac{T-T_g}{w}\right)\right] + \left(T-T_g\right)\left(\frac{M+G}{2}\right) + c \qquad (A.1)$$

where c is the value of the film thickness at $T = T_g$, and w is the width of the transition between the rubbery and glassy states.   In this study, the value of w was restricted to be smaller than 35°C considering the temperature range of the T_g measurement. M and G correspond to the thermal coefficients of expansion of the rubbery and glassy state, respectively.

A.2   Bulk zero-shear viscosity measurement

The zero-shear viscosity, η, of PiBMA was measured with a TA Instruments AR2000 rheometer in a parallel-plate geometry, where the shear rate was varied from 10^{-3} to 10^{-1} s^{-1}.   Figure A.2 displays the zero-shear viscosity as a function of temperature. We fit the data to the Williams-Landel-Ferry (WLF) equation:

149

$$\eta = \eta_0 \exp\left[-\frac{c_1(T-T_r)}{c_2+(T-T_r)}\right] \tag{A.2}$$

assuming the reference temperature, T_r, to be 85°C, whereat the zero-shear viscosity was $\eta_0 = 2.17\times10^6$ Pa·s. From the fits, we determined that $c_1 = 11.3$, $c_2 = 42.6$°C. The best fit line is shown by the solid line in Figure A.1.

Figure A.1:   Zero-shear viscosity as a function of temperature measured by a TA Instruments AR2000 rheometer (circles).   The solid line represents the best fit to the WLF equation (Eq. A.2).

A.3   Thin film effective viscosity measurements

The effective viscosity of a film was determined by studying how the power spectral density (PSD) evolved with annealing time, t, at the measurement temperature, T. To obtain the PSD, we first measured the surface topography of the film by using tapping-mode atomic force microscopy (AFM).   Then each set of topographic data was converted to its PSD by multiplying the data with a Welch function then Fourier-transforming it.[2-5]   Afterward, the Fourier spectrum was radial averaged to produce the

PSD.   It is important to mention that we limited the annealing times to within the initial roughening stage, where the film roughness was less than 10% of the average film thickness, and no holes were detectable by AFM. These steps ensured that linear analysis was applicable.   Figure A.2 displays the effective viscosity η_{eff} obtained from thick films of PiBMA/SiO$_x$ (h_0 = 120nm) plotted versus temperature.   The solid line in the same graph denotes the zero-shear viscosity measurement of the bulk polymer reported above. Good agreement between different measurements is apparent.
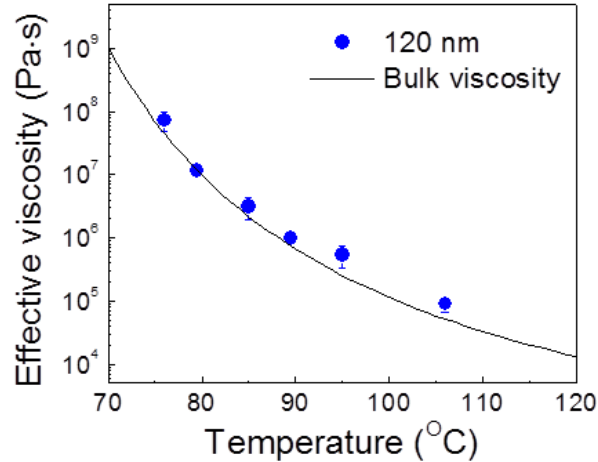
Figure A.2:   Illustration of the η_{eff} of thick films (h_0 = 120nm) of PiBMA/SiO$_x$ measured by AFM (circles).   The solid line denotes the best WLF fit to the bulk viscosity measured by a rheometer.

A.4   Determination of the Hamaker constant of the PiBMA/SiO$_x$ films

After we acquired a series of PSD curves at various t, the effective viscosity η_{eff} was determined by fitting the PSD series to Eq. 3.1 in Chapter 3, which is reproduced below:

$$A_q^2(t) = A_q^2(0)\exp(2\Gamma t) + \left[\frac{k_B T}{d^2 G(h_0)/dh^2 + \gamma q^2}\right](1-\exp(2\Gamma t))$$

(A.3)

where

$$\Gamma(\boldsymbol{q}) = -M_{\text{tot}}\left[(d^2 G(h_0)/dh^2)q^2 + \gamma q^4\right]$$

(A.4)

and $M_{\text{tot}} \equiv h_0^3/(3\eta_{\text{eff}})$. The other parameters, namely t, T, h_0, $G(h_0)$ and γ, were fixed as follows. The time t, temperature T and film thickness h_0, were set equal to the experimental values. The surface tension γ was determined by fitting the high-q portion of the PSDs to the expression $\lim\limits_{q\to\infty} A_q^2(t) = \dfrac{k_B T}{\gamma q^2}$. Physically, it means that the amplitude of the capillary wave modes with high q's had reached equilibrium when the experimental time was sufficiently longer than the relaxation time (= $1/\Gamma(q)$) of the mode.[6] The fitted values of γ typically lie between 0.03 and 0.05 N/m, which are consistent with published values.[7] As for the van der Waals potential, $G(h_0)$, we expressed it in the usual form: [8]

$$G(h_0) = -\frac{A_{\text{Ham}}}{12\pi h_0^2}$$

(A.4)

where A_{HAM} is the Hamaker constant and generally varies with h_0. To determine A_{HAM} of the PiBMA/SiO$_2$ system, we optimized the PSD fits at several different thicknesses by co-varying the values of η_{eff} and A_{HAM}. Specifically, the optimization was achieved by minimizing the mean-square percentage difference between the experimental and model values (Δ^2):

$$\Delta^2 = \frac{1}{n-1}\sum_{i=1}^{n}\frac{\left[A_q^2\left(t=t_i\right)_{theory} - A_q^2\left(t=t_i\right)_{expt}\right]^2}{A_q^2\left(t=t_i\right)_{theory}}$$

(A.5)

Figure A.3 shows plots of the Δ^2 parameter and η_{eff} versus A_{HAM} for PiBMA/SiO$_x$ films with $h_0 = 10$, 15 and 120 nm. From this figure, one sees that the optimized value

of A_{HAM}, is independent of the film thickness. In addition, thinner films are more sensitive to the value of A_{HAM} than thicker films. Based on this result, we adopt -1×10^{-19} J for the A_{HAM} of the PiBMA/SiO$_x$ films.
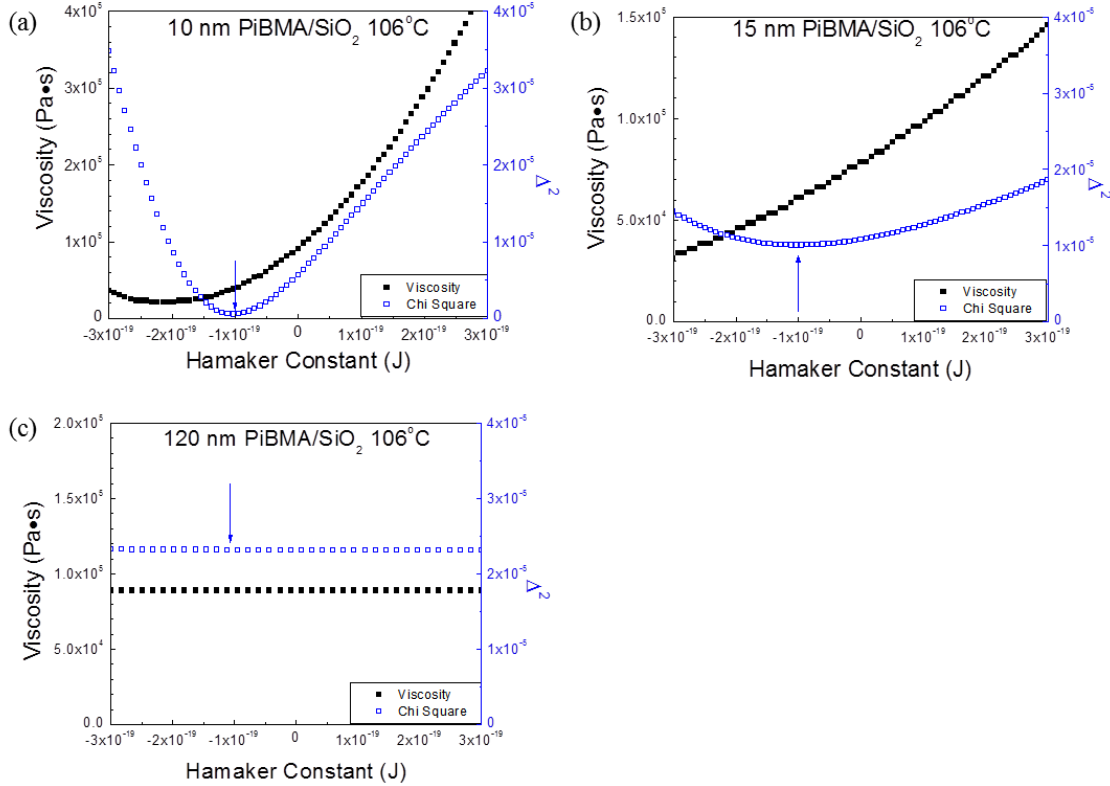
Figure A.3: Plots of the mean-square percentage difference Δ^2 (blue) and η_{eff} (black) versus Hamaker constant, A_{HAM}, assumed for the PiBMA films with $h_0 = $ (a) 10, (b) 15 and (c) 120 nm. In each plot, the arrow indicates the optimal Hamaker constant that minimizes Δ^2. The optimal Hamaker constants of all three films were found to be essentially the same, equal to $-(1 \pm 0.1) \times 10^{-19}$ J.

A.5 Adsorbed layer thickness measurements

The thickness of the irreversibly adsorbed layer of PiBMA was measured using a procedure detailed in a previous study.[9] A 120 nm thick PiBMA film (2.5 cm × 2.5 cm)

was spin-coated on a base-washed Si wafer with 1.5 nm thick native oxide, and annealed at 120 $^{\circ}$C for 20 min under vacuum.   This PiBMA film was then annealed at 106 $^{\circ}$C for 18 h under a slow argon purge to mimic the FRAPP measurement environment.   After the annealing, the film was placed on the spin-coater for 45 s at 3500 rpm where it was washed 5 times with tetrahydrofuran (THF), a good solvent for PiBMA.   The film was then soaked in 100 mL THF for 10 min to remove any remaining unattached PiBMA. After washing the surface with isopropanol and drying with filtered air, the thickness of the residual layer, or irreversibly adsorbed layer, was measured by a spectroscopic ellipsometer (J.A. Woollam M-2000D) using a wavelength range of 500 nm to 1000 nm. The spot size of the incident light beam of the ellipsometer was 5 mm in diameter, and the thickness was measured at five different locations.   For an un-annealed sample, irreversibly adsorbed PiBMA layer was not observed within the resolution of the spectroscopic ellipsometer.   Table A.1 shows the thickness and optical constants of the adsorbed layer at different locations on the sample.   The Cauchy model of the refractive index (n) as a function of wavelength (λ) was used for the fittings ($n(\lambda) = A + B/\lambda^2 + C/\lambda^4$).   The optical constant A for the adsorbed layer in the Cauchy model was 1.31, which is smaller than A_{bulk} (1.46), and is consistent with a previous study.[10]   From these measurements, the adsorbed layer thickness was determined to be 0.9 ± 0.3 nm. The adsorbed layer thickness was observed to be independent of additional annealing time at 106°C (7 separate samples were examined between 0 and 40 hours of annealing), indicating the adsorbed layer thickness was established during the 120°C at 20 min anneal.   Furthermore, the average adsorbed layer thickness from the 7 samples in this annealing time study was consistent with the average data from Table A.1.

154

Location number	1	2	3	4	5	Average	Standard deviation
Thickness (nm)	0.67	0.78	0.60	1.31	0.88	0.9	0.3
A	1.430	1.273	1.475	1.136	1.253	1.313	0.138
B	-0.153	-0.104	-0.146	-0.039	-0.088	-0.106	0.046
C	0.025	0.019	0.024	0.007	0.015	0.018	0.008

Table A.1:   Adsorbed layer thickness and optical constants measured by spectroscopic ellipsometry.

B.1   Miscibility of PCHE and PiBMA

Miscibility of PCHE and PiBMA was examined by differential scanning
calorimetry (DSC).   PiBMA and PCHE were mixed in a 1:1 weight ratio and annealed
at 200°C for 20 min under vacuum to achieve a homogeneous mixture.   The T_g of the
mixture was measured by DSC with a heating rate of 10°C/min as shown in Figure B.1.
Both the first and second heating cycle exhibit two different T_gs, which confirms that
PiBMA and PCHE are immiscible. The midpoint T_g of neat PiBMA and PCHE are listed
in Table B.1.
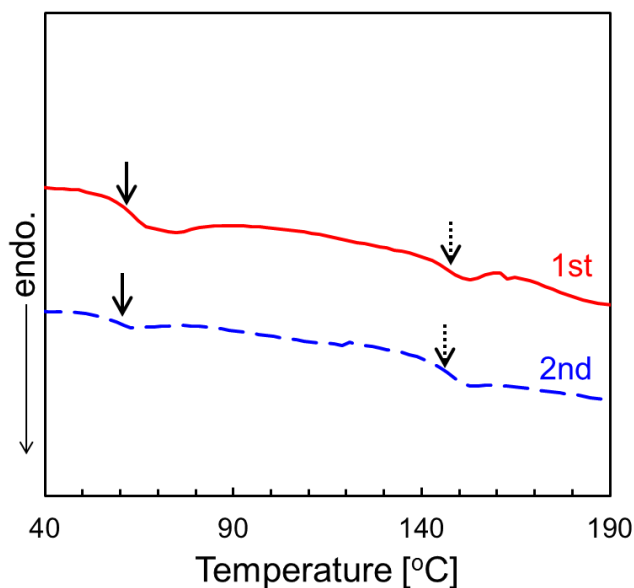
Figure B.1:   DSC heating scans of a mixture of PiBMA and PCHE with a heating rate of
10°C/min.   The solid line and the dashed line correspond to the 1st and 2nd
scan, respectively.   The solid arrows are the midpoint T_g of the PiBMA
component and the broken arrows represent that of PCHE.

156

Sample name	1st scan T_g [^oC]	2nd scan T_g [^oC]
PiBMA	58.2	58.1
PCHE	144	146

Table B.1: T_g of PiBMA and PCHE evaluated by DSC with a heating rate of 10^oC/min.

B.2   Fitting of T_g data to an empirical equation

Relationships between T_g and PiBMA film thickness (h) were obtained by fitting experimental data with an empirical equation, $T_g(h) = T_{g,\text{bulk}}\{1\pm(\alpha/h)^\delta\}$ [11], where α, and δ are the fitting parameters as listed in Table B.2.

	Air/PiBMA/SiO$_2$	Air/PiBMA/PCHE	PCHE/PiBMA/SiO$_2$	PCHE/PiBMA/PCHE
α [nm]	3.78	6.57	10.7	8.28
δ	3.42	2.65	4.04	4.30

Table B.2:   Fitting parameters for T_g-h relationship.

B.3   Viscosity measurement of bulk PiBMA

The zero-shear viscosity of PiBMA was measured by a rheometer by changing its shear rate from 10^{-3} to 10^{-1} sec^{-1}.   Figure B.2 shows the zero-shear viscosity as a function of temperature.   The obtained data was fit to the WLF equation:

$$\eta = \eta_0 \exp\left[-\frac{c_1(T-T_r)}{c_2+(T-T_r)}\right]$$

(B.1)

where, $\eta_0 = 1.61 \times 10$, $c_1 = 28.8$, and $c_2 = 160^oC$ are the fitting parameters and $T_r = 85^oC$ is the reference temperature. The fitting curve obtained by Eq. B.1 is shown as a solid line in Figure B.2.
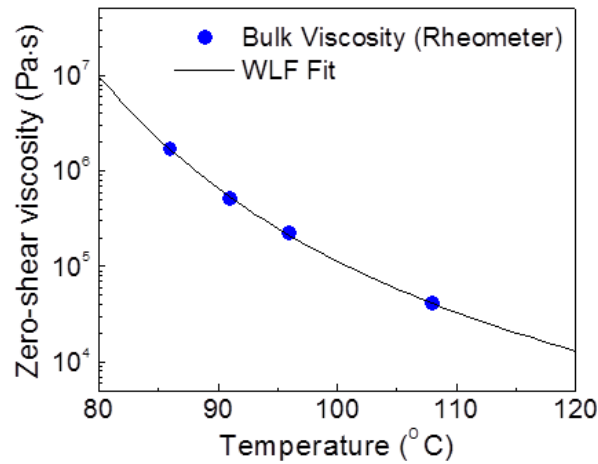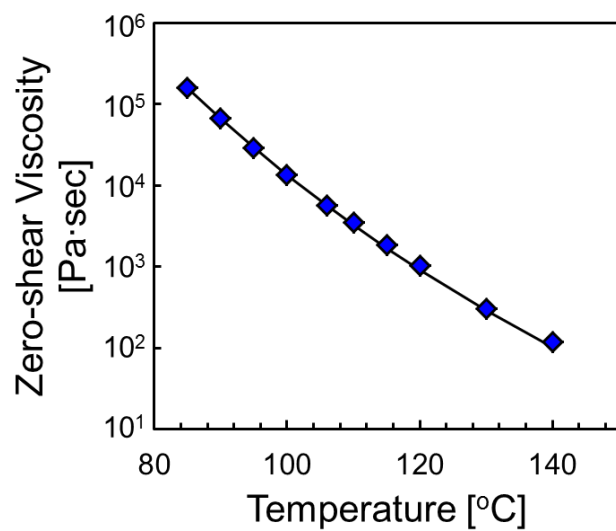
Figure B.2: Zero-shear viscosity as a function of temperature measured by a shear rheometer.   The solid line represents the best fit by the WLF equation as shown in Eq. B.1.
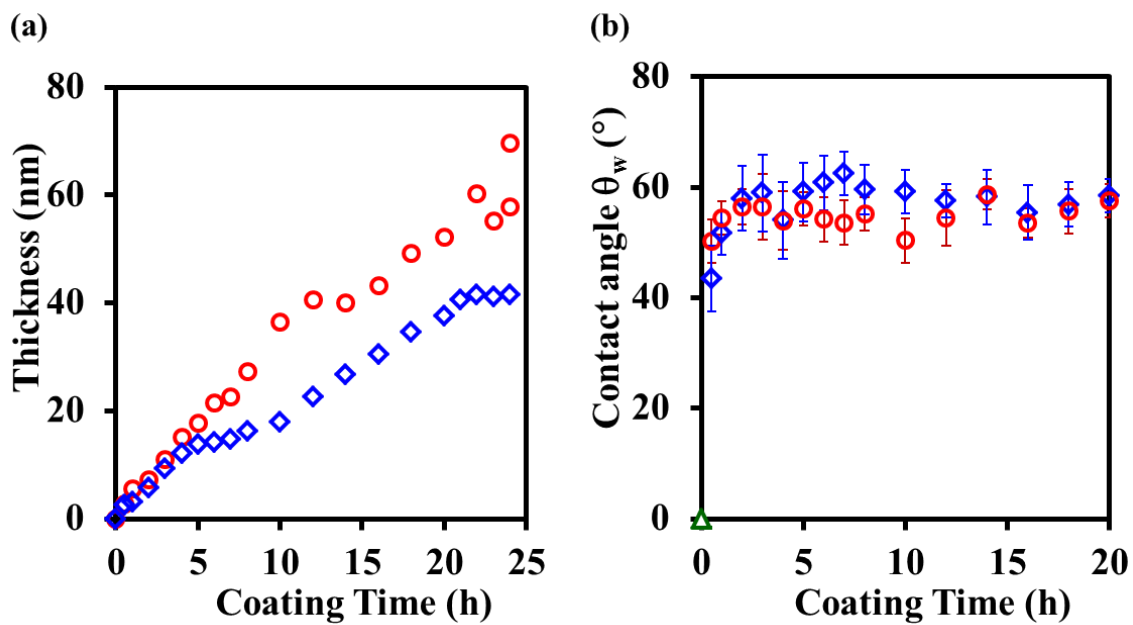
Figure C.1: Long-time thickness and static contact angles of PDA coatings on bare Si wafters (green open triangle) before (red open circle) and after (blue open diamond) sonication as a function of coating time.
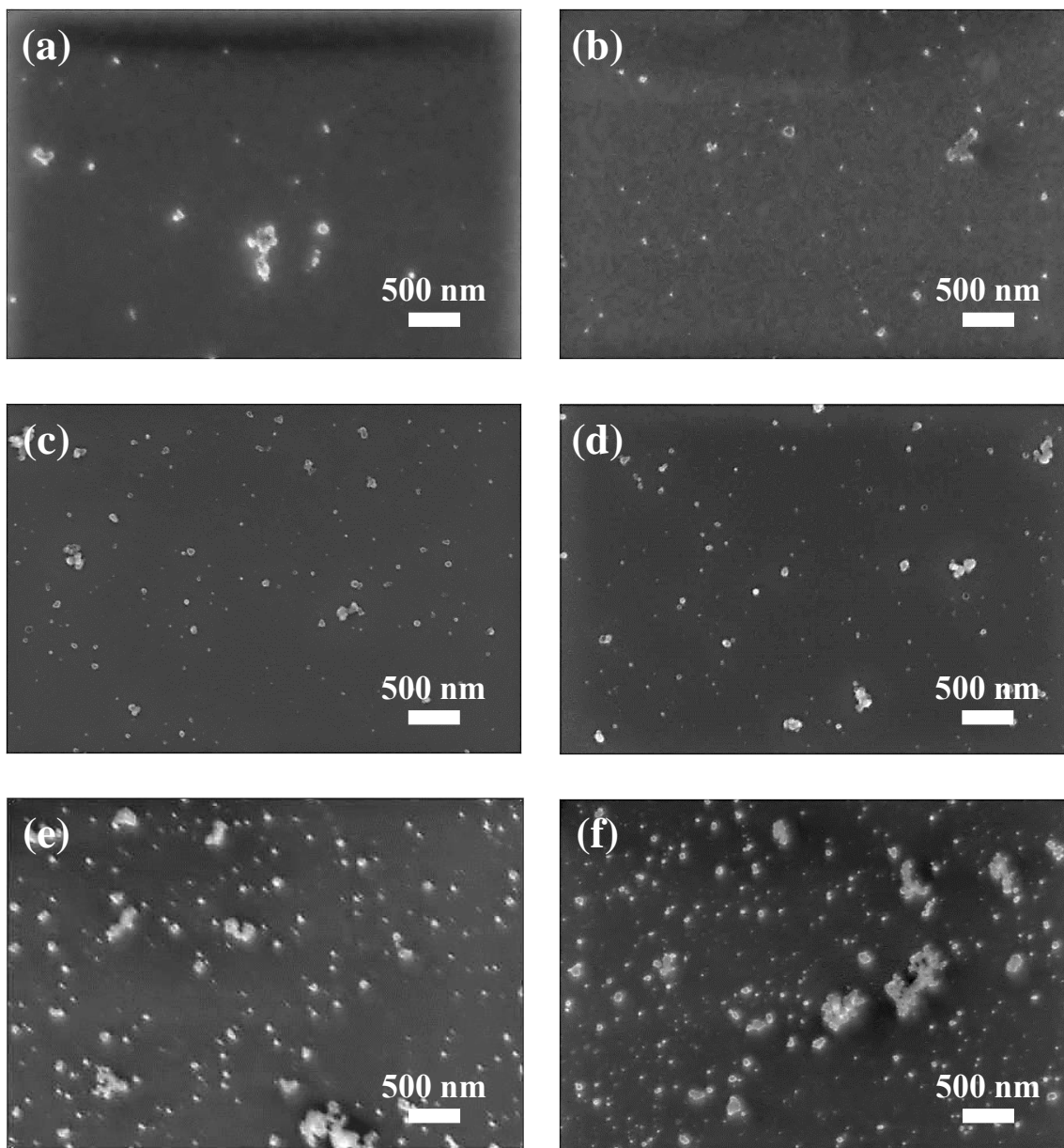
Figure C.2:   Representative SEM images of PDA-coated Si wafers after (a) 0.5 h, (b) 1 h, (c) 2 h, (d) 3 h, (e) 4 h, and (f) 5 h of coating time (no sonication).
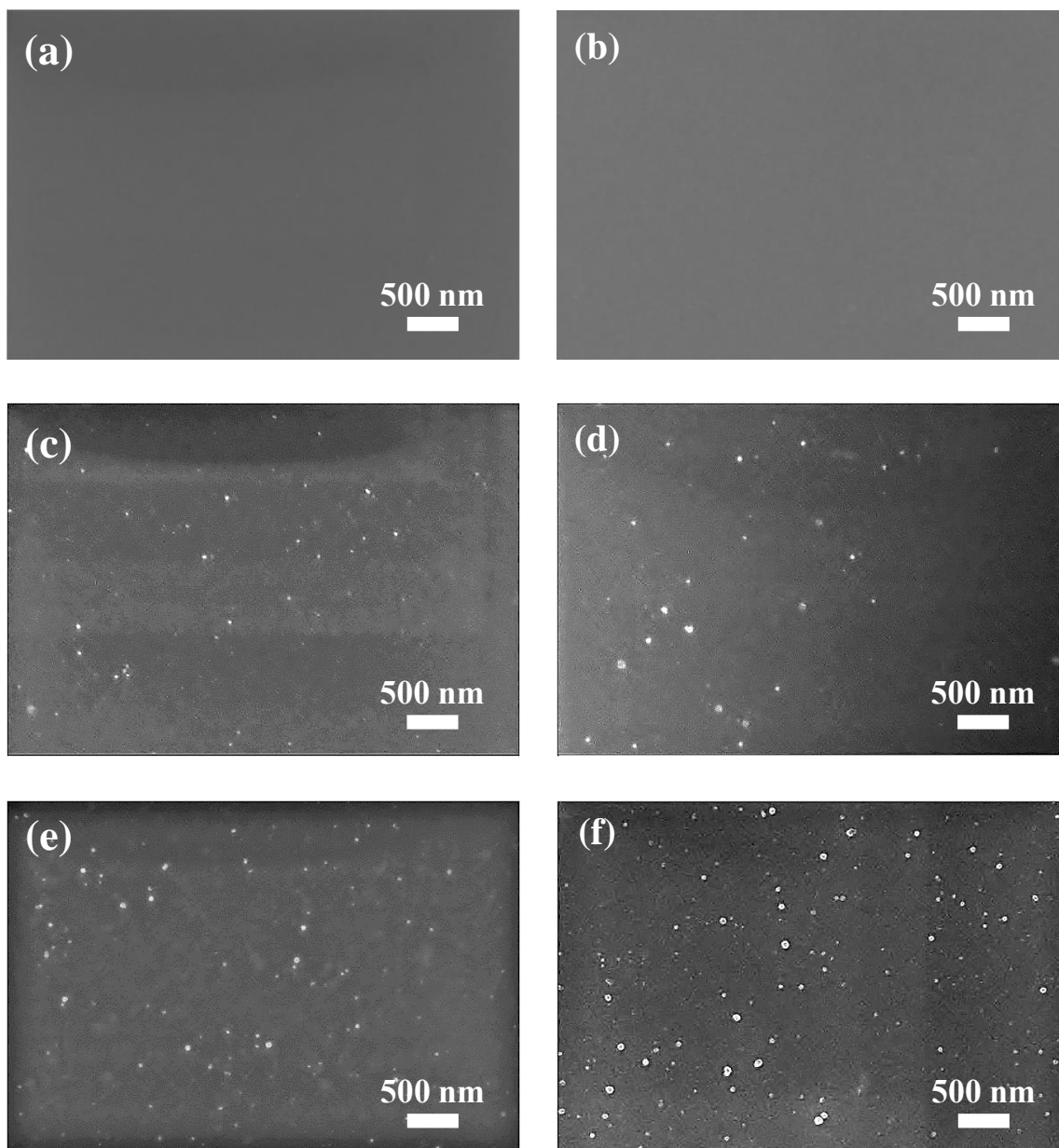
Figure C.3: Representative SEM images of PDA-coated Si wafers after(a) 0.5 h, (b) 1 h, (c) 2 h, (d) 3 h, (e) 4 h, and (f) 5 h, which were then sonicated for 100 min.
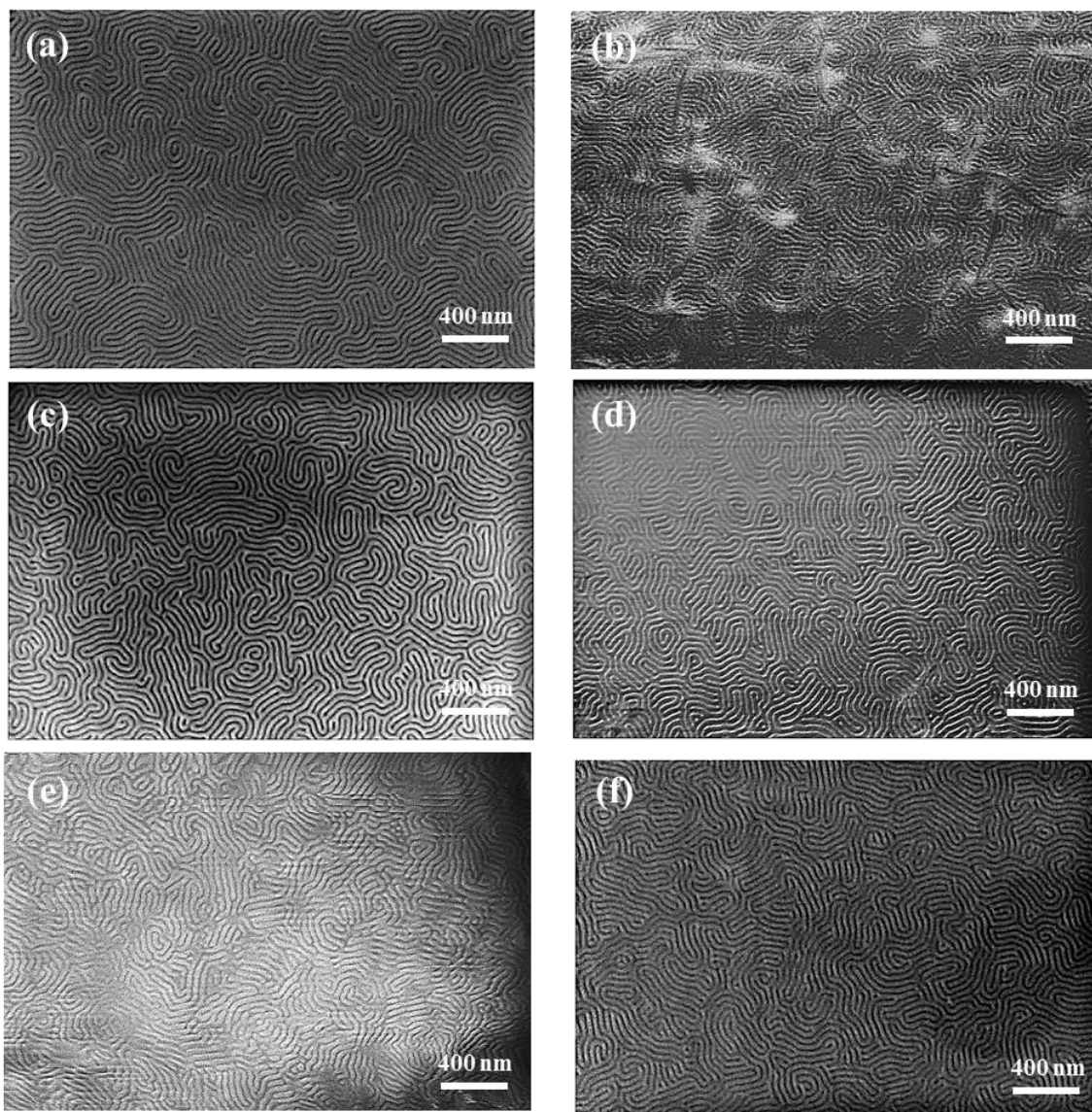
Figure C.4:   Representative SEM images of perpendicularly oriented PS-*b*-PMMA
domains on (a) PTFE brush SAM, (b) Teflon tape, (c) polyimide thin film,
(d) Kapton tape, (e) PET film, and (f) Si after PDA coating.

Control: No PDA Layer   PDA Layer Included

(a)

(b)

500 nm
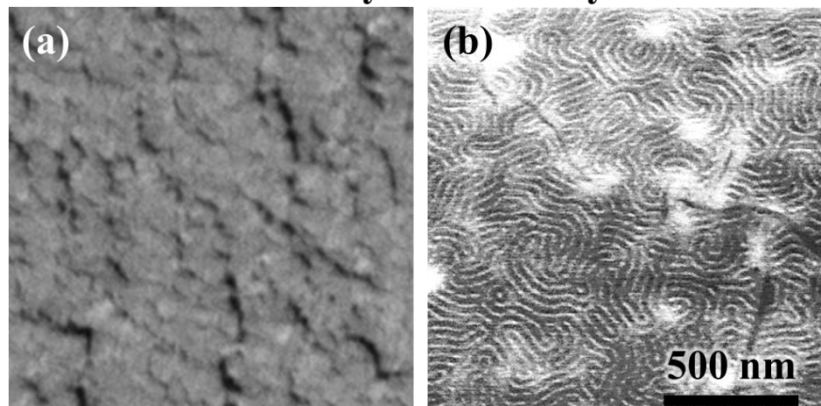
Figure C.5:   Representative SEM images of (a) unsuccessful nanopatterning on Teflon tape without PDA (b) successful nanopatterning on Teflon tape with PDA.

APPENDIX D: LARGE AREA FABRICATION OF GRAPHENE NANORIBBONS BY WETTING TRANSPARENCY-ASSISTED BLOCK COPOLYMER LITHOGRAPHY

D.1 Atomic force microscopy (AFM)

Atomic force microscopy (AFM) was used to image the GNR after etching. The data was collected on an Asylum Research MFP-3D Origin AFM. The silicon tips used had a radius of 9 ± 2 nm with a resonance frequency of 300 kHz and were purchased from Asylum Research. Each scan had 1024 points/line and 1024 lines, and the scan rate was 3 μm/s.
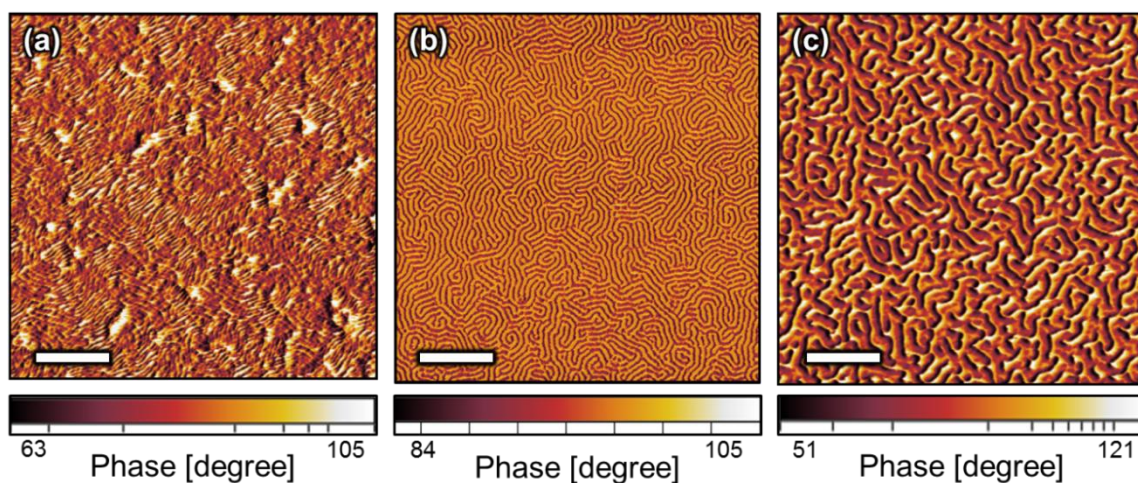
Figure D.1: AFM images of GNR arrays with a width of (a) 13 nm, (b) 22 nm, and (c) 51 nm. The image in (a) is more faint due to the small size of the structures relative to the tip radius. All scales bars represent 500 nm.

D.2   Orientation of BCP microdomains on mild plasma treated graphene without SNT
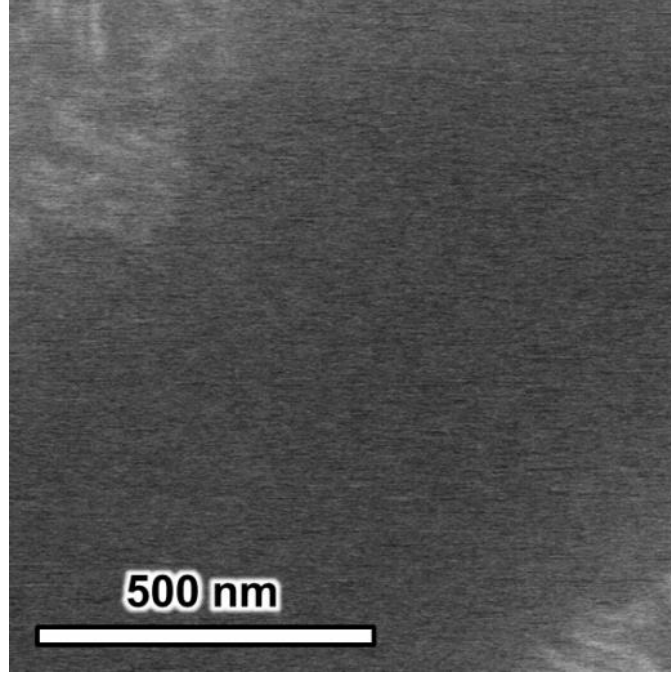
Figure D.2:   SEM image of orientations of BCP on mild plasma treated graphene without an underlying SNT layer.   The perpendicular orientation was patchy and only observed in a few isolated areas.

D.3   Young's contact angle (θ_Y) calculation

Advancing contact angle (θ_A) and receding contact angle (θ_R) were obtained by fitting dynamic contact angle as a function of time ($\theta(t)$) with a Fourier series ($n = 8$) as shown in Eq. D.1 and D.2.   The fitted line is shown as a dotted line in Figure D.3.

$$\theta(t) = a_0 + \sum_{n=1}^{8} a_n \cos\left(\frac{2n\pi}{T}t\right) + \sum_{n=1}^{8} b_n \sin\left(\frac{2n\pi}{T}t\right)$$

(D.1)

$$\theta_A = a_0 + \sum_{n=1}^{8} a_n$$

$$\theta_R = a_0 + \sum_{n=1}^{8} b_n$$

(D.2)

where a_n and b_n are the amplitudes of $(\theta(t)$ and T is the characteristic time. Young's contact angle (θ_Y), equivalent to the static contact angle, was calculated using Tadmor *et al.*'s theory[12] as shown in Eq. D.3. The calculated θ_A, θ_R, and θ_Y are shown in Figure D.3.

$$\theta_Y = \arccos\left(\frac{\Gamma_A \cos\theta_A + \Gamma_R \cos\theta_R}{\Gamma_A + \Gamma_R}\right)$$

$$\Gamma_i = \left(\frac{\sin^3\theta_i}{2 - 3\cos\theta_i + \cos^3\theta_i}\right)^{1/3}\Bigg|_{i=A,R} \tag{D.3}$$

In order to calculate the propagations of error for θ_Y from $\delta\theta_A$ and $\delta\theta_R$, the partial derivative of Eq. D.3 was calculated as shown in Eq. D.4-8. Here, $\delta\theta_A$ and $\delta\theta_R$ are the standard deviation of each contact angle for five measurements.

$$\delta\theta_Y = \sqrt{\left(\frac{\partial\theta_Y}{\partial\theta_A}\right)^2 (\delta\theta_A)^2 + \left(\frac{\partial\theta_Y}{\partial\theta_R}\right)^2 (\delta\theta_R)^2} \tag{D.4}$$

$$\theta_Y = \arccos(X)$$

$$X = \frac{\Gamma_A \cos\theta_A + \Gamma_R \cos\theta_R}{\Gamma_A + \Gamma_R} \tag{D.5}$$

$$\frac{d\theta_Y}{d\theta_A} = -\left(1 - X^2\right)^{-1/2} \cdot \frac{dX}{d\theta_A} \tag{D.6}$$

$$\Gamma' = \frac{\partial\Gamma_i}{\partial\theta_i} = \frac{2\cos\theta_i - 3\cos^2\theta_i + \cos^4\theta_i - \sin^2\theta_i + \sin^2\theta_i \cos^2\theta_i}{\left(2 - 3\cos\theta_i + \cos^3\theta_i\right)^{4/3}} \tag{D.7}$$

$$\frac{dX}{d\theta_A} = \frac{-1}{\left(\Gamma_A + \Gamma_R\right)^2}\left\{\left(\Gamma_A \cos\theta_A + \Gamma_R \cos\theta_R\right)\Gamma_A' - \left(\Gamma_A' \cos\theta_A - \Gamma_A \sin\theta_A\right)\left(\Gamma_A + \Gamma_R\right)\right\}$$

$$\frac{dX}{d\theta_R} = \frac{-1}{\left(\Gamma_A + \Gamma_R\right)^2}\left\{\left(\Gamma_A \cos\theta_A + \Gamma_R \cos\theta_R\right)\Gamma_R' - \left(\Gamma_R' \cos\theta_R - \Gamma_R \sin\theta_R\right)\left(\Gamma_A + \Gamma_R\right)\right\}$$

$$\tag{D.8}$$
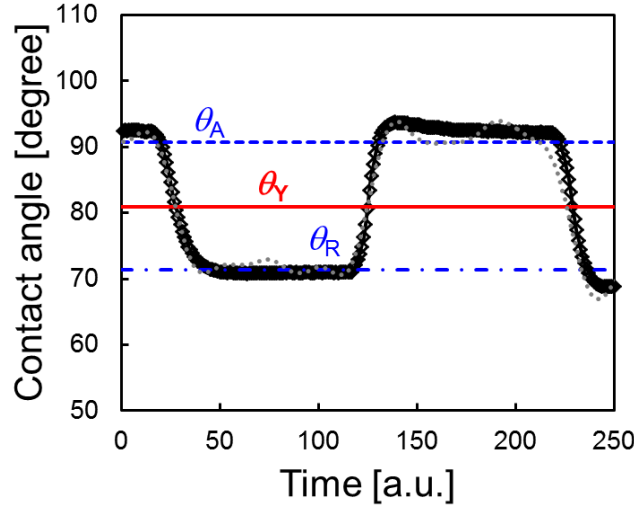
Figure D.3:   A sample analysis of dynamic contact angle.   The open diamond symbols represent the dynamic contact angle of water on bare SNT substrate.   The dotted line shows the fitting using an 8th order of Fourier series.   The obtained θ_A and θ_R are shown as broken blue lines.

D.4   Surface energy calculation

Surface energies were calculated from θ_Y for water (θ_{water}) and DIM (θ_{DIM}) using the Owens-Wendt model[13] as shown in Eq. 7.1[13] in Chapter 7,

$$(1+\cos\theta_{water})\gamma_{L,water} = 2\left(\sqrt{\gamma_S^{Dispersive}\gamma_{L,water}^{Dispersive}} + \sqrt{\gamma_S^{Polar}\gamma_{L,water}^{Polar}}\right)$$

$$(1+\cos\theta_{DIM})\gamma_{L,DIM} = 2\left(\sqrt{\gamma_S^{Dispersive}\gamma_{L,DIM}^{Dispersive}} + \sqrt{\gamma_S^{Polar}\gamma_{L,DIM}^{Polar}}\right) \tag{D.9}$$

where $\gamma_{L,X}^{Dispersive}$ and $\gamma_{L,X}^{Polar}$ represent the dispersive and polar components of liquid X (DIM and water), respectively, and these values were taken from literature.[13]   Constants were defined as shown in Table D.1 to solve Eq. D.1 by Eq. D.9.

$$\gamma_S^{Dispersive} = \left(\frac{a_1 b_3 - a_3 b_1}{a_2 b_3 - a_3 b_2}\right)^2$$

$$\gamma_S^{Polar} = \left(\frac{a_1 b_2 - a_2 b_1}{a_3 b_2 - a_2 b_3}\right)^2 \tag{D.10}$$

The propagation of the error from $\delta\theta_Y$ to $\delta\gamma_S$ was estimated using Eq. D.10.

167

$$\delta\gamma_S^{\ D} = \sqrt{\left(\frac{\partial\gamma_S^{\ D}}{\partial\theta_W}\right)^2 (\delta\theta_W)^2 + \left(\frac{\partial\gamma_S^{\ D}}{\partial\theta_D}\right)^2 (\delta\theta_D)^2}$$

$$\delta\gamma_S^{\ P} = \sqrt{\left(\frac{\partial\gamma_S^{\ P}}{\partial\theta_W}\right)^2 (\delta\theta_W)^2 + \left(\frac{\partial\gamma_S^{\ P}}{\partial\theta_D}\right)^2 (\delta\theta_D)^2}$$

$$(D.11)$$

The partial derivatives were calculated as shown in Eq. D.11, where $K = (a_2b_3 - a_3b_2)^2$.

$$\frac{\partial\gamma_S^{\ D}}{\partial\theta_W} = \frac{2b_3}{K}\left(-\frac{1}{2}\gamma_{L,W}\sin\theta_W\right)\left\{\frac{b_3}{2}(1+\cos\theta_W)\gamma_{L,W} - a_3b_1\right\}$$

$$\frac{\partial\gamma_S^{\ D}}{\partial\theta_D} = \frac{-2a_3}{K}\left(-\frac{1}{2}\gamma_{L,D}\sin\theta_D\right)\left\{a_1b_3 - \frac{a_3}{2}(1+\cos\theta_D)\gamma_{L,D}\right\}$$

$$\frac{\partial\gamma_S^{\ P}}{\partial\theta_W} = \frac{2b_2}{K}\left(-\frac{1}{2}\gamma_{L,W}\sin\theta_W\right)\left\{\frac{b_2}{2}(1+\cos\theta_W)\gamma_{L,W} - a_2b_1\right\}$$

$$\frac{\partial\gamma_S^{\ P}}{\partial\theta_D} = \frac{-2a_2}{K}\left(-\frac{1}{2}\gamma_{L,D}\sin\theta_D\right)\left\{a_1b_2 - \frac{a_2}{2}(1+\cos\theta_D)\gamma_{L,D}\right\}$$

$$(D.12)$$

	$\gamma_{L,water}$ Dispersive	$\gamma_{L,water}$ Polar	$\gamma_{L,DIM}$ Dispersive	$\gamma_{L,DIM}$ Polar
Surface energy [mJ/m^2]	21.8	51.0	50.8	0.00

a_1	a_2	a_3
$(1+\cos\theta_{water})\gamma_{L,water}/2$	$(\gamma_{L,water}^{Dispersive})^{1/2}$	$(\gamma_{L,water}^{Polar})^{1/2}$

b_1	b_2	b_3
$(1+\cos\theta_{DIM})\gamma_{L,DIM}/2$	$(\gamma_{L,DIM}^{Dispersive})^{1/2}$	$(\gamma_{L,DIM}^{Polar})^{1/2}$

Table D.1: Values[13] and definitions of a_1, a_2, a_3, b_1, b_2, and b_3 used for surface energy calculations

APPENDIX E: REFERENCES

1.   Dalnoki-Veress, K.; Forrest, J. A.; Murray, C.; Gigault, C.; Dutcher, J. R. *Phys. Rev. E* **2001,** 63, 031801.
2.   Wang, Y. J.; Lam, C. H.; Zhang, X.; Tsui, O. K. C. *Eur. Phys. J.: Spec. Top.* **2007,** 141, 181-187.
3.   Wang, Y. J.; Tsui, O. K. C. *Langmuir* **2006,** 22, 1959-1963.
4.   Wang, Y. J.; Tsui, O. K. C. *J. Non-Cryst. Solids* **2006,** 352, 4977-4982.
5.   Yang, Z.; Lam, C.-H.; DiMasi, E.; Bouet, N.; Jordan-Sweet, J.; Tsui, O. K. C. *Appl. Phys. Lett.* **2009,** 94, 251906.
6.   Yang, Z. H.; Wang, Y. J.; Todorova, L.; Tsui, O. K. C. *Macromolecules* **2008,** 41, 8785-8788.
7.   Jones, R. A. L.; Richards, R. W. R., *Polymers at Surfaces and Interfaces*. Cambridge University Press: Cambridge, UK, 1999.
8.   Israelachvili, J., *Intermolecular and Surface Forces*. Academic Press: London, UK, 1992.
9.   Fujii, Y.; Yang, Z.; Leach, J.; Atarashi, H.; Tanaka, K.; Tsui, O. K. C. *Macromolecules* **2009,** 42, 7418-7422.
10.   Koga, T.; Jiang, N.; Gin, P.; Endoh, M. K.; Narayanan, S.; Lurio, L. B.; Sinha, S. K. *Phys. Rev. Lett.* **2011,** 107, 225901.
11.   Keddie, J. L.; Jones, R. A. L.; Cory, R. A. *Europhys. Lett.* **1994,** 27, (1), 59-64.
12.   Tadmor, R. *Langmuir* **2004,** 20, (18), 7659-7664.
13.   Owens, D. K.; Wendt, R. C. *J. Appl. Polym. Sci.* **1969,** 13, (8), 1741-1747.

Bibliography

Adam, G., and J. H. Gibbs. 1965. "The Temperature Dependence of Cooperative Relaxation in Glass-Forming Liquids." *Journal of Chemical Physics* 43:139-146.

Akinwande, Deji, Nicholas Petrone, and James Hone. 2014. "Two-dimensional Flexible Nanoelectronics." *Nat. Commun.* 5:5678. doi: 10.1038/ncomms6678.

Alcoutlabi, M. , and G. B. McKenna. 2005a. "Effects of confinement on material behavior at nanometre size scale." *Journal of Physics: Condensed Matter* 17:R461-R524.

Alcoutlabi, M., and G. B. McKenna. 2005b. "Effects of confinement on material behaviour at the nanometre size scale." *J. Phys. Condens. Matter* 17 (15):R461-R524. doi: Doi 10.1088/0953-8984/17/15/R01.

Arshad, Talha A., Chae Bin Kim, Nathan A. Prisco, Joshua M. Katzenstein, Dustin W. Janes, Roger T. Bonnecaze, and Christopher J. Ellison. 2014. "Precision Marangoni-driven patterning." *Soft Matter*. doi: 10.1039/C4SM01284D.

Ata, S., M. Muramatsu, J. Takeda, T. Ohdaira, R. Suzuki, K. Ito, Y. Kobayashi, and T. Ougizawa. 2009. "Free volume behavior in spincast thin film of polystyrene by energy variable positron annihilation lifetime spectroscopy." *Polymer* 50 (14):3343-3346. doi: 10.1016/j.polymer.2009.04.060.

Aubouy, M., O. Guiselin, and E. Raphaël. 1996. "Scaling Description of Polymer Interfaces: Flat Layers." *Macromolecules* 29 (22):7261-7268. doi: 10.1021/ma9604348.

Axelrod, D., D. E. Koppel, J. Schlessinger, E. Elson, and W. W. Webb. 1976. "Mobility measurement by analysis of fluorescence photobleaching recovery kinetics." *Biophys. J.* 16 (9):1055-1069. doi: http://dx.doi.org/10.1016/S0006-3495(76)85755-4.

Bai, Jingwei, Xing Zhong, Shan Jiang, Yu Huang, and Xiangfeng Duan. 2010. "Graphene nanomesh." *Nat. Nanotechnol.* 5 (3):190-194. doi: http://www.nature.com/nnano/journal/v5/n3/suppinfo/nnano.2010.8_S1.html.

Ball, Vincent, Doriane Del Frari, Valérie Toniazzo, and David Ruch. 2012. "Kinetics of Polydopamine Film Deposition as a Function of pH and Dopamine Concentration: Insights in the Polydopamine Deposition Mechanism." *J. Colloid Interface Sci.* 386 (1):366-372. doi: http://dx.doi.org/10.1016/j.jcis.2012.07.030.

Bang, J., J. Bae, P. Löwenhielm, C. Spiessberger, S. A Given-Beck, T. P Russell, and C. J Hawker. 2007. "Facile Routes to Patterned Surface Neutralization Layers for Block Copolymer Lithography." *Adv. Mater.* 19 (24):4552-4557. doi: 10.1002/adma.200701866.

Bassereau, P., D. Brodbreck, T. P. Russell, H. R. Brown, and K. R. Shull. 1993. "Topological coarsening of symmetric diblock copolymer films: Model 2D systems." *Phys. Rev. Lett.* 71 (11):1716-1719.

Bates, Christopher M., Michael J. Maher, Dustin W. Janes, Christopher J. Ellison, and C. Grant Willson. 2014. "Block Copolymer Lithography." *Macromolecules* 47 (1):2-12. doi: 10.1021/ma401762n.

Bates, Christopher M., Takehiro Seshimo, Michael J. Maher, William J. Durand, Julia D. Cushen, Leon M. Dean, Gregory Blachut, Christopher J. Ellison, and C. Grant Willson. 2012. "Polarity-Switching Top Coats Enable Orientation of Sub–10-nm Block Copolymer Domains." *Science* 338 (6108):775-779. doi: 10.1126/science.1226046.

Bates, Christopher M., Jeffrey R. Strahan, Logan J. Santos, Brennen K. Mueller, Benjamin O. Bamgbade, Jonathan A. Lee, Joshua M. Katzenstein, Christopher J. Ellison, and C. Grant Willson. 2011. "Polymeric Cross-Linked Surface Treatments for Controlling Block Copolymer Orientation in Thin Films." *Langmuir* 27 (5):2000-2006. doi: 10.1021/la1042958.

Bates, Frank S., and Glenn H. Fredrickson. 1999. "Block Copolymers—Designer Soft Materials." *Phys. Today* 52 (2):32-38. doi: 10.1063/1.882522.

Beaulieu, Michael R., Jayanta K. Baral, Nicholas R. Hendricks, YuYing Tang, Alejandro L. Briseño, and James J. Watkins. 2013. "Solution Processable High Dielectric Constant Nanocomposites Based on ZrO2 Nanoparticles for Flexible Organic Transistors." *ACS Appl. Mater. Interfaces* 5 (24):13096-13103. doi: 10.1021/am404129u.

Berthier, L., G. Biroli, J.-P. Bouchaud, L. Cipelletti, D. El Masri, D. L'Hôte, F. Ladieu, and M. Pierno. 2005. "Direct Experimental Evidence of a Growing Length Scale Accompanying the Glass Transition." *Science* 310 (5755):1797-1800. doi: 10.1126/science.1120714.

Bicerano, J. 2002. *Prediction of Polymer Properties*. New York: Marcel Dekker, Inc.

Brandrup, J., E. H. Immergut, and E. A. Grulke, eds. 1999. *Polymer Handbook*. 4th ed. New York: Wiley-Interscience.

Brandup, J., E. H. Immergut, and E. A. Grulke. 1999. *Polymer handbook Fourth edition*. 4th editio ed: A Wiley-Interscience Publication.

Campbell, C. G., and B. D. Vogt. 2007. "Examination of the influence of cooperative segmental dynamics on the glass transition and coefficient of thermal expansion in thin films probed using poly(n-alkyl methacrylate)s." *Polymer* 48:7169-7175.

Carroll, Gregory T., Melissa E. Sojka, Xuegong Lei, Nicholas J. Turro, and Jeffrey T. Koberstein. 2006. "Photoactive Additives for Cross-Linking Polymer Films: Inhibition of Dewetting in Thin Polymer Films." *Langmuir* 22 (18):7748-7754. doi: 10.1021/la0611099.

Chai, Y., T. Salez, J. D. McGraw, M. Benzaquen, K. Dalnoki-Veress, E. Raphaël, and J. a Forrest. 2014. "A direct quantitative measure of surface mobility in a glassy polymer." *Science* 343 (6174):994-9. doi: 10.1126/science.1244845.

Chai, Y., T. Salez, J. D. McGraw, M. Benzaquen, K. Dalnoki-Veress, E. Raphael, and J. A. Forrest. 2013. "A Direct Quantitative Measure of Surface Mobility in a Glassy Polymer." *Science* 343:994.

Chen, F., D. Peng, C.-H. Lam, and O. K. C. Tsui. 2015a. "Viscosity and Surface-Promoted Slippage of Thin Polymer Films Supported by a Solid Substrate." *Macromolecules* 48:5034-5039. doi: (10.1021/acs.macromol.5b01002.

Chen, F., D. Peng, Y. Ogata, K. Tanaka, Z. Yang, Y. Fujii, N. L. Yamada, C.-H. Lam, and O. K. C. Tsui. 2015. "Effect of Confinement on the Effective Viscosity of Plasticized Polymer Films." *Macromolecules* 48:7719-7726. doi: (10.1021/acs.macromol.5b01780.

Chen, Fei, Dongdong Peng, Chi-Hang Lam, and Ophelia K. C. Tsui. 2015b. "Viscosity and Surface-Promoted Slippage of Thin Polymer Films Supported by a Solid Substrate." *Macromolecules*. doi: 10.1021/acs.macromol.5b01002.

Chen, Yen-Chia, Ting Cao, Chen Chen, Zahra Pedramrazi, Danny Haberer, Dimas G. de Oteyza, Felix R. Fischer, Steven G. Louie, and Michael F. Crommie. 2015. "Molecular bandgap engineering of bottom-up synthesized graphene nanoribbon heterojunctions." *Nat. Nanotechnol.* 10 (2):156-160. doi: 10.1038/nnano.2014.307 http://www.nature.com/nnano/journal/v10/n2/abs/nnano.2014.307.html#supplementary-information.

Chen, Zhihong, Yu-Ming Lin, Michael J. Rooks, and Phaedon Avouris. 2007. "Graphene nano-ribbon electronics." *Physica E: Low Dimens. Syst. Nanostruct.* 40 (2):228-232. doi: http://dx.doi.org/10.1016/j.physe.2007.06.020.

Cheng, Joy Y., Charles T. Rettner, Daniel P. Sanders, Ho-Cheol Kim, and William D. Hinsberg. 2008. "Dense Self-Assembly on Sparse Chemical Patterns: Rectifying and Multiplying Lithographic Patterns Using Block Copolymers." *Adv. Mater.* 20 (16):3155-3158. doi: 10.1002/adma.200800826.

Chien, Hsiu-Wen, Wei-Hsuan Kuo, Meng-Jiy Wang, Shiao-Wen Tsai, and Wei-Bor Tsai. 2012. "Tunable Micropatterned Substrates Based on Poly(dopamine) Deposition via Microcontact Printing." *Langmuir* 28 (13):5775-5782. doi: 10.1021/la300147p.

Cho, Joon Hee, Kadhiravan Shanmuganathan, and Christopher J. Ellison. 2013. "Bioinspired Catecholic Copolymers for Antifouling Surface Coatings." *ACS Appl. Mater. Interfaces* 5 (9):3794-802. doi: 10.1021/am400455p.

Choi, Jonathan W., Myungwoong Kim, Nathaniel S. Safron, Eungnak Han, Michael S. Arnold, and Padma Gopalan. 2015. "A facile route for fabricating graphene nanoribbon array transistors using graphoepitaxy of a symmetric block copolymer." doi: 10.1117/12.2085836 Proc. of SPIE.

Chung, Hoyong, and Robert H. Grubbs. 2012. "Rapidly Cross-Linkable DOPA Containing Terpolymer Adhesives and PEG-Based Cross-Linkers for Biomedical Applications." *Macromolecules* 45 (24):9666-9673. doi: 10.1021/ma3017986.

Cicerone, Marcus T., F. R. Blackburn, and M. D. Ediger. 1995a. "Anomalous Diffusion of Probe Molecules in Polystyrene: Evidence for Spatially Heterogeneous Segmental Dynamics." *Macromolecules* 28 (24):8224-8232. doi: 10.1021/ma00128a036.

Cicerone, Marcus T., F. R. Blackburn, and M. D. Ediger. 1995b. "How do molecules move near Tg? Molecular rotation of six probes in o‑terphenyl across 14 decades in time." *J. Chem. Phys.* 102 (1):471-479. doi: doi:http://dx.doi.org/10.1063/1.469425.

Clodt, Juliana Isabel, Volkan Filiz, Sofia Rangou, Kristian Buhr, Clarissa Abetz, Daniel Höche, Janina Hahn, Adina Jung, and Volker Abetz. 2013. "Double Stimuli-Responsive Isoporous Membranes via Post-Modification of pH-Sensitive Self-Assembled Diblock Copolymer Membranes." *Adv. Funct. Mater.* 23 (6):731-738. doi: 10.1002/adfm.201202015.

Cui, Nuanyang, Jinmei Liu, Long Gu, Suo Bai, Xiaobo Chen, and Yong Qin. 2015. "Wearable Triboelectric Generator for Powering the Portable Electronic Devices." *ACS Appl. Mater. Interfaces* 7 (33):18225-18230. doi: 10.1021/am5071688.

Cushen, Julia D., Issei Otsuka, Christopher M. Bates, Sami Halila, Sébastien Fort, Cyrille Rochas, Jeffrey a Easley, Erica L. Rausch, Anthony Thio, Redouane Borsali, C. Grant Willson, and Christopher J. Ellison. 2012. "Oligosaccharide/Silicon-Containing Block Copolymers with 5 nm Features for Lithographic Applications." *ACS Nano* 6 (4):3424-33. doi: 10.1021/nn300459r.

Cushen, Julia, Lei Wan, Gregory Blachut, Michael J. Maher, Thomas R. Albrecht, Christopher J. Ellison, C. Grant Willson, and Ricardo Ruiz. 2015. "Double-Patterned Sidewall Directed Self-Assembly and Pattern Transfer of Sub-10 nm PTMSS-b-PMOST." *ACS Appl. Mater. Interfaces* 7 (24):13476-13483. doi: 10.1021/acsami.5b02481.

d'Ischia, Marco, Alessandra Napolitano, Alessandro Pezzella, Paul Meredith, and Tadeusz Sarna. 2009. "Chemical and Structural Diversity in Eumelanins: Unexplored Bio-Optoelectronic Materials." *Angew. Chem., Int. Ed.* 48 (22):3914-3921. doi: 10.1002/anie.200803786.

Dalnoki-Veress, K., J. A. Forrest, C. Murray, C. Gigault, and J. R. Dutcher. 2001. "Molecular weight dependence of reductions in the glass transition temperature of thin, freely standing polymer films." *Phys. Rev. E Stat. Nonlin. Soft Matter Phys.* 63 (3 Pt 1):031801. doi: 10.1103/PhysRevE.63.031801.

Davoust, Jean, P. F. Devaux, and L. Leger. 1982. "Fringe pattern photobleaching, a new method for the measurement of transport coefficients of biological macromolecules." *EMBO J.* 1 (10):1233-1238.

Deen, William M. 2011. *Analysis of Transport Phenomena*: Oxford University Press.

Deppe, Denise D., Ali Dhinojwala, and John M. Torkelson. 1996. "Small Molecule Probe Diffusion in Thin Polymer Films Near the Glass Transition: A Novel Approach Using Fluorescence Nonradiative Energy Transfer1." *Macromolecules* 29 (11):3898-3908. doi: 10.1021/ma960024j.

Doi, M., and S.F. Edwards. 1988. *The Theory of Polymer Dynamics*: Clarendon Press.

Dreyer, D. R., D. J. Miller, B. D. Freeman, D. R. Paul, and C. W. Bielawski. 2013a. "Perspectives on poly(dopamine)." *Chemical Science* 4 (10):3796-3802. doi: Doi 10.1039/C3sc51501j.

Dreyer, Daniel R., Daniel J. Miller, Benny D. Freeman, Donald R. Paul, and Christopher W. Bielawski. 2012. "Elucidating the Structure of Poly(dopamine)." *Langmuir* 28 (15):6428-6435. doi: 10.1021/la204831b.

Dreyer, Daniel R., Daniel J. Miller, Benny D. Freeman, Donald R. Paul, and Christopher W. Bielawski. 2013b. "Perspectives on Poly(dopamine)." *Chem. Sci.* 4 (10):3796-3802. doi: 10.1039/C3SC51501J.

Ediger, M D. 1991. "Time-Resolved Optical Studies of Local Polymer Dynamics." *Annu. Rev. Phys. Chem.* 42 (1):225-250. doi: doi:10.1146/annurev.pc.42.100191.001301.

Ediger, M. D. 2000. "SPATIALLY HETEROGENEOUS DYNAMICS IN SUPERCOOLED LIQUIDS." *Annu. Rev. Phys. Chem.* 51 (1):99-128. doi: 10.1146/annurev.physchem.51.1.99.

Ediger, M. D., and J. A. Forrest. 2014. "Dynamics near Free Surfaces and the Glass Transition in Thin Polymer Films: A View to the Future." *Macromolecules* 47 (2):471-478. doi: 10.1021/ma4017696.

Ellison, C. J., M. K. Mundra, and J. M. Torkelson. 2005. "Impacts of Polystyrene Molecular Weight and Modification to the Repeat Unit Structure on the Glass Transition-Nanoconfinement Effect and the Cooperativity Length Scale." *Macromolecules* 38:1767-1778.

Ellison, C. J., and J. M. Torkelson. 2003a. "The distribution of glass-transition temperatures in nanoscopically confined glass formers." *Nature Materials* 2:695-670.

Ellison, C. J., and J. M. Torkelson. 2003b. "The distribution of glass-transition temperatures in nanoscopically confined glass formers." *Nat. Mater.* 2 (10):695-700. doi: 10.1038/nmat980.

Evans, Christopher M., Suresh Narayanan, Zhang Jiang, and John M. Torkelson. 2012. "Modulus, Confinement, and Temperature Effects on Surface Capillary Wave Dynamics in Bilayer Polymer Films Near the Glass Transition." *Phys. Rev. Lett.* 109 (3):038302-038302. doi: 10.1103/PhysRevLett.109.038302.

Fakhraai, Z., and J. a Forrest. 2008. "Measuring the surface dynamics of glassy polymers." *Science* 319 (5863):600-4. doi: 10.1126/science.1151205.

Farmer, Damon B., Daniel Rodrigo, Tony Low, and Phaedon Avouris. 2015. "Plasmon–Plasmon Hybridization and Bandwidth Enhancement in Nanostructured Graphene." *Nano Lett.* 15 (4):2582-2587. doi: 10.1021/acs.nanolett.5b00148.

Ferrari, A. C., J. C. Meyer, V. Scardaci, C. Casiraghi, M. Lazzeri, F. Mauri, S. Piscanec, D. Jiang, K. S. Novoselov, S. Roth, and A. K. Geim. 2006. "Raman Spectrum of Graphene and Graphene Layers." *Phys. Rev. Lett.* 97 (18):187401.

Fetters, L. J., D. J. Lohse, and S. T. Milner. 1999. "Packing Length Influence in Linear Polymer Melts on the Entanglement, Critical, and Reptation Molecular Weights." *Macromolecules* 32:6847-6851.

Forrest, J. A., K. Dalnoki-Veress, J. R. Stevens, and J. R. Dutcher. 1996. "Effect of Free Surfaces on the Glass Transition Temperature of Thin Polymer Films." *Phys. Rev. Lett.* 77 (10):2002-2005.

Forrest, J.A. 2002. "A decade of dynamics in thin films of polystyrene: Where are we now?" *Eur. Phys. J. E Soft Matter* 8 (2):261-266. doi: 10.1007/pl00022336.

Forrest, James A., and Kari Dalnoki-Veress. 2001. "The glass transition in thin polymer films." *Adv. Colloid Interface Sci.* 94 (1–3):167-195. doi: http://dx.doi.org/10.1016/S0001-8686(01)00060-4.

Frank, B., A. P. Gast, T. P. Russell, H. Brown, and C. Hawker. 1996a. "Polymer mobility in thin films." *Macromolecules* 29:6531-6534

Frank, B., A. P. Gast, T. P. Russell, H. R. Brown, and C. J. Hawker. 1996b. "Polymer mobility in thin films." *Macromolecules* 29 (20):6531-6534. doi: Doi 10.1021/Ma960749n.

Fujii, Y., Z. Yang, J. Leach, H. Atarashi, K. Tanaka, and O. K. C. Tsui. 2009. "Affinity of Polystyrene Films to Hydrogen-Passicated Silicon and Its Relevance to the Tg of the Films." *Macromolecules* 42:7418-7422.

Fukao, K., and Y. Miyamoto. 2000. "Glass transitions and dynamics in thin polymer films: dielectric relaxation of thin films of polystyrene." *Phys. Rev. E Stat. Nonlin. Soft Matter Phys.* 61 (2):1743-54.

Fulcher, Gordon S. 1925. "ANALYSIS OF RECENT MEASUREMENTS OF THE VISCOSITY OF GLASSES." *J. Am. Ceram. Soc.* 8 (6):339-355. doi: 10.1111/j.1151-2916.1925.tb16731.x.

Gao, Siyang, Yung P. Koh, and Sindee L. Simon. 2013. "Calorimetric Glass Transition of Single Polystyrene Ultrathin Films." *Macromolecules* 46 (2):562-570. doi: 10.1021/ma3020036.

García de Abajo, F. Javier. 2014. "Graphene Plasmonics: Challenges and Opportunities." *ACS Photonics* 1 (3):135-152. doi: 10.1021/ph400147y.

Geng, K., and O. K. C. Tsui. 2016. "Effects of Polymer Tacticity and Molecular Weight on the Glass Transition Temperature of Poly(methyl methacrylate) Films on Silica." *Macromolecs* 49:2671-2678.

Guardingo, M., M. J. Esplandiu, and D. Ruiz-Molina. 2014. "Synthesis of Polydopamine at the Femtoliter Scale and Confined Fabrication of Ag Nanoparticles on Surfaces." *Chem. Commun.* 50 (83):12548-12551. doi: 10.1039/C4CC02500H.

Guvendiren, Murat, David A. Brass, Phillip B. Messersmith, and Kenneth R. Shull. 2009. "Adhesion of DOPA-Functionalized Model Membranes to Hard and Soft Surfaces." *J. Adhesion* 85 (9):631-645. doi: 10.1080/00218460902997000.

Ha, Minjeong, Jonghwa Park, Youngoh Lee, and Hyunhyub Ko. 2015. "Triboelectric Generators and Sensors for Self-Powered Wearable Electronics." *ACS Nano* 9 (4):3421-3427. doi: 10.1021/acsnano.5b01478.

Han, E., K. O. Stuen, Y. H. La, P. F. Nealey, and P. Gopalan. 2008. "Effect of Composition of Substrate-Modifying Random Copolymers on the Orientation of Symmetric and Asymmetric Diblock Copolymer Domains." *Macromolecules* 41 (23):9090-9097. doi: Doi 10.1021/Ma8018393.

Han, Eungnak, Karl O. Stuen, Melvina Leolukman, Chi-Chun Liu, Paul F. Nealey, and Padma Gopalan. 2009. "Perpendicular Orientation of Domains in Cylinder-

Forming Block Copolymer Thick Films by Controlled Interfacial Interactions." *Macromolecules* 42 (13):4896-4901. doi: 10.1021/ma9002903.

Hawker, Craig J., and Thomas P. Russell. 2005. "Block Copolymer Lithography: Merging "Bottom-Up" with "Top-Down" Processes." *MRS Bull.* 30 (12):952-966. doi: doi:10.1557/mrs2005.249.

Hempel, E., G. Hempel, A. Hensel, C. Schick, and E. Donth. 2000. "Characteristic Length of Dynamic Glass Transition near Tg for a Wide Assortment of Glass-Forming Substances." *Journal of Physical Chemistry B* 104:2460-2466.

Hiemenz, P. C., and T. P. Lodge. 2007. *Polymer Chemistry*. 2nd ed. Boca Raton, FL: CRC Press.

Hirai, Tomoyasu, Melvina Leolukman, Chi Chun Liu, Eungnak Han, Yun Jun Kim, Yoshihito Ishida, Teruaki Hayakawa, Masa-aki Kakimoto, Paul F. Nealey, and Padma Gopalan. 2009. "One-Step Direct-Patterning Template Utilizing Self-Assembly of POSS-Containing Block Copolymers." *Adv. Mater.* 21 (43):4334-4338. doi: 10.1002/adma.200900518.

Hong, Seonki, Yun Suk Na, Sunghwan Choi, In Taek Song, Woo Youn Kim, and Haeshin Lee. 2012. "Non-Covalent Self-Assembly and Covalent Polymerization Co-Contribute to Polydopamine Formation." *Adv. Funct. Mater.* 22 (22):4711-4717. doi: 10.1002/adfm.201201156.

Hu, Hanqiong, Manesh Gopinadhan, and Chinedum O. Osuji. 2014. "Directed self-assembly of block copolymers: a tutorial review of strategies for enabling nanotechnology with soft matter." *Soft Matter* 10 (22):3867-3889. doi: 10.1039/C3SM52607K.

Hutcheson, S. A., and G. B. McKenna. 2007. "Comment on "The properties of free polymer surfaces and their influence on the glass transition temperature of thin polystyrene films" by J.S. Sharp, J.H. Teichroeb and J.A. Forrest." *Eur. Phys. J. E Soft Matter* 22 (4):281-6; discussion 287-91. doi: 10.1140/epje/e2007-00030-1.

Inoue, Takejiro, Dustin W. Janes, Jiaxing Ren, Hyo Seon Suh, Xuanxuan Chen, Christopher J. Ellison, and Paul F. Nealey. 2015. "Molecular Transfer Printing of Block Copolymer Patterns over Large Areas with Conformal Layers." *Adv. Mater. Interfaces* 2 (10):1500133. doi: 10.1002/admi.201500133.

Israelachvili, J. 1992. *Intermolecular and Surface Forces*. London, UK: Academic Press.

Israelachvili, Jacob N. 2011. "Chapter 14 - Electrostatic Forces between Surfaces in Liquids." In *Intermolecular and Surface Forces (Third Edition)*, edited by Jacob N. Israelachvili, 291-340. San Diego: Academic Press.

Jablan, Marinko, Hrvoje Buljan, and Marin Soljačić. 2009. "Plasmonics in graphene at infrared frequencies." *Phys. Rev. B: Condens. Matter Mater. Phys.* 80 (24):245435.

Janes, Dustin W., Michael J. Maher, Gregory T. Carroll, David M. Saylor, and Christopher J. Ellison. 2015. "Modulating Solubility and Enhancing Reactivity of Photo-Cross-Linkable Poly(styrene sulfonyl azide-alt-maleic anhydride) Thin Films." *Macromolecules* 48 (22):8361-8368. doi: 10.1021/acs.macromol.5b01875.

Janes, Dustin W., Christopher J. Thode, C. Grant Willson, Paul F. Nealey, and Christopher J. Ellison. 2013. "Light-Activated Replication of Block Copolymer Fingerprint Patterns." *Macromolecules* 46 (11):4510-4519. doi: 10.1021/ma400065t.

Jeong, Seong-Jun, Ju Young Kim, Bong Hoon Kim, Hyoung-Seok Moon, and Sang Ouk Kim. 2013. "Directed self-assembly of block copolymers for next generation nanolithography." *Mater. Today* 16 (12):468-476. doi: http://dx.doi.org/10.1016/j.mattod.2013.11.002.

Jeong, Seong-Jun, Hyoung-Seok Moon, Bong Hoon Kim, Ju Young Kim, Jaeho Yu, Sumi Lee, Moon Gyu Lee, HwanYoung Choi, and Sang Ouk Kim. 2010. "Ultralarge-Area Block Copolymer Lithography Enabled by Disposable Photoresist Prepatterning." *ACS Nano* 4 (9):5181-5186. doi: 10.1021/nn101212q.

Ji, Shengxiang, Lei Wan, Chi-Chun Liu, and Paul F. Nealey. 2016. "Directed self-assembly of block copolymers on chemical patterns: A platform for nanofabrication." *Prog. Polym. Sci.* 54–55:76-127. doi: http://dx.doi.org/10.1016/j.progpolymsci.2015.10.006.

Jiao, Liying, Liming Xie, and Hongjie Dai. 2012. "Densely aligned graphene nanoribbons at ~35 nm pitch." *Nano Res.* 5 (4):292-296. doi: 10.1007/s12274-012-0209-2.

Jourdainne, Laurent, Sigolène Lecuyer, Youri Arntz, Catherine Picart, Pierre Schaaf, Bernard Senger, Jean-Claude Voegel, Philippe Lavalle, and Thierry Charitat. 2008. "Dynamics of poly(L-lysine) in hyaluronic acid/poly(L-lysine) multilayer films studied by fluorescence recovery after pattern photobleaching." *Langmuir* 24 (15):7842-7. doi: 10.1021/la7040168.

Kang, Seok Hee, Wan Sik Hwang, Zhiqun Lin, Se Hun Kwon, and Suck Won Hong. 2015. "A Robust Highly Aligned DNA Nanowire Array-Enabled Lithography for Graphene Nanoribbon Transistors." *Nano Lett.* 15 (12):7913-7920. doi: 10.1021/acs.nanolett.5b02946.

Karapanagiotis, I., and W. W. Gerberich. 2006. "Surface diffusivity of thin polymer films measured by a curvature driven flow and Rouse dynamics." *Surf. Sci.* 600 (5):1178-1184. doi: DOI 10.1016/j.susc.2006.01.022.

Katzenstein, J. M., D. W. Janes, H. E. Hocker, J. K. Chandler, and C. J. Ellison. 2012a. "Nanoconfined Self-Diffusion of Poly(isobutyl methacrylate) in Films with a Thickness-Independent Glass Transition." *Macromolecules* 45 (3):1544-1552. doi: Doi 10.1021/Ma202362j.

Katzenstein, J. M., D. W. Janes, H. E. Hocker, J. K. Chandler, and C. J. Ellison. 2012b. "Nanoconfined Self-Diffusion of Poly(isobutyl methacrylate) in Films with a Thickness-Independent Glass Transition." *Macromolecules* 45:1544-1552.

Katzenstein, Joshua M., Dustin W. Janes, Julia D. Cushen, Nikhil B. Hira, Dana L. McGuffin, Nathan a Prisco, and Christopher J. Ellison. 2012. "Patterning by Photochemically Directing the Marangoni Effect." *ACS Macro Lett.* 1 (10):1150-1154. doi: 10.1021/mz300400p.

Katzenstein, Joshua M., Chae Bin Kim, Nathan A. Prisco, Reika Katsumata, Zhenpeng Li, Dustin W. Janes, Gregory Blachut, and Christopher J. Ellison. 2014. "A Photochemical Approach to Directing Flow and Stabilizing Topography in Polymer Films." *Macromolecules* 47 (19):6804-6812. doi: 10.1021/ma5010698.

Keddie, J. L., R. A. L. Jones, and R. A. Cory. 1994a. "Size-Dependent Depression of the Glass-Transition Temperature in Polymer-Films." *Europhys. Lett.* 27 (1):59-64. doi: Doi 10.1209/0295-5075/27/1/011.

Keddie, J. L., R. A. L. Jones, and R. A. Cory. 1994b. "Size-dependent depression of the glass transition temperature in polymer films." *Europhysics Letters* 27:59-64.

Keddie, Joseph L., Richard A. L. Jones, and Rachel A. Cory. 1994c. "Interface and surface effects on the glass-transition temperature in thin polymer films." *Farad. Discuss.* 98 (0):219-230. doi: 10.1039/FD9949800219.

Kim, Bong Hoon, Ju Young Kim, Seong-Jun Jeong, Jin Ok Hwang, Duck Hyun Lee, Dong Ok Shin, Sung-Yool Choi, and Sang Ouk Kim. 2010. "Surface Energy Modification by Spin-Cast, Large-Area Graphene Film for Block Copolymer Lithography." *ACS Nano* 4 (9):5464-5470. doi: 10.1021/nn101491g.

Kim, Bong Hoon, Duck Hyun Lee, Ju Young Kim, Dong Ok Shin, Hu Young Jeong, Seonki Hong, Je Moon Yun, Chong Min Koo, Haeshin Lee, and Sang Ouk Kim. 2011. "Mussel-Inspired Block Copolymer Lithography for Low Surface Energy Materials of Teflon, Graphene, and Gold." *Adv. Mater.* 23 (47):5618-5622. doi: 10.1002/adma.201103650.

Kim, Chae Bin, Dustin W. Janes, Sunshine X. Zhou, Austin R. Dulaney, and Christopher J. Ellison. 2015. "Bidirectional Control of Flow in Thin Polymer Films by Photochemically Manipulating Surface Tension." *Chem. Mater.* 27 (13):4538-4545. doi: 10.1021/acs.chemmater.5b01744.

Kim, Jihoon, Jingxiu Wan, Shinji Miyazaki, Jian Yin, Yi Cao, Young Jun Her, Hengpeng Wu, Jianhui Shan, Kazunori Kurosawa, and Guanyang Lin. 2013. "The SMART[TM] Process for Directed Block Co-Polymer Self-Assembly." *J. Photopolym. Sci. Technol.* 26 (5):573-579. doi: 10.2494/photopolymer.26.573.

Kim, Myungwoong, Nathaniel S. Safron, Eungnak Han, Michael S. Arnold, and Padma Gopalan. 2010. "Fabrication and Characterization of Large-Area, Semiconducting Nanoperforated Graphene Materials." *Nano Lett.* 10 (4):1125-1131. doi: 10.1021/nl9032318.

Kim, S., S. A. Hewlett, C. B. Roth, and J. M. Torkelson. 2009. "Confinement effects on glass transition temperature, transition breadth, and expansivity: Comparison of ellipsometry and fluorescence measurements on polystyrene films." *European Physical Journal E* 30:83-92.

Kim, Sang Ouk, Harun H. Solak, Mark P. Stoykovich, Nicola J. Ferrier, Juan J. de Pablo, and Paul F. Nealey. 2003. "Epitaxial Self-assembly of Block Copolymers on Lithographically Defined Nanopatterned Substrates." *Nature* 424 (6947):411-414.

Kim, Seyong, Hyun Suk Wang, Youngson Choe, Soo-Hyung Choi, and Joona Bang. 2016. "Controlling the microdomain orientation in block copolymer thin films via cross-linkable random copolymer neutral layer." *Polym. J.* 48 (4):333-340. doi: 10.1038/pj.2016.9.

Klosterman, Luke, John K. Riley, and Christopher John Bettinger. 2015. "Control of Heterogeneous Nucleation and Growth Kinetics of Dopamine-Melanin by Altering Substrate Chemistry." *Langmuir* 31 (11):3451-3458. doi: 10.1021/acs.langmuir.5b00105.

Koga, T., C. Li, M. K. Endoh, J. Koo, M. Rafailovich, S. Narayanan, D. R. Lee, L. B. Lurio, and S. K. Sinha. 2010. "Reduced viscosity of the free surface in entangled polymer melt films." *Phys. Rev. Lett.* 104 (6):066101.

Koo, Kyosung, Hyungju Ahn, Sang-Woo Kim, Du Yeol Ryu, and Thomas P. Russell. 2013. "Directed self-assembly of block copolymers in the extreme: guiding microdomains from the small to the large." *Soft Matter* 9 (38):9059-9071. doi: 10.1039/C3SM51083B.

Korhonen, Juuso T., Tommi Huhtamäki, Olli Ikkala, and Robin H. A. Ras. 2013. "Reliable Measurement of the Receding Contact Angle." *Langmuir* 29 (12):3858-3863. doi: 10.1021/la400009m.

Kosynkin, Dmitry V., Amanda L. Higginbotham, Alexander Sinitskii, Jay R. Lomeda, Ayrat Dimiev, B. Katherine Price, and James M. Tour. 2009. "Longitudinal unzipping of carbon nanotubes to form graphene nanoribbons." *Nature* 458 (7240):872-876. doi: http://www.nature.com/nature/journal/v458/n7240/suppinfo/nature07872_S1.html.

Kozbial, Andrew, Zhiting Li, Caitlyn Conaway, Rebecca McGinley, Shonali Dhingra, Vahid Vahdat, Feng Zhou, Brian D'Urso, Haitao Liu, and Lei Li. 2014. "Study on the Surface Energy of Graphene by Contact Angle Measurements." *Langmuir* 30 (28):8598-8606. doi: 10.1021/la5018328.

Ku, Sook Hee, Joon Seok Lee, and Chan Beum Park. 2010. "Spatial Control of Cell Adhesion and Patterning through Mussel-Inspired Surface Modification by Polydopamine." *Langmuir* 26 (19):15104-15108. doi: 10.1021/la102825p.

Lakowicz, Joseph R. 2006. *Principles of Fluorescence Spectroscopy* 3rd ed: Springer US.

Lakowicz, Joseph R., and Gregorio Weber. 1973. "Quenching of fluorescence by oxygen. Probe for structural fluctuations in macromolecules." *Biochemistry* 12 (21):4161-4170. doi: 10.1021/bi00745a020.

Lam, C.-H., and O. K. C. Tsui. 2013. "Crossover to surface flow in supercooled unentangled polymer films." *Physical Review E* 88:042604.

Lam, C. -H., O. K. C. Tsui, and D. Peng. 2012. "Surface Dynamics of Noisy Viscoelastic Films by Adiabatic Approximation." *Langmuir* 28:10217-10222.

Lang, Ryan J., Weston L. Merling, and David S. Simmons. 2014. "Combined Dependence of NanoconfinedTgon Interfacial Energy and Softness of Confinement." *ACS Macro Lett.* 3:758-762. doi: 10.1021/mz500361v.

Lange, F., P. Judeinstein, C. Franz, B. Hartmann-Azanza, S. Ok, M. Steinhart, and K. Saalwachter. 2015. "Large-Scale Diffusion of Entangled Polymers along Nanochannels." *ACS Macro Letters* 4:561-565.

Lange, Frank, Patrick Judeinstein, Cornelius Franz, Brigitte Hartmann-Azanza, Salim Ok, Martin Steinhart, and Kay Saalwächter. 2015. "Large-Scale Diffusion of Entangled Polymers along Nanochannels." *ACS Macro Lett.*:561-565. doi: 10.1021/acsmacrolett.5b00213.

Lee, Changgu, Xiaoding Wei, Jeffrey W. Kysar, and James Hone. 2008. "Measurement of the Elastic Properties and Intrinsic Strength of Monolayer Graphene." *Science* 321 (5887):385-388. doi: 10.1126/science.1157996.

Lee, Haeshin, Shara M. Dellatore, William M. Miller, and Phillip B. Messersmith. 2007. "Mussel-Inspired Surface Chemistry for Multifunctional Coatings." *Science* 318 (5849):426-430.

Lee, Haeshin, Norbert F. Scherer, and Phillip B. Messersmith. 2006. "Single-molecule Mechanics of Mussel Adhesion." *Proc. Natl. Acad. Sci. USA* 103 (35):12999-13003. doi: 10.1073/pnas.0605552103.

Li, Mingqi, and Christopher K. Ober. 2006. "Block copolymer patterns and templates." *Mater. Today* 9 (9):30-39. doi: http://dx.doi.org/10.1016/S1369-7021(06)71620-0.

Li, R. N., F. Chen, C.-H. Lam, and O. K. C. Tsui. 2013a. "Viscosity of Polymethylmethacrylate on Silica: Epitome of Systems with Strong Polymer−Substrate Interactions." *Macromolecules* 46:7889-7893.

Li, R. N., Fei Chen, Chi-hang Lam, and O. K. C. Tsui. 2013b. "Viscosity of PMMA on Silica: Epitome of Systems with Strong Polymer–Substrate Interactions." *Macromolecules* 46 (19):7889-7893.

Li, Xiaolin, Xinran Wang, Li Zhang, Sangwon Lee, and Hongjie Dai. 2008. "Chemically Derived, Ultrasmooth Graphene Nanoribbon Semiconductors." *Science* 319 (5867):1229-1232. doi: 10.1126/science.1150878.

Li Xu, Veronika Kozlovskay, Eugenia Kharlampieva, and and Svetlana A. Sukhishvili John F. Ankner. 2012. "Anisotropic Diffusion of Polyelectrolyte Chains within Multilayer

Films." *ACS Macro Lett.* 2012 (1):127-130. doi: 10.1021/mz200075x.Anisotropic.

Li, Xuesong, Weiwei Cai, Jinho An, Seyoung Kim, Junghyo Nah, Dongxing Yang, Richard Piner, Aruna Velamakanni, Inhwa Jung, Emanuel Tutuc, Sanjay K. Banerjee, Luigi Colombo, and Rodney S. Ruoff. 2009. "Large-Area Synthesis of High-Quality and Uniform Graphene Films on Copper Foils." *Science* 324 (5932):1312-1314. doi: 10.1126/science.1171245.

Li, Xuesong, Yanwu Zhu, Weiwei Cai, Mark Borysiak, Boyang Han, David Chen, Richard D. Piner, Luigi Colombo, and Rodney S. Ruoff. 2009. "Transfer of Large-Area Graphene Films for High-Performance Transparent Conductive Electrodes." *Nano Letters* 9 (12):4359-4363. doi: 10.1021/nl902623y.

Li, Zhiting, Yongjin Wang, Andrew Kozbial, Ganesh Shenoy, Feng Zhou, Rebecca McGinley, Patrick Ireland, Brittni Morganstein, Alyssa Kunkel, Sumedh P. Surwade, Lei Li, and Haitao Liu. 2013. "Effect of airborne contaminants on the

wettability of supported graphene and graphite." *Nat. Mater.* 12 (10):925-931. doi: 10.1038/nmat3709
http://www.nature.com/nmat/journal/v12/n10/abs/nmat3709.html#supplementary-information.

Liang, Xiaogan, Yeon-Sik Jung, Shiwei Wu, Ariel Ismach, Deirdre L. Olynick, Stefano Cabrini, and Jeffrey Bokor. 2010. "Formation of Bandgap and Subbands in Graphene Nanomeshes with Sub-10 nm Ribbon Width Fabricated via Nanoimprint Lithography." *Nano Lett.* 10 (7):2454-2460. doi: 10.1021/nl100750v.

Liang, Xiaogan, and Sungjin Wi. 2012. "Transport Characteristics of Multichannel Transistors Made from Densely Aligned Sub-10 nm Half-Pitch Graphene Nanoribbons." *ACS Nano* 6 (11):9700-9710. doi: 10.1021/nn303127y.

Liebscher, Jürgen, Radosław Mrówczyński, Holger A. Scheidt, Claudiu Filip, Niculina D. Hădade, Rodica Turcu, Attila Bende, and Sebastian Beck. 2013. "Structure of Polydopamine: A Never-Ending Story?" *Langmuir* 29 (33):10539-10548. doi: 10.1021/la4020288.

Lipson, J. E. G., and S. T. Milner. 2010. "Local and Average Glass Transitions in Polymer Thin Films." *Macromolecules* 43:9874-9880.

Liu, Chi-Chun, Eungnak Han, M. Serdar Onses, Christopher J. Thode, Shengxiang Ji, Padma Gopalan, and Paul F. Nealey. 2011. "Fabrication of Lithographically Defined Chemically Patterned Polymer Brushes and Mats." *Macromolecules* 44 (7):1876-1885. doi: 10.1021/ma102856t.

Liu, Chi-Chun, Abelardo Ramírez-Hernández, Eungnak Han, Gordon S. W. Craig, Yasuhiko Tada, Hiroshi Yoshida, Huiman Kang, Shengxiang Ji, Padma Gopalan, Juan J. de Pablo, and Paul F. Nealey. 2013. "Chemical Patterns for Directed Self-Assembly of Lamellae-Forming Block Copolymers with Density Multiplication of Features." *Macromolecules* 46 (4):1415-1424. doi: 10.1021/ma302464n.

Liu, Guanxiong, Yanqing Wu, Yu-Ming Lin, Damon B. Farmer, John A. Ott, John Bruley, Alfred Grill, Phaedon Avouris, Dirk Pfeiffer, Alexander A. Balandin, and Christos Dimitrakopoulos. 2012. "Epitaxial Graphene Nanoribbon Array Fabrication Using BCP-Assisted Nanolithography." *ACS Nano* 6 (8):6786-6792. doi: 10.1021/nn301515a.

Liu, Guoliang, François Detcheverry, Abelardo Ramírez-Hernández, Hiroshi Yoshida, Yasuhiko Tada, Juan J. de Pablo, and Paul F. Nealey. 2012. "Nonbulk Complex Structures in Thin Films of Symmetric Block Copolymers on Chemically Nanopatterned Surfaces." *Macromolecules* 45 (9):3986-3992. doi: 10.1021/ma202777s.

Liu, Guoliang, Mark P. Stoykovich, Shengxiang Ji, Karl O. Stuen, Gordon S. W. Craig, and Paul F. Nealey. 2009. "Phase Behavior and Dimensional Scaling of Symmetric Block Copolymer−Homopolymer Ternary Blends in Thin Films." *Macromolecules* 42 (8):3063-3072. doi: 10.1021/ma802773h.

Low, Tony, and Phaedon Avouris. 2014. "Graphene Plasmonics for Terahertz to Mid-Infrared Applications." *ACS Nano* 8 (2):1086-1101. doi: 10.1021/nn406627u.

Luo, Yingdong, Damien Montarnal, Sangwon Kim, Weichao Shi, Katherine P. Barteau, Christian W. Pester, Phillip D. Hustad, Matthew D. Christianson, Glenn H. Fredrickson, Edward J. Kramer, and Craig J. Hawker. 2015. "Poly(dimethylsiloxane-b-methyl methacrylate): A Promising Candidate for Sub-10 nm Patterning." *Macromolecules* 48 (11):3422-3430. doi: 10.1021/acs.macromol.5b00518.

Maher, Michael J., Christopher M. Bates, Gregory Blachut, Matthew C. Carlson, Jeffrey L. Self, Dustin W. Janes, William J. Durand, Austin P. Lane, Christopher J. Ellison, and C. Grant Willson. 2014. "Photopatternable Interfaces for Block Copolymer Lithography." *ACS Macro Lett.* 3 (8):824-828. doi: 10.1021/mz500370r.

Maher, Michael J., Christopher M. Bates, Gregory Blachut, Stephen Sirard, Jeffrey L. Self, Matthew C. Carlson, Leon M. Dean, Julia D. Cushen, William J. Durand, Colin O. Hayes, Christopher J. Ellison, and C. Grant Willson. 2014. "Interfacial Design for Block Copolymer Thin Films." *Chem. Mater.* 26 (3):1471-1479. doi: 10.1021/cm403813q.

Maier, Greg P., Michael V. Rapp, J. Herbert Waite, Jacob N. Israelachvili, and Alison Butler. 2015. "Adaptive Synergy between Catechol and Lysine Promotes Wet Adhesion by Surface Salt Displacement." *Science* 349 (6248):628-632. doi: 10.1126/science.aab0556.

Mallamace, F., C. Branca, C. Corsaro, N. Leone, J. Spooren, S. H. Chen, and H. E. Stanley. 2010. "Transport properties of glass-forming liquids suggest that dynamic crossover temperature is as important as the glass transition temperature." *Proc. Natl. Acad. Sci. USA* 107 (52):22457-62. doi: 10.1073/pnas.1015340107.

Mansky, P., Y. Liu, E. Huang, T. P. Russell, and C. Hawker. 1997. "Controlling Polymer-Surface Interactions with Random Copolymer Brushes." *Science* 275 (5305):1458-1460. doi: 10.1126/science.275.5305.1458.

Masson, Jean-Loup, and Peter F. Green. 2002. "Viscosity of entangled polystyrene thin film melts: Film thickness dependence." *Phys. Rev. E Stat. Nonlin. Soft Matter Phys.* 65 (3):031806.

Matsumoto, Hidetoshi, Shinji Imaizumi, Yuichi Konosu, Minoru Ashizawa, Mie Minagawa, Akihiko Tanioka, Wei Lu, and James M. Tour. 2013. "Electrospun Composite Nanofiber Yarns Containing Oriented Graphene Nanoribbons." *ACS Applied Materials & Interfaces* 5 (13):6225-6231. doi: 10.1021/am401161b.

McGraw, J. D., N. M. Jago, and K. Dalnoki-Veress. 2011. "Capillary levelling as a probe of thin film polymer rheology." *Soft Matter* 7 (17):7832-7838. doi: Doi 10.1039/C1sm05261f.

Meinzer, Nina, William L. Barnes, and Ian R. Hooper. 2014. "Plasmonic meta-atoms and metasurfaces." *Nat. Photon.* 8 (12):889-898. doi: 10.1038/nphoton.2014.247.

Meyvis, Tom K. L., Stefaan C. De Smedt, Patrick Van Oostveldt, and Joseph Demeester. 1999. "Fluorescence Recovery After Photobleaching: A Versatile Tool for

Mobility and Interaction Measurements in Pharmaceutical Research." *Pharmaceut. Res.* 16 (8):1153-1162. doi: 10.1023/A:1011924909138.

Mi, Hongyi, Solomon Mikael, Chi-Chun Liu, Jung-Hun Seo, Gui Gui, Alice L. Ma, Paul F. Nealey, and Zhenqiang Ma. 2015. "Creating periodic local strain in monolayer graphene with nanopillars patterned by self-assembled block copolymer." *Appl. Phys. Lett.* 107 (14):143107. doi: doi:http://dx.doi.org/10.1063/1.4932657.

Owens, D. K., and R. C. Wendt. 1969. "Estimation of the surface free energy of polymers." *J. Appl. Polym. Sci.* 13 (8):1741-1747. doi: 10.1002/app.1969.070130815.

Paeng, K., S. F. Swallen, and M. D. Ediger. 2011a. "Direct Measurement of Molecular Motion in Freestanding Polystyrene Thin Films." *Journal of the American Chemical Society* 133:8444-8447.

Paeng, Keewook, and M. D. Ediger. 2011. "Molecular Motion in Free-Standing Thin Films of Poly(methyl methacrylate), Poly(4-tert-butylstyrene), Poly(α-methylstyrene), and Poly(2-vinylpyridine)." *Macromolecules* 44 (17):7034-7042. doi: 10.1021/ma201266r.

Paeng, Keewook, Ranko Richert, and M. D. Ediger. 2012. "Molecular mobility in supported thin films of polystyrene, poly(methyl methacrylate), and poly(2-vinyl pyridine) probed by dye reorientation." *Soft Matter* 8 (3):819-819. doi: 10.1039/c1sm06501g.

Paeng, Keewook, Stephen F. Swallen, and M. D. Ediger. 2011b. "Direct measurement of molecular motion in freestanding polystyrene thin films." *J. Am. Chem. Soc.* 133 (22):8444-7. doi: 10.1021/ja2022834.

Park, Seokhan, Je Moon Yun, Uday Narayan Maiti, Hyoung-Seok Moon, Hyeong Min Jin, and Sang Ouk Kim. 2014. "Device-oriented Graphene Nanopatterning by Mussel-inspired Directed Block Copolymer Self-assembly." *Nanotechnology* 25 (1):014008.

Pearson, D. S., G. Ver Strate, E. Von Meerwall, and F. C. Schilling. 1987. "Viscosity and Self-Diffusion Coefficient of Linear Polyethylene." *Macromolecules* 20:1133-1141.

Pintauer, Tomislav, and Krzysztof Matyjaszewski. 2008. "Atom transfer radical addition and polymerization reactions catalyzed by ppm amounts of copper complexes." *Chemical Society Reviews* 37:1087-1097.

Plazek, Donald J., and Joseph H. Magill. 1966. "Physical Properties of Aromatic Hydrocarbons. I. Viscous and Viscoelastic Behavior of 1:3:5‐Tri‐α‐Naphthyl Benzene." *J. Chem. Phys.* 45 (8):3038-3050. doi: doi:http://dx.doi.org/10.1063/1.1728059.

Postma, Almar, Yan Yan, Yajun Wang, Alexander N. Zelikin, Elvira Tjipto, and Frank Caruso. 2009. "Self-Polymerization of Dopamine as a Versatile and Robust Technique to Prepare Polymer Capsules." *Chem. Mater.* 21 (14):3042-3044. doi: 10.1021/cm901293e.

Priestley, R. D., M. K. Mundra, N. J. Barnett, L. J. Broadbelt, and J. M. Torkelson. 2007a. "Effects of Nanoscale Confinement and Interfaces on the Glass Transition

Temperatures of a Series of Poly(n-methacrylate) Films." *Australian Journal of Chemistry* 60:765-771.

Priestley, R. D., M. K. Mundra, N. J. Barnett, L. J. Broadbelt, and J. M. Torkelson. 2007b. "Effects of nanoscale confinement and interfaces on the glass transition temperatures of a series of poly(n-methacrylate) films." *Aust. J. Chem.* 60 (10):765-771. doi: Doi 10.1071/Ch07234.

Pujari, Saswati, Michael A. Keaton, Paul M. Chaikin, and Richard A. Register. 2012. "Alignment of Perpendicular Lamellae in Block Copolymer Thin Films by Shearing." *Soft Matter* 8 (19):5358-5363. doi: 10.1039/C2SM25270H.

Pye, J. E., and C. B. Roth. 2011. "Two Simultaneous Mechanisms Causing Glass Transition Temperature Reductions in High MolecularWeight Freestanding Polymer Films as Measured by Transmission Ellipsometry." *Physical Review Letters* 107:235701.

Rafiee, Javad, Xi Mi, Hemtej Gullapalli, Abhay V. Thomas, Fazel Yavari, Yunfeng Shi, Pulickel M. Ajayan, and Nikhil A. Koratkar. 2012. "Wetting transparency of graphene." *Nat. Mater.* 11 (3):217-222. doi: http://www.nature.com/nmat/journal/v11/n3/abs/nmat3228.html#supplementary-information.

Rafiee, Javad, Mohammad A. Rafiee, Zhong-Zhen Yu, and Nikhil Koratkar. 2010. "Superhydrophobic to Superhydrophilic Wetting Control in Graphene Films." *Adv. Mater.* 22 (19):2151-2154. doi: 10.1002/adma.200903696.

Reid, Dariya K., Marcela Alves Freire, Haiqing Yao, Hung-Jue Sue, and Jodie L. Lutkenhaus. 2015. "The Effect of Surface Chemistry on the Glass Transition of Polycarbonate Inside Cylindrical Nanopores." *ACS Macro Lett.* 4 (2):151-154. doi: 10.1021/mz500725s.

Reinsberg, S. A., X. H. Qiu, M. Wilhelm, H. W. Spiess, and M. D. Ediger. 2001. "Length Scale of Dynamic Heterogeneity in Supercooled Glycerol near Tg." *The Journal of Chemical Physics* 114:7299-7302.

Reiter, G. 1993. "Mobility of Polymers in Films Thinner than Their Unperturbed Size." *Euro. Phys. Lett.* 23 (8):579.

Richert, R. 2011. "Dynamics of nanoconfined supercooled liquids." *Annu. Rev. Phys. Chem.* 62:65-84. doi: 10.1146/annurev-physchem-032210-103343.

Robeson, J. L., and R. D. Tilton. 1995. "Effect of concentration quenching on fluorescence recovery after photobleaching measurements." *Biophys. J.* 68 (5):2145-55. doi: 10.1016/S0006-3495(95)80397-8.

Rodrigo, Daniel, Odeta Limaj, Davide Janner, Dordaneh Etezadi, F. Javier García de Abajo, Valerio Pruneri, and Hatice Altug. 2015. "Mid-infrared plasmonic biosensing with graphene." *Science* 349 (6244):165-168. doi: 10.1126/science.aab2051.

Rogers, John A., Takao Someya, and Yonggang Huang. 2010. "Materials and Mechanics for Stretchable Electronics." *Science* 327 (5973):1603-1607. doi: 10.1126/science.1182383.

Roland, C. M., K. L. Ngai, P. G. Santangelo, X. H. Qiu, M. D. Ediger, and D. J. Plazek. 2001. "Temperature Dependence of Segmental and Terminal Relaxation in Atactic Polypropylene Melts." *Macromolecules* 34:6159-6160.

Roth, C. B., K. L. McNerny, W. F. Jager, and J. M. Torkelson. 2007. "Eliminating the enhanced mobility at the free surface of polystyrene: Fluorescence studies of the glass transition temperature in thin bilayer films of immiscible polymers." *Macromolecules* 40 (7):2568-2574. doi: Doi 10.1021/Ma062864w.

Roth, C., and J. Dutcher. 2005a. "Glass transition and chain mobility in thin polymer films." *J. Electroanal. Chem.* 584 (1):13-22. doi: 10.1016/j.jelechem.2004.03.003.

Roth, Connie B., and John R. Dutcher. 2005b. "Mobility on Different Length Scales in Thin Polymer Films." In *Soft Materials: Structure and Dynamics*, edited by J. R. Dutcher and A. G. Marangoni, 1-38. N.Y.: Marcel Dekker.

Roth, Connie B., and John R. Dutcher. 2006. "Hole growth as a microrheological probe to measure the viscosity of polymers confined to thin films." *J. Polym. Sci. Part B Polym. Phys.* 44 (20):3011-3021. doi: 10.1002/polb.20918.

Ruiz, Ricardo, Huiman Kang, François A. Detcheverry, Elizabeth Dobisz, Dan S. Kercher, Thomas R. Albrecht, Juan J. de Pablo, and Paul F. Nealey. 2008. "Density Multiplication and Improved Lithography by Directed Block Copolymer Assembly." *Science* 321 (5891):936-939.

Russell, Thomas P., G. Coulon, V. R. Deline, and D. C. Miller. 1989. "Characteristics of the surface-induced orientation for symmetric diblock PS/PMMA copolymers." *Macromolecules* 22 (12):4600-4606. doi: 10.1021/ma00202a036.

Ryu, Du Yeol, Kyusoon Shin, Eric Drockenmuller, Craig J. Hawker, and Thomas P. Russell. 2005. "A Generalized Approach to the Modification of Solid Surfaces." *Science* 308 (5719):236-239.

Schiener, B., R. V. Chamberlin, G. Diezemann, and R. Böhmer. 1997. "Nonresonant dielectric hole burning spectroscopy of supercooled liquids." *J. Chem. Phys.* 107 (19):7746-7761. doi: doi:http://dx.doi.org/10.1063/1.475089.

Schlessinger, J., D. E. Koppel, D. Axelrod, K. Jacobson, W. W. Webb, and E. L. Elson. 1976. "Lateral transport on cell membranes: mobility of concanavalin A receptors on myoblasts." *Proc. Natl. Acad. Sci. USA* 73 (7):2409-2413.

Schmidt-Rohr, K., and H. W. Spiess. 1991. "Nature of nonexponential loss of correlation above the glass transition investigated by multidimensional NMR." *Phys. Rev. Lett.* 66 (23):3020-3023.

Seemann, Ralf, Stephan Herminghaus, Chiara Neto, Stefan Schlagowski, Daniel Podzimek, Renate Konrad, Hubert Mantz, and Karin Jacobs. 2005. "Dynamics and structure formation in thin polymer melt films." *J. Phys. Condens. Matter* 17 (9):S267-S290. doi: 10.1088/0953-8984/17/9/001.

Segalman, R. A., H. Yokoyama, and E. J. Kramer. 2001. "Graphoepitaxy of Spherical Domain Block Copolymer Films." *Adv. Mater.* 13 (15):1152-1155. doi: 10.1002/1521-4095(200108)13:15<1152::AID-ADMA1152>3.0.CO;2-5.

Selin, Victor, John F. Ankner, and Svetlana A. Sukhishvili. 2015. "Diffusional Response of Layer-by-Layer Assembled Polyelectrolyte Chains to Salt Annealing." *Macromolecules* 48 (12):3983-3990. doi: 10.1021/acs.macromol.5b00361.

Sharp, J. S., and J. A. Forrest. 2003. "Free surfaces cause reductions in the glass transition temperature of thin polystyrene films." *Phys. Rev. Lett.* 91 (23):235701. doi: 10.1103/PhysRevLett.91.235701.

Shelton, C. K., and T. H. Epps. 2015. "Decoupling Substrate Surface Interactions in Block Polymer Thin Film Self-Assembly." *Macromolecules* 48 (13):4572-4580. doi: 10.1021/acs.macromol.5b00833.

Shih, Chih-Jen, Qing Hua Wang, Shangchao Lin, Kyoo-Chul Park, Zhong Jin, Michael S. Strano, and Daniel Blankschtein. 2012. "Breakdown in the Wetting Transparency of Graphene." *Phys. Rev. Lett.* 109 (17):176101.

Shin, Young Jun, Yingying Wang, Han Huang, Gopinadhan Kalon, Andrew Thye Shen Wee, Zexiang Shen, Charanjit Singh Bhatia, and Hyunsoo Yang. 2010. "Surface-Energy Engineering of Graphene." *Langmuir* 26 (6):3798-3802. doi: 10.1021/la100231u.

Si, Lun, Michael V. Massa, Kari Dalnoki-Veress, Hugh R. Brown, and Richard a L. Jones. 2005. "Chain Entanglement in Thin Freestanding Polymer Films." *Phys. Rev. Lett.* 94 (12):1-4. doi: 10.1103/PhysRevLett.94.127801.

Silveiro, Ivan, Juan Manuel Plaza Ortega, and FJavier Garcia de Abajo. 2015. "Quantum nonlocal effects in individual and interacting graphene nanoribbons." *Light: Sci. Appl.* 4:e241. doi: 10.1038/lsa.2015.14.

Simons, J. K., J. M. Chen, J. W. Taylor, and R. A. Rosenberg. 1993. "Fluorescence studies of the vacuum ultraviolet, synchrotron radiation-induced photochemistry of polystyrene." *Macromolecules* 26 (13):3262-3266. doi: 10.1021/ma00065a003.

Singh, Gurpreet, Saurabh Batra, Ren Zhang, Hongyi Yuan, Kevin G. Yager, Miko Cakmak, Brian Berry, and Alamgir Karim. 2013. "Large-Scale Roll-to-Roll Fabrication of Vertically Oriented Block Copolymer Thin Films." *ACS Nano* 7 (6):5291-5299. doi: 10.1021/nn401094s.

Smith, B. A. 1982. "Measurement of Diffusion in Polymer-Films by Fluorescence Redistribution after Pattern Photobleaching." *Macromolecules* 15 (2):469-472. doi: Doi 10.1021/Ma00230a052.

Smith, B. A., and H. M. McConnell. 1978. "Determination of molecular motion in membranes using periodic pattern photobleaching." *Proc. Natl. Acad. Sci. USA* 75 (6):2759-2763.

Sokolov, Alexei P., and Kenneth S. Schweizer. 2009. "Resolving the Mystery of the Chain Friction Mechanism in Polymer Liquids." *Phys. Rev. Lett.* 102 (24):248301.

Son, Jeong Gon, Myungwoo Son, Kyeong-Joo Moon, Byoung Hun Lee, Jae-Min Myoung, Michael S. Strano, Moon-Ho Ham, and Caroline A. Ross. 2013. "Sub-10 nm Graphene Nanoribbon Array Field-Effect Transistors Fabricated by Block

Copolymer Lithography." *Adv. Mater.* 25 (34):4723-4728. doi: 10.1002/adma.201300813.

Stafford, C. M., B. D. Vogt, C. Harrison, D. Julthongpiput, and R. Huang. 2006a. "Elastic Moduli of Ultrathin Amorphous Polymer Films." *Macromolecules* 39:5095-5099.

Stafford, C. M., B. D. Vogt, C. Harrison, D. Julthongpiput, and R. Huang. 2006b. "Elastic moduli of ultrathin amorphous polymer films." *Macromolecules* 39 (15):5095-5099. doi: Doi 10.1021/Ma060790i.

Stein, Gila E., Nikhila Mahadevapuram, and Indranil Mitra. 2015. "Controlling interfacial interactions for directed self assembly of block copolymers." *J. Polym. Sci., Part B: Polym. Phys.* 53 (2):96-102. doi: 10.1002/polb.23502.

Stoykovich, M. P., K. Yoshimoto, and P. F. Nealey. 2008. "Mechanical properties of polymer nanostructures: measurements based on deformation in response to capillary forces." *Applied Physics A* 90:277-283.

Stoykovich, Mark P., Huiman Kang, Kostas Ch Daoulas, Guoliang Liu, Chi-Chun Liu, Juan J. de Pablo, Marcus Müller, and Paul F. Nealey. 2007. "Directed Self-Assembly of Block Copolymers for Nanolithography: Fabrication of Isolated Features and Essential Integrated Circuit Geometries." *ACS Nano* 1 (3):168-175. doi: 10.1021/nn700164p.

Stoykovich, Mark P., Marcus Müller, Sang Ouk Kim, Harun H. Solak, Erik W. Edwards, Juan J. de Pablo, and Paul F. Nealey. 2005. "Directed Assembly of Block Copolymer Blends into Nonregular Device-Oriented Structures." *Science* 308 (5727):1442-1446. doi: 10.1126/science.1111041.

Strobl, Gert. 2007. *The Physics of Polymers*: Springer-Verlag Berlin Heidelberg. Reprint, 3.

Suk, Ji Won, Alexander Kitt, Carl W. Magnuson, Yufeng Hao, Samir Ahmed, Jinho An, Anna K. Swan, Bennett B. Goldberg, and Rodney S. Ruoff. 2011. "Transfer of CVD-Grown Monolayer Graphene onto Arbitrary Substrates." *ACS Nano* 5 (9):6916-6924. doi: 10.1021/nn201207c.

Sussman, Daniel M., Wei-Shao Tung, Karen I. Winey, Kenneth S. Schweizer, and Robert A. Riggleman. 2014. "Entanglement Reduction and Anisotropic Chain and Primitive Path Conformations in Polymer Melts under Thin Film and Cylindrical Confinement." *Macromolecules* 47 (18):6462-6472. doi: 10.1021/ma501193f.

Swallen, S. F., K. Traynor, R. J. McMahon, M. D. Ediger, and T. E. Mates. 2009. "Self-diffusion of supercooled tris-naphthylbenzene." *J. Phys. Chem. B* 113 (14):4600-8. doi: 10.1021/jp808912e.

Tadmor, Rafael. 2004. "Line Energy and the Relation between Advancing, Receding, and Young Contact Angles." *Langmuir* 20 (18):7659-7664. doi: 10.1021/la049410h.

Tammann, G., and W. Hesse. 1926. "Z. Anorg. Allg. Chem." *Z. Anorg. Allg. Chem* 156 (1):245-257. doi: 10.1002/zaac.19261560121.

Tapasztó, Levente, Gergely Dobrik, Philippe Lambin, and Laszlo P. Biro. 2008. "Tailoring the atomic structure of graphene nanoribbons by scanning tunnelling

microscope lithography." *Nat. Nanotechnol.* 3 (7):397-401. doi: http://www.nature.com/nnano/journal/v3/n7/suppinfo/nnano.2008.149_S1.html.

Thongrattanasiri, Sukosin, Alejandro Manjavacas, and F. Javier García de Abajo. 2012. "Quantum Finite-Size Effects in Graphene Plasmons." *ACS Nano* 6 (2):1766-1775. doi: 10.1021/nn204780e.

Torres, J. M., C. M. Stafford, and B. D. Vogt. 2009a. "Elastic Modulus of Amorphous Polymer Thin Films: Relationship to the Glass Transition Temperature." *ACS Nano* 3:2677-2685.

Torres, J. M., C. M. Stafford, and B. D. Vogt. 2009b. "Elastic modulus of amorphous polymer thin films: relationship to the glass transition temperature." *ACS Nano* 3 (9):2677-85. doi: 10.1021/nn9006847.

Torres, J. M., C. M. Stafford, and B. D. Vogt. 2010. "Manipulation of the Elastic Modulus of Polymers at the Nanoscale: Influence of UV Ozone Cross-Linking and Plasticizer." *ACS Nano* 4:5357-5365.

Tour, James M. 2014. "Top-Down versus Bottom-Up Fabrication of Graphene-Based Electronics." *Chem. Mater.* 26 (1):163-171. doi: 10.1021/cm402179h.

Tseng, K. C., N. J. Turro, and C. J. Durning. 2000. "Molecular mobility in polymer thin films." *Phys. Rev. E Stat. Nonlin. Soft Matter Phys.* 61 (2):1800-1811.

Tsui, O. K. C., T. P. Russell, and C. J. Hawker. 2001. "Effect of interfacial interactions on the glass transition of polymer thin films." *Macromolecules* 34 (16):5535-5539. doi: Doi 10.1021/Ma000028v.

Tsui, O. K. C., Y. J. Wang, F. K. Lee, C. -H. Lam, and Z. Yang. 2008. "Equilibrium Pathway of Spin-Coated Polymer Films." *Macromolecules* 41:1465-1468.

Tsui, O. K. C., and H. F. Zhang. 2001. "Effect of Chain Ends and Chain Entanglement on Glass Transition Temperature of Polymer Thin Films." *Macromolecules* 34:9139-9142.

Urakawa, O., S. F. Swallen, M. D. Ediger, and E. D. von Meerwall. 2004. "Self-diffusion and viscosity of low molecular weight polystyrene over a wide temperature range." *Macromolecules* 37 (4):1558-1564. doi: Doi 10.1021/Ma0352025.

van Schoot, Jan, Koen van Ingen Schenau, Chris Valentin, and Sascha Migura. 2015. "EUV lithography scanner for sub-8nm resolution."

Vo, Timothy H., U. Gayani E. Perera, Mikhail Shekhirev, Mohammad Mehdi Pour, Donna A. Kunkel, Haidong Lu, Alexei Gruverman, Eli Sutter, Mircea Cotlet, Dmytro Nykypanchuk, Percy Zahl, Axel Enders, Alexander Sinitskii, and Peter Sutter. 2015. "Nitrogen-Doping Induced Self-Assembly of Graphene Nanoribbon-Based Two-Dimensional and Three-Dimensional Metamaterials." *Nano Lett.* 15 (9):5770-5777. doi: 10.1021/acs.nanolett.5b01723.

Vogel, Hans. 1921. "The law of the relation between the viscosity of liquids and the temperature." *Phys. Z* 22:645-646.

Walton, D. G., G. J. Kellogg, A. M. Mayes, P. Lambooy, and T. P. Russell. 1994. "A Free Energy Model for Confined Diblock Copolymers." *Macromolecules* 27 (21):6225-6228. doi: 10.1021/ma00099a045.

Wan, Lei, Ricardo Ruiz, He Gao, Kanaiyalal C. Patel, Thomas R. Albrecht, Jian Yin, Jihoon Kim, Yi Cao, and Guanyang Lin. 2015. "The Limits of Lamellae-Forming PS-b-PMMA Block Copolymers for Lithography." *ACS Nano* 9 (7):7506-14. doi: 10.1021/acsnano.5b02613.

Wang, Y. J., and O. K. C. Tsui. 2006. "Unconventional spinodal surface fluctuations on polymer films." *Langmuir* 22:1959-1963.

Wei, Qingshuo, Eunyoung You, Nicholas R. Hendricks, Alejandro L. Briseno, and James J. Watkins. 2012. "Flexible Low-Voltage Polymer Thin-Film Transistors Using Supercritical CO2-Deposited ZrO2 Dielectrics." *ACS Appl. Mater. Interfaces* 4 (5):2322-2324. doi: 10.1021/am300371d.

Wenzel, Robert N. 1936. "RESISTANCE OF SOLID SURFACES TO WETTING BY WATER." *Ind. Eng. Chem. Res.* 28 (8):988-994. doi: 10.1021/ie50320a024.

Williams, Malcolm L., Robert F. Landel, and John D. Ferry. 1955. "The Temperature Dependence of Relaxation Mechanisms in Amorphous Polymers and Other Glass-forming Liquids." *J. Am. Chem. Soc.* 77 (14):3701-3707. doi: 10.1021/ja01619a008.

Wong, J. S. S., L. A. Hong, S. C. Bae, and S. Granick. 2010. "Fluorescence Recovery after Photobleaching Measurements of Polymers in a Surface Forces Apparatus." *J. Polym. Sci. Part B Polym. Phys.* 48 (24):2582-2588. doi: Doi 10.1002/Polb.22118.

Wong, William S., and Alberto Salleo. 2009. *Flexible electronics: materials and applications*. Vol. 11. New York: Springer.

Wu, Mei-Ling, and Dong Wang. 2016. "Microdomain orientation control of PS-b-PMMA films enabled by wettability relay of graphene." *RSC Adv.* 6 (9):7527-7531. doi: 10.1039/C5RA24953H.

Wu, Souheng. 1970. "Surface and interfacial tensions of polymer melts. II. Poly(methyl methacrylate), poly(n-butyl methacrylate), and polystyrene." *J. Phys. Chem. A* 74 (3):632-638. doi: 10.1021/j100698a026.

Xia, Fengnian, Han Wang, Di Xiao, Madan Dubey, and Ashwin Ramasubramaniam. 2014. "Two-dimensional material nanophotonics." *Nat. Photonics* 8 (12):899-907. doi: 10.1038/nphoton.2014.271.

Xu, Li, Victor Selin, Aliaksandr Zhuk, John F. Ankner, and Svetlana A. Sukhishvili. 2013. "Molecular Weight Dependence of Polymer Chain Mobility within Multilayer Films." *ACS Macro Lett.* 2 (865):12-15.

Yamamoto, Shinpei, Muhammad Ejaz, Yoshinobu Tsujii, Mutsuo Matsumoto, and Takeshi Fukuda. 2000. "Surface Interaction Forces of Well-Defined, High-Density Polymer Brushes Studied by Atomic Force Microscopy. 1. Effect of Chain Length." *Macromolecules* 33 (15):5602-5607. doi: 10.1021/ma991733a.

Yan, Hugen, Xuesong Li, Bhupesh Chandra, George Tulevski, Yanqing Wu, Marcus Freitag, Wenjuan Zhu, Phaedon Avouris, and Fengnian Xia. 2012. "Tunable infrared plasmonic devices using graphene/insulator stacks." *Nat. Nanotechnol.* 7 (5):330-334. doi:

http://www.nature.com/nnano/journal/v7/n5/abs/nnano.2012.59.html#supplementary-information.

Yang, Hao-Cheng, Jianquan Luo, Yan Lv, Ping Shen, and Zhi-Kang Xu. 2015. "Surface Engineering of Polymer Membranes via Mussel-inspired Chemistry." *J. Membr. Sci.* 483:42-59. doi: http://dx.doi.org/10.1016/j.memsci.2015.02.027.

Yang, Qiuyan, Qun Xu, and Katja Loos. 2015. "Enhanced Polystyrene Surface Mobility under Carbon Dioxide at Low Temperature for Nanoparticle Embedding Control." *Macromolecules* 48 (6):1786-1794. doi: 10.1021/ma5025686.

Yang, Shixuan, Ying-Chen Chen, Luke Nicolini, Praveenkumar Pasupathy, Jacob Sacks, Su Becky, Russell Yang, Sanchez Daniel, Yao-Feng Chang, Pulin Wang, David Schnyer, Dean Neikirk, and Nanshu Lu. 2015. ""Cut-and-Paste" Manufacture of Multiparametric Epidermal Sensor Systems." *Adv. Mater.* 27 (41):6423-6430. doi: 10.1002/adma.201502386.

Yang, Z., Y. Fujii, F. K. Lee, C. -H. Lam, and O. K. C. Tsui. 2010a. "Glass Transition Dynamics and Surface Layer Mobility in Unentangled Polystyrene Films." *Science* 328:1676-1679.

Yang, Z., Y. Fujii, F. K. Lee, C. H. Lam, and O. K. Tsui. 2010b. "Glass transition dynamics and surface layer mobility in unentangled polystyrene films." *Science* 328 (5986):1676-9. doi: 10.1126/science.1184394.

Yang, Z., C. -H. Lam, E. DiMasi, N. Bouet, J. Jordan-Sweet, and O. K. C. Tsui. 2009. "Method to Measure the Viscosity of Nanometer Liquid Films from the Surface Fluctuations." *Applied Physics Letters* 94:251906.

Ye, C., C. G. Wiener, M. Tyagi, D. Uhrig, S. V. Orski, C. L. Soles, B. D. Vogt, and D. S. Simmons. 2015. "Understanding the Decreased Segmental Dynamics of Supported Thin Polymer Films Reported by Incoherent Neutron Scattering." *Macromolecules* 48:801-808.

Ye, Changhuai, Clinton G. Weiner, Madhusudan Tyagi, David Uhrig, Sara V. Orski, Christopher L. Soles, Bryan D. Vogt, and David S. Simmons. 2015. "Understanding the Decreased Segmental Dynamics of Supported Thin Polymer Films Reported by Incoherent Neutron Scattering." *Macromolecules*. doi: 10.1021/ma501780g.

Ye, Qian, Feng Zhou, and Weimin Liu. 2011. "Bioinspired Catecholic Chemistry for Surface Modification." *Chem. Soc. Rev.* 40 (7):4244-4258. doi: 10.1039/C1CS15026J.

Yoon, H., and G. B. McKenna. 2014. "Substrate Effects on Glass Transition and Free Surface Viscoelasticity of Ultrathin Polystyrene Films." *Macromolecules* 47 (24):8808-8818. doi: Doi 10.1021/Ma501630g.

Zangmeister, Rebecca A., Todd A. Morris, and Michael J. Tarlov. 2013. "Characterization of Polydopamine Thin Films Deposited at Short Times by Autoxidation of Dopamine." *Langmuir* 29 (27):8619-8628. doi: 10.1021/la400587j.

Zhang, Kai, Lei Zhang, Fung Ling Yap, Peng Song, Cheng-Wei Qiu, and Kian Ping Loh. 2016. "Large-Area Graphene Nanodot Array for Plasmon-Enhanced Infrared Spectroscopy." *Small* 12 (10):16. doi: 10.1002/smll.201503016.

Zhao, H., Y. J. Wang, and O. K. C. Tsui. 2005. "Dewetting induced by complete versus nonretarded van der Waals forces." *Langmuir* 21:5817-5824.

Zheng, X., M. H. Rafailovich, J. Sokolov, Y. Strzhemechny, S. A. Schwarz, B. B. Sauer, and M. Rubinstein. 1997. "Long-range effects on polymer diffusion induced by a bounding interface." *Phys. Rev. Lett.* 79 (2):241-244. doi: DOI 10.1103/PhysRevLett.79.241.

Zheng, X., M. Rafailovich, J. Sokolov, Y. Strzhemechy, and S. A. Schwarz. 1997. "Long-range effects on polymer diffusion induced by a bounding interface." *Physical Review Letters* 79:241-244.

Zhou, Yun-fei, Yong-bo Yuan, Ling-fang Cao, Jie Zhang, Hong-qi Pang, Jia-rong Lian, and Xiang Zhou. 2007. "Improved Stability of OLEDs with Mild Oxygen Plasma Treated PEDOT:PSS." *J. Lumin.* 122–123:602-604. doi: http://dx.doi.org/10.1016/j.jlumin.2006.01.236.

Zhu, Weinan, Maruthi N. Yogeesh, Shixuan Yang, Sandra H. Aldave, Joon-Seok Kim, Sushant Sonde, Li Tao, Nanshu Lu, and Deji Akinwande. 2015. "Flexible Black Phosphorus Ambipolar Transistors, Circuits and AM Demodulator." *Nano Lett.* 15 (3):1883-1890. doi: 10.1021/nl5047329.